TECHNISCHE UNIVERSITÄT MÜNCHEN
Ingenieurfakultät Bau Geo Umwelt
Professur für Hydromechanik

# Large-Eddy Simulation of the flow around a wall-mounted cylinder

Wolfgang Schanderl

Vollständiger Abdruck der an der Ingenieurfakultät Bau Geo Umwelt der Technischen Universität München zur Erlangung des akademischen Grades eines

Doktor-Ingenieurs

genehmigten Dissertation.

| | |
|---|---|
| Vorsitzender: | Prof. Dr. sc. techn. Peter Rutschmann |
| Prüfer der Dissertation: | 1. Prof. Dr.-Ing. Michael Manhart<br>2. Prof. Dr.-Ing. Oscar Link |

Die Dissertation wurde am 15.11.2017 bei der Technischen Universität München eingereicht und durch die Ingenieurfakultät Bau Geo Umwelt am 02.03.2018 angenommen.

Dies ist eine kumulative Dissertation basierend auf Veröffentlichungen in internationalen Fachzeitschriften.

# Abstract

Large-Eddy Simulation was conducted to investigate the flow around a circular cylinder mounted vertically on the flat bottom wall of an open channel. A boundary layer approaching such a cylinder causes a down-flow in the cylinder front, and thus high momentum fluid is brought close to the bottom wall. The interaction of this fluid with the wall constitutes a vortex structure with complex dynamics and enhanced wall shear stresses. Wanted or unwanted effects of this vortex structure in a vast number of engineering applications aroused the scientific interest in this kind of flow. The aim of this dissertation was to evaluate the wall shear stress in front of the cylinder, to describe how this wall shear stress is caused by the vortex system and the according near-wall flow structures and to work out the measures it takes to estimate this wall shear stress by a numerical simulation in a reliable way.

Among other measures, the data was validated by a comparison to the results of an associated experiment conducted by Ulrich Jenssen. The comparison included not only the inflow condition and the flow topology, but also the second and third order moments of the statistics of the flow field as well as the production, the convection and the turbulent transport of turbulent kinetic energy. Furthermore, a grid study demonstrated that the results were converged over grid refinement. In the region of interest, the grid resolution - less than two Kolmogorov length scales in the wall-normal direction and less than eight Kolmogorov length scales in the horizontal directions - was fine enough to resolve the bottom wall and to ensure that the influence of the subgrid-stress model was small.

The down-flow in the cylinder front was deflected in the upstream direction when it hit the bottom wall and was subject to large acceleration. This acceleration gave rise to a negative production of turbulent kinetic energy which in turn prevented an increase of the turbulence level there and caused a region of relatively calm turbulence. As a consequence, the wall shear stress scaled with the square-root of the Reynolds number similar to the one of a laminar boundary layer. Nevertheless, as the boundary layer along the bottom wall which caused this wall shear stress was in a non-equilibrium state and three dimensional, all terms of the near-wall stress balance - including the ones based on the wall-parallel gradients - had to be considered to close this balance and thus influence a possible modelling of the wall shear stress. However, to resolve the according near-wall region a relative fine data resolution was necessary as the significant three-dimensional gradients reached close to the wall. The viscous sublayer was thinner than five wall units. The fact that the linear part was that thin, the necessity to capture all gradients and the consequence that assumptions usually employed for wall modelling do not apply on the flow considered make the wall shear stress estimation challenging. This can explain why the wall shear stress was underestimated in previously published studies.

# Zusammenfassung

Mit Large-Eddy Simulationen wurde die Strömung um einen senkrecht in einem Freispiegelgerinne stehenden Kreiszylinder untersucht. Eine Grenzschichtströumung, die auf so einen Zylinder trifft, erzeugt vor dem Zylinder eine Abwärtsströmung, wodurch Fluid mit großem Impuls in den Bereich nahe der Gerinnesohle gelangt. Durch die Interaktion dieses Fluids mit der Gerinnesohle entsteht ein Wirbelsystem mit komplexer Dynamik und erhöhte Wandshubspannungen an der Sohle. Das wissenschaftliche Interesse an dieser Art von Strömungen resultiert aus gewollten oder ungewollten Effekten, das dieses Wirbelsystem in einer Vielzahl von Anwendungsfällen hat. Der Schwerpunkt dieser Dissertation liegt darauf, die Wandschubspannung vor dem Zylinder zu bestimmen, zu beschreiben, wie diese Wandschubspannung durch das Wirbelsystem und die zugehörige wandnahe Strömung erzeugt wird und abzuschätzen, unter welchen Bedingungen die Wandschubspannung verlässlich anhand einer numerischen Simulation vorhergesagt werden kann.

Validiert wurden die vorgestellten Daten unter anderem anhand der Messungen aus einem zugehörigen, von Ulrich Jenssen durchgeführten Experiment. Es wurden nicht nur die Einlaufrandbedingung und die Strömungstopologie aus Simulation und Experiment verglichen, sondern auch die Momente zweiter und dritter Ordnung der Strömungsstatistik sowie die Produktion, die Konvektion und der turbulente Transport turbulenter kinetischer Energie. Eine Gitterstudie zeigte zudem, dass die Ergebnisse über die Gitterweite konvergiert sind. In der untersuchten Region war die Gitterweite klein genug (kleiner als das zweifache Kolmogorovsche Längenmaß in vertikaler Richtung und kleiner als das achtfache in den horizontalen Richtungen), um die viskose Unterschicht an der Gerinnesohle aufzulösen und um sicherzustellen, dass der Einfluss des Turbulenzmodells gering ist.

Die Abwärtsströmung vor dem Zylinder wurde an der Sohle des Gerinnes nach oberstrom abgelenkt, wodurch die wandnahe Strömung starke beschleunigte. Die dadurch verursachte negative Produktion turbulenter kinetischer Energie verhinderte einen Anstieg des Turbulenzeniveaus und erzeugt so eine Region mit relativ wenig Turbulenz. Die Amplitude der Wandschubspannung skalierte deshalb ähnlich der einer laminaren Grenzschicht mit der Quadratwurzel der Reynoldszahl. Weil die Grenzschicht an der Bodenplatte des Gerinnes dreidimensional und im Ungleichgewicht war, mussten alle Terme der Spannungsbilanz berücksichtigt werden, um die Bilanz zu schließen und beeinflussen so eine mögliche Wandmodellierung - auch die Terme, die Gradienten in wandparallele Richtungen beinhalten. Eine relativ hohe Auflösung der Datenpunkte ist notwendig, um den wandnahen Bereich aufzulösen, da die dreidimensionalen Geschwindigkeitsgradienten sehr nahe an die Wand heran reichen. Die lineare Unterschicht ist deutlich dünner als fünf Wandeinheiten. Dass alle Gradienten berücksichtigt werden müssen, dass die lineare Unterschicht so dünn ist und dass deshalb Annahmen nicht zutreffen, die gemeinhin bei der Wandmodellierung getroffen werden, erschwert es, die Wandschubspannung zu bestimmen und kann erklären, warum die Wandschubspannung in bisherigen Publikationen unterschätzt wurde.

# Preface

This cumulative dissertation is based on the following journal papers:

- W. Schanderl and M. Manhart. Reliability of wall shear stress estimations of the flow around a wall-mounted cylinder. *Comp. and Fluids*, 128, pages 16-29, 2016.
- W. Schanderl, U. Jenssen, C. Strobl and M. Manhart. The structure and budget of turbulent kinetic energy in front of a wall-mounted cylinder. *Journal of Fluid Mechanics*, 827, pages 285-321, 2017.
- W. Schanderl, U. Jenssen and M. Manhart. Near-wall stress balance in front of a wall-mounted cylinder. *Flow, Turbulence and Combustion*, DOI 10.1007/s10494-017-9865-3, 2017
- W. Schanderl, and M. Manhart. Dissipation of turbulent kinetic energy in a cylinder wall junction flow. Submitted to *Flow, Turbulence and Combustion*, 2017
- W. Schanderl, U. Jenssen, C. Strobl and M. Manhart. Wall shear stress scaling in front of a wall-mounted cylinder. *Draft*, 2017.

The first three publications have been published already. The fourth paper was submitted in October 2017. The last paper is a draft and will be submitted in late 2017. Beside these journal publications, the following contributions to conferences originated from this dissertation. All of them except the ones for the European Turbulence Conferences (ETC) included a short peer-reviewed paper.

- U. Jenssen, W. Schanderl and M. Manhart. Cylinder wall junction flow: Particle Image Velocimetry and Large Eddy Simulation. *11th International ERCOFTAC Symposium on Engineering Turbulence Modelling and Measurements*, Palermo, 2016.
- W. Schanderl and M. Manhart. Large-eddy simulation of the flow around a wall-mounted circular cylinder. *3rd IAHR Europe Congress*, Porto, 2014.
- W. Schanderl and M. Manhart. Reliability of wall shear stress estimations in front of a wall-mounted cylinder. *Direct and Large Eddy Simulation 10*, Limassol, 2015.
- W. Schanderl and M. Manhart. Non-equilibrium near wall velocity profiles in the flow around a cylinder mounted on a flat plate. *15th European Turbulence Conference*, Delft, 2015.
- W. Schanderl, O. Chmiel, P. Huttner, S. Zischkale and M. Manhart. Application and validation of sediment erosion models to time dependent wall shear stresses around a wall-mounted circular cylinder. *7th River Flow Conference*, Lausanne, 2014.
- W. Schanderl, O. Link and M. Manhart. Discussion of the impact of pressure fluctuations on local scouring. In Book of Proceedings of *International Symposium on River Sedimentation*, Stuttgart, 2016.
- W. Schanderl, U. Jenssen and M. Manhart. Turbulence structure in front of a wall-mounted cylinder. *11th International ERCOFTAC Symposium on Engineering Turbulence Modelling and Measurements*, Palermo, 2016.

- W. Schanderl and M. Manhart. Dissipation in front of a wall-mounted bluff body. *Direct and Large Eddy Simulation 11*, Pisa, 2017.
- W. Schanderl and M. Manhart. The role of pressure fluctuations in the turbulent kinetic energy budget. *16th European Turbulence Conference*, Stockholm, 2017.

Even though this dissertation is a cumulative one, I have tried to maintain the structure of a monograph. There is an introduction to lead the reader into the topic, there is a part explaining and justifying the used methods and at the very end there is a discussion which evaluates the achieved results. However, the part presenting the scientific results was skipped and replaced by a one-page summary of each of the five journal papers listed above. The papers are included in the appendix. Furthermore, the appendix contains a declaration of consent between the authors for each paper, which documents the contribution of the individual authors to the corresponding paper. At the very end of the appendix, the permissions from the publishers to use the already published papers in the scope of this dissertation are included.

# Contents

# List of Tables

# List of Figures

# Nomenclatur

The definitions given below regard to the definitions in the synoptic part of this dissertation. The definitions in the journal papers this dissertation is based on may vary.

### Roman letters

| | |
|---|---|
| $C$ | Convection of turbulent kinetic energy |
| $c_f$ | Friction coefficient |
| $c_p$ | Pressure coefficient |
| $D$ | Cylinder diameter |
| $E$ | Kinetic energy |
| $g$ | Gravity constant |
| $g$ | Component of the gravity vector in the $i$-direction |
| $H$ | Flow depth |
| $k$ | Turbulent kinetic energy |
| $p$ | Pressure |
| $P$ | Production of turbulent kinetic energy |
| $R$ | Residual of the budget of turbulent kinetic energy |
| $Re$ | Reynolds number |
| $Re_D = \frac{u_b D}{\nu}$ | Reynolds number |
| $s'$ | Fluctuation of the strain rate tensor $S$ |
| $T_{conv}$ | Turbulent convection of turbulent kinetic energy |
| $T_{pres}$ | Pressure transport of turbulent kinetic energy |
| $T_{visc}$ | Viscous diffusion of turbulent kinetic energy |
| $u_b$ | Bulk velocity in the symmetry plane of the inflow |
| $u_i$ | Velocity component in the $i$-direction |
| $u'_i$ | Fluctuation of the velocity component $u_i$ |
| $u_K$ | Kolmogorov velocity scale |
| $W$ | Width of the open channel |
| $x$ | Coordinate in the streamwise direction |
| $x_i$ | Coordinate in the $i$-direction |
| $\Delta x$ | Grid spacing in the $x$-direction |
| $\Delta x^+$ | Grid spacing in the $x$-direction in wall units |
| $\Delta x_i$ | Grid spacing in the $i$-direction |

| | |
|---|---|
| $y$ | Coordinate in the spanwise direction |
| $\Delta y$ | Grid spacing in the $y$-direction |
| $\Delta y^+$ | Grid spacing in the $y$-direction in wall units |
| $z$ | Coordinate in the vertical direction |
| $z^+$ | Coordinate in the vertical direction in wall units |
| $\Delta z$ | Grid spacing in the $z$-direction |
| $\Delta z^+$ | Grid spacing in the $z$-direction in wall units |
| $\Delta z^+_{wall}$ | Grid spacing in the $z$-direction in wall units directly at the bottom wall |

## Greek letters

| | |
|---|---|
| $\epsilon$ | Dissipation |
| $\eta_K$ | Kolmogorov length scale |
| $\nu$ | Kinematic viscosity |
| $\nu_t$ | Modelled viscosity, turbulent viscosity |
| $\rho$ | Density |
| $\tau^{SGS}$ | Subgrid-stress tensor |
| $\tau_w$ | Wall shear stress |
| $\tau_{w,i}$ | Component of the wall shear stress vector in the $i$-direction |

## Symbols and operators

| | |
|---|---|
| $\frac{D}{Dt}$ | Material derivative |
| $\frac{\partial}{\partial x_i}$ | Partial derivative in the $i$-direction |
| $\langle \Phi \rangle$ | Time average of a quantity $\Phi$ |
| $\overline{\Phi}$ | A quantity $\Phi$ filtered over a cell volume |

## Abbreviations

| | |
|---|---|
| DNS | Direct numerical simulation |
| IBM | Immersed boundary method |
| LES | Large-eddy simulation |
| PIV | Particle image velocimetry |
| RANS | Reynolds-averaged simulation |
| WALE | Wall-adapting local eddy-viscosity model |

# 1. Introduction

Due to its wide relevance for engineering applications, the flow around bluff bodies mounted on a flat plate has attracted scientific interest for several decades. Wanted or unwanted effects from the distinct vortex system in such a flow arise at the mounting of turbo machinery blades, at the junction of an aircraft's body to its wing or at the struts inside a heat exchanger. The flow around wall-mounted bodies has attracted the attention of our research group because of its impact on bridge piers placed in rivers and the surrounding river bed. The flow field around the bridge pier exhibits a distinct vortex system and thus locally increased velocities and pressure fluctuations, which in turn can trigger erosion and cause local scouring. However, how the scouring process is caused by the vortex system and its fluctuations is not fully understood yet. The highly charged nature of this topic becomes clear when considering that the main reason for the loss of stability of bridges is scouring around its piers (Imhof, 2004).

When predicting the scouring process around an obstacle, one has to face two challenges. A sediment transport model has to be applied to model the erosion and deposition of sediment caused by the flow appropriately. However, to estimate the erosion due to the flow, the flow itself has to be predicted first. If the prediction of the flow and the stresses it exerts on the sediment is imprecise, the effects of these stresses are imprecise as well and the sediment transport model thus has to be calibrated. Our project tackles this issue by investigating the flow field and the according wall shear stresses - which is assumed to be the main agent of scouring - around a cylinder mounted on a flat plate. The emphasis is placed on the region in front of the cylinder, since the scouring is typically observed to start in the lateral front and the equilibrium scour hole is deepest in the symmetry plane in front of the cylinder (Link et al., 2008). This study explicitly investigates the flow field and its dynamics solely. The geometry of the bottom plate is a flat plate for all considerations.

In section 1.1, the state of the art regarding the flow field in front of a wall-mounted bluff body is summarised briefly. This literature review shall elaborate the main open questions regarding such a flow which are discussed by the research community at the moment. In section 1.2 an outlook is given on what this study contributes to the ongoing discussion. Section 1.3 gives an overview over the structure of the subsequent thesis.

## 1.1. Bluff body flow - the state of the art

The large interest in the flow around wall-mounted bluff bodies has led to a vast number of scientific studies addressing this topic. It is impossible to discuss all of them in the scope of this dissertation. However, a literature review is made easier by two points, namely the limited number of degrees of freedom and the invariance of the flow to minor changes of the geometry and the Reynolds number.

Even though the flow around such a wall-mounted bluff body is complex and bears rich dynamics, such flow cases can be described by a limited number of geometric and dynamic parameters. The geometry of a cube, plate or circular cylinder mounted on a plate is simple to describe. The number of degrees of freedom which have to match between the different setups to enable comparison is thus limited.

Second, the flow structure in general is invariant to minor changes of the geometry, especially the shape of the body, and the Reynolds number. Even though the variety of geometries investigated in the past is huge, most of the work is done on single bodies placed on a flat surface, especially circular cylinders (e.g. (Dargahi, 1989)), streamlined wings (e.g. (Devenport and Simpson, 1990)) and blocks/cubes (e.g. (Castro and Robins, 1977; Martinuzzi and Tropea, 1993)) as summarised in detail by Simpson (2001). Comparisons of the flow in front of a circular cylinder with the one in front of a wing-shaped cylinder show only marginal differences (Simpson, 2001). Also, Martinuzzi and Tropea (1993) investigated the flow around a wall-mounted cube, and even though a cube is obviously more bluff than a circular cylinder, the flow topology they observed was in general the same as the one for more slender bodies. In addition, various studies (Roulund et al., 2005; Apsilidis et al., 2015; Kirkil and Constantinescu, 2015) suggest that the flow pattern in general does not change with the Reynolds number as long as the Reynolds number is moderate[1]. Schofield and Logan (1990) summarised: "The responses of a wide range of turbulent shear layers to an obstacle attached to a wall can be collapsed if appropriate non-dimensionalising length scales are used." Even though the exact position and the amplitude of certain flow features differ between the studies discussed in the following, the flow topology can be expected to be similar in these flow cases.

Hence, the following discussion does not distinguish between the exact shapes of the bodies and different moderate Reynolds numbers. Due to its relevance for the scouring process, the focus is on studies addressing the flow in front of the body.

### 1.1.1. Time-averaged flow field

The time-averaged flow in front of a wall-mounted bluff body is characterised by a distinct vortex system close to the bottom wall with spanwise axis of rotation. This vortex system is illustrated in figure 1.1, where the streamlines in the symmetry plane in front of the body were plotted. The data was taken from a simulation conducted in the scope of this dissertation. As the body was a circular cylinder, the vertical coordinate $z$ and the streamwise coordinate $x$ were normalised by the cylinder diameter $D$. The main vortex denoted as V1 obtains its momentum from a down-flow along the flow facing side of the body. The down-flow in turn is driven by a vertical pressure gradient, which is caused by the boundary layer approaching the body. When the down-flow meets the bottom wall, most of it is deflected in the upstream direction along this wall (black and red streamlines in figure 1.1), while a minor amount (green) forms a small corner vortex V3 directly at the junction of the body and the bottom wall. Parts of the fluid moving in the upstream direction (black) roll up

---

[1] The ranges can be defined as follows: $Re < 5 \cdot 10^3$: low Reynolds number, including laminar flow; $5 \cdot 10^3 < Re < 5 \cdot 10^5$: moderate Reynolds number; $5 \cdot 10^5 < Re$: large Reynolds number.

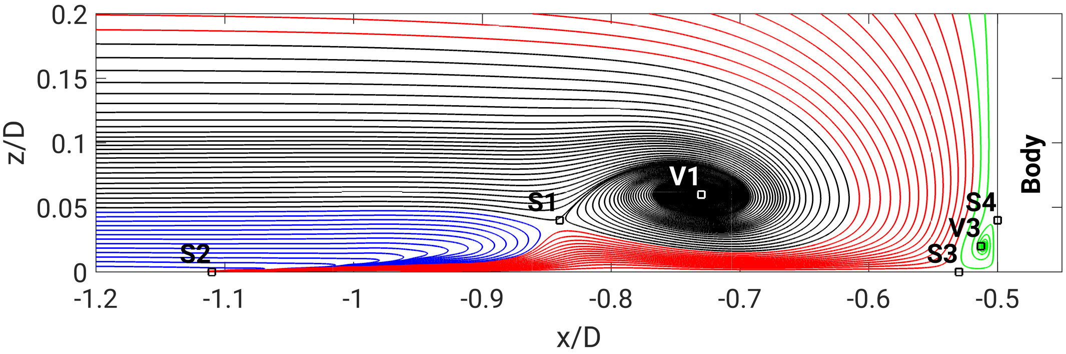

**Figure 1.1:** Streamlines in the symmetry plane in front of the cylinder.

and form the main vortex V1. Other parts (red) establish an upstream-directed jet along the bottom wall which passes under V1.

A fluid particle moving along a time-averaged streamline through the wall jet underneath vortex V1 is subject to a distinct pattern of acceleration and deceleration. The down-flow entrains large momentum fluid towards the bottom wall. Due to the adverse pressure gradient in front of the body, the fluid accelerates in the upstream direction along the bottom wall first. Afterward, the jet decelerates approximately when passing underneath the core of vortex V1. Here the time-averaged representation of the jet gains height and lifts off the wall. The jet reaches its maximum height under stagnation point S1, which borders vortex V1 in the upstream direction. The streamline patterns along the bottom wall (Paik et al., 2007) and the images of an oil film visualisation (Devenport and Simpson, 1990) indicate a large amount of fluid to leave the region in front of the body in the spanwise direction here. The rest of the fluid accelerates again towards the most upstream stagnation point S2.

The fluid has to bypass the body, thus the flow accelerates in the spanwise direction, and the vortex system is stretched and bent around the body. Figure 1.2 shows two different instantaneous samples of the flow field around the cylinder taken from a simulation conducted in the scope of this dissertation. Evaluated was the top view on isosurfaces of the q-criterion, which is the second invariance of the velocity gradient tensor. The colors in figure 1.2 are not linked to the ones in figure 1.1. Seen from above the resulting vortex has the shape of a horseshoe, wherefore the vortex system has its name: horseshoe vortex.

The basic time-averaged structure (down-flow - main vortex V1 - corner vortex V3 - wall jet) is uncontested by the community investigating junction flows (Dargahi, 1989; Devenport and Simpson, 1990; Simpson, 2001; Escauriaza and Sotiropoulos, 2011; Apsilidis et al., 2015). The discussion is on the vortices accompanying the main vortex, especially on the recirculation zone downstream of S2 and upstream of S1. Dargahi (1989) did hydrogen bubble visualisations of the flow in front of a wall-mounted cylinder at a Reynolds number of $Re_D = 39000$ based on the diameter of the cylinder $D$ and the bulk velocity of the incoming flow. Dargahi observed the main vortex V1 to be convoyed by an upstream vortex V2 of approximately the same size, rotating in the same direction. This assumption was confirmed by Escauriaza and Sotiropoulos (2011), who conducted detached-eddy simulation of the same setup. They observed a flat but long drawn-out vortex upstream of V1. Such

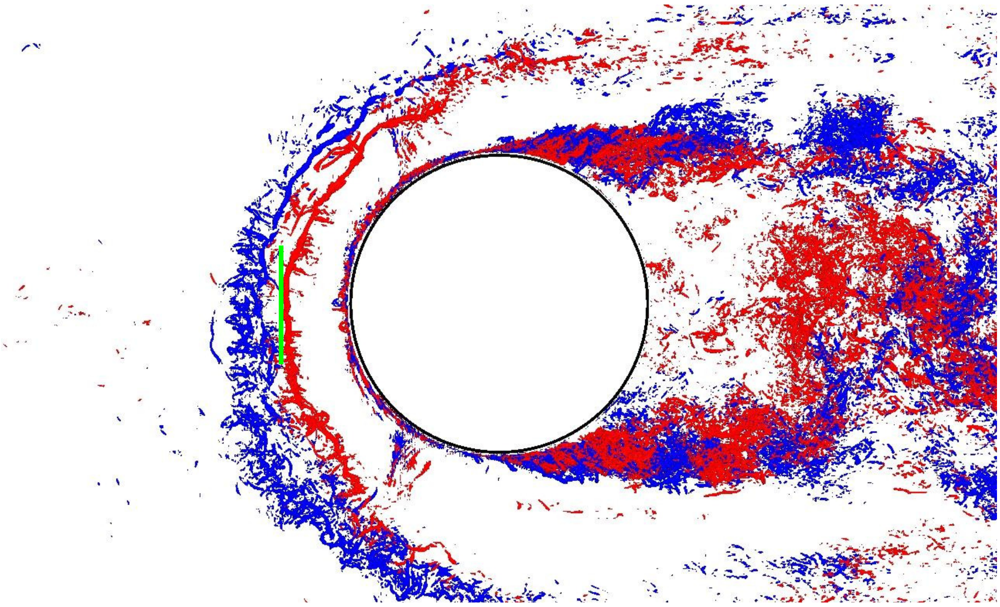

**Figure 1.2:** Top view on two instantaneous samples of the flow field around the cylinder. Presented are iso-surfaces of the q-criterion. The colors are not linked to the colors in figure 1.1.

a vortex was also observed by Apsilidis et al. (2015), who did particle image velocimetry at a slightly higher Reynolds number. However, in their experiment it was significantly smaller than the main vortex. Apsilidis et al. (2015) stated that this small vortex V2 is the time-averaged representation of a train of various small instantaneous vortices. In contrast, Devenport and Simpson (1990) observed a zone of weak backflow upstream of the main vortex in their experiment. Devenport and Simpson (1990) applied oil film visualisation as well as laser doppler anemometry to investigate the flow field around a wing-shaped cylinder at a Reynolds number of $Re_D = 119000$. In their impressive publication, they reported backflow in the near wall layer in this region, but they did not report any further vortex upstream of V1. Krajnović (2011) conducted large-eddy simulation of the flow around a finite height cylinder at $Re_D \approx 20000$ and mentioned an additional vortex V2 upstream of the main vortex V1. However, this point was not further elaborated in his study. The rather weak evidence given by Krajnović (2011) for vortex V2 does not indicate the fluid to make a full turn or V2 to have a defined vortex core. The presented streamline pattern in fact can also represent a backflow zone as discussed by Devenport and Simpson (1990).

The wall shear stress distribution at the bottom wall is the footprint of the flow above this wall. Devenport and Simpson (1990) did not measure the wall shear stress explicitly but interpreted their oil film visualisation. They reported two distinct regions of negative wall shear stress: A region of strong wall shear stress underneath vortex V1 and the wall jet and an additional region of low negative wall shear stress upstream of the first region, where the jet accelerates a second time. Furthermore, according to Devenport and Simpson (1990) these two regions are not separated by a region of positive wall shear stress (which would indicate an additional vortex rotating in the opposite direction of V1, or at least a region of positive streamwise velocity) but they are connected by a thin strip of negative wall shear stress of small amplitude.

Dargahi (1989) reported the wall shear stress amplification in the symmetry plane in front of the cylinder relative to the wall shear stress in the undisturbed flow without bluff body. In contrast to Devenport and Simpson (1990), he documented only one broad peak of negative wall shear stress, which was located underneath vortex V1 and the wall jet. Dargahi (1989) did not report a second region of enhanced wall shear stress, even though he assumed the vortex system to consist of more than one vortex close to the wall. Upstream of the documented peak the wall shear stress became positive and increased towards the undisturbed value. There was no footprint of an additional vortex V2 or of a backflow zone upstream the main vortex. Even though the wall shear stress distribution documented by Dargahi (1989) obviously does not fit to the topology of the corresponding near wall flow, it was repeatedly applied to validate numerical results. However, one has to ask the question how reliable the wall shear stress distribution measured by Dargahi (1989) is and hence the results validated by and matching to this wall shear stress.

### 1.1.2. Dynamics of the flow field

The flow topology described above is the average of instantaneous samples of a highly dynamic flow field. Similar to the time-averaged topology, the main mechanism of these dynamics is uncontested by the research community. Devenport and Simpson (1990) found the main vortex not to fluctuate randomly but to jump between two preferred modes. In the so-called backflow mode, the main vortex V1 is further upstream of the cylinder while the wall jet impinges far into the oncoming boundary layer. The so-called zero-flow mode is characterised by V1 being closer to the cylinder. The wall jet does not penetrate the oncoming boundary layer but lifts off the bottom wall and ejects vertically directly upstream of V1. The corresponding movement of the main vortex is also illustrated by the two different instantaneous samples of the flow field in figure 1.2. In the red sample, V1 is located closer to the cylinder, while it is further upstream in the blue sample. However, it should be noted that these two positions do not necessarily indicate the preferred positions of V1 in the backflow and zero-flow mode, since the two presented samples are chosen randomly.

The bimodal dynamics of the horseshoe vortex system have enormous impact on technical applications. According to Simpson (2001) the ”bimodal aperiodic chaotic large-scale horseshoe vortex phenomena [...] are responsible for observed high turbulence intensities, surface pressure fluctuations, heat transfer rates, and scour in front of the obstacle.” However, the discussion on the exact bimodal process and what triggers this process is still going on. Devenport and Simpson (1990) suggested that the flapping process is triggered by turbulent structures in the incoming flow. Rotational fluid packets of low momentum entrained in the vortex system are ”particularly susceptible to cross-stream pressure gradients and [are] lost fairly rapidly” from the region in front of the body (Devenport and Simpson, 1990). These fluid packets cause a relatively small recirculation zone (zero-flow mode), and the wall jet is not able to penetrate into the oncoming boundary layer (Devenport and Simpson, 1990). In contrast, irrotational fluid packets of large momentum will presumably maintain their irrotationality, they are less susceptible for spanwise acceleration and thus form a jet along the bottom wall as well as a larger recirculation zone (backflow mode) (Devenport and Simpson, 1990). In the experiment of Devenport and Simpson (1990), the boundary layer was not covering the whole height of the approaching flow. They thus concluded that the rotational low momentum fluid packets stem from the outer region of the boundary layer and the irrotational large momentum packets from the free stream. However, the bimodal dynamics of the vortex system were also observed by Escauriaza and Sotiropoulos (2011). In their detached-eddy simulation a fully-developed boundary layer simulated by a separated Reynolds-averaged simulation was applied as inflow condition. Such an inflow profile does not exhibit a region of free stream since the boundary layer is covering the whole height of the inflow profile. Furthermore, as the inflow was pre-simulated by a Reynolds-averaged approach, it only contains a time-averaged and thus constant level of turbulence. The rotation and the momentum of fluid packets entrained into the horseshoe vortex system does not fluctuate in such a simulation. Since the bimodal dynamics were still observed, fluctuations in rotation and momentum of the incoming flow cannot explain these dynamics.

Since then, various studies that investigated the bimodal dynamics of the horseshoe vortex based on the observations of Devenport and Simpson (1990) were published. There are various tools to capture these phenomena. From inspecting a sequence of snapshots of spanwise vorticity distributions, Paik et al. (2007) concluded a complex interaction of the main vortex V1 and the bottom wall to cause the bi-modality. In a well-organised state (backflow mode), the vicinity of V1 to the wall "leads to the extraction of a tongue of wall vorticity of opposite sign" (Paik et al., 2007) than the vorticity of V1. These tongues of counteracting vorticity wrap around the main vortex and cause it to break down. This less organised structure is then washed downstream towards the bluff body (zero-flow mode). In addition, by applying proper orthogonal decomposition Paik et al. (2007) observed this process to be quasiperiodic and to be dominated by a small number of frequencies.

Among other analysis, Apsilidis et al. (2015) did a frame by frame inspection of their particle image velocimetry data in the symmetry plane in front of a wall-mounted cylinder. Furthermore, they discussed probability density functions of the position of the core of V1 as well as of the velocity close to the bottom wall. They suggested to establish a third mode next to the backflow and the zero-flow mode, the so-called intermediate mode. In the latter, none of the features associated with the original modes is present. Apsilidis et al. (2015) also suggested to decouple the position of the main vortex from the state of the wall jet. According to them, the jet in the backflow mode and the main vortex in its position further away from the cylinder are not necessarily connected. In the observations of Devenport and Simpson (1990), these phenomena were linked co-actively.

The advantage of inspecting instantaneous samples of the flow field frame by frame is that the examined data represent a flow field which actually occurred in the simulation or experiment. However, due to the chaotic component of turbulent flow each instantaneous flow topology is different. Thus, one has to step gently when drawing general conclusions from a randomly chosen set of instantaneous flow topologies, since the observed features may be contained in the chosen set of samples only, but not in a different set. Information contained by the disregarded samples is lost.

In contrast, time-averaged data represents artificial fields which never had appeared in the flow. Information regarding flow fields as they had actually happened is lost in the averaging process. However, every instantaneous samples contributes equally to the time-averaged data and the uncertainty of choosing some samples and disregarding the others is avoided. Approaches based on this time-averaged data aim in capturing the flow dynamics by examining the statistics of the flow field an its higher order moments. Especially these higher order moments (covariance, skewness, kurtosis) contain information about the correlation of individual flow features which can help to understand the dynamic processes. Furthermore, many time-averaged physical processes can be described by these moments of higher order, e.g. the production, the turbulent transport and the dissipation of turbulent kinetic energy. The understanding of these processes can help to understand the flow dynamics itself. Thus, some of these quantities (production and parts of the turbulent transport) are discussed in almost all aforementioned studies. However, it is challenging to evaluate the full budget of turbulent kinetic energy[2]. On the one hand, one needs the full three dimensional data of the flow to be able to capture every single term of the budget, which is hard achieve in most experimental setups. On the other hand, various terms are based on spatial gradients. An accurate estimation of these gradients in turn requires a high spatial resolution, which is costly in both experimental and numerical resources. Nevertheless, the evaluation of the full turbulent kinetic energy budget based on the explicit estimation of every single term might valuably contribute to the ongoing discussion on the dynamics of the horseshoe vortex system in front of a wall-mounted bluff body. The understanding of the dynamics of the vortex system is crucial to predict the flow in the near-wall region. The latter in turn is what determines the wall shear stress.

## 1.2. Contribution of this study

In this dissertation highly resolved large-eddy simulation (LES) of the flow around a circular cylinder mounted on the flat bottom wall of an open channel at three moderate Reynolds numbers is presented. The evaluation of the results shall contribute to the ongoing discussion on the horseshoe vortex system and elaborate the factors that determine the corresponding wall shear stress. In particular, the following questions are investigated:
(i) **To what extend does the inflow profile influence the horseshoe vortex system and the wall shear stress distribution?** As Kirkil and Constantinescu (2015) pointed out, the accurate prediction of the flow features in front of a wall-mounted bluff body by a numerical simulation requires an unsteady, eddy-resolving inflow boundary condition. The present study aims in a detailed comparison of the flow features resulting from a fully-developed, turbulent open-channel flow as inflow condition to those resulting from less sophisticated inflow conditions. This way the effect of the inflow condition is isolated and examined.
(ii) **What technical measures (in terms of wall resolution) does it take to measure the wall shear stress around a wall-mounted cylinder in a reliable way?** As pointed out in section 1.1.1, the time-averaged wall shear stress distribution presented by Dargahi (1989) is widely used to validate numerical results. However, it is not consistent with the time-averaged flow topology above the corresponding wall. Can this discrepancy be explained by an insufficient data resolution at the wall? The present study discusses the wall shear

---

[2] In this context also the impressive study of Hussein and Martinuzzi (1996) should be mentioned, who investigated the budget of turbulent kinetic energy at the upper end of a wall-mounted cube. They took special care to evaluate as many terms as possible and gained the remaining terms from the closure of the budget.

stress distribution and links it to the according flow topology. Furthermore, the influence of the grid resolution on the results is evaluated.

(iii) **How do the outer flow and the vortex system interact with the near-wall flow and thus the wall shear stress?** To gain further insight into the dynamics of the vortex system, the complete budget of turbulent kinetic energy is evaluated and documented in detail. This evaluation includes an explicit estimation of the dissipation rate. The investigation of the budget of turbulent kinetic energy is accompanied by an evaluation of the stress balance in the near-wall flow. This way it can be highlighted which flow features of the outer flow play a significant role in the stress balance of the near-wall flow and therefore directly act on the wall shear stress.

(iv) **How does the wall shear stress scale with the Reynolds number?** Even though most practical engineering problems have large Reynolds numbers, both experimental and numerical studies are limited to low and moderate Reynolds numbers due to the challenge of resolving the near-wall layer. Is there a distinct scaling behavior of the wall shear stress which allows to draw conclusions from lower Reynolds number flows to higher Reynolds number flows? This question is addressed by the evaluation of the wall shear stress at three different moderate Reynolds numbers and the corresponding wall shear stress scaling.

## 1.3. Structure of this thesis

The questions defined in section 1.2 are addressed in the following way. Chapter 2 describes the investigated physical setup. How this setup is transformed into a numerical simulation is explained afterward: Chapter 3 introduces the mathematical expressions describing the flow and chapter 4 the numerical discretisation of these mathematical expressions. The validation and the known limitations of the applied approach are discussed in chapter 5. Subsequently, the chapters 6 to 10 give a short summary of the results published in the journal papers this dissertation is based on. The publications themselves can be found in the appendix. If the defined goals of this dissertation are achieved is assessed in chapter 11.

# 2. Flow configuration

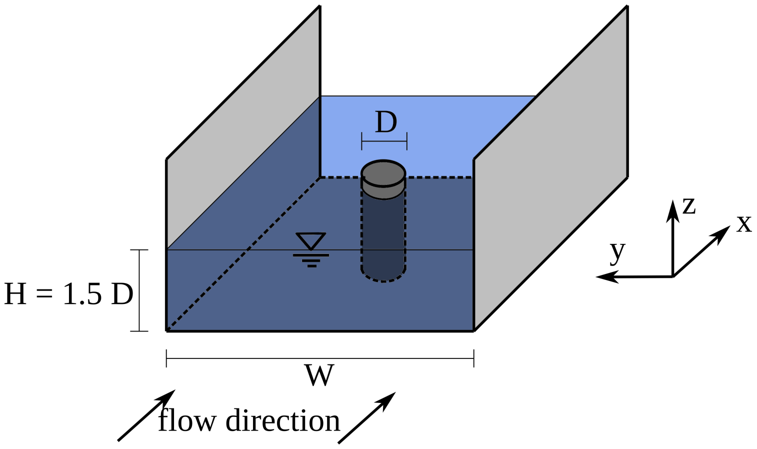

**Figure 2.1:** Setup investigated: A cylinder was placed vertically in a straight flume. The origin of the coordinate system was at the junction of bottom wall and cylinder axis.

The questions defined in section 1.2 were addressed by investigating the flow around a circular cylinder placed vertically in a straight water channel with free surface. The Froude number was considered small, and the Reynolds numbers were $Re_D = 20000$, $Re_D = 39000$ and $Re_D = 78000$ based on the cylinder diameter $D$ and the velocity of the incoming flow averaged over the whole cross section. The setup is sketched in figure 2.1. The water depth was $H = 1.5D$. The flume had a width of $W = 11.7D$ in the low and the medium Reynolds number case and $W = 7.8D$ in the large Reynolds number simulation. This was done to assure comparability to an associated experiment (Jenssen et al., 2016; Schanderl et al., 2017c). In the experiment, the water depth had to be increased in the large Reynolds number case to keep the Froude number small. As the ratio of flow depth to cylinder diameter was considered to have a larger influence on the flow than the width to diameter ratio, the diameter was increased to keep $H = 1.5D$. This resulted in a smaller width to diameter ratio. The inflow was a fully-developed, turbulent open-channel flow including the secondary flow structures of Prantl's second kind (Nezu and Nakagawa, 1993).

The configuration had been chosen such that it was consistent with former experiments of our research group (Pfleger, 2011). It differed slightly from the experiment of Dargahi (1989) in terms of the flow depth, which was $H = 1.33D$ there. The experiments of Apsilidis et al. (2015) were conducted in the same range of Reynolds numbers but with a significantly smaller ratio of boundary layer thickness to cylinder diameter. The body in the experiments of Devenport and Simpson (1990) was a wing-shaped cylinder. Furthermore the investigated Reynolds number was larger while the ratio of the boundary layer thickness to cylinder diameter was smaller in their setup. However, as discussed in section 1.1, the flow topology and its features were similar in all these studies.

# 3. Governing equations

In the previous chapter the physical flow configuration was introduced. However, to be examined the flow physics needs to be expressed by mathematical equations. This chapter gives a brief overview of the equations by which Newtonian flow can be described according to the argumentation of Pope (2011) and Schlichting and Gersten (2006). Afterward, chapter 4 addresses how these equations were discretised numerically.

## 3.1. Navier-Stokes and Reynolds equations

When describing fluid motion, two fundamentals have to be considered: the conservation of mass and the conservation of momentum[1]. In an incompressible flow, the conservation of mass is fulfilled if the divergence of the flow field is zero:

$$\frac{\partial u_i}{\partial x_i} = 0 \tag{3.1}$$

The Navier-Stokes equations for constant-property Newtonian flow

$$\rho \frac{D u_i}{D t} = -\frac{\partial p}{\partial x_i} + \nu \rho \frac{\partial^2 u_i}{\partial x_j^2} - \rho g_i \tag{3.2}$$

formulate the conservation of momentum. In both equation 3.1 and equation 3.2 $u_i$ is the velocity component in the direction $x_i$, while $p$ is the pressure. As the fluid properties density $\rho$ and kinematic viscosity $\nu$ are considered isotropic and homogeneous, the flow is incompressible. $g_i$ is the component of the gravity vector in the direction $x_i$. This vector is considered to be constant.

The operator $D/Dt$ denotes the material derivative of a quantity. Applied on a velocity $Du_i/Dt$, it gives the material acceleration of a fluid particle, which is the sum of the local acceleration $\partial u_i/\partial t$ and convective acceleration $u_j \partial u_i/\partial x_j$. The resulting change of momentum $\rho Du_i/Dt$ of a fluid particle is balanced by: the pressure gradient $-\partial p/\partial x_i$; the viscous (friction) term $\nu\rho\partial^2 u_i/\partial x_j^2$; and the gradient of the gravitational potential $\rho g_i$. Since these terms can be interpreted as gradients of stresses, a stress balance can be obtained by a spatial integration of equation (3.2) (section 3.2).

Turbulent flow is complex. Even though turbulence follows distinct laws, a single instantaneous sample of a turbulent flow field might appear random. To come to general conclusions,

---

[1] The conservation of energy can neglected for incompressible flow of Newtonian fluids, since the motion can be described by the conservation of mass and momentum. Although kinetic energy is converted to heat by inner friction, the effect of the respective increase of temperature is negligible.

it is common practice to not investigate instantaneous quantities but the statistics of these quantities. To do so, the velocity $u_i$ (as well as the pressure) is split into its time-averaged mean $\langle u_i \rangle$ and the instantaneous deviation of this mean $u_i'$:

$$u_i = \langle u_i \rangle + u_i' \tag{3.3}$$

Equation 3.3 is the so-called Reynolds decomposition (Pope, 2011). Applying this decomposition to equation 3.2 and restructuring the terms gives the Reynolds equations:

$$\frac{D\langle u_i \rangle}{Dt} = -\frac{1}{\rho}\frac{\partial \langle p \rangle}{\partial x_i} + \nu \frac{\partial^2 \langle u_i \rangle}{\partial x_j^2} - \frac{\partial \langle u_i' u_j' \rangle}{\partial x_j} - g_i \tag{3.4}$$

Due to nonlinear terms in the material derivative, the application of the Reynolds decomposition to the Navier-Stokes equation (equation 3.2) creates an additional term containing the covariances of the velocity field $\langle u_i' u_j' \rangle = \langle u_i u_j \rangle - \langle u_i \rangle \langle u_j \rangle$. Even though the stresses are actually $-\rho \langle u_i' u_j' \rangle$, this covariances are called Reynolds stresses (Pope, 2011). Physically, the Reynolds stresses represent the momentum transfer due to velocity fluctuations. Pope (2011) indicates the major role of the Reynolds stresses in a turbulent flow field by underlining that the corresponding term is what makes the difference[2] between equation 3.2 and equation 3.4 and causes the fundamental difference of time-averaged and instantaneous flow field.

## 3.2. Wall shear stress

As mentioned above, the terms of the Navier-Stokes equations (equation (3.2)) can be interpreted as the gradients of stresses. Thus, integrating equation (3.2) gives a stress balance. If the integration is done in the wall-normal direction (here the $z$-direction), the corresponding integration constant is the shear stress between the wall and the fluid, the wall shear stress $\tau_w$:

$$\tau_{w,i} = -\int_{z=0}^{z} \frac{\partial p}{\partial x_i} dz - \rho \int_{z=0}^{z} u_j \frac{\partial u_i}{\partial x_j} dz + \rho\nu \int_{z=0}^{z} \frac{\partial^2 u_i}{\partial x_j^2} dz + \rho g_i z \tag{3.5}$$

Here $\tau_{w,i}$ is the component of the wall shear stress in the direction $x_i$ and the wall is located at $z = 0$. At a rigid wall, the velocity of the fluid is the velocity of the wall, here $u_i = u_j = 0$. In the present considerations gravity is not relevant. Directly at the wall, the pressure gradient as well as the velocity gradients in the wall parallel directions are significantly smaller than the velocity gradient in the wall-normal direction. Thus, close to the wall equation (3.5) reduces to

$$\tau_{w,i} = \rho\nu \frac{\partial u_i}{\partial z} \tag{3.6}$$

---

[2] If $\langle u_i' u_j' \rangle = 0$, the equations for $u_i$ and $\langle u_i \rangle$ would be the same.

The wall shear stress depends on the fluid properties ($\rho$ and $\nu$) and the wall-normal velocity gradient at the wall. Furthermore, from equation (3.6) follows that the wall-normal velocity profile is linear in a region, which is close enough to the wall so that the simplifications made above are valid. This region is called linear sublayer or viscous sublayer and its the thickness depends on the Reynolds number. The stress balance of the near-wall flow in the configuration considered in the scope of this dissertation is evaluated in the publication summarised in chapter 8 (Schanderl et al., 2017a).

## 3.3. Budget of turbulent kinetic energy

Analogue to the velocity, the kinetic energy can be split into two parts: the kinetic energy of the mean flow field $E$

$$E = \frac{1}{2}\langle u_i \rangle^2 \tag{3.7}$$

and the turbulent kinetic energy $k$

$$k = \frac{1}{2}\langle u_i'^2 \rangle \tag{3.8}$$

which is the time-averaged kinetic energy of the velocity fluctuations. One of the key aspects of this study was the investigation of the latter one as well as its budget: The production term $P$

$$P = -\langle u_i' u_j' \rangle \frac{\partial \langle u_i \rangle}{\partial x_j} \tag{3.9}$$

transforms mean kinetic energy into turbulent kinetic energy (if $P > 0$) and vice versa (Pope, 2011). Due to its structure, $P$ can be interpreted as an amplification of $k$ where the flow decelerates and a damping of $k$ where the flow accelerates. On the one hand, the turbulent kinetic energy is redistributed in space by the convection due to the mean flow field $C$ which is

$$C = -\langle u_i \rangle \frac{\partial k}{\partial x_i} \tag{3.10}$$

in a statistical steady flow (Pope, 2011). On the other hand, there are turbulent transport processes (Pope, 2011): turbulent convection $T_{conv}$, pressure transport $T_{pres}$, and viscous diffusion $T_{visc}$

$$T_{conv} = -\frac{1}{2}\frac{\partial}{\partial x_i}\langle u_i' u_j' u_j' \rangle \tag{3.11}$$

$$T_{pres} = -\frac{1}{\rho}\frac{\partial}{\partial x_i}\langle u_i' p' \rangle \tag{3.12}$$

$$T_{visc} = 2\nu \frac{\partial}{\partial x_i} \langle u'_j s'_{ij} \rangle \tag{3.13}$$

where $s'_{ij}$ is the fluctuation of the strain rate tensor

$$s'_{ij} = \frac{1}{2} \left( \frac{\partial u'_i}{\partial x_j} + \frac{\partial u'_j}{\partial x_i} \right) \quad . \tag{3.14}$$

The dissipation rate $\epsilon$ transforms kinetic energy into heat by friction (Pope, 2011)

$$\epsilon = 2\nu \langle s'_{ij} s'_{ij} \rangle \tag{3.15}$$

As changes of temperature are neglected, dissipated energy is in fact lost. In statistical steady flow, the mentioned contributors to the budget of turbulent kinetic energy must balance each other:

$$0 = C + T_{conv} + T_{pres} + T_{visc} + P - \epsilon \quad . \tag{3.16}$$

The budget of turbulent kinetic energy is discussed in more detail by Pope (2011) and Schlichting and Gersten (2006). The application of these budget terms on the flow case considered in this study is done in the publication summarised in chapter 7 (Schanderl et al., 2017b).

# 4. Numerical methods

After introducing the continuous governing equations in the previous chapter, this chapter provides insight in how this system of equations was discretised to enable its computation, and which operations were performed on the resulting discretised equations. First the basic concepts applied in computational fluid dynamics are laid out briefly (section 4.1), before the numerical methods used in this study are described (section 4.2). Afterward, the computational grid, on which the discretised system of equations is solved, is documented (section 4.3). To build a certain degree of confidence in the used methods and grids, the following chapter 5 discusses the measures taken to validate the achieved results and their known limitations.

## 4.1. Simulation techniques

A feature of turbulent flow are the dynamics on a large range of both time and length scales. The largest scales are in the order of magnitude of the scales of the outer boundary conditions. In the setup considered, the flow around a cylinder in a flume, these largest scales - e.g. the ones of the coherent structures in the approaching flow, of the horseshoe vortex in the cylinder front or of the von Karman vortices shedding from the cylinder - can be described by means of the cylinder diameter $D$ and the bulk velocity of the approaching flow. Large scale motions decay continuously into motions of smaller scales until they reach a physical lower limit. At this lower limit, motion can be described by the means of the Kolmogorov length scale $\eta_K = (\nu^3/\epsilon)^{1/4}$ and the Kolmogorov velocity $u_K = (\nu\epsilon)^{1/4}$ (Pope, 2011), where $\epsilon$ is the dissipation rate (equation 3.15). The Kolmogorov scales depend on the Reynolds number $Re$: the larger $Re$, the smaller the scales (Pope, 2011). Thus, the range of scales increases with Reynolds number for given boundary conditions. To gain meaningful results, a numerical simulation has to regard all these scales. Especially in high Reynolds number flow - like most of the industrial and engineering applications - this is challenging. There are three principal approaches to handle this challenge. These three approaches are explained in the context of a finite volume method Pope (2011), in which the quantities of the flow are averaged over a defined volume. This volume corresponds to the cell volume of the applied computational grid.

(i) Direct numerical simulation (DNS) resolves the whole domain by a computational grid fine enough to capture the smallest scales. The resulting data corresponds to data averaged in space over the volume of the grid cells as well as in time over a period corresponding to the applied time step. Thus, both time step and volume have to be small enough to ensure that the resulting data approximates the smallest scales without significant deviation, even though it is averaged in space and time. If this condition is fulfilled, the resulting data actually corresponds to an instantaneous flow field. According to Pope (2011) grid spacing of $\Delta x_i \lesssim 2.1\eta_K$ is required to resolve the small scales sufficiently. Since this high resolution, which depends on the Reynolds number, has to be provided over a domain large enough to capture the large scale motions, which depend on the geometry of the setup, a relative large number of grid points is necessary to discretise the domain. Linked to that is the necessity of large computational resources. Today, DNS can only be performed for low and medium Reynolds number flow in a geometrically restricted domain.

(ii) Reynolds-averaged Navier-Stokes simulation (RANS) solves the Reynolds equation (equation 3.4) for the time-averaged velocities $\langle u_i \rangle$ only. The covariances of the velocity field $\langle u_i' u_j' \rangle$ are modelled. The corresponding models exploit that $\langle u_i' u_j' \rangle$ act like stresses: The Reynolds stresses are treated like viscous stresses caused by an artificial turbulent viscosity $\langle \nu_t \rangle$, which results in $\langle \nu_t \rangle \partial^2 \langle u_i \rangle / \partial x_j^2$. The turbulent viscosity is estimated by the model. These artificial viscous stresses furnish the function of the small scale structures in the flow. The result is a time-averaged velocity field without any time-resolved information.

Main advantage of the RANS approach are the weak requirements on the grid. Since only large scale structures have to be resolved, the grid spacing can be designed by means of the outer scaling of the geometry. The grid depends weakly on the Reynolds number only. However, this approach has two shortcomings: First, the data resolution is as coarse as the grid resolution. Time-averaged structures which are not resolved by the grid are not included in the results and cannot be reproduced. Second, as pointed out in section 3.1, the Reynolds stresses are what make the significant difference between the time-averaged and the instantaneous flow field. The Reynolds stresses thus have an enormous influence on the results of the simulation. This influence is laid completely in the hands of a model. There is a vast number of models, each having its own strengths and limitations. Even though modern RANS-models do not require an a priori calibration, they call for an a posteriori validation by an experiment or a more sophisticated simulation.

(iii) Large-eddy simulation (LES), which was employed in this dissertation, combines both approaches named above. The idea is to solve equation 4.1 for the filtered flow field $\overline{u_i}$ and $\overline{p}$.

$$\frac{D\overline{u_i}}{Dt} = -\frac{1}{\rho}\frac{\partial \overline{p}}{\partial x_i} + \nu \frac{\partial^2 \overline{u_i}}{\partial x_j^2} - \frac{\partial \tau_{ij}^{SGS}}{\partial x_j} - g_i \tag{4.1}$$

As the conducted LES used an implicit filter, the filter width was defined by grid spacing. $\overline{u_i}$ and $\overline{p}$ represent values spatially averaged over the cell volume and time averaged over the step size of the time integration, thus scales of motion smaller than the grid spacing are not resolved. The motion on the smallest scales have to modelled by an approach similar to the one of RANS: An artificial viscosity is employed to increase the inner friction and thus to take over the part of the smallest scales. The model acts on equation (4.1) via the subgrid-stress tensor $\tau^{SGS} = \overline{u_i u_j} - \overline{u_i}\,\overline{u_j}$ analogus to the Reynolds stress tensor in equation (3.4) (Pope, 2011). However, in contrast to RANS the solution includes time-resolved information about the dynamics of the flow on scales larger than the filter width. The range of resolved scales depends on the grid spacing: An LES with relative coarse grid has a smooth transition to RANS on the one hand. On the other hand, the LES solution converges towards the solution of DNS if the grid is sufficiently fine (Bose et al., 2010). The finer the grid, the lager is the computational effort. However, since less scales of motion have to be modelled on a finer grid, the influence of the turbulence model and its possible limitations is less as well.

As the discussion of the grids (section 4.3) and the corresponding validation (section 5.1) indicate, the grids of the present LES were close to grids required for DNS. The influence of the subgrid-stress model was consequently small (Schanderl and Manhart, 2016) and thus neglected in most terms of the budget of turbulent kinetic energy (Schanderl et al., 2017b). Even though the results of the simulation were filtered flow fields, the differences to instantaneous ones were considered small as well. To ease the denomination of data and its mathematical representation, this difference is neglected in the remainder of this study (equation 4.2).

$$u_i = \overline{u_i} \quad ; \qquad p = \overline{p} \tag{4.2}$$

LES can be - depending on the grid resolution - wall-resolved or wall-modelled[1]. In a wall-modelled simulation, the linear sublayer is not resolved by the computational grid. This has the advantage of relative low computational costs, but the drawback that the wall shear stress cannot be evaluated by equation (3.6). As the simplifications made to derive equation (3.6) are not valid at the position of the grid point closest to the wall in this case, the full stress balance (equation (3.5) has to be considered. Since the velocity profile between this grid point and the wall is unknown, the integrals in the stress balance (equation (3.5) have to be modelled. However, it is challenging to model the near-wall flow in a complex, three-dimensional flow situation as the considered one in front of a wall-mounted cylinder. The reliability of the results might therefore suffer from representing the near-wall flow by a model (Rodi et al., 1997; Pope, 2011).

In a wall-resolved simulation as the present ones, the linear sublayer (section 3.2) is resolved by the computational grid. Since the velocity profile in the linear sublayer is linear, the wall shear stress can be evaluated explicitly by equation (3.6). However, since the grid resolution of a wall-resolved simulation has to be relatively high, it is linked to large computational costs.

## 4.2. Flow solver

The simulations were conducted using the scientific in-house flow solver MGLET (Manhart et al., 2001), which is a finite volume code based on a Cartesian grid. The variables are arranged in a staggered manner on the grid. Spatial gradients are approximated via second order central differences, time integration by a third order Runge-Kutta procedure. To model a curved surface like the one of the cylinder on a Cartesian grid, a conservative, second order immersed boundary method (IBM) is available (Peller et al., 2006; Peller, 2010). In addition, the code contains an algorithm to refine the grid in the regions of interest by locally embedded grids (Manhart, 2004). How this algorithm was used will be discussed in detail in section 4.3. MGLET is well established in the scientific community and has already been applied in various studies, e.g. Werner (1991); Manhart (1998); Breuer et al. (2009); Jiang et al. (2016).

---

[1] DNS is always wall-resolved, while RANS is always wall-modelled.

The subgrid stresses were modelled using the wall-adapting local eddy-viscosity (WALE-) Model (Nicoud and Ducros, 1999). The turbulent viscosity $\nu_t$ decreases naturally with proximity to the wall with the correct limiting behavior in this model. Thus, no damping function has to be applied, which is a fundamental advantage when modelling curved surfaces in on Cartesian grid via an IBM (Peller, 2010). In addition, unlike other eddy-viscosity models, the WALE model is suited for complex flow situations on the one hand and requires relatively low computational resources on the other hand (Nicoud and Ducros, 1999).

## 4.3. Domain and grid

The computational domain consisted of two major parts (figure 4.1): a precursor grid to simulate a fully-developed inflow profile and a base grid which held the cylinder. To match the flow configuration defined in chapter 2, bottom and side walls were furnished with a no-slip boundary condition[2], which represented the walls of a flume. The top boundary was equipped with a slip condition[3] to model the free surface of an open channel. Since this slip condition prevented all surface deformations, the Froude number was infinitesimal.

The precursor had periodic boundary conditions in the streamwise direction ($x$-direction) to simulate a fully-developed, turbulent open-channel flow including the characteristic secondary flow structures of Prantl's second kind (Nezu and Nakagawa, 1993). The precursor was one-way coupled to the base grid, such that an instantaneous sample of the flow profile in the precursor was set as the inflow condition at the base grid.

First, the grid at $Re_D = 39000$ was designed. In the region around the cylinder, the grid was refined locally by nested grids. The position of these grids is indicated in grey in figure 4.1. Each of these embedded grids refined the grid spacing by a factor of two. Three levels of grid refinement were applied, which resulted in a refinement factor of eight of the finest grid (level 3) compared to the precursor and the base grid (level 0). A grid study (section 5.1) showed these three refinement levels to be sufficient to gain results converged over grid spacing.

---

[2] A no-slip boundary condition means that the velocity of the fluid is equivalent to the velocity of the wall, which was zero in the present study.

[3] A slip boundary condition is equivalent to set the wall normal velocity and wall parallel stresses to zero at the corresponding location.

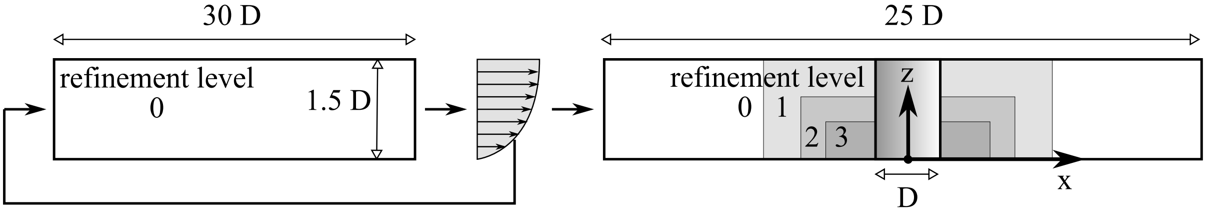

**Figure 4.1:** Side view of the precursor (left) and the base grid (right). Locally embedded grids are marked in grey.

The grid is stretched vertically ($z$-direction) by a factor smaller than 1.01%. However, since this stretching was applied to the grids with refinement level 0 (precursor and base grid), only every eighth cell was augmented on refinement level 3. In a second step, the grids for $Re_D = 20000$ and $Re_D = 78000$ were designed. These were stretched in such a way that the expected grid spacing in wall units was the same as the one for $Re_D = 39000$. This approach was validated by a separate grid study for every Reynolds number. The resulting grid parameters in the region of interest around the cylinder are listed in table 4.1.

Due to the small stretching factor and a relative large extend of the finest embedded grid, the fine resolution was maintained in the whole region of interest around the cylinder. According to Pope (2011) a grid spacing of $\Delta x_i \lesssim 2.1\eta_K$ is required for DNS without turbulence model. The provided grid spacing in the region covered by the horseshoe vortex was $\Delta z \approx 1.6\eta_K$ and $\Delta x = \Delta y \approx 6.4\eta_K$ in the vertical ($z$-) direction and in the horizontal ($x$-, $y$-) directions respectively (Schanderl et al., 2017b; Schanderl and Manhart, 2017). The wall normal grid resolution was thus sufficient for DNS but the horizontal resolution was too coarse. This is in line with the fraction of modelled dissipation in the total dissipation, which was approximately one third, which is small for LES. Schanderl et al. (2017b); Schanderl and Manhart (2017).

| $Re_D$ | cells per diameter **horizontal**/vertical | grid spacing $\Delta x^+/\Delta y^+/\Delta z^+_{wall}$ | total number of grid cells |
|---|---|---|---|
| 20000 | **148**/571 | **7.0**/**7.0**/1.8 | $166 \cdot 10^6$ |
| 39000 | **250**/1000 | **7.4**/**7.4**/1.9 | $400 \cdot 10^6$ |
| 78000 | **440**/1778 | **7.8**/**7.8**/1.9 | $1.6 \cdot 10^9$ |

**Table 4.1:** Grid parameters for all three Reynolds numbers. The resolutions in both outer and inner scaling refer to the finest grid in the region of interest around the cylinder. Inner units are based on the wall shear stress of the approaching flow.

# 5. Validation and known limitations

At this point in the present dissertation, several steps of simplification, transformation and modelling have been performed. To investigate the research questions defined in chapter 1, a flow configuration was chosen (chapter 2) in which the appropriate flow phenomena appear. A set of equations was introduced (chapter 3) which covers the underlying flow physics. This set of equations was discretised by numerical schemes and boundary conditions were applied to solve these equations (chapter 4). However, each step performed generated inaccuracies in the best case and systematic errors in the worst case. To create confidence in the resulting data set, it is important to exclude systematic errors if possible and to be aware of the order of magnitude of the inaccuracies of the solution. Therefore, several measures of validation were taken. In the following (sections 5.1 to 5.4) the measures employed in this study and their outcomes are described, was are the possible sources of error/inaccuracy addressed by these measures. The chapter concludes with a discussion of the known limitations and shortcomings of the approach presented (section 5.5). In later chapters, the results of the applied procedure are evaluated and conclusions are drawn.

## 5.1. Grid study and influence of the turbulence model

The euqations describing flow physics are continuous. However, in a numerical simulation these equations are solved not continuously but for discrete postions only, which are defined by the computational grid. However, if the grid spacing (and thus the finite volumes) is too large, the discretised equations do not reproduce the behavior of the original continuous equations and the results are not consistent with flow physics. If the grid resolution is fine enough, flow physics are reproduced by the discretised equations but it suffers from inaccuracies depending on grid spacing. In this so-called convergent region, the inaccuracy is reduced as grid spacing is reduced. If the grid is sufficiently fine, the solution does not change significantly any further if the grid is further refined. In this case the solution is converged over grid refinement and inaccuracies due to the numerical discretisation are considered small.

That the solution of the present LES was converged over grid refinement is exemplified in figure 5.1, where the friction coefficient $c_f = \langle\tau_w\rangle/(0.5\rho u_b^2)$ in the symmetry plane in front of the cylinder at $Re_D = 78000$ is documented. Here $\langle\tau_w\rangle$ is the time-averaged local wall shear stress, $\rho$ the fluid density and $u_b$ the bulk velocity in the symmetry plane of the approaching flow. Simulations with one to three levels of grid refinement were conducted, which means that grid spacing was successively reduced by a factor of two. The simulation denoted as LES78k #1 held one locally embedded grid, simulation LES78k #2 two local grids and the grid of simulation LES78k #3 was refined by three nested grids around the

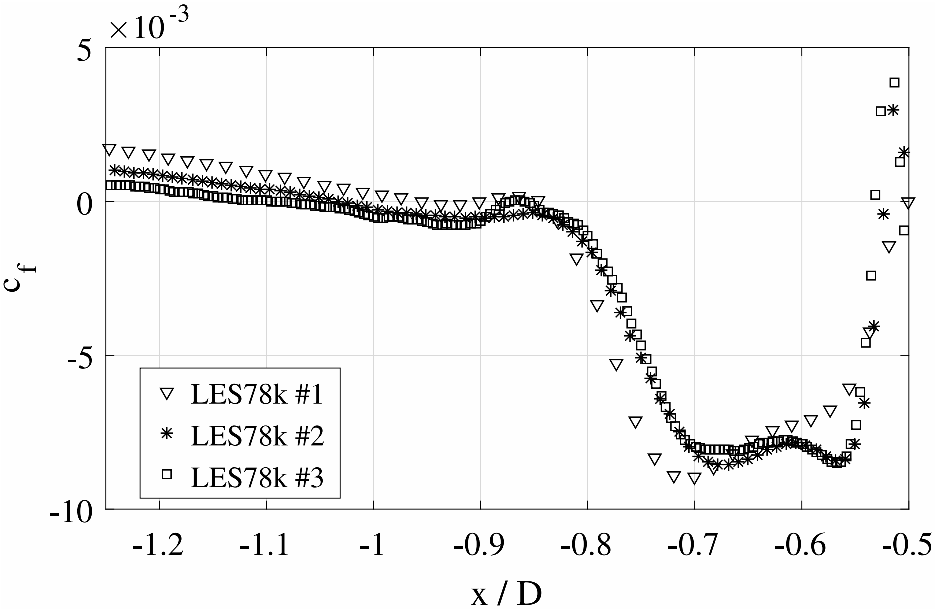

**Figure 5.1:** Friction coefficient $c_f$ from three simulations with different grid refinement at $Re_D = 78000$. For reasons of visualisation, only every second data point is plotted.

cylinder. Therefore, the grid of LES78k #3 was four times finer than that of LES78k #1.

The wide peak of negative $c_f$ in figure 5.1 at $-0.85D < x < -0.53D$ resembles the footprint of the main horseshoe vortex V1. The small peak of positive $c_f$ between stagnation point S3 at $x = -0.53D$ and the flow facing edge of the cylinder at $x = -0.5D$ was caused by the small corner vortex V3. Figure 5.1 reveals that there were noticeable differences between the results of LES78k #1 and LES78k #2. The wide peak of negative $c_f$ showed a single-peak shape in LES78k #1 while it had a double-peak shape in the simulations with finer grids. In addition, this grid of LES78k #1 was too coarse to resolve the small peak of positive $c_f$ close to the cylinder.

The differences between LES78k #2 and LES78k #3 were significantly smaller. In wide regions, both results matched each other without observable deviation. Therefore, the solution of LES78k #3 was considered converged over grid refinement and the grid dependency of the solution on the corresponding grid was considered small. Furthermore, since the amplitude of the wall shear stress (and thus the magnitude of the estimated velocity gradient at the wall, equation (3.6)) did not further increase with grid refinement, which indicated that the grid point closest to the wall was in the linear sublayer. Thus, no wall model had to be applied, and the wall shear stresses were directly evaluated via the wall gradient of the velocity field (Pope, 2011). This procedure was confirmed and discussed in detail for $Re_D = 39000$ by Schanderl and Manhart (2015, 2016); Schanderl et al. (2017a). An analogous grid study was done for all three Reynolds numbers. A detailed discussion of the grid study at $Re_D = 39000$ can be found in Schanderl and Manhart (2016); Schanderl et al. (2017b,a).

The grid study did not only indicate that the solution was converged over grid refinement. Furthermore, it showed how the influnence of the subgrid-stress model on the results decreased with increasing grid resolution and that this influence was small in the simulation

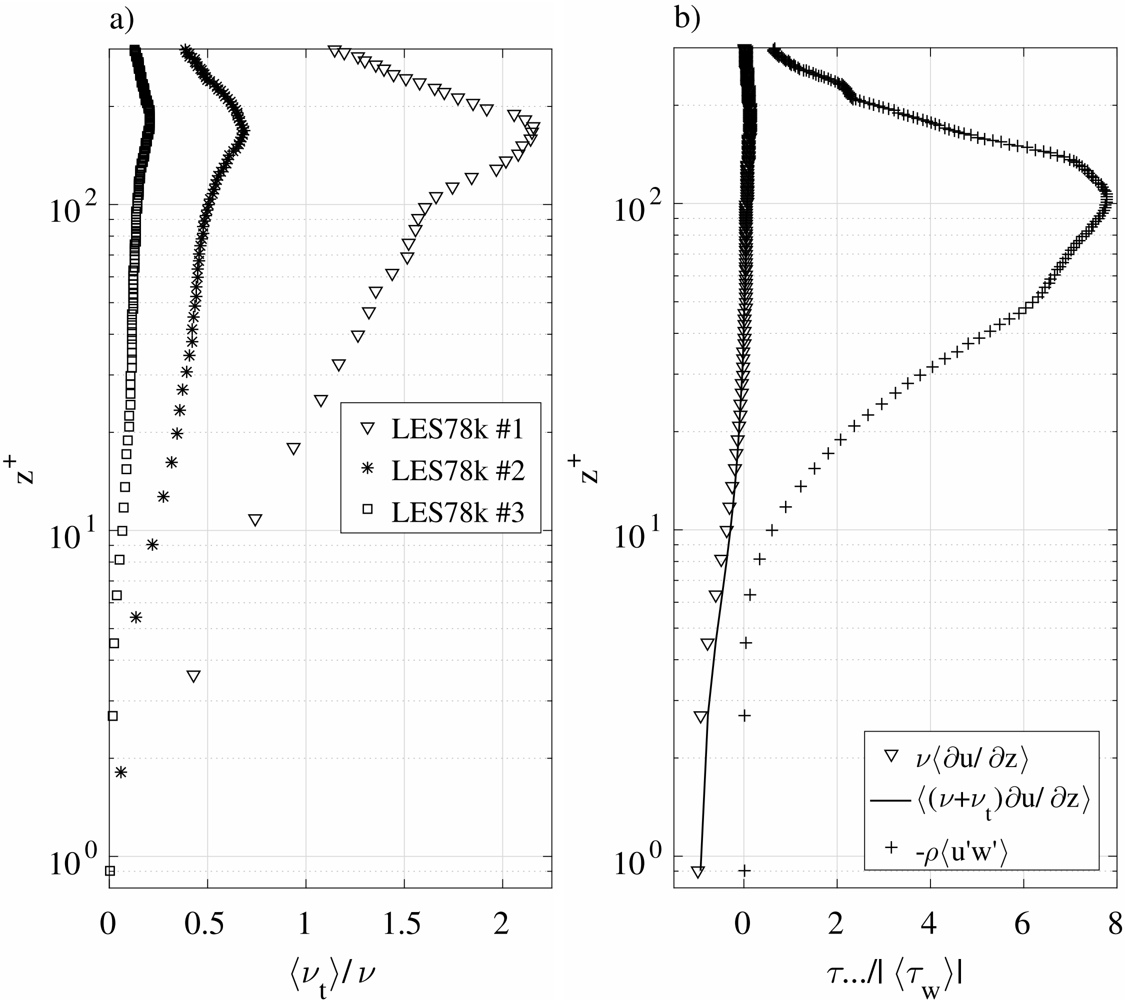

**Figure 5.2:** Wall-normal profiles of the time-averaged turbulent viscosity $\langle \nu_t \rangle$ for the three simulations with different grid resolution (a) and contributors to the stress balance (equation (3.5)) taken from the simulation with the finest grid LES78k #3 (b). The streamwise position was $x = -0.76D$, which corresponded to the core of V1 at this Reynolds number $Re_D = 78000$.

with the finest grid.

In figure 5.2a the time-averaged turbulent (modelled) viscosity stemming from the model normalised by the molecular viscosity $\langle \nu_t \rangle / \nu$ on a wall-normal profile is plotted. The Reynolds number was $Re_D = 78000$. The data was evaluated in the symmetry plane in front of the cylinder at a streamwise position of $x = -0.76D$, which corresponded to the position of the center of the main vortex V1 at this Reynolds number. The data was taken from the three simulations with different levels of grid refinement[1]. In figure 5.2a the distinct peak of $\langle \nu_t \rangle$ at $z^+ \approx 175$ indicates the vertical position of the vortex core of V1. It can be seen in this figure that in the WALE model (Nicoud and Ducros, 1999) the modelled viscosity decays towards the wall, even though no damping function was applied.

---

[1] However, it should be noted that the wall shear stress applied to evaluate $z^+$ was taken from the simulation with the finest grid LES78k #3 for all three data sets.

As the grid was refined and the filter width reduced, a larger range of scales of motion was resolved by the grid and thus a smaller share had to be modelled. Figure 5.2a illustrates a quadratic decay of the turbulent viscosity. As the grid spacing was reduced by a factor of two from LES78k #1 to LES78k #2 and from LES78k #2 to LES78k #3, the turbulent viscosity was reduced by a factor of approximately four each time. Furthermore, in LES78k #3 with the finest grid, the time-averaged modelled viscosity $\langle \nu_t \rangle$ was significantly smaller than the molecular viscosity $\nu$.

How the modelled viscosity acted on the flow physics is visualised in figure 5.2b. Here contributors to the stress balance (equation (3.5)) in the streamwise ($x$-) direction were evaluated: an instance of the resolved Reynolds stresses $-\rho\langle u'w' \rangle$, one of the viscous terms without the modelled contribution $\nu\langle \partial u/\partial z \rangle$ and including the modelled contribution $\langle (\nu + \nu_t)\partial u/\partial z \rangle$. All data were taken from LES78k #3, the simulation with the finest grid at $Re_D = 78000$. $-\rho\langle u'w' \rangle$ peaked at $z^+ \approx 100$ slightly under the core of the main vortex V1. The distributions of $\nu\langle \partial u/\partial z \rangle$ and $\langle (\nu + \nu_t)\partial u/\partial z \rangle$ almost covered each other. Both had two peaks: one at the bottom wall and one at $z^+ \approx 175$. Even though it is hardly visible in figure 5.2b, there were small deviations between the viscous terms including and excluding the modelled contribution, which is in line with the peak of $\langle \nu_t \rangle$ in figure 5.2a. However, around V1 neither the viscous nor the modelled stresses dominated the flow as the resolved Reynolds stresses were larger by orders of magnitudes. In the investigated range of Reynolds numbers the viscous stresses dominated the flow close to the wall only. Here the deviation between $\nu\langle \partial u/\partial z \rangle$ and $\langle (\nu + \nu_t)\partial u/\partial z \rangle$ was small, which is also indicated by the small $\langle \nu_t \rangle$ in figure 5.2a. From these observations it was concluded that there was no position in the flow where the modelled stresses dominated the stress balance. Even though the small contribution of the turbulence model was important to gain reasonable results, its share was small. Possible inaccuracies due to the simplifications this model is based on were considered small, too.

An analogous discussion of the influence of the modelled stresses at $Re_D = 39000$ can be found in Schanderl and Manhart (2016); Schanderl et al. (2017a). The magnitude of the modelled share of turbulent kinetic energy is reviewed in Schanderl et al. (2017b).

## 5.2. Residual of the budget of turbulent kinetic energy

In a numerical study, not only convergence in a numerical sense as discussed above but also consistency in a physical sense has to be guaranteed. That the applied set of governing equations is consistent in itself was indicated by the evaluation of the total budget of turbulent kinetic energy (equation (3.16)). This budget involves the production, the transport and the dissipation of turbulent kinetic energy. As discussed in section 3.3, the named mechanisms have to balance each other in a stationary flow, which means that the residual $R$ of the budget (which is the right hand side of equation (3.16)) has to be small. Figure 5.3 indicates that this residual was sufficiently small in the presented simulations. In figure 5.3 $R$ in the symmetry plane in front of the cylinder close to the bottom at $Re_D = 78000$ is evaluated. In wide regions the absolute residual was $|R| < 0.03D/u_b^3$, which corresponded to approximately 5% of the production of turbulent kinetic energy (Schanderl et al., 2017b). Here, $D$ was the diameter of the cylinder and $u_b$ the bulk velocity in the symmetry plane of the approaching flow. Small positive values of the residual which alternate with small negative ones suggest that there was no systematic over- or underestimation of single contributors to the budget, neither by the used set of equations nor by the numerical method.

In narrow regions along the bottom wall, the residual reached $|R| \lesssim 0.1D/u_b^3$, corresponding to approximately 15% of the production. Considering the overall complexity of the evaluation of single terms involved in the budget of turbulent kinetic energy, this is still satisfying. Along the flow facing edge of the cylinder, the amplitude of the residual was slightly larger, in narrow regions it reached values of $|R| < 0.3D/u_b^3$. The reason for this is discussed in section 5.5.

## 5.3. Comparison with an experiment

To provide a strong degree of reliability, the same flow configuration was tackled by two completely independent methods. The numerical results were accompanied by an associated experiment by Ulrich Jenssen (Jenssen et al., 2016; Schanderl et al., 2017b), who conducted highly resolved particle image velocimetry (PIV). Special care was turned to assure geometric and dynamic similarity. Furthermore, being aware of the strong influence of the inflow condition on the flow topology around the cylinder Schanderl and Manhart (2016), it was ascertained to have similar inflow boundary conditions in both setups.

First, second and third order moments of the statistics of the flow field in the symmetry plane in front of the cylinder were compared and discussed in detail by Jenssen et al. (2016); Schanderl et al. (2017b). The achieved accordance of PIV and LES underlined the reliability of the presented numerical data and the applied numerical methods. Nevertheless, small deviations between PIV and LES existed (Jenssen et al., 2016; Schanderl et al., 2017b), which might be caused by slight differences of the inflow conditions. The influence of the inflow condition on the flow around the cylinder is discussed in the following.

## 5.4. Inflow profile

To evaluate in which way deviations of the inflow profile cause deviations of the vortex system in front of the cylinder and the corresponding wall shear stress distribution, two additional simulations with different inflow profiles were conducted. In these simulations the precursor was replaced by less sophisticated inflow profiles: (i) a block profile, constant in time as well as in spanwise and vertical direction and (ii) a profile corresponding to the profile from the precursor, but averaged in time and in the spanwise direction. The mean velocity averaged over the whole cross section was the same in all three setups. These additional simulations were conducted at $Re_D = 39000$ only. In the remainder of this section, the simulation with precursor grid is referred to as LES39k #prec, the one with block profile as LES39k #block and the one with time-averaged logarithmic profile as LES39k #log.

Figure 5.4 shows the friction coefficient $c_f$ in the symmetry plane in front of the cylinder for the three simulations with different inflow conditions. LES39k #prec exhibited a distribution

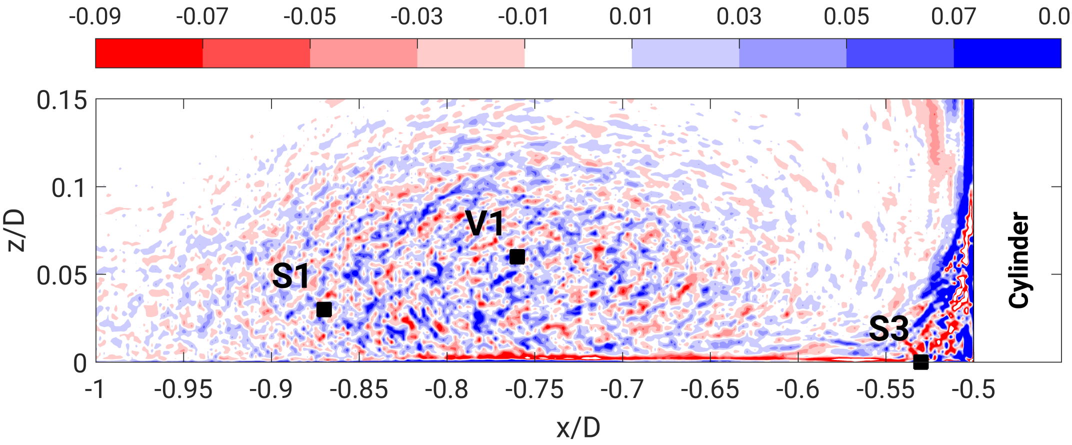

**Figure 5.3:** Residual of the budget of turbulent kinetic energy $R$ in the symmetry plane in front of the cylinder at $Re_D = 78000$, taken from LES78k #3.

similar to the one discussed in section 5.1 taken from simulation LES78k #3. There was a small peak of positive $c_f$ close to the cylinder as a result of the corner vortex V3. The broad peak of negative $c_f$ indicateed the presents of the wall jet, and further upstream a region of weak negative $c_f$ denoted the backflow region upstream of the main vortex V1. While LES39k #log resembled the broad peak in the region of the wall jet with only small deviations in the amplitude, the peak of LES39k #block was significantly more slender. This hints at a less pronounced and smaller vortex system in LES39k #block, which is in line an evaluation of the according flow topology and can be explained by a smaller boundary layer thickness of the flow approaching the cylinder Schanderl and Manhart (2016).

Furthermore, both LES39k #block and LES39k #log exhibited an additional recirculation zone upstream of $x = -1.2D$ (LES39k #block) and $x = -1.5D$ (LES39k #log) indicated by a negative friction coefficient, which was not present in LES39k #prec (figure 5.4). It should be recalled that the precursor provided a turbulent inflow condition, while the block profile and the time-averaged logarithmic profile did not contain any fluctuations. Except for close to the bottom wall, the latter two profiles were laminar therefore when they approached the cylinder Schanderl and Manhart (2016). The limited transport of momentum in the wall-normal direction in these laminar flows facilitated flow separation from the wall in presents of an adverse pressure gradient, which in turn caused the additional recirculation zones in LES39k #block and LES39k #log. In contrast, the larger momentum transport in the wall-normal direction in simulation LES39k #prec prevented a separation of the flow from the bottom wall in the region upstream of $x = -1.2D$.

The differences between the simulations discussed here and the influence of the incoming flow profile on the flow topology and the wall shear stress around the cylinder were discussed in more detail by Schanderl and Manhart (2016).

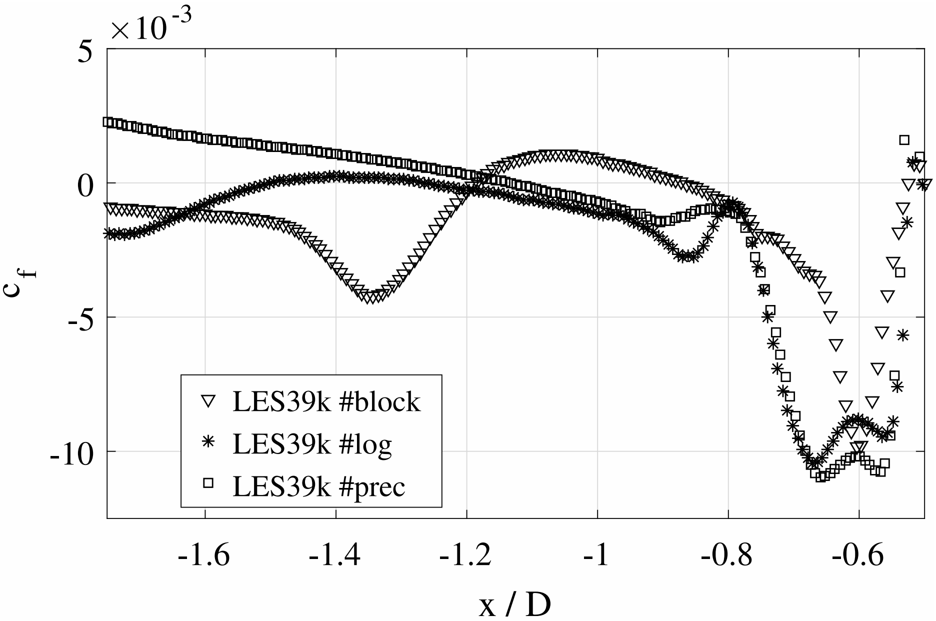

**Figure 5.4:** Friction coefficient $c_f$ take from three simulations with different inflow profiles at $Re_D = 39000$. For reasons of visualisation, only every second data point was plotted.

## 5.5. Known limitations

The LES was carefully validated by various measures. However, these measures also revealed some shortcomings of the conducted simulations. These shortcomings as well as general limitations of the present study are discussed in the following.

In the region of the horseshoe vortex, the modelled contributions to the momentum balance (Schanderl and Manhart, 2016) as well as the ones to the budget of turbulent kinetic energy were considered small (Schanderl et al., 2017b). Thus, when evaluating single terms of the budget, modelled contributions were neglected except for the dissipation rate, where the modelled dissipation was approximately one third of the total dissipation. That this approach was justified was discussed in section 5.2. However, there were some spots of increased $R$ along the cylinder wall (figure 5.3). It should be recalled that the grid resolution held an aspect ratio of four: In the horizontal directions, the resolution was four times coarser than in the vertical direction. The grid was designed this way since the main goal of this dissertation was to gain a reliable estimation of the wall shear stress at the bottom wall in a first place. Along the bottom wall the linear sublayer was resolved, while this was not the case at the cylinder surface, which in turn caused small but noticeable contributions of the subgrid stresses there. Neglecting these subgrid stresses caused the spots of the increased residual along the cylinder in figure 5.3. The assumption of a small contribution of the subgrid stress model to the solution had to be questioned in this locally constrained region. Even though the grid almost sufficed DNS, one has to recall that the conducted simulation was LES in fact.

Besides this internal issue, one has to mention limitations concerning the transferability of the presented results to engineering applications and experiments. First, the Froude number was infinitesimal in the conducted simulations since the slip boundary condition prevented all surface deformations. Even though the Froude number might be small in a natural open-channel flow, it is not infinitesimal. This has to be considered when drawing conclusions from the presented results to natural open-channel flows like rivers or to laboratory experiments.

Second, the conducted study featured moderate Reynolds numbers only. Even though the Reynolds number scaling of the flow topology was found to be weak in the range of moderate Reynolds numbers (Apsilidis et al., 2015; Schanderl et al., 2017c), the transfer to setups with significantly larger Reynolds numbers has to be done with caution.

Third, in the presented LES the boundary condition at the inflow of the investigated domain was simulated by a precursor grid. Due to its periodic boundary conditions in the streamwise direction, the precursor simulated an infinite long distance and assured this way that the flow profile was a well-defined fully-developed, turbulent open-channel flow (Schanderl and Manhart, 2016). However, neither in experimental studies nor in engineering applications there is something like an infinite long inflow distance for a flow to develop. Thus, no natural river will feature a fully-developed flow profile with distinct and symmetric secondary flow structure of Prantl's second kind. How difficult it was to reproduce such an inflow profile in a laboratory flume, where most factors influencing a natural open-channel flow are eliminated, was discussed by Schanderl et al. (2017b). In an experiment or an engineering application, the inflow profile can only be an approximation of a fully-developed flow. However, the applied inflow condition was chosen since it was considered more natural and to hold less degrees of freedom than any synthetically generated profile.

The observations regarding the friction coefficient in section 5.4 underline the sensitivity of the flow topology and the wall shear stress distribution around the cylinder on the inflow profile. This is true not only for the time-averaged profile of the inflow, but also for its turbulence intensity. A transfer of conclusions drawn in this study to a setup with different inflow condition thus has to be done with caution.

# 6. Reliability of the wall shear stress estimation

Next, the main findings of the publication “Reliability of wall shear stress estimations of the flow around a wall-mounted cylinder” are discussed briefly. It was published in the journal *Computers & Fluids* in 2016 (Schanderl and Manhart, 2016).

## 6.1. Main results

In this paper, the flow field and the wall shear stresses around a wall-mounted cylinder (chapter 2) at $Re_D = 39000$ were discussed (chapter 4). Main issue was the validation of the simulation in terms of grid resolution, the inflow condition and the contribution of the turbulence model. A grid study indicated the first order statistics to be converged over grid refinement. This was not only true for the region covered by the horseshoe vortex, but also for the wall shear stress. Furthermore, the fine grid ensured the modelled contributors to the momentum balance (equation 4.1) to be significantly smaller than the viscous and the resolved turbulent stresses.

The observations made in this paper indicated the flow topology as well as the wall shear stresses distribution to depend on the inflow condition. A comparison of streamline patterns of the simulation with precursor to those of simulations with less sophisticated inflow conditions showed significant deviations, especially regarding the extend of the vortex system.

Furthermore, the published data showed that the wall shear stress amplification in front of the cylinder was underestimated by former studies (Dargahi, 1989; Tseng et al., 2000; Roulund et al., 2005; Escauriaza and Sotiropoulos, 2011). Due to the geometrical limitations of the applied experimental methods, the data resolution close to the wall was insufficient in a primary experiment (Dargahi, 1989) and the linear sublayer was thus not resolved. The presented LES showed that this linear sublayer is relatively thin. Due to the non-equilibrium character of the flow in the cylinder front, modelling the near wall region is challanging. Resolving the linear region by a grid at least as fine as the one proposed cannot be omitted to gain a reliable estimation of the wall shear stress.

## 6.2. Division of work between the authors

The numerical simulation was conducted and evaluated by Wolfgang Schanderl under guidance of Michael Manhart. Both authors contributed to the ideas and the concept of the paper. Wolfgang Schanderl and Michael Manhart prepared the manuscript.

# 7. Budget of turbulent kinetic energy

The main findings of the publication “The structure and budget of turbulent kinetic energy in front of a wall-mounted cylinder” are summerazied in the following. It was published in the journal *Journal of Fluid Mechanics* in 2017 (Schanderl et al., 2017b).

## 7.1. Main results

Objective of this publication was to investigate the turbulence structure in the setup considered (chapter 2) at $Re_D = 39000$ by applying both LES and PIV. Special care was turned to assure similarity between experiment and simulation, especially regarding the inflow profile. The accordance of the experiment and the simulation validated both data sets alongside the measures discussed by Schanderl and Manhart (2016) (chapter 6).

Every term of the budget of turbulent kinetic energy (section 3.3) was evaluated and linked to the time-averaged topology and the dynamics of the flow field. Two main sources of turbulent kinetic energy were detected: the bimodality of the vortex system and a region close to the bottom wall, were the upstream-directed jet along the wall decelerated. Closer to the cylinder, where this jet accelerated, the acceleration damped the turbulent kinetic energy (cf. the structure of the production term, equation 3.9) and thus lead to a relative calm region between cylinder and main horseshoe vortex V1.

In the cylinder front the dissipation was about one eighth of the production rate only, which documented the non-equilibrium nature of the flow. Thus the budget had to be closed by strong turbulent and pressure transport as well as by the mean flow convection.

## 7.2. Division of work between the authors

The LES was conducted and evaluated by Wolfgang Schanderl under guidance of Michael Manhart. The PIV was done by Ulrich Jenssen under guidance of Michael Manhart. The single-pixel algorithm was developed, implemented and executed by Claudia Strobl under guidance of Michael Manhart. Wolfgang Schanderl, Ulrich Jenssen and Michael Manhart contributed to the ideas and the concept of the paper. Wolfgang Schanderl and Michael Manhart prepared the manuscript with support of Ulrich Jenssen and Claudia Strobl.

# 8. Near-wall stress balance

The publication "Near-wall stress balance in front of a wall-mounted cylinder" (Schanderl et al., 2017a) was part of a special issue of the journal *Flow, Turbulence and Combustion* in 2017 to which we were invited to contribute. Its main findings are summarised below.

## 8.1. Main results

The publication addresses the near-wall flow in front of the wall-mounted cylinder at $Re_D = 39000$ by discussing the single contributors to the balance of stresses in the streamwise direction. The strong pressure gradient in the cylinder front causes acceleration and deceleration of the flow. On those conditions, classical approaches to model the near-wall region have to fail (Pope, 2011). To assess, which contributors to the stress balance have a significant influence on the near-wall flow and thus have to be considered by an approach modelling this flow, the stress balance was applied on statistical data taken from the LES. The stress balance was gained from integrating the Reynolds equation (equation (3.4)) in the vertical direction.

The evaluation indicated that the relative magnitude of the single contributors strongly depends on the exact location in the cylinder front. In the relative calm region between the main vortex and the cylinder, where the wall jet accelerates, the acceleration of the mean flow caused the most significant stresses in the flow. Further upstream, in the region of deceleration of the jet, the increase of Reynolds stresses (especially of Reynolds normal stresses in the streamwise direction) dominated the flow. In addition, even though some contributors were small compared to others, at a wall distance of thirty to fifty wall units all contributors[1] were significantly larger than the wall shear stress. This was also true for stresses based on wall-parallel derivatives. It was concluded that a local approach is not sufficient for wall modelling in such a complex flow situation and thus a spatial approach has to be applied, which is not only including local flow quantities, but also information regarding the adjacent flow.

## 8.2. Division of work between the authors

The LES was conducted and evaluated by Wolfgang Schanderl under guidance of Michael Manhart. Idea and concept of the paper were formulated by Wolfgang Schanderl and discussed with Ulrich Jenssen and Michael Manhart. Wolfgang Schanderl prepared the manuscript with support of Michael Manhart.

---

[1] Except viscous stresses due to wall-parallel velocity gradients.

# 9. Dissipation of turbulent kinetic energy

In the following, the main findings of the publication "Dissipation of turbulent kinetic energy in a cylinder wall junction flow" (Schanderl and Manhart, 2017) are briefly summed up. This paper was submitted in late 2017 to the journal *Flow, Turbulence and Combustion* as a part of a special issue to which we were invited to contribute.

## 9.1. Main results

In the present LES the grid was fine enough to resolve approximately two thirds of the dissipation of turbulent kinetic energy. This allowed for an evaluation of the dissipation in which the influence and thus a possible bias of the turbulence model on the dissipation was small.

The dissipation $\epsilon$ in front of the wall-mounted cylinder normalised by the macro scale parameters bulk velocity and cylinder diameter $u_b^3/D$ showed no significant Reynolds number dependency. At all three Reynolds numbers investigated, the distribution of the dissipation followed the distinct c-shape of the turbulent kinetic energy. The amplitude was increasing only mildly with Reynolds number. Its maximum was $\epsilon \approx 0.08 u_b^3/D$ in all three cases.

At the Reynolds numbers investigated, the small scale structures were not isotropic in the flow configuration considered, as the investigation of individual terms of the pseudo dissipation tensor Schlichting and Gersten (2006) revealed. The pseudo dissipation facilitates the evaluation of individual contributors regarding their spatial direction. Some terms of the pseudo dissipation tensor were significantly larger than the others. These large terms showed no Reynolds number dependency, while the amplitude of the smaller terms increased with Reynlods number noticeably. The flow became more isotropic, as the energy cascade was longer at the higher Reynolds number and the turbulence thus had a larger chance to develop towards an isotropic state. This caused a mild enhancement of the total dissipation with Reynolds number.

## 9.2. Division of work between the authors

The simulations were conducted and evaluated by Wolfgang Schanderl under guidance of Michael Manhart. Idea and concept of the paper were formulated by Wolfgang Schanderl with support of Michael Manhart. Wolfgang Schanderl prepared the manuscript with support with Michael Manhart.

# 10. Scaling of the wall shear stress

The main findings of the draft “Wall shear stress scaling in front of a wall-mounted cylinder” are summerasied in the following. **This is a premature draft.** We intend to submit it to the *Journal of Fluid Mechanics* in late 2017 (Schanderl et al., 2017c).
It should be noted that some experimental results presented in this paper contradict the experimental results in the publication Schanderl et al. (2017b) as the experimental data in the latter was scaled in an incorrect way. However, my dissertation is about the numerical data. The validity of the numerical data and of the corresponding conclusions is not restricted by the incorrect scaling of the experimental data in Schanderl et al. (2017b).

## 10.1. Main results

In this paper, we addressed the Reynolds number scaling of the wall shear stress in front of the cylinder and proposed the following scaling law of the friction coefficient $c_f$ in the region of the upstream-directed wall jet:

$$c_f \sim \frac{1}{\sqrt{Re_D}} \tag{10.1}$$

This scaling law corresponds to the one of a laminar boundary layer and can be explained by the distinct turbulence structure in front of the cylinder. The evaluation of both numerical and experimental results revealed that there was relative calm turbulence in the region between the main horseshoe vortex and the cylinder. Furthermore, the acceleration of the fluid in the jet along to the bottom wall gave rise to negative production of turbulent kinetic energy, which further damped or at least prevented an increase of the turbulence in this region. As the flow topology did not change in general with Reynolds number, the negative production and in turn the calm turbulence was maintained when the Reynolds number was increased. This enabled the thin boundary layer along the bottom wall established by wall jet to behave like a laminar boundary layer.

## 10.2. Division of work between the authors

The LES was conducted and evaluated by Wolfgang Schanderl under guidance of Michael Manhart. The PIV was done by Ulrich Jenssen under guidance of Michael Manhart. The single-pixel algorithm was developed, implemented and executed by Claudia Strobl under guidance of Michael Manhart. Wolfgang Schanderl, Ulrich Jenssen and Michael Manhart contributed to the ideas and the concept of the paper. Wolfgang Schanderl prepared the manuscript with support of Ulrich Jenssen, Claudia Strobl and Michael Manhart.

# 11. Conclusions

In chapter 1 the main aspects subject to this dissertation were defined. This last chapter assesses the outcomes regarding these aspects and their relevance related to engineering applications and scientific questions (section 11.1). The dissertation is concluded by a brief outlook on challenges addressed right now or in the near future (section 11.2).

## 11.1. Main findings

The flow around a wall-mounted cylinder in a water channel with free surface at three moderate Reynolds numbers was investigated by LES. The results were carefully validated, among other measures by a close comparison to a companion experiment (Jenssen et al., 2016; Schanderl et al., 2017b). The evaluation of the total budget of turbulent kinetic energy gave a reasonable small residual (Schanderl et al., 2017b).

To assess the influence of the incoming flow on the flow topology around the cylinder, the horseshoe vortex system resulting from a fully-developed, turbulent open-channel flow approaching the cylinder was compared to the ones resulting from less sophisticated inflow conditions. It was shown that not only the mean inflow but also its turbulent quantities have a major influence on the flow topology. The precisness of an eddy-resolving simulation technique thus can only be fully exploited in the considered flow case when special care is take to set an appropriate, eddy-resolving inflow condition (Schanderl and Manhart, 2016).

The vortex system leaves its footprint in the wall shear stress distribution at the bottom wall. Similar to the vortex system itself, the wall shear stress depends on the inflow condition in both distribution and amplitude (Schanderl and Manhart, 2016). Furthermore, it was shown that a relative high grid resolution is necessary to resolve the linear sublayer and to enable the prediction of the wall shear stress via the wall gadient. At the Reynolds number investigated, the required wall-normal grid spacing was $\Delta z \leqq 0.001D$ (Schanderl and Manhart, 2016). Studies relying on coarser grid spacing are likely to underestimate the amplitude and to misinterpret the shape of the wall shear stress distribution (Schanderl and Manhart, 2016). This high resolution is necessary due to the non-equilibrium behaviour of the near-wall flow. It causes the linear sublayer to be significantly thinner than in equilibrium boundary layers (Schanderl et al., 2017a), where it is approximately five wall units. In addition, the non-equilibrium behavior prevents an appropriate modelling of the near-wall flow by classical wall models. As the evaluation of the stress balance has shown, all of its terms (except viscous stresses due to wall-parallel velocity gradients) have to be considered to close the stress balance. This includes local terms as well as terms based on the surrounding flow situation. Neglecting one of these contributors in a model will lead to a misinterpretation of the wall shear stress (Schanderl et al., 2017a).

Furthermore, the amplitude of the friction coefficient in front of a wall-mounted bluff body at a moderate Reynolds number scales with the squareroot of the Reynolds number. This scaling was attributed to the quasi-laminar behavior of the upstream-directed wall jet under the vortex system. The acceleration of the flow in the jet damps the turbulence and thus causes a flow situation similar to the one in a Blasius boundary layer.

The total dissipation of turbulent kinetic energy $\epsilon$ in front of the wall-mounted cylinder scales rather weak with Reynols number. In the presented LES, the distribution of the dissipation exhibited a c-shape similar to the one of the turbulent kinetic energy. The amplitude was increasing only mildly with Reynolds number. The dissipation was not isotropic but became slightly more isotropic with increasing Reynolds number, as the energy cascade was longer at the higher Reynolds number and the turbulence thus had a larger chance to develop towards an isotropic state.

The present evaluation of the dissipation of turbulent kinetic energy can help to further understand the flow field in front of a wall-mounted bluff body and its dynamics. Furthermore, it can serve as comparative data for future simulations and the development or validation of turbulence models. To the authors knowledge, this was the first time that the dissipation of turbulent kinetic energy and its contributors were evaluated explicitly in this kind of flow at moderate Reynolds numbers.

## 11.2. Future work

One of the main engineering applications referred to in this study is the scour process around bridge piers in sandy river beds. However, this scouring obviously deforms the river bed. If at all, the setup investigated - a cylinder on a flat plate - is a valid approximation at the beginning of the scour process. To investigate how the flow topology and its dynamics change with the developing scour hole, simulations with a cylinder in a scour geometry are initiated at the moment. The flow at different Reynolds numbers will be investigated in simulations with at least two different stages of the scouring process. The results will hopefully be published in near future.

This dissertation presented simulations at three moderate Reynolds numbers only. This does not allow for conclusions regarding the flow field and the corresponding wall shear stress at high Reynolds numbers, which characterise most engineering applications. However, as computational recources are growing constantly, simulation at higher Reynolds number might be possible at a time which is remote future for a greenly doctoral candidate.

# References

Apsilidis, N., Diplas, P., Dancey, C. L., and Bouratsis, P. (2015). Time-resolved flow dynamics and reynolds number effects at a wall-cylinder junction. *Journal of Fluid Mechanics*, 776:475–511.

Bose, S. T., Moin, P., and You, D. (2010). Grid-independent large-eddy simulation using explicit filtering. *Physics of Fluids*, 22(10):105103.

Breuer, M., Peller, N., Rapp, C., and Manhart, M. (2009). Flow over periodic hills – Numerical and experimental study in a wide range of Reynolds numbers. *Computers & Fluids*, 38(2):433–457.

Castro, I. P. and Robins, A. G. (1977). Flow around a surface-mounted cube in uniform and turbulent streams. *Journal of Fluid Mechanics*, 79:307–335.

Dargahi, B. (1989). The turbulent flow field around a circular cylinder. *Experiments in Fluids*, 8(1-2):1–12.

Devenport, W. J. and Simpson, R. L. (1990). Time-dependent and time-averaged turbulence structure near the nose of a wing-body junction. *Journal of Fluid Mechanics*, 210:23–55.

Escauriaza, C. and Sotiropoulos, F. (2011). Reynolds Number Effects on the Coherent Dynamics of the Turbulent Horseshoe Vortex System. *Flow, Turbulence and Combustion*, 86(2):231–262.

Hussein, H. J. and Martinuzzi, R. J. (1996). Energy balance for turbulent flow around a surface mounted cube placed in a channel. *Physics of Fluids*, 8.

Imhof, D. (2004). *Risk assessment of existing bridge structures.* PhD thesis, University of Cambridge.

Jenssen, U., Schanderl, W., and Manhart, M. (2016). Cylinder wall junction flow: Particle Image Velocimetry and Large Eddy Simulation. In *ERCOFTAC Symposium on Engineering Turbulence Modelling and Measurements.*

Jiang, F., Andersson, H. I., Gallardo, J. P., and Okulov, V. L. (2016). On the peculiar structure of a helical wake vortex behind an inclined prolate spheroid. *Journal of Fluid Mechanics*, 801:1–12.

Kirkil, G. and Constantinescu, G. (2015). Effects of cylinder reynolds number on the turbulent horseshoe vortex system and near wake of a surface-mounted circular cylinder. *Physics of Fluids*, 27:075102.

Krajnović, S. (2011). Flow around a tall finite cylinder explored by large eddy simulation. *Journal of Fluid Mechanics*, 676:294–317.

Link, O., Pfleger, F., and Zanke, U. (2008). Characteristics of developing scour-holes at a sand-embedded cylinder. *International Journal of Sediment Research*, 23(3):258–266.

Manhart, M. (1998). Vortex Shedding from a Hemisphere in a Turbulent Boundary Layer. *Theoretical and Computational Fluid Dynamics*, 12(1):1–28.

Manhart, M. (2004). A zonal grid algorithm for DNS of turbulent boundary layers. *Comput. Fluids*, 33(3):435–461.

Manhart, M., Tremblay, F., and Friedrich, R. (2001). MGLET: a parallel code for efficient DNS and LES of complex geometries. In Jenssen, C. B., Kvamdal, T., Andersson, H. I., Pettersen, B., Ecer, A., Periaux, J., Satofuka, N., and Fox, P., editors, *Parallel Computational Fluid Dynamics 2000*, Amsterdam. Elsevier Science B.V.

Martinuzzi, R. and Tropea, C. (1993). The flow around surface-mounted, prismatic obstacles placed in a fully-developed channel flow. *Journal of Fluids Engineering - Transactions of the ASME*, 115(1):85–92.

Nezu, I. and Nakagawa, H. (1993). *Turbulence in Open-Channel Flows*. IAHR Monograph. A.A. Balkema, Rotterdam.

Nicoud, F. and Ducros, F. (1999). Subgrid-Scale Stress Modelling Based on the Square of the Velocity Gradient Tensor. *Flow, Turbulence and Combustion*, 62(3):183–200.

Paik, J., Escauriaza, C., and Sotiropoulos, F. (2007). On the bimodal dynamics of the turbulent horseshoe vortex system in a wing-body junction. *Physics of Fluids*, 19:045107.

Peller, N. (2010). *Numerische Simulation turbulenter Strömungen mit Immersed Boundaries*. PhD thesis, Technische Universität München.

Peller, N., Duc, A. L., Tremblay, F., and Manhart, M. (2006). High-order stable interpolations for immersed boundary methods. *Int. J. Numer. Methods Fluids*, 52:1175–1193.

Pfleger, F. (2011). *Experimentelle Untersuchung der Auskolkung um einen zylindrischen Brückenpfeiler*. PhD thesis, Technische Universität München.

Pope, S. B. (2011). *Turbulent Flows*. Cambridge University Press.

Rodi, W., Ferziger, J., Breuer, M., and Pourquiée, M. (1997). Status of Large Eddy Simulation: Results of a Workshop. *ASME. Journal of Fluids Engineering*, 119(2):248–262.

Roulund, A., Sumer, B. M., Fredsoe, J., and Michelsen, J. (2005). Numerical and experimental investigation of flow and scour around a circular pile. *Journal of Fluid Mechanics*, 534:351–401.

Schanderl, W., Jenssen, U., and Manhart, M. (2017a). Near-wall stress balance in front of a wall-mounted cylinder. *Flow, Turbulence and Combustion.*

Schanderl, W., Jenssen, U., Strobl, C., and Manhart, M. (2017b). The structure and the budget of turbulent kinetic energy in front of a wall-mounted cylinder. *Journal of Fluid Mechanics*, 827:285–321.

Schanderl, W., Jenssen, U., Strobl, C., and Manhart, M. (2017c). Wall shear stress scaling in front of a wall-mounted cylinder. *Draft.*

Schanderl, W. and Manhart, M. (2015). Non-equilibrium near wall velocity profiles in the flow around a cylinder mounted on a flat plate. In *15th European Turbulence Conference*.

Schanderl, W. and Manhart, M. (2016). Reliability of wall shear stress estimations of the flow around a wall-mounted cylinder. *Computers and Fluids*, 128:16–29.

Schanderl, W. and Manhart, M. (2017). Dissipation of turbulent kinetic energy in a cylinder wall junction flow. *submitted to Flow, Turbulence and Combustion*.

Schlichting, H. and Gersten, K. (2006). *Boundary Layer Theory*. Springer.

Schofield, W. H. and Logan, E. (1990). Turbulent shear-flow over surface mounted obstacles. *Journal of Fluids Engineering - Transactions of the ASME*, 112(4):376–385.

Simpson, R. L. (2001). Junction flows. *Annual Review of Fluid Mechanics*, 33:415–443.

Tseng, M.-H., Yen, C.-L., and Song, C. C. S. (2000). Computation of three-dimensional flow around square and circular piers. *Int. J. Numer. Meth. Fluids*, 34(3):207–227.

Werner, H. (1991). *Grobstruktursimulation der turbulenten Strömung über eine querliegende Rippe in einem Plattenkanal bei hoher Reynoldszahl*. PhD thesis, Technische Universität München.

# A. Appendix: Publication 1, summarised in chapter 6

Computers and Fluids 128 (2016) 16–29

Contents lists available at ScienceDirect

Computers and Fluids

journal homepage: www.elsevier.com/locate/compfluid

# Reliability of wall shear stress estimations of the flow around a wall-mounted cylinder

Wolfgang Schanderl, Michael Manhart*

*Chair of Hydromechanics, Technische Universität München, Arcisstr. 21, München 80333, Germany*

ARTICLE INFO

*Article history:*
Received 10 March 2015
Revised 9 October 2015
Accepted 6 January 2016
Available online 19 January 2016

*Keywords:*
Large-Eddy Simulation
Wall-mounted cylinder
Boundary layer
Horseshoe vortex
Wall shear stress

ABSTRACT

The flow field and wall shear stresses around a wall-mounted cylinder for a Reynolds number of $Re_D = 39000$, based on the diameter of the cylinder and the bulk velocity, was investigated applying Large-Eddy Simulation (LES). We used a Finite-Volume method on a Cartesian grid with staggered arrangement of the variables. The curved surface of the cylinder has been approximated by a conservative second order Immersed Boundary method.

We carefully validate our simulation in terms of grid resolution, inflow condition and contribution of subgrid scale stresses. Around the cylinder, local grid refinement provides spacings of 7.5 wall units in horizontal and 1.9 wall unit in vertical direction based on the the wall shear stress of the oncoming flow. Thus, the contributions of the modeled subgrid scale stresses remain small compared to other stresses and the flow variables converge with grid resolution.

We demonstrate that the flow structure and predicted wall shear stresses strongly depend on the inflow condition, which has to take into account turbulent fluctuations and the secondary flow, if present. A maximum amplification factor of the time-averaged wall shear stress of 12.0 with respect to the one in the oncoming flow field shows up in the lateral front of the cylinder. Instantaneous wall shear stresses however reach a maximum amplification factor of up to 40 in the wake of the cylinder.

## 1. Introduction

About sixty percent of all bridge failures in the last decades are caused by scour problems [1]. The case of a flow around a bridge pier seems to be simple at first glance, but the prediction of the scour process, its final shape and its maximum depth is a challenge which hasn't been solved yet. This challenge is not even solved for experiments in laboratories, although laboratory conditions exclude most of the uncertainties a natural river provides [2]. Both the behavior of the sediment and the flow pattern to which the sediment is exposed is not fully understood until now. A better and more robust prediction of scour depth evolution is expected by coupling of Computational Fluid Dynamics with models for sediment dynamics [3]. However, such an approach relies on the accurate prediction of the flow field and its interaction with sediment motion. The former is the focus of this paper.

The evolution of a scour hole around a bridge pier in a mobile bed strongly depends on the local flow field induced by the cylinder which in turn depends on the approach flow conditions. The undisturbed free surface flow in a river or laboratory flume develops a boundary layer on the river ground which is disturbed by secondary flows but can be expected to extend up to the free surface. Thus, the water depth is equivalent with the boundary layer thickness. The velocity gradient in the boundary layer flow approaching a cylinder leads to a vertical pressure gradient on the front of the cylinder which results in a strong downwards flow in front of the cylinder. In combination with the horizontally adverse pressure gradient that is due to the blocking effect of the cylinder, a complex vortex system at the bottom plate is formed. This vortex system is transported around the cylinder by the flow in streamwise direction, resulting in the so-called horseshoe vortex. The horseshoe vortex and the acceleration of the flow around the cylinder lead to an amplification of the wall shear stress around the cylinder which comes along with a higher potential of erosion and scouring. The flow characteristics and scour mechanism are extensively discussed in literature. The basic patterns of the flow field around wall-mounted bluff bodies were described by Hjorth [4], Melville and Raudkivi [5], Dargahi [6,7] and others.

Even though the principal shape of the vortex system is uncontested, there are still discrepancies in the detailed description of the flow field. Devenport and Simpson [8] conducted

---

* Corresponding author. Tel.+49 8928922583.
*E-mail address:* michael.manhart@tum.de, m.manhart@bv.tu-muenchen.de (M. Manhart).

http://dx.doi.org/10.1016/j.compfluid.2016.01.002

experimental investigations of the flow around a wall-mounted wing-shaped cylinder at a Reynolds number of $Re_D = 119000$ in a wind tunnel. They described the bimodal dynamics of the horseshoe vortex system which manifests itself in wall shear stress PDF's that have bimodal peaks. In addition, they qualitatively distinguished between one small and two large zones in the wall shear stress distribution in front of the body, each being the footprint of a vortex above.

Measurements of the wall shear stress distributions around the cylinder are extremely difficult due to thin viscous layers and large fluctuation levels. Several different methods have been employed. Preston's method has been used by Melville and Raudkivi [5] and Dargahi [6,7]. Hot film probes have been used by Hjorth [4], Dargahi [6,7] and Roulund et al. [3]. Graf and Istiarto [9] have found strong deviations in wall shear stresses estimated by different approaches using velocity measurements above the wall. To the authors' knowledge, the most reliable wall shear stress measurements were conducted by Roulund et al. [3], who used a flush mounted hot film probe to measure wall shear stresses around a cylinder at a large Reynolds number of $Re_D = 170000$ and a boundary layer to diameter ratio of $\frac{\delta}{D} = 1$.

Dargahi [6] conducted experiments at a Reynolds number of $Re_D = 39000$ and a water depth to diameter ratio of $\frac{\delta}{D} = 1.33$. Besides flow visualization with hydrogen bubble technique, he measured wall shear stresses in the symmetry plane in front of the cylinder using the Preston tube method and velocity probes at a wall distance of $z = 0.0033D$. His wall shear stress measurements indicate the footprint of one large horseshoe vortex in front of the cylinder, although his sketches based on hydrogen bubble images show more than one vortex.

Dargahi's results [6] have been used to validate various numerical results [3,10,11]. Tseng et al. [10] conducted a LES and obtained good agreement of the amplitude of the wall shear stress amplification. His results also show one region of large wall shear stresses in front of the cylinder, which is a little longer than in Dargahi's results [6]. Escauriaza and Sotiropoulos [11] conducted simulations applying a coupled RANS and LES solver at $Re_D = 39000$. The overall amplitude of the wall shear stress amplification is in good agreement to the one by Dargahi [6]. Though Escauriaza and Sotiropoulos [11] also report three distinct regions in the wall shear stress pattern in front of the cylinder, there are some differences to the flow pattern Devenport and Simpson [8] described. In a series of papers, the dynamics of the horseshoe vortex in front of a wall-mounted cylinder and a wall-mounted wing has been investigated using various eddy resolving techniques by, e.g., [11–14]. However, comparing various results, it can be concluded that numerical method, turbulence model, mesh and inflow condition seem to play a significant role for the position and topology of the vortex system in front of an obstacle mounted on a flat plate, compare e.g. [11] and [15], see also [14].

The present study focuses on a highly resolved LES of the flow around a cylinder mounted on a flat plate. We consider a Reynolds number of $Re_D = 39000$ based on the bulk velocity $u_b$ and the diameter of the cylinder D. This configuration is comparable to the one used by Pfleger [16] who measured sediment grain motion in a scour hole around a circular cylinder in a sand bed and to the experiment of Dargahi [7] who measured pressure distributions, velocity profiles, turbulence characteristics and wall shear stresses in front of the cylinder at a comparable Reynolds number. We intend to answer the question how accurate and reliable such a simulation can be. We took special care to apply a fully developed turbulent boundary layer flow of thickness $\delta = 1.5D$ as inflow profile using a precursor domain coupled to the grid containing the cylinder. To assess the influence of the oncoming flow on the vortex system, we compare this inflow condition with less sophisticated boundary conditions, namely a block profile and a time constant logarithmic shaped profile. In addition, a diligent grid study was done to show convergence over grid refinement.

Against the background of previously mentioned studies, we carefully discuss the reliability of our results in particular for wall shear stress estimation in such a setup. We focus on the region influenced by the horseshoe vortex system in front of the cylinder.

The paper is organized as follows. In Section 2 we describe the applied flow solver and the computational domain, followed by a detailed description of simulating the inflow profile by applying a precursor simulation in Section 3. Section 4 deals with the influence of this inflow profile on the flow around the cylinder as well as with the influence of grid resolution and subgrid stress model. In Section 5 the results of the presented study are compared to those provided by literature and carefully discussed. Finally, Section 6 emphasis the time-dependent component of the flow pattern and its influence on the wall shear stress distribution.

## 2. Computational configuration

### 2.1. Numerical method

The flow solver MGLET uses a Finite Volume method based on a staggered arrangement of variables on a non-equidistant Cartesian grid. It provides a second order spatial approximation and a third order Runge–Kutta time integration. The curved surface of the cylinder is approximated by a conservative second order Immersed Boundary method [17,18]. In addition, MGLET provides an algorithm for grid refinement by zonally embedded grids [19], each refining the grid resolution by a factor of two. The subgrid scale stresses are parametrized by the Wall-Adapting Local Eddy-Viscosity (WALE) model [20], which defines the turbulent viscosity $\nu_t$ as shown by Eq. 1.

$$\nu_t = C_w \overline{\Delta}^2 \frac{(S^d_{ij} S^d_{ij})^{3/2}}{(\bar{S}_{ij}\bar{S}_{ij})^{5/2} + (S^d_{ij} S^d_{ij})^{5/4}} \tag{1}$$

Here, $C_w = 0.1$ and

$$S^d_{ij} = \frac{1}{2}\left(\bar{g}^2_{ij} + \bar{g}^2_{ji}\right) - \frac{1}{3}\delta_{ij}\bar{g}^2_{kk}, \tag{2}$$

where $\bar{g}_{ij} = \frac{\partial u_i}{\partial x_j}$. The WALE model has the advantage that the subgrid-scale viscosity decreases naturally towards the wall with the correct limiting behaviour of $\nu_t \propto y^3$.

The applied solver has been used and validated by several authors in various configurations, e.g. [21–23].

### 2.2. Computational domain

The computational domain consists of two major parts: a precursor grid, which is used to generate the fully developed turbulent open channel flow, and a grid containing the cylinder (diameter $D$), using the turbulent open channel flow as inflow condition, see Fig. 1. The latter one has a domain size of $L_x = 25D$, $L_y = 12D$ and $L_z = 1.5D$ in streamwise (x-), spanwise (y-) and wall-normal (z-)direction, respectively. The origin of the coordinate system is located in the center of the cylinder which is placed in the center of the domain. The spanwise and wall-normal dimensions are based on the experimental setup used in previous studies [16]. To simulate an open channel flow in a flume, the bottom and side walls are defined as no-slip. At the top wall, a slip boundary condition models a free surface at a vanishing Froude number. This implies that no pile up or depression occurs in front or in the back of the cylinder. At the inflow boundary, the grid is coupled to the precursor grid, in which a fully turbulent boundary layer is simulated using periodic streamwise boundary conditions. The precursor simulation will be described in the next section.

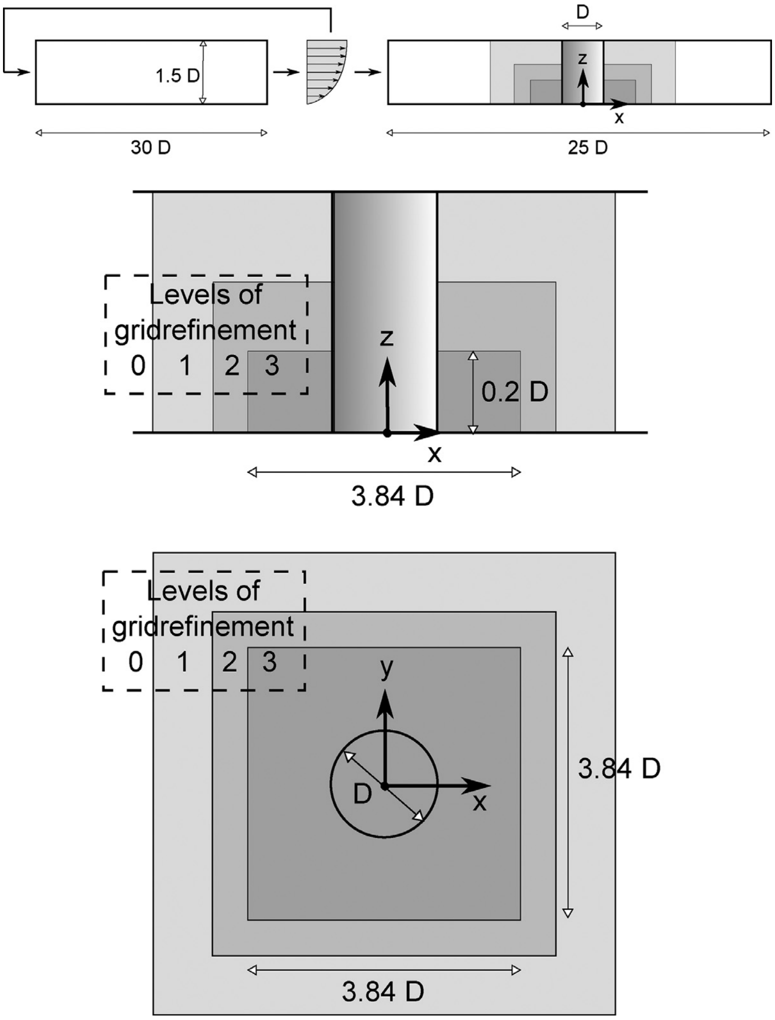

**Fig. 1.** Side and top view of the computational domain. The zonally embedded grids are marked in gray.

**Table 1**
Overview of the grids used for the simulations reported here. Inner units refer to the wall shear stress in precursor simulation, averaged over the spanwise region $-1.25 \le y/D \le 1.25$. $\Delta z^+_{wall}$ is the wall-normal resolution on the bottom wall. The grids are stretched in wall-normal direction with stretching factors less than 1%.

| Grid | Levels of refinement | Cells per diameter **horizontal**/vertical | Grid spacing $\Delta x^+/\Delta y^+/\Delta z^+_{wall}$ | Grid cells |
|---|---|---|---|---|
| Precursor | 0 | | **60**/**60**/15 | $44 \cdot 10^6$ |
| Base | 0 | **31.25**/125 | **60**/**60**/15 | $35 \cdot 10^6$ |
| Grid 1 | 1 | **62.5**/250 | **30**/**30**/7.5 | $80 \cdot 10^6$ |
| Grid 2 | 2 | **125**/500 | **15**/**15**/3.7 | $64 \cdot 10^6$ |
| Grid 3 | 3 | **250**/1000 | **7.5**/**7.5**/1.9 | $177 \cdot 10^6$ |

**Table 2**
Performed simulations with different levels of refinement and boundary conditions.

| Simulation | Grid | Inflow condition | Total number of cells |
|---|---|---|---|
| #1 | 1 | Precursor | $159 \cdot 10^6$ |
| #2 | 2 | Precursor | $223 \cdot 10^6$ |
| #3 | 3 | Precursor | $400 \cdot 10^6$ |
| #4 | 3 | **Block profile** | $207 \cdot 10^6$ |
| #5 | 2 | **Log. profile** | $179 \cdot 10^6$ |

A base grid which is refined towards the bottom wall covers the complete computational domain. The region of interest around the cylinder is refined by up to three locally embedded grids [19] which provide grid refinement, see Table 1 and Fig. 1. In total, five different simulations have been performed, see Table 2. The first three simulations use fully turbulent inflow conditions from the precursor simulation and differ by the levels of refinement around the cylinder. Simulation #1 is refined with one locally embedded grid, corresponding to a refinement factor of two with respect to the base grid. Simulation #2 uses two levels of refinement and the finest simulation #3 holds three local grids and therefore a refinement factor of eight, resulting in a grid spacing of $\Delta z = 0.001D$ in vertical and $\Delta x = \Delta y = 0.004D$ in horizontal direction in the region of interest at the bottom plate around the cylinder of diameter D. The base grid has spacings of $\Delta z^+_{wall} = 15$ and $\Delta x^+ = \Delta y^+ = 60$, based on the wall shear stress in the precursor simulation averaged over a span of $-1.25 < y/D < 1.25$. The wall-tangential velocity vectors are therefore defined at a position $z^+ = 7.5$ which allows avoiding a wall model to determine the wall shear stress. The placement of the local grids is indicated in Fig. 1.

The simulations were performed on the high performance computer SUPERMUC of the Bavarian Academy of Sciences. On 800 cores, the simulation #3 needed about 4.8 seconds per time step. This adds up to about 2 million CPU-hours once the statistically steady state has been achieved.

We investigated the influence of the inflow condition by using a constant (in time and space) velocity as inflow for simulation #4 and a time constant profile using the time averaged velocity profile

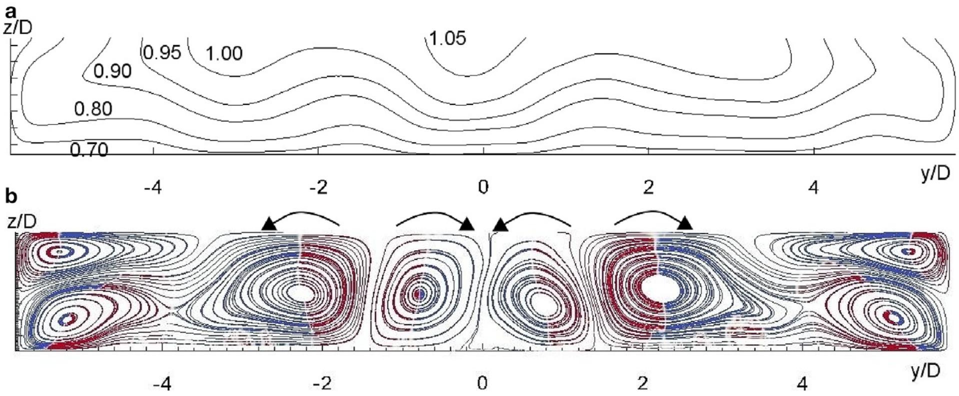

**Fig. 2.** Velocity distribution in the precursor grid. Isolines of the streamwise velocity component (a) and streamlines of secondary currents (b). Upward flow is marked by red and downward flow by blue streamlines. (For interpretation of the references to color in this figure legend, the reader is referred to the web version of this article.)

from the precursor simulation, denoted as ‘logarithmic profile’ for simulation #5. Grid 3 in simulation #4 is of smaller spatial extend than in the other simulations. Nevertheless, further discussion will show that the differences between refinement level 2 and 3 are rather small, see Section 4.1. Therefore we omitted redoing simulation #4 with the same extended grid than simulation #3. Simulation #5 was simulated by only two levels of refinement for reasons of computational cost.

## 3. Precursor simulation

Considering a possibly strong influence of the approaching flow on the flow structure around the cylinder [24], we took special care to design a precursor simulation to generate a fully developed turbulent open channel flow at a flow depth of $\delta = 1.5D$ and a width of $L_y = 12D$. A streamwise length of $L_x = 30D$ has been chosen to reduce superposition and therefore self-amplification of long meandering structures in the logarithmic region of the boundary layer flow, so-called superstructures [25].

The grid resolution of the precursor simulation can be seen from Table 1. The first grid point at the wall is just at the limit of the viscous sublayer thus we do not use wall functions. The subgrid-scale viscosity is damped towards the wall by use of the WALE eddy viscosity model [20]. We employ periodic streamwise boundary conditions and a volume force to drive the flow. The volume force is equivalent to a streamwise slope of a flume or a streamwise pressure gradient.

In open channel flows, secondary flow structures develop [26]. Fig. 2a shows isolines of the streamwise velocity component in the precursor grid. The data is not only averaged in time, but also in streamwise direction. The distribution of the streamwise velocity indicates the presence of secondary flow structures due to the influence of the side walls. In the region next to the side walls at about $y < -4D$ and $y > 4D$, this influence leads to a submerged maximum of the velocity profile. Fig. 2b shows the streamlines of the secondary currents in the precursor simulation, colored by the vertical velocity component: Red color is indicating a flow direction in positive z-direction (upwards), blue color in negative z-direction (downwards). The direction of rotation is also indicated by arrows above the vortices. One can identify two nearly triangular-shaped vortices on top of each other in the corners of the channel. These vortices induce four counter rotating vortices next to each other which span the whole channel height in the center of the channel. The central vortices have widths of approximately the channel height. A further description and discussion of secondary flow structures in open channel flow can be found in literature [26,27].

**Table 3**
Bulk velocity and wall shear stress in the precursor for different velocity probes.

| Probe | $\tau_{ref}$ | $u_{ref}$ | $Re_D = \frac{u_{ref}D}{\nu}$ |
|---|---|---|---|
| Whole cross section | $0.9514\tau_0$ | $0.934u_b$ | 39000 |
| $-1.25D < y < 1.25D$ | $\tau_0$ | $u_b$ | 41756 |
| Symmetry plane | $1.026\tau_0$ | $1.039u_b$ | 43384 |

Due to the secondary currents, the streamwise velocity is depending on the spanwise position even in the central part of the channel. Therefore, also the wall shear stress varies over the spanwise position. When looking at reference values for velocity and wall shear stress, several possibilities arise, which are given in Table 3. A measurement in the symmetry plane could best be realized in an experiment. These values are greater than the ones integrated over a spanwise region of $-1.25D < y < 1.25D$, which we take as reference values for our subsequent analysis. One could as well integrate the bulk velocity over the whole cross section and the wall shear stress over the whole wetted perimeter. The latter is in equilibrium with the cross sectional integral of the volume force $\partial p/\partial x$ multiplied by the hydraulic radius $R_{hyd}$ of the open channel. The different definitions can lead to approximately 7% difference in wall shear stress and 11% difference in $u_b$. We assume that the values integrated over $-1.25D < y < 1.25D$ best characterize the oncoming flow and would be less sensitive than others with respect to changes in aspect ratio of the channel. Therefore all values characterizing the inflow profile are averaged in spanwise direction over a region of $-1.25D < y < 1.25D$. Among other parameters, this was done for the data shown in Fig. 3 and the wall shear stress and the bulk velocity[1] of the undisturbed oncoming flow profile $\tau_0$ and $u_b$.

Velocity and Reynolds stress profiles averaged over time and in spanwise direction in the region $-1.25D < y < 1.25D$ are documented in Fig. 3. The velocity profile follows closely the logarithmic law of the wall in the considered region and shows a distinct wake region. The wall nearest grid point in the precursor grid - corresponding to a refinement level of zero - lies at about $z^+ = 7.5$ above the bottom plate. Even though the velocity in this wall nearest grid point is slightly overestimated, both velocity profile and Reynolds stresses are in accordance with boundary layer data from experimental studies [28]. We therefore conclude that our precursor simulation is a good representative for a fully developed open channel flow at the considered Reynolds number.

---

[1] Note, that for $Re_D = 39000$, we take the cross sectional averaged velocity as reference.

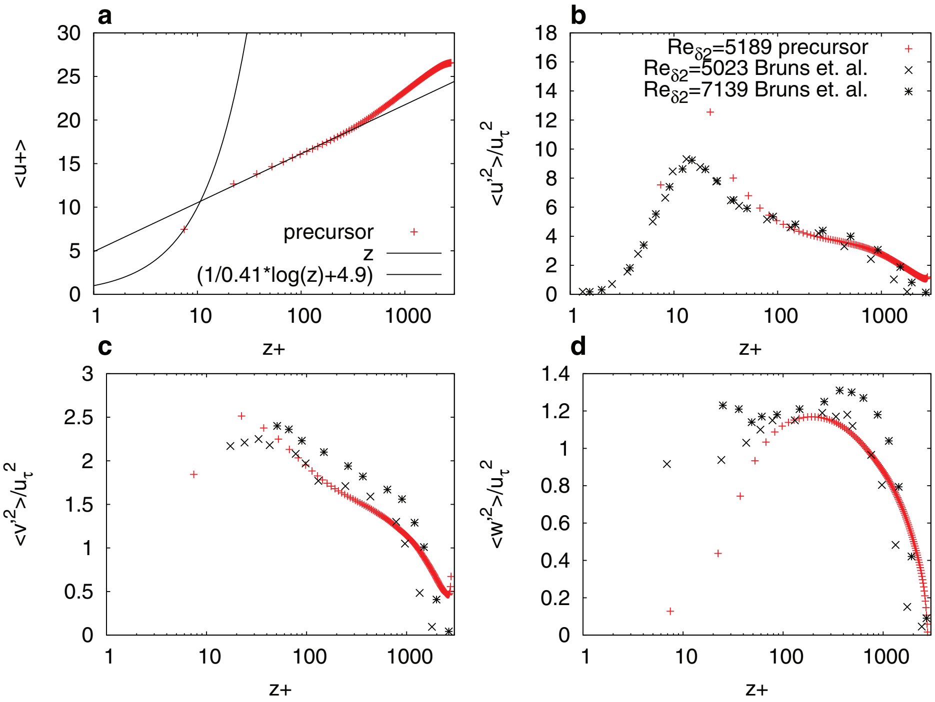

**Fig. 3.** Time-averaged velocity profile (a) and Reynolds normal stresses (b, c and d) in the precursor grid [24]. The experimental data of Bruns et al. [29] has been taken from Fernholz and Finley [28].

The influence of the inflow condition on the flow around the cylinder will be investigated in Section 4.1.

## 4. Influence of numerical configuration on the flow around the cylinder

In this section we carefully assess the influence of the inflow condition and the grid resolution on the flow around the cylinder. We also quantify the contributions of the modeled SGS stresses on the momentum balance in front of the cylinder. This can be viewed as a validation of the results. We start with a discussion of the influence of the inflow condition as it has an impact on the vortex structure in front of the cylinder.

### *4.1. Influence of inflow condition*

We first examine the development of the wall shear stress in front of the cylinder and the region of influence of the cylinder in the simulation using the precursor boundary condition (simulation #3) and the two simulations using time constant inflow conditions (simulations #4 and #5). Fig. 4 shows the wall shear stresses upstream of the cylinder for different inflow conditions. Note that these wall shear stresses are averaged over $-1.25D < y < 1.25D$ and therefore do not match the wall shear stresses in the symmetry plane that are discussed later.

Downstream of the inflow plane, the precursor wall shear stress is sustained in simulation #3 for about $4D$ until it slowly departs from this value due to the upstream influence of the cylinder at $x/D = -8$. The region of influence by the cylinder can be identified as eight cylinder diameters. The kink in the wall shear stress at about $x = -4D$ results from the interface of the first locally embedded grid.

Since both simulations with fixed inflow conditions do not use a precursor simulation, turbulent fluctuations sustaining the wall shear stress are missing. Therefore, the wall shear stress drops immediately downstream of the inflow plane (Fig. 4), no matter if a block profile or a logarithmic profile was used. As the wall shear stresses in both simulations continue to decrease during the approach of the cylinder, $\tau_0$ is evaluated as average over $-11.7D < x < -4D$ for the simulations with time constant inflow conditions. A distinct region of influence can not clearly be identified in the two simulations using time constant inflow conditions, however it seems to be smaller than in the simulation with fully turbulent inflow condition.

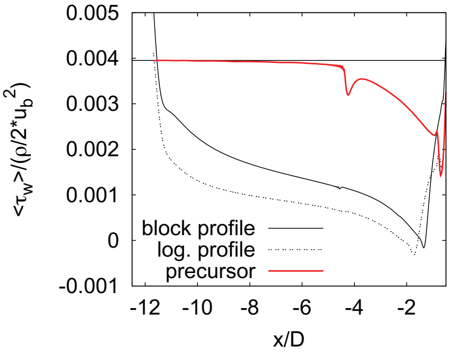

**Fig. 4.** Wall shear stresses averaged over $-1.25 < y/D < 1.25$ and normalized by $u_b$ upstream of the cylinder for simulation #3 (precursor), #4 (block profile) and #5 (logarithmic profile).

Moreover, the flow profiles of the two time constant boundary conditions remain laminar until they reach the cylinder (not shown). This leads to a wall shear stress much smaller than the one of the turbulent flow profile in the precursor setup. Therefore it is argued, that the so-called amplification factor of the wall shear stress $\tau_w/\tau_0$, which is often used in literature, requires a careful discussion of the undisturbed wall shear stress $\tau_0$.

The problem of choosing a suitable reference for the wall shear stress is illustrated by Fig. 5. It compares the wall shear stresses in the symmetry plane in front of the cylinder for different inflow

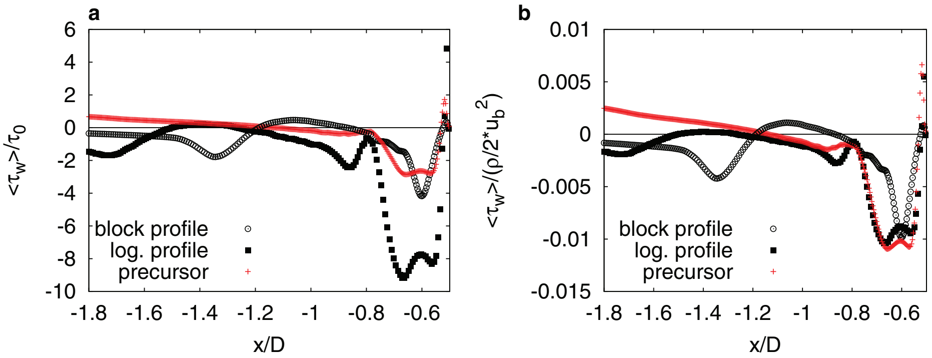

**Fig. 5.** Wall shear stress in the symmetry plane in front of the cylinder for different inflow conditions; (a) normalized with $\tau_0$ and (b) normalized with $u_b$.

conditions. The ones normalized by the undisturbed wall shear stress $\tau_0$ (Fig. 5a) are contrasted to the ones normalized by the bulk velocity $u_b$ (Fig. 5b). Positive values indicate time-averaged velocity in streamwise direction in the near-wall region, negative values represent backflow, accordingly.

Three regions can be identified in the wall shear stress, each being the footprint of a vortex as described later. Simulation #3 (with precursor) reveals a large zone of backflow extending to $x = -1.13D$ which is divided into a zone of negative wall shear stress with large magnitude ($-0.53 < x/D < -0.82$) and a zone with relatively small magnitude in $-0.82D < x < -1.13D$. The regions are separated by a local maximum at $x/D = -0.82$ (which is a local minimum in absolute wall shear stress). Right in front of the cylinder we can identify a small zone of relatively large positive wall shear stress which reaches nearly twice the value of the oncoming flow. There must be a small corner vortex in front of the cylinder which rotates anti-clockwise.

Simulation #5 (with time constant log-law as inflow) shares features with simulation #3 in that the double peak in the primary backflow region appears and that the corner vortex is clearly visible. The zone of relatively small negative wall shear stress for $x/D < 0.82$ obtains a different wall shear stress development upstream containing a small forward flow and a long backflow around $x \approx -2D$, which is also visible in the spatially averaged wall shear stresses shown in Fig. 4. This zone of negative wall shear stress indicates an additional vortex in this region, which also appears in simulation #4 (with constant block profile inflow).

However, simulation #4 shows a wall shear stress distribution of completely different shape for $-0.82 < x/D$. There is only one narrow peak at $x = -0.6D$. Also, the maximum right in front of the cylinder under the corner vortex is hardly in evidence, so does the local maximum at $x = -0.8D$ (Fig. 5). Instead, there is a strong backflow around $x = -1.4D$ which is not present in simulations with other inflow profiles.

Only considering the amplification factor based on the definition of $\tau_0$ as given above leads to an overestimation of the wall shear stresses for the setup with log profile. In fact, the wall shear stresses are not overestimated around the cylinder, but underestimated in the undisturbed region, see Fig. 4. One will never get rid of that problem but by using a precursor simulation, which provides a truly undisturbed and uniform region to measure $\tau_0$.

Fig. 5b, in which $\tau_w$ is normalized by $u_b$, indicates the results from simulation #5 to follow the shape of the simulation with precursor quite well for $x > -0.82D$. Furthermore, both simulations, #4 with block profile and #5 with time constant log profile meet the maximum wall shear stress in front of the cylinder with minor deviations of 5% (simulation #5) and 10% (simulation #4). Note, that those deviations depend on which definition of the bulk velocity has been chosen to normalize the wall shear stresses, compare Table 3.

Combining these observations might lead to the conclusion that the shape of the wall shear stress profile in front of the cylinder depends on the shape of the inflow profile and that the maximum wall shear stress depends more on the momentum of the oncoming flow, $\rho u_b^2$, than on the wall shear stress upstream, $\tau_0$. In addition, including turbulent fluctuations to the inflow profile further increases the maximum wall shear stress based on $u_b$ averaged over $-1.25 < y/D < 1.25$. One might argue that the difference in the wall shear stresses between the simulation with fully turbulent inflow and the simulation with time constant log profile is due to the different grid resolution used for theses studies. This argument is discussed and debilitated in Section 4.2.

The wall shear stress is the footprint of the flow pattern above the wall. This flow pattern is made visible by time-averaged streamlines in Fig. 6 for all three inflow conditions. Fig. 6a shows results of simulation #3 with precursor simulation and three levels of grid refinement. Three vortices are forming the horseshoe vortex system. There is a main clockwise rotating vortex of ellipsoidal shape V1, located at $-0.83D < x < -0.53D$ with its center at $(x, z) = (-0.73D, 0.06D)$. A stagnation point S1, located at about $(x, z) = (-0.83D, 0.05D)$ separates this vortex from another clockwise rotating vortex V2. The point S2 where the oncoming flow separates from the bottom plate can be found at $x = -1.1D$. A small anti-clockwise rotating vortex V3 can be found between a stagnation point S3 at $x = -0.53D$ and the cylinder edge. V3 is formed by the strong boundary layer flow going downwards along the cylinder. The associated stagnation point S4 is located right above. It is interesting to note that the region, where the streamlines are most densely packed and therefore the velocity is largest, is not directly below the main vortex, but shifted slightly towards the cylinder. In addition, it is remarkable that there is no stagnation point right on the bottom plate between the vortices V1 and V2. This implies that theses vortices are sharing the same streamlines and merging in close vicinity to the wall. This is also supported by the wall shear stress (see Fig. 5), which has a local minimum in magnitude at $x = -0.82D$ for simulation #3, but does not disappear there.

In the simulation #5 with steady logarithmic inflow profiles (Fig. 6b), V1 and V3 have a slightly smaller and V2 a little larger extent than the ones in the simulation #3. However, between $x = -1.2D$ and the cylinder the flow patterns of both simulations looks quite similar. Nevertheless, there is an additional vortex or backflow region, respectively, indicated as V4 upstream of the additional stagnation point S5 at $x = -1.5D$, see also Fig. 5. The point of separation S6 upstream of V4 at $x = -2.3D$ is outside of the domain plotted. Vortex V4 seems to be unimpressive, but it changes the whole flow pattern upstream of S2 by introducing a additional region of backflow.

Fig. 6c shows the time-averaged streamlines for simulation #4. Using a block profile as inflow boundary condition leads to a

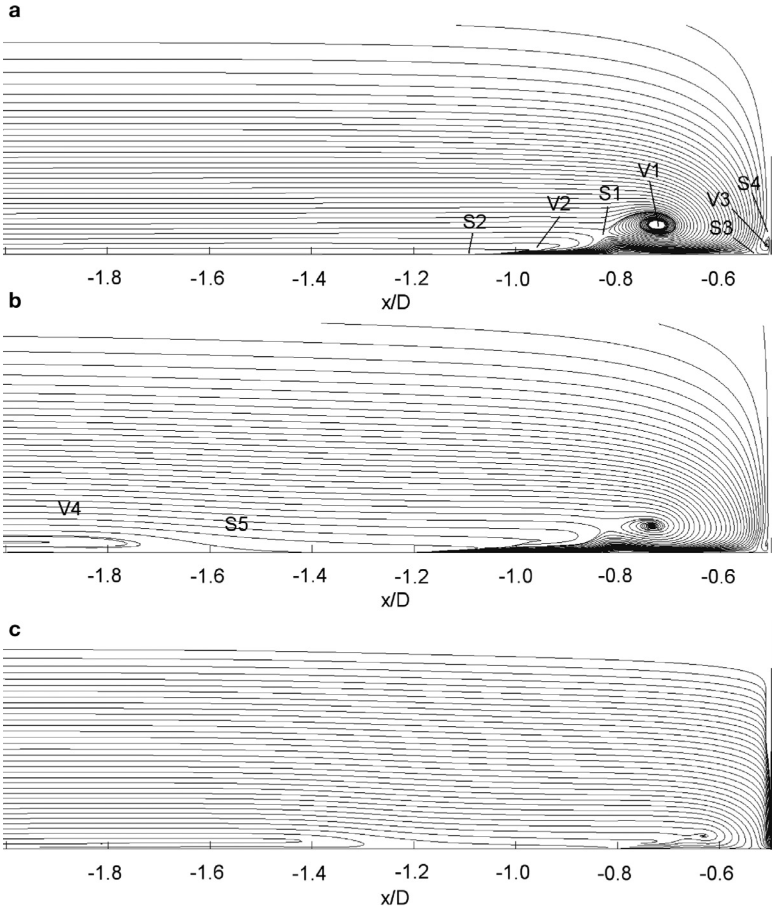

**Fig. 6.** Time-averaged streamlines in the symmetry plane in front of the cylinder for the three inflow conditions precursor (a), fixed log. profile (b) and fixed block profile (c).

boundary layer thickness of approximately $\delta = 0.2D$ when the flow is approaching the cylinder compared to $\delta = 1.5D$ in the other simulations. While in the lower region the vertical velocity gradient is large, it is almost zero in the region above $\delta$. Thus, the vertical pressure gradient at the cylinder front is restricted to the lower part of the domain. Therefore the down-flow appears only in the lower part and the resulting vortex system (V1 and V2) is compressed to a small region. Also, vortex V3 is not visible anymore in the streamlines. Compared to the setup with fixed logarithmic profile, V4 is shifted downstream, but it has almost the same vertical extension. V4 appears in both setups with fixed inflow condition, so it seems to be independent of the actual shape of the inflow profile. Since V4 does not appear in simulation #3 with a turbulent inflow profile, we assume the turbulent fluctuations and the momentum transport connected with them to be responsible for suppressing the vortex V4.

### 4.2. Grid resolution

In order to validate our simulations in terms of grid resolution, we performed three simulations at different refinement levels according to Tables 1 and 2. We assess the wall shear stresses in the symmetry plane in front of the cylinder and along a line at 90° in spanwise direction (Fig. 7). One can observe the convergence of the wall shear stress in front of the cylinder over grid refinement (Fig. 7a), differences between grid 2 and 3 are systematically smaller than differences between grid 1 and 3. Grid 2 and grid 3, the finest one, match quite well, although grid 2 is not able to resolve the maximum amplification under the small anti-clockwise rotating vortex V3 and the local maximum of the wall shear stress under the stagnation point S1 ($x/D \approx -0.82$) is shifted upstream a little bit. Nevertheless, in large regions under the main vortex V1 it almost follows the solution of simulation #3 without deviations.

Convergence can not be proven completely for the region lateral of the cylinder (Fig. 7b). Here, the wall shear stress in a plane lateral of the cylinder, normal to the symmetry plane, is shown. Right next to the cylinder, one can see a strong velocity overshoot which is fed by the acceleration of the fluid around the cylinder and amplified by the horseshoe vortex system. The peak value predicted by grid 2 is almost 15% smaller than the one predicted by grid 3 which reaches $7\tau_0$. This peak is decreasing to an amplification factor of about three at $y = 0.6D$. The amplification is further decreasing and reaching a value of one at approximately $y = 4D$, which is not shown in Fig. 7b. For $y > 0.57D$ the two finer grids match in a satisfying way. To obtain full convergence in close vicinity of the cylinder, it would be necessary to refine the grid by a fourth local grid. This is omitted due to the enormous computational costs linked to that. The coarse grid (grid 1) is performing well in regions $y > 0.7D$, but the overshoot next to the cylinder is underestimated by approximately 30%.

The maximum amplification factor of the time-averaged wall shear stresses around the cylinder can be seen in Table 4. The largest wall shear stresses are located in the lateral front of the cylinder at about 55° to the symmetry plane, see Fig. 8 or Section 6. While grid 1 underestimates the maximum amplification by about 25%, grid 2 comes quite close to the value of the finest grid (grid 3). Being aware of the narrow peak of the wall shear stress maximum, see Fig. 8, it becomes evident that a coarse grid

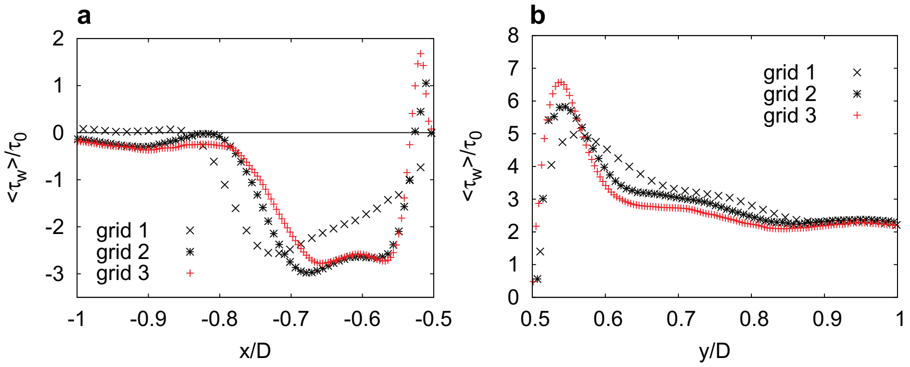

**Fig. 7.** Amplification of the wall shear stress at different grid resolutions. In the symmetry plane in front of the cylinder (a) and normal to the symmetry plane lateral of the cylinder (b) [24].

**Table 4**
Maximum time-averaged wall shear stresses around the cylinder.

| Setup | Grid | Max. $\frac{<\tau_w>}{<\tau_0>}$ | Max. $\frac{<\tau_w>}{\frac{\rho}{2}u_b^2}$ |
|---|---|---|---|
| Simulation #1 | 1 | 8.99 | 0.0396 |
| Simulation #2 | 2 | 12.1 | 0.0535 |
| Simulation #3 | 3 | 12.0 | 0.0529 |
| Simulation #4 | 3 | 16.7 | 0.0396 |
| Simulation #5 | 2 | 51.0 | 0.0570 |

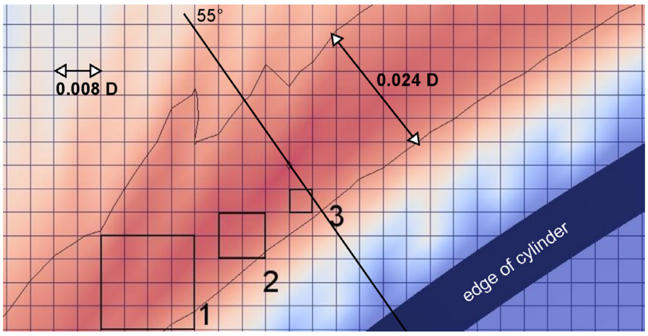

**Fig. 8.** Maximum time-averaged amplification of the wall shear stress in the lateral front of the cylinder. The isoline is marking a amplification factor of ten, the squares indicate the grid spacings of the corresponding refinement levels.

like the one used in simulation #1 will hardly be able to predict its amplitude correctly. The isolines in Fig. 8 mark a value of the amplification factor of ten. In the area between the two isolines the wall shear stress is larger than $10\tau_0$. This area is quite narrow, and resolved by about four grid cells of grid 3, which is the finest one. The small squares are representing the grid cells of the finest local grid, used for simulation #3. The largest square represents the finest grid spacing of grid 1. Therefore, the narrow wall shear stress peak is resolved by two cells of grid 2 and only one cell of grid 1. It is obvious that grid 1 is not sufficiently fine in horizontal directions to represent such spatial wall shear stress distributions.

Table 4 demonstrates the importance of the normalization of the wall shear stress around the cylinder. While there is large scatter when the wall shear stress is normalized by the one of the oncoming flow, $\tau_0$, all simulations give similar values when normalized by the oncoming bulk velocity. This underlines the necessity of careful evaluation and simulation of the oncoming flow field. Besides that, simulation #4, using a block profile as inflow condition underestimates the maximum wall shear stress by 25%, even with the finest grid resolution. As opposed to that, simulation #5, using a logarithmic profile as inflow conditions, overestimates the maximum wall shear stress by about 8%.

### *4.3. Influence of the subgrid scale model*

For modeling the subgrid stresses, the WALE model as described by Eq. (1) was applied. Due to the enormous computational costs, it was omitted to run simulations with different subgrid scale models to evaluate its influence on the solution. Instead it shall be shown that the contribution of the modeled stresses to the momentum balance is small compared to other contributors and thus the SGS stresses are of minor influence on the solution of the flow field.

On the highest level of grid refinement, grid 3, the ratio of time-averaged modeled viscosity to molecular viscosity reaches a maximum of $\langle \nu_t \rangle / \nu = 3$. This maximum is located in the shear layer in the wake of the cylinder which is downstream of the regions of large averaged wall shear stresses.

For assessing the SGS contributions to the wall shear stresses in front and aside of the cylinder, we consider the contributions of the instantaneous and time-averaged SGS viscosity in the symmetry plane in front of the cylinder, see Fig. 9. The values are taken from simulation #3. Here the time-averaged values reach their maximum of $\langle \nu_t \rangle / \nu = 0.39$ at the junction of cylinder and bottom plate where the anti-clockwise rotating vortex V3 is located, compare Fig. 9a. In the region of the main vortex V1, the time-averaged modeled viscosity reaches values of up to $0.25\nu$. Away from these two vortices, the modeled viscosity remains below $0.1\nu$.

Instantaneous values of $\frac{\nu_t}{\nu}$ in the symmetry plane in front of the cylinder are plotted in Fig. 9b. In this randomly chosen time step of simulation #3 the maximum instantaneous ratio of modeled to molecular viscosity is $\frac{\nu_t}{\nu} = 1.5$.

A better estimation of the contribution of the SGS model to the flow dynamics is given by the modeled SGS stresses, see Fig. 10. We investigate the modeled SGS stresses in the zone of the horseshoe vortex at a position $(x, y) = (-0.7D, 0)$ which is the zone in which the averaged SGS viscosity is relatively large. We compare the time-averaged modeled shear stresses $\langle \nu_t \frac{\partial u}{\partial z} \rangle$ obtained with three different grids (simulations with precursor inflow condition) in Fig. 10a. All three profiles show a distinct maximum when passing the center of vortex V1. One can observe a quadratic dependence on grid spacing between grid 2 and grid 3. This indicates convergent behaviour of the flow fields at those grid resolutions. Grid 1, however, does not yet seem to be in the convergent regime for the SGS stresses.

Fig. 10b compares the modeled shear stress in grid 3 to other contributors to the momentum balance, namely the time-averaged molecular shear stress $\nu \frac{\partial \langle u \rangle}{\partial z}$ and the resolved turbulent shear stresses $-\rho \langle u'w' \rangle$. Close to the wall the molecular shear stress is

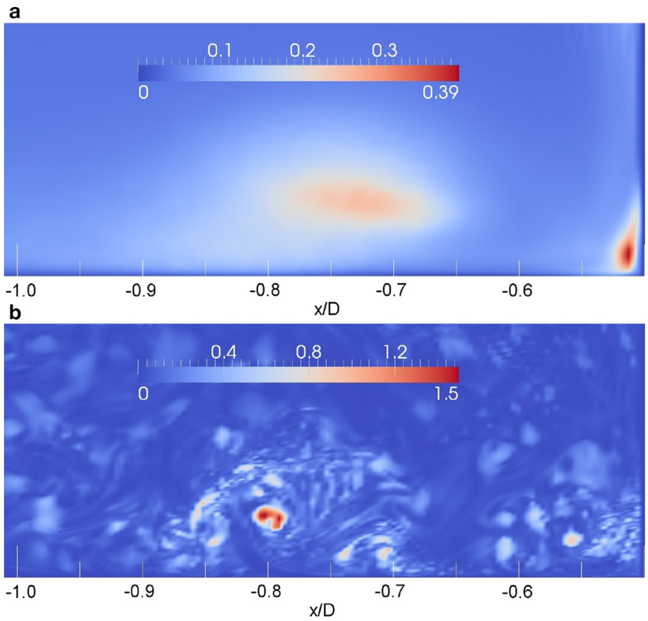

**Fig. 9.** Time-averaged $\langle\nu_t\rangle/\nu$ (a) and instantaneous $\nu_t/\nu$ (b) ratio of modeled to molecular viscosity in the symmetry plane in front of the cylinder (simulation #3).

dominating the flow. Away from the wall, the resolved turbulent shear stress and the pressure gradient - which is not shown in the plot - are dominant. Theses stresses are exceeding the modeled shear stress by two orders of magnitude. There is no point at which the modeled SGS shear stress $\langle\nu_t \frac{\partial u}{\partial z}\rangle$ dominates the momentum balance. The influence of the subgrid stress model on the solution therefore can be considered to be small.

## 5. Cross-validation with findings from the literature

In the previous sections, we documented our efforts to validate our simulations with respect to inflow conditions, grid resolution and contribution of SGS stresses. In this section, we will compare our results with experimental ones published by Devenport and Simpson [8,30], Dargahi [6,7] and Roulund et al. [3]. We concentrate on flow topology and quantitative prediction of the wall shear stress in the symmetry plane upstream of the cylinder.

We first concentrate on the flow topology that has been carefully documented by Devenport and Simpson [8,30]. Fig. 11 shows streamlines along the bottom plate obtained from simulation #3. Fig. 11a gives an overview over the area around the cylinder, while Fig. 11b zooms to the junction between bottom plate and cylinder. Downstream of the saddle point at $x/D \approx -1.13$, we can identify four regions. The regions (i) and (ii) between two saddle points are formed by the regions of large (i) and small (ii) negative wall shear stress (compare Fig. 7). They can be described as the footprints of the vortices V1 and V2 (compare Fig. 6). The saddle point at $x/D \approx -1.13$ is the point of separation S2 in the symmetry plane (compare Fig. 6). The saddle point at $x/D = -0.53$ is the stagnation point S3 in the symmetry plane. Downstream of this the forward flow region (iii) is formed as the footprint of the vortex V3. The fourth region (iv) does not appear in the symmetry plane, but starts to develop about 6° away from the symmetry plane. This region indicates an extra vortex V5 rotating in clockwise direction in the lateral front at the junction of bottom wall and cylinder. Vortex V5 has been also reported by Paik et al. [12], but they observed it

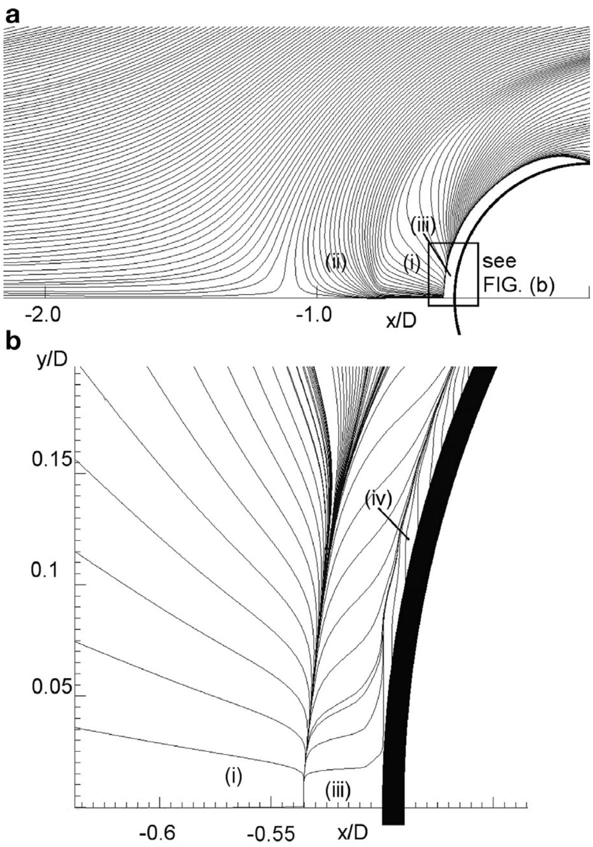

**Fig. 11.** Time-averaged streamlines at the bottom plate around the cylinder from simulation #3.

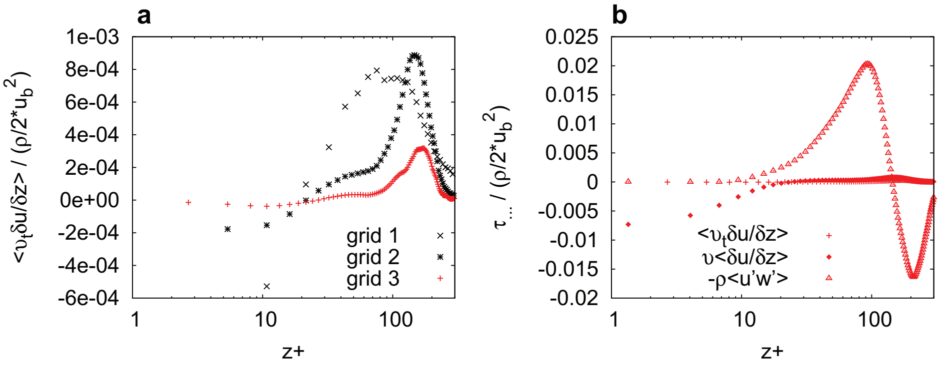

**Fig. 10.** Modeled shear stresses normalized by $\rho u_b^2$ at $x = -0.7D$ in the symmetry plane in front of the cylinder for different grid resolutions (a) and compared to other contributors to the momentum balance (b). Wall units are based on the local wall shear stress.

not only in the lateral front but also going through the symmetry plane.

The magnitude of the corresponding wall shear stresses are shown in Fig. 7. Region (i) is corresponding to the area of maximum wall shear stress amplification at $-0.7D < x < -0.55D$ in Fig. 7a. Region (ii) can be found upstream of region (i) between the point of separation S2 and the local wall shear stress maximum under S1. Region (iii) is formed by the small anti-clockwise rotating vortex right at the junction of wall and cylinder and corresponding to the region of positive values in Fig. 7a.

The flow topology described above was also observed by Devenport and Simpson [8]. They used surface oil-flow visualization to investigate the near-wall flow pattern around a wall-mounted wing-shaped cylinder at $Re_D = 119000$. It is remarkable how statements by Devenport and Simpson [8] can be used literally to describe observations made in our study. In front of the cylinder under the horseshoe vortex, they found (i) “a strip of high surface stresses adjacent to the [cylinder]”, (ii) “a crescent-shaped region of apparently lower shear stresses upstream” of region (i) and (iii) “a region of secondary separation in the corner between the wall and the [cylinder]”.

The flow topology presented by Devenport and Simpson [8] shows two backflow regions, region (i) and region (ii). They also note: “Close to the plane of symmetry this line [which is dividing region (i) and (ii)] is not a separation or reattachment since the oil streaks here pass through it. Measurements made by Devenport and Simpson [30] show this to be a line of low streamwise shear.”, which is in good accordance to the flow topology presented in this study. Fig. 7 does not show a zero wall shear stress at $x = -0.78D$ but a region of low shear stress.

After having discussed the footprint of the flow field around the cylinder, we now turn to the flow field and turbulence characteristics in the symmetry plane in front of the cylinder. We compare our results with results from Devenport and Simpson [8] provided as an ERCOFTAC data base [31]. They used laser Doppler anemometry to measure velocity profiles in front of a wing-flat plate junction in a turbulent boundary layer. They had a Reynolds number of $Re = 1.15 \times 10^5$ and a ratio of boundary layer thickness $\delta_{99.5}$ to maximum width of the wing $T$ of $\delta_{99.5}/T = 0.5$. This is smaller than our depth-to-diameter ratio of $\delta/D = 1.5$. They measured vertical profiles for a limited number of streamwise positions. Keeping the differences in the configurations and the limited streamwise resolution of the measurements in mind, a quantitative comparison between their and our cases should be undertaken with care. However, a similar comparison has been undertaken by Escauriaza and Sotiropoulos [11] between a Detached Eddy Simulation of our flow case with Devenport and Simpson's measurements. They found that both flows share a lot of common features.

The time-averaged vorticity around the y-axis $\omega_y^* = (\frac{\partial <u>}{\partial z} - \frac{\partial <w>}{\partial x})\frac{D}{u_b}$ in the symmetry plane in front of the cylinder is compared with the one measured by Devenport and Simpson [8] in Fig. 12. The vorticity is normalized by the diameter of the cylinder $D$ and the bulk velocity $u_b$. All three vortices described above can also be observed in Fig. 12. In the center of the main vortex, the vorticity reaches a maximum of $\omega_y^* = 20.6$, which is close to the one measured by Devenport and Simpson. A thin layer of negative vorticity can be observed in close vicinity to the wall which is lifted up towards the stagnation point S1 at $x \approx -0.83D$. The maximum vorticity can be found at $(x, y) \approx (-0.7D, 0.05D)$ while it is a little closer at the wall and the cylinder in Devenport and Simpson's case. This could be explained by the thinner boundary layer of the latter. Overall, the position, shape and magnitude of the main vortex V1 and the thin shear layer beneath it, increase the overall trust in the simulation.

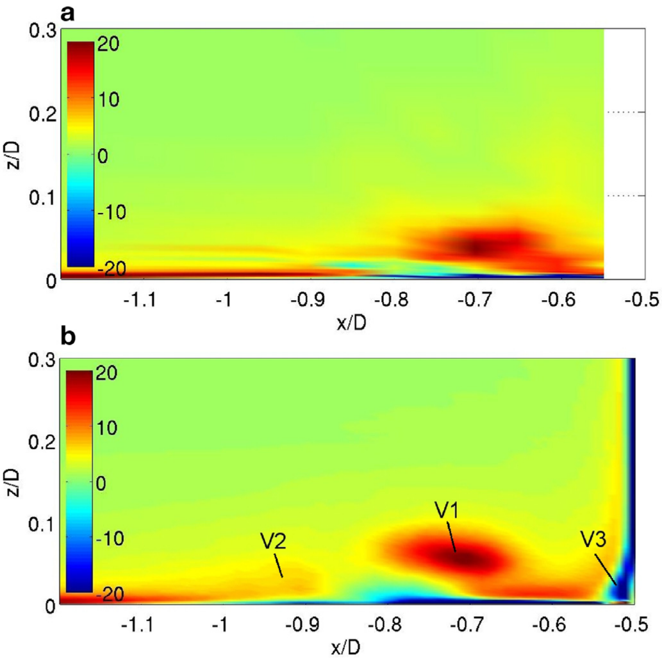

**Fig. 12.** Normalized vorticity in the symmetry plane in front of the cylinder. (a): measurements by Devenport and Simpson [8]; (b): simulation #3.

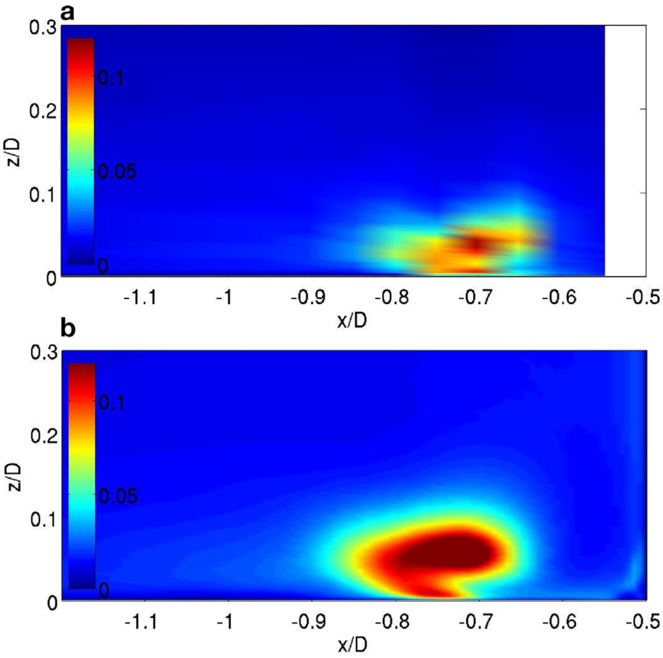

**Fig. 13.** Normalized in-plane turbulent kinetic energy, $(\langle u'^2\rangle + \langle w'^2\rangle)/u_{ref}^2$, in the symmetry plane in front of the cylinder. (a): measurements by Devenport and Simpson [8]; (b): simulation #3.

The topology of the time-averaged flow field obtained in our simulation #3 does in fact fully agree with the one Devenport and Simpson have reported. In addition, the vortex system presented in this study bears the same bimodal dynamics as described by Devenport and Simpson [8]. However, the dynamics of the horseshoe vortex is not within the scope of this paper.

The distribution of the normalized in-plane turbulent kinetic energy, $(\langle u'^2\rangle + \langle w'^2\rangle)/u_b^2$ is compared to the one by Devenport and Simpson in Fig. 13. The turbulent kinetic energy peaks in the center of the horseshoe vortex. Its particular shape, a “C-shaped

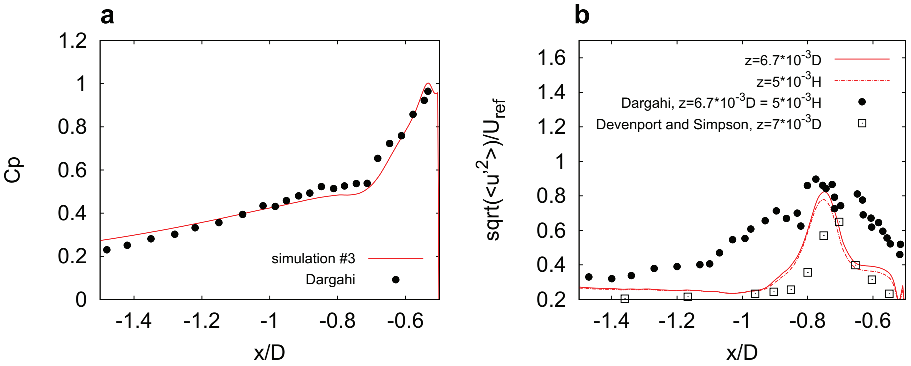

**Fig. 14.** Pressure coefficient $C_p$ at the bottom plate (a) and turbulence intensity (b) in the symmetry plane in front of the cylinder compared to measurements by Dargahi [7] and Devenport and Simpson [8].

pocket of high TKE" [11], exhibits two peaks, one in the center of the main vortex and the other at the wall underneath the main peak. This shape stems from the distribution of the streamwise fluctuation intensity $\langle u'^2 \rangle$. Escauriaza and Sotiropoulos [11] have demonstrated how this particular distribution of turbulent kinetic energy is linked to the dynamics of the main horseshoe vortex. The measured distribution of the turbulent kinetic energy is not as smooth which could be partly explained by the coarse streamwise resolution of the measurements and by some statistical scatter in the measured data. However both simulation and measurement share shape and level, the main difference being the height of the main peak which is thinner in Devenport and Simpson's case than in ours. This can be explained with the smaller boundary layer thickness in the experiment.

We now turn to a quantitative comparison of our results with experimental ones obtained by Dargahi [6,7] who performed measurements of a well comparable configuration at a Reynolds number of $Re_D = 39000$. The data are complemented by measurement of Roulund et al. [3] for the same geometry at $Re_D = 170000$ and the measurements of Devenport and Simpson [8]. The experimental values were digitized by hand from the figures in the publications except the latter ones who have been taken from the ERCOFTAC data base [31].

Fig. 14a compares the pressure coefficient $C_p = \frac{\langle p \rangle - p_{ref}}{\rho/2 \cdot u_b^2}$ in the symmetry plane in front of the cylinder from simulation #3 to the results of Dargahi [7]. $p_{ref}$ is adjusted in such a way that $C_p$ of our LES meets Dargahi's results in the junction of bottom plate and cylinder at $x = -0.5D$. The results of our LES follow the ones measured by Dargahi closely. The maximum can be found in the stagnation Point S3 at $(x, z) = (-0.53D, 0)$. Both, the steep slope upstream of S3 and the distinct kink at about $(x, z) = (-0.7D, 0)$ can be observed in the experimental as well as in the numerical data set.

Fig. 14b compares the turbulence intensity $I = \frac{\sqrt{\langle u'^2 \rangle}}{u_{ref}}$ in the symmetry plane in front of the cylinder to Dargahi's measurements [7]. The corresponding profile from Devenport and Simpson [8] has been added for a cross-check. Dargahi's probes are located at a wall distance of $z = 0.00667D$, which corresponds to a height below the center of the main horseshoe vortex V1. $u_{ref}$ is the time-averaged velocity in the oncoming flow at the respective wall distance. All results peak in the region of the vortex V1. It appears that all three cases have similar peak values. However, the distribution in Dargahi's measurements is wider than the peak in the other results. A final explanation for this deviation cannot be given here. A reason might be the measuring technique. Dargahi [7] used a hot film probe, which is an intrusive method. The sensor might have caused a disturbance on this complex three dimensional vortex system. The laser based measurements by Devenport and Simpson [8] deliver a peak which is as narrow as the one of our simulation, see Fig. 14b.

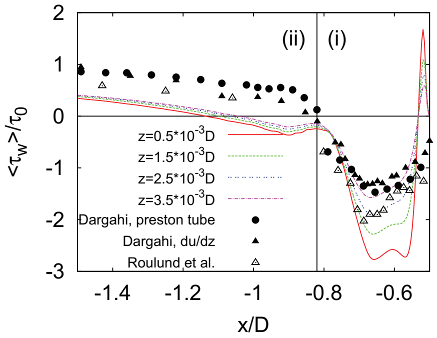

**Fig. 15.** Wall shear stress amplification in the symmetry plane in front of the cylinder compared to measurements by Dargahi [7] and Roulund et al. [3].

The wall shear stress amplification in front of the cylinder is of special interest, because this is the quantity driving scour and erosion. We compare our results to measurements of Dargahi [7] and Roulund et al. [3] in Fig. 15. Even though all of our values were taken from the finest local grid in simulation #3, we plotted wall shear stresses computed from velocities at four different wall distances: at the wall next point at $z_1 = 0.0005D$, at $z_2 = 0.0015D$, at $z_3 = 0.0025D$ and at $z_4 = 0.0035D$.

The experimental results by Dargahi [6,7] and Roulund et al. [3] share their main features, i.e. the shape of the wall shear stress distribution in the main recirculation zone under the main vortex V1. However, there are some differences as well. Roulund et al.'s amplification factors are considerably lower than 1.0 in the plotted region upstream of $x/D = -1.0$ which indicates that in their experiment the influence of the cylinder on the wall shear stress is more upstream than what the measurements of Dargahi suggest. Roulund et al. normalized their wall shear stresses by the undisturbed one measured in the center line of the channel without a cylinder. Note, that the influence of the cylinder reaches $8D$ upstream in our simulation, see Fig. 4. The flow seems to separate earlier in Roulund et al.'s experiment and the maximum wall shear stress is considerably larger. All this might be attributed to the different experimental conditions, such as water depth-to-cylinder diameter ratio and Reynolds numbers. However, Roulund et al. did also simulations using a Reynolds averaged Navier–Stokes solver. Their numerical results suggest that, (i) the influence of the ratio water depth-to-cylinder is very small for water depths above one cylinder diameter, (ii) the point of separation moves towards the cylinder when the Reynolds number is increased from $10^4$ to $10^5$, and (iii) the wall shear stress amplification factor

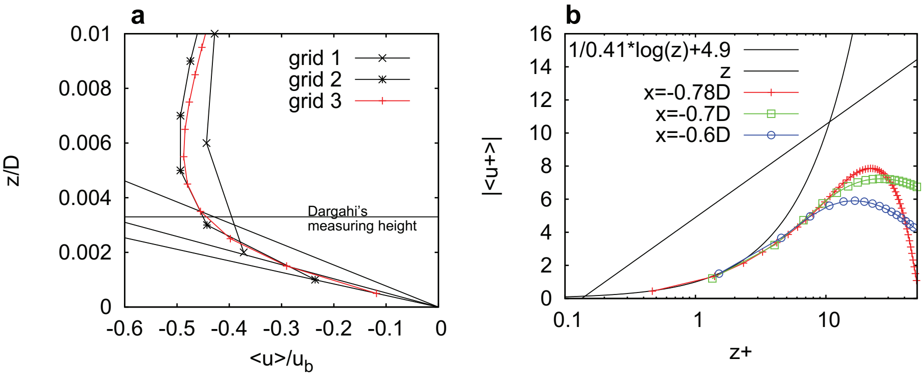

**Fig. 16.** Vertical profiles of the streamwise velocity component under the horseshoe vortex; (a) at $x = -0.65D$ for different grid resolutions and (b) at different positions for the finest grid (grid 3).

continuously decreases with increasing Reynolds number in the covered Reynolds number range, i.e. Dargahi uses $Re_D = 39000$, Roulund et al. $Re_D = 170000$ and our results have been obtained at $Re_D = 39000$. The differences between Roulund et al. and Dargahi can not be explained by the Reynolds number effects. Furthermore, it is obvious that the normalization of the wall shear stress has to be taken into account when quantitative information are sought, e.g. if Rolound et al. [3] normalized their wall shear stress by its value at $x/D = -2.5$ as Dargahi [7] did, the differences among the experiments in Fig. 15 would even be more pronounced.

There is a fundamental difference between our simulation results and Dargahi's measurements in the region (ii) upstream of $x < -0.82D$, see Fig. 11. While we observe backflow in this region, Dargahi [7] measured forward flow near the wall. This would imply, that in this experiment, vortex V2 was not present. A final explanation for this discrepancy cannot be given here. Nevertheless, his sketches imply that he assumed more than one backflow region. It is important to note that Dargahi measured wall shear stresses by a Preston tube and a hot film probe. Both are dependent on flow direction and can not be used in flow situations with strongly varying flow direction in time.

A possible explanation for discrepancies between Dargahi's and our results could be the different wall roughness applied in the studies. While Devenport and Simpson [8], Roulund et al. [3] and the present LES have smooth walls, Dargahi [6,7] glued grains with a diameter of $D_{50} = 2.4 \cdot 10^{-3}D$ to the wall. He estimated the roughness height to about 4.5 wall units and therefore assumed the wall to be smooth. Nevertheless, this assumption is only valid in the undisturbed oncoming flow profile. In the region around the cylinder the thickness of the viscous sublayer might change and the wall therefore become rough. This roughness might have had an influence on the flow, suppressing vortex V2 by increasing fluctuations and momentum transport.

In the region (i) – see Fig. 15 – below the main vortex V1, the shape of our results agrees well with both experiments. Our maximum is, however, larger than both experiments. Our larger amplification factor with respect to Roulund et al. can be explained by the aforementioned Reynolds number effect. However, the quantitative difference to Dargahi's measurements can not be explained by the Reynolds number effect observed by Roulund et al. in his RANS simulations. Dargahi calculated the wall shear stresses based on velocity probes measured at a height of $z = 0.0033D$. If we compare his results with ours computed from the velocity at a height of $z_4 = 0.0035D$, we find good quantitative accordance in region (i), see Fig. 15.

Nevertheless, reducing the wall distance to $z_1 = 0.0005D$ the amplitude of $\tau_w/\tau_0$ increases and develops a double peak. Here, the maximum amplification factor shows an amplitude which is larger by a factor of two than the value measured by Dargahi [7]. One could speculate that Dargahi's velocity probe at a height of $z = 0.0033D$ is outside of the viscous sublayer. Estimating wall shear stresses based on these probes and assuming a linear velocity profile to the wall therefore underestimates the wall shear stress.

This conclusion is supported by Fig. 16. It shows the velocity profile in streamwise direction in the symmetry plane in front of the cylinder for the simulations using fully turbulent inflow condition with different grid resolutions at $x = -0.65D$. The wall nearest point of simulation #3 is located at $z_1 = 0.0005D$, which corresponds to $z^+ = 1.5$ based on the local wall shear stress. Fig. 16 implies, that at this position the viscous sublayer has a thickness of about three wall units only. The wall nearest point of simulation #2 is still in the linear layer. The second grid point of simulation #3 (finest grid) is already outside of the linear layer. The measuring height Dargahi [7] has reported is as well outside of the linear sublayer. Assuming a linear velocity distribution would lead to wrong wall shear stress estimations. In this case, a wall shear stress which was 50% too small would have been obtained. The larger wall shear stresses obtained in the present simulation compared to the measurements of Dargahi [7] can therefore fully be explained by the finite size of the Preston tubes used and the non-equilibrium velocity profiles under the main vortex S1.

## 6. Wall shear stress distribution

Having carefully validated our wall shear stress predictions, we now discuss spatial distributions of time-averaged and instantaneous wall shear stresses. In Fig. 17 the amplification factor is plotted which is obtained by normalizing the wall shear stress by the time-averaged wall shear stress in the precursor simulation in a region without influence of the sidewalls, $\tau_0$. The values of 3, 6, 9 and 11 are indicated by isolines.

Time-averaged wall shear stresses larger than $6\tau_0$ are found at angles from 23° to 97° to the symmetry plane in a thin strip with a width of $0.1D$. Values larger than 11 are located between at angles from 48° to 58° to the symmetry plane. Here a maximum amplification factor of $\frac{\langle \tau_w \rangle}{\tau_0} > 12.0$ is reached, see also Table 4 or Fig. 8.

These findings are in principle accordance to the experimental results of Hjorth [4]. He measured wall shear stress distributions for combinations of Reynolds numbers of $7500 < Re_D < 22500$ and boundary layer thickness to diameter ratios of $1.33 < \frac{\delta}{D} < 4$. Hot-film anemometry was applied at certain points around the cylinder, values in between were interpolated. The setup closest to our setup holds a Reynolds number of $Re_D = 22500$ and a boundary layer thickness to diameter ratio of $\frac{\delta}{D} = 1.33$. In front and lateral of the cylinder, the shape of the experimentally evaluated isolines

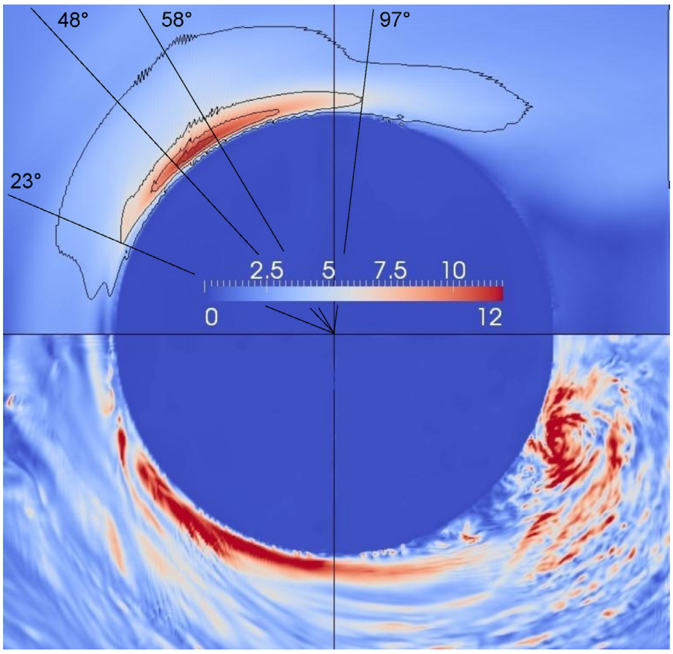

**Fig. 17.** Instantaneous (bottom) and time-averaged (top) amplification of the wall shear stress around the cylinder. The isolines show amplification factors of 3, 6, 9 and 11 relative to the wall shear stress in the precursor simulation [32].

bear good resemblance to the ones in Fig. 17. The plot by Hjorth [4] shows a maximum wall shear stress amplification of $\frac{\langle\tau_w\rangle}{\tau_0} > 9$. Nevertheless, in the lateral back of the cylinder at about 130° to the symmetry plane, plots by Hjorth [4] show a spot of high wall shear stress amplification $\frac{\langle\tau_w\rangle}{\tau_0} > 7$, too, which does not appear in our numerical results. This spot does not appear in all setups in the study of Hjorth [4], so one might be tempted to explain this difference with the different Reynolds numbers used. Hjorth [4] also reports a maximum amplification factor of “about 12”, but it becomes not clear for which combination of $Re_D$ and $\frac{\delta}{D}$ this maximum has been observed.

The significance of the instantaneous wall shear stress distribution becomes obvious from Fig. 17 (bottom). In the symmetry plane close to the cylinder and the bottom plate, time-averaged velocities have to be small for geometric reasons. Nevertheless, instantaneous wall shear stresses reach values larger than $12\tau_0$ in front and $40\tau_0$ in the wake of the cylinder. This extremely large values in the wake can be explained by the von Karman-vortex street which leads to vortex shedding downstream of the cylinder. These vortices come along with large velocity fluctuations, especially in spanwise direction. Additionally, the Karman-vortices are amplified by the combination of various effects: the downflow in front of the cylinder transports fluid of high momentum from outer regions to regions close to the wall. The high momentum fluid, deflected in spanwise direction in the wake of the cylinder, increases the instantaneous wall shear stresses in spanwise direction.

## 7. Summary and conclusions

In this study, wall shear stress predictions by a Large-Eddy Simulation of the flow around a wall-mounted cylinder were carefully validated and discussed. We applied a precursor simulation to generate a fully developed turbulent open channel flow approaching the cylinder and took special care to assess the influences of the grid resolution, the inflow boundary condition and the subgrid scale model on the prediction of the wall shear stresses.

We reached convergent solutions with respect to grid resolutions with small deviations of the second fine grid from the finest one. Simulations using a coarser grid give partly strong deviations from this solution. We therefore emphasize the necessity of the grid resolution used – see Table 2 – in close vicinity of the cylinder for the applied Reynolds number.

The inflow condition has a strong influence on the results. A time constant inflow condition leads to a early separation in front of the cylinder and qualitatively wrong predictions of the wall shear stresses under the main horseshoe vortex. If the time-averaged inflow profile was not met, the downwash on the front of the cylinder will not be recovered correctly which results in a qualitatively wrong prediction of the main horseshoe vortex and wall shear stress underneath.

We demonstrated that in the finest grid used, the contribution of the modeled stresses to the horseshoe vortex system around the cylinder remains negligible. The time-averaged SGS viscosity decreased at second order with respect to grid spacing between the finest and the second finest grid. Thus, we conclude that our simulations provide high fidelity in the predicted wall shear stresses.

Compared to experimental results from literature, we see partly very good accordance and partly quantitative discrepancies. We predict considerably larger wall shear stresses in the symmetry line in front of the cylinder than were measured by Dargahi [7] in a comparable configuration. We suggest that this discrepancy could be explained by the finite size of the Preston tube and the wall distance of the velocity probes which were used by Dargahi to determine the wall shear stress. This explanation is supported by numerical results and measurements of Roulund et al. [3]. We explain the strong effect of the probe size for wall shear stress measurements by velocity profiles which strongly deviate from the law of the wall and have a linear layer thickness of only three wall units under the horseshoe vortex.

Especially when wall shear stresses around the cylinder are estimated, coarse grids fail due to two effects: (i) the velocity profiles are in strong non-equilibrium under the horseshoe vortex having a very thin linear region of less than three wall units; and (ii) the horizontal extensions of the wall shear stress peaks are very narrow, thus fine grids are required parallel to the wall to capture those peaks. Spatial resolution is therefore as well crucial for experimental estimation of wall shear stress amplitudes.

We observed instantaneous wall shear stresses at considerably larger amplitudes than the time-averaged ones. While time-averaged wall shear stress amplifications reached values of $12\tau_0$ at an angle of about 45° to the symmetry plane, the largest instantaneous wall shear stresses appeared in the wake of the cylinder and reached values of up to $40\tau_0$. Note that in the wake of the cylinder the instantaneous wall shear stresses mainly stem from spanwise velocities due to the von Karman vortex shedding. Those spanwise velocities and wall shear stresses are leveled out when time-averaging was applied. Thus, the large instantaneous wall shear stresses are not seen in the time-averaged ones.

## Acknowledgments

The authors gratefully acknowledge the financial support of the DFG under grant no. MA2062/11. Computing time was granted by the Leibniz Computing Center (LRZ) of the Bavarian Academy of Sciences under project no. pr84gi.

## References

[1] Imhof D. Risk assessment of existing bridge structures. University of Cambridge; 2004. Ph.D. thesis.
[2] Brandimarte L, Paron P, Di Baldassarre G. Bridge pier scour: A review of processes, measurements and estimates. Environ Eng Manag J 2012;11(5):975–89.

[3] Roulund A, Sumer BM, Fredsoe J, Michelsen J. Numerical and experimental investigation of flow and scour around a circular pile. J Fluid Mech 2005;534:351–401. doi:10.1017/s0022112005004507.

[4] Hjorth P. Studies on the nature of local scour. Bulletin Series A, vol. 46. Lund: University of Lund; 1975.

[5] Melville BW, Raudkivi AJ. Flow characteristics in local scour at bridge piers. J Hydraul Res 1977;15(4):373–80. doi:10.1080/00221687709499641.

[6] Dargahi B. Flow flied and local scouring around a cylinder. Technical Report. Hydraulics Laboratory - The Royal Institute of Technology Stockholm Sweden; 1987.

[7] Dargahi B. The turbulent flow field around a circular cylinder. Exp Fluids 1989;8(1–2):1–12. doi:10.1007/bf00203058.

[8] Devenport WJ, Simpson RL. Time-dependent and time-averaged turbulence structure near the nose of a wing-body junction. J Fluid Mech 1990;210:23–55.

[9] Graf W, Istiarto I. Flow pattern in der scour hole around a cylinder. J Hydraul Res 2002;40(1):13–20.

[10] Tseng M-H, Yen C-L, Song CCS. Computation of three-dimensional flow around square and circular piers. Int J Numer Meth Fluids 2000;34(3):207–27. doi:10.1002/1097-0363(20001015)34:3\%3C207::aid-fld31\%3E3.0.co;2-r.

[11] Escauriaza C, Sotiropoulos F. Reynolds number effects on the coherent dynamics of the turbulent horseshoe vortex system. Flow Turbul Combust. 2011;86(2):231–62. doi:10.1007/s10494-010-9315-y.

[12] Paik J, Escauriaza C, Sotiropoulos F. On the bimodal dynamics of the turbulent horseshoe vortex system in a wing-body junction. Phys Fluids 2007;19:045107.

[13] Paik J, Escauriaza C, Sotiropoulos F. Coherent structure dynamics in turbulent flows past in-stream structures: some insights gained via numerical simulation. J Hydraul Eng 2010;136.

[14] Kirkil G, Constantinescu G. Effects of cylinder reynolds number on the turbulent horseshoe vortex system and near wake of a surface-mounted circular cylinder. Phys Fluids 2015;27:075102.

[15] Apsilidis N, Khosronejad A, Sotiropoulos F, Dancey C, Diplas P. Physical and numerical modeling of the turbulent flow field upstream of a bridge pier. In: Proceedings of the International Conference on Scour and Erosion 6. Paris; 2012.

[16] Pfleger F. Experimentelle untersuchung der auskolkung um einen zylindrischen brückenpfeiler. TU Muenchen; 2011. Ph.D. thesis.

[17] Peller N, Duc AL, Tremblay F, Manhart M. High-order stable interpolations for immersed boundary methods. Int J Numer Methods Fluids 2006;52:1175–93.

[18] Peller N. Numerische simulation turbulenter strömungen mit immersed boundaries. Technische Universität München; 2010. Ph.D. thesis.

[19] Manhart M. A zonal grid algorithm for DNS of turbulent boundary layers. Comput Fluids 2004;33(3):435–61.

[20] Nicoud F, Ducros F. Subgrid-scale stress modelling based on the square of the velocity gradient tensor. Flow, Turbul Combust 1999;62(3):183–200. doi:10.1023/a:1009995426001.

[21] Manhart M. Vortex shedding from a hemisphere in a turbulent boundary layer. Theor Comput Fluid Dyn 1998;12(1):1–28. doi:10.1007/s001620050096.

[22] Breuer M, Peller N, Rapp C, Manhart M. Flow over periodic hills numerical and experimental study in a wide range of Reynolds numbers. Comput. Fluids 2009;38(2):433–57. doi:10.1016/j.compfluid.2008.05.002.

[23] Gallardo JP, Andersson HI, Pettersen B. Turbulent wake behind a curved circular cylinder. J Fluid Mech 2014;742:192–229. doi:10.1017/jfm.2013.622.

[24] Schanderl W, Manhart M. Large-eddy simulation of the flow around a wall-mounted circular cylinder. In: Proceedings of the 3rd IAHR Europe Congress, Book of Proceedings, 2014, Porto -Portugal; 2014.

[25] Hutchins N, Marusic I. Evidence of very long meandering features in the logarithmic region of turbulent boundary layers. J Fluid Mech 2007;579:1–28. doi:10.1017/s0022112006003946.

[26] Nezu I, Nakagawa H. Turbulence in Open-Channel Flows. IAHR Monograph. Rotterdam: A.A. Balkema; 1993.

[27] Nikora V, Roy AG. Secondary flows in rivers: theoretical framework, recent advances, and current challenges. John Wiley & Sons, Ltd; 2012. doi:10.1002/9781119952497.ch1.

[28] Fernholz HH, Finley PJ. The incompressible zero-pressure-gradient turbulent boundary layer: an assessment of the data. Prog Aerosp Sci 1996;32(4):245–311. doi:10.1016/0376-0421(95)00007-0.

[29] Bruns J, Dengel P, Fernholz HH. Mean flow and turbulence measurements in an incompressible two-dimensional turbulent boundary layer. Part I: data.. Technical Report. Herman-Föttinger-Institut für Thermo- und Fluiddynamik, TU Berlin; 1992.

[30] Devenport WJ, Simpson RL. Time-dependent structure in wing-body junction flows. In: André J-C, Cousteix J, Durst F, Launder B, Schmidt F, Whitelaw J, editors. Turbulent Shear Flows 6. Springer Berlin Heidelberg; 1989. p. 232–48. doi:10.1007/978-3-642-73948-4_20.

[31] Devenport W., Simpson R., Fleming J. Wing/Body junction with separation. ERCOFTAC Database C.08, 1988. http://cfd.mace.manchester.ac.uk/ercoftac [Online; accessed 8-October-2015].

[32] Schanderl W, Chmiel O, Huttner P, Zischkale S, Manhart M. Application and validation of sediment erosion models to time dependent wall shear stresses around a wall-mounted circular cylinder. In: Proceedings of the 7th river flow conference. Lausanne; 2014.

# B. Appendix: Publication 2, summarised in chapter 7

*J. Fluid Mech.* (2017), *vol.* 827, *pp.* 285–321. © Cambridge University Press 2017
doi:10.1017/jfm.2017.486

# The structure and budget of turbulent kinetic energy in front of a wall-mounted cylinder

**Wolfgang Schanderl**[1], **Ulrich Jenssen**[1], **Claudia Strobl**[1]
**and Michael Manhart**[1],†

[1]Chair of Hydromechanics, Department of Civil, Geo and Environmental Engineering,
Technische Universität München, Arcisstr. 21, 80333 München, Germany

(Received 7 October 2016; revised 30 June 2017; accepted 11 July 2017;
first published online 22 August 2017)

We investigate the flow and turbulence structure in front of a cylinder mounted on a flat plate by a combined study using highly resolved large-eddy simulation and particle image velocimetry. The Reynolds number based on the bulk velocity and cylinder diameter is $Re_D = 39\,000$. As the cylinder is placed in an open channel, we take special care to simulate open-channel flow as the inflow condition, including secondary flows that match the inflow in the experiment. Due to the high numerical resolution, subgrid contributions to the Reynolds stresses are negligible and the modelled dissipation plays a minor role in major parts of the flow field. The accordance of the experimental and numerical results is good. The shear in the approach flow creates a vertical pressure gradient, inducing a downflow in the cylinder front. This downflow, when deflected in the upstream direction at the bottom plate, gives rise to a so-called horseshoe vortex system. The most upstream point of flow reversal at the wall is found to be a stagnation point which appears as a sink instead of a separation point in the symmetry plane in front of the cylinder. The wall shear stress is largest between the main (horseshoe) vortex and the cylinder, and seems to be mainly governed by the strong downflow in front of the cylinder as turbulent stresses are small in this region. Due to a strong acceleration along the streamlines, a region of relatively small turbulent kinetic energy is found between the horseshoe vortex and the cylinder. When passing under the horseshoe vortex, the upstream-directed jet formed by the deflected downflow undergoes a deceleration which gives rise to a strong production of turbulent kinetic energy. We find that pressure transport of turbulent kinetic energy is important for the initiation of the large production rates by increasing the turbulence level in the upstream jet near the wall. The distribution of the dissipation of turbulent kinetic energy is similar to that of the turbulent kinetic energy. Large values of dissipation occur around the centre of the horseshoe vortex and near the wall in the region where the jet decelerates. While the small scales are nearly isotropic in the horseshoe vortex centre, they are anistotropic near the wall. This can be explained by a vertical flapping of the upstream-directed jet. The distribution and level of dissipation, turbulent and pressure transport of turbulent kinetic energy are of crucial interest to turbulence modelling in the Reynolds-averaged context. To the best of our knowledge, this is the first time that these terms have been documented in this kind of flow.

**Key words:** separated flows, turbulent boundary layers, turbulent flows

---

† Email address for correspondence: michael.manhart@tum.de

## 1. Introduction

Flows around bluff bodies mounted on a flat plate appear in various technical applications, such as, e.g., turbomachinery blade flows or aircraft wing–body flows. We are interested in cylinder–wall junction flows because of their enormous importance in scour development around bridge piers in sandy river beds. The mechanism of scour development and its dependence on the flow field upstream of a pier was described many years ago (Melville & Raudkivi 1977). A major role has been attributed to the horseshoe vortex forming in front of a bridge pier. Such a horseshoe vortex has been observed in many different configurations of protuberances embedded in boundary layer flows. Due to the broad relevance of the horseshoe vortex for technical applications as well as for the fundamental understanding of flow physics, it is not surprising that in recent years a vast number of investigations addressing wall–body junction flows have been published – not only from the viewpoint of scour development but also concerning the flow field alone. We concentrate on findings addressing the dynamics of flows around long slender bodies such as cylinders, wings or bars, mounted perpendicularly on a flat plate. Many features occurring in such flows seem to be independent of the detailed structure of the fore-body (Escauriaza & Sotiropoulos 2011; Schanderl & Manhart 2016).

If a boundary layer flow approaches a bluff body, the shear in the boundary layer gives rise to a vertical pressure gradient along the front of the body, driving the flow downwards to the wall. This downwash is deflected by the bottom wall and forms a spanwise vortex system (Devenport & Simpson 1990). Parts of the downwash that become deflected by the bottom wall in front of the bluff body wrap up into a ellipsoidal main vortex V1. Other parts of the downwash feed an upstream-directed jet along the bottom wall underneath V1. After passing V1, the jet penetrates under the oncoming boundary layer and forms an extended recirculation zone. This eventually can wrap up into a second vortex V2 (Apsilidis *et al.* 2015), which was not mentioned by Devenport & Simpson (1990), maybe due to a lack of resolution. Along the flow facing wall of the bluff body, the downwash establishes a boundary layer. Before reaching the bottom plate, this boundary layer has to separate from the body wall for the same reasons as the main flow separates from the bottom wall when approaching the bluff body. This separation leads to a third vortex V3 directly at the wall–cylinder junction rotating in the opposite direction to V1.

Due to the fact that the flow needs to bypass the protuberance, strong stretching in the spanwise direction occurs, increasing the spanwise vorticity of the vortex system and especially reinforcing the main vortex to an intense vortex, which is stretched around the body. Because their vortex axes are bent around the obstacle, such vortex systems are denoted as horseshoe vortices and associated with large wall stresses in the zone between the vortex and the body (Dargahi 1989; Devenport & Simpson 1990).

However, the discussion on the described flow topology is not complete. Apsilidis *et al.* (2015) suggested the possibility that vortex V2 is not a coherent flow structure but the time-averaged representation of a train of various small vortices. In accordance with Dargahi (1989), Escauriaza & Sotiropoulos (2011) observed two main vortices instead of only one. Furthermore, Escauriaza & Sotiropoulos (2011) stated that the number of vortices decreases with increasing Reynolds number, as long as the Reynolds number is within the investigated moderate range. On the contrary, Apsilidis *et al.* (2015) observed the time-averaged flow topology to be mainly invariant with the body Reynolds number (Apsilidis *et al.* 2015) for moderate Reynolds numbers.

In addition to the topology of the time-averaged flow, in instantaneous flow fields, a variety of complicated phenomena have been observed. Devenport & Simpson (1990) described the wall jet underneath the horseshoe vortex as flipping between two modes: in the back-flow mode, the wall jet – having large upstream momentum – penetrates far into the oncoming boundary layer; in the zero-flow mode, the wall jet separates from the bottom wall relatively early and the fluid is ejected vertically away from the wall. In the zero-flow mode, V1 takes up a position further downstream than in the back-flow mode. Devenport & Simpson (1990) proposed that instantaneous structures in the incoming flow trigger the flipping between the two modes. Large-momentum fluid from the outer flow entering the vortex system might cause the back-flow mode, while fluid containing less momentum results in the zero-flow mode. However, they were not able to prove this hypothesis. Paik, Escauriaza & Sotiropoulos (2007) associated the back-flow mode with a well-organized vortex system, which undergoes instabilities due to its vicinity to the bottom wall. They descriptively discussed how hairpin vortices wrap around the main vortex, causing it to collapse and to be pushed towards the bluff body. They associated the resulting less organized vortex structure with the zero-flow mode.

Apsilidis *et al.* (2015) proposed that a third mode is present for a significant fraction of the time, the so-called intermediate mode, which bears none of the features associated with the back-flow and zero-flow modes. In this mode, the wall jet neither penetrates far into the oncoming flow nor is ejected vertically, but is diffused when running into the approaching boundary layer. The intermediate mode becomes more dominant with increasing Reynolds number (Apsilidis *et al.* 2015). They furthermore stated that the position of the main vortex does not depend on the flow mode, as instantaneous flow topologies can be observed, in which V1 is located close to the cylinder even though the wall jet is in the back-flow mode. In addition, Apsilidis *et al.* (2015) observed that for a considerable fraction of the time, the flow topology cannot be associated with any of the modes due to a lack of visible coherent structures. With increasing Reynolds number, this fraction of time is decreasing.

The rich dynamics of the flow results in a typical distribution of turbulent kinetic energy. Devenport & Simpson (1990) observed large Reynolds stresses in the streamwise direction underneath the main vortex V1 close to the bottom plate and large Reynolds normal stresses in the vertical direction in the region covered by V1. Addition of both components of the Reynolds normal stresses leads to a vertical c-shaped pattern of turbulent kinetic energy $k$ (Paik *et al.* 2007). This distinct c-shape was confirmed and discussed in detail by Apsilidis *et al.* (2015), who studied the distribution of $k$ as well as of its in-plane contributors for a range of moderate Reynolds numbers. They found that the turbulent kinetic energy in the second patch of high turbulent kinetic energy, which forms the lower branch of the c-shape, increases with Reynolds number, while there is no clear trend for the amplitude of the turbulent kinetic energy in the upper branch around the vortex core.

While the basic distribution of turbulent kinetic energy as observed by Devenport & Simpson (1990) in front of a wall-mounted bluff body has been confirmed by several research groups (Escauriaza & Sotiropoulos 2011; Kirkil & Constantinescu 2015; Ryu *et al.* 2016; Schanderl & Manhart 2016), the discussion on the detailed mechanism causing such a shape is still ongoing. Devenport & Simpson (1990) proposed that the flipping of the main vortex V1 in the streamwise direction leads to large Reynolds normal stresses in the vertical as well as the streamwise direction in the region covered by V1. They furthermore suggested that the fluctuation behaviour of the wall jet causes the large Reynolds normal stresses in the lower branch of the c-shape: the amplitude of the streamwise velocity component is large in the back-flow mode here, while it is close to zero in the zero-flow mode. In contrast, Escauriaza & Sotiropoulos (2011), who observed two main vortices in the time-averaged flow topology, hypothesized a complex interaction of these two separated vortices and attributed the large amplitudes of the turbulent kinetic energy in the upper branch of the c-shape to the quasi-periodic merging, collapsing and regeneration of these vortices.

Our contribution to this ongoing discussion is the evaluation of the turbulence structure in front of a wall-mounted cylinder. The corresponding set-up is described in § 2. To gain a holistic set of data, we conducted both particle image velocimetry (§ 3) and large-eddy simulation (LES) (§ 4). Based on the time-averaged flow topology (§ 5) and its bimodality, we discuss the distribution of the turbulent kinetic energy as well as every single term of the budget of the turbulent kinetic energy, including production, convection, turbulent transport processes and dissipation (§ 6). We particularly intend to elucidate how these budget terms are linked to features of the time-averaged flow field, especially to acceleration and deceleration regions, and how they interact with each other.

## 2. Flow configuration

We investigate the flow around a cylinder placed vertically on the bottom wall in a water channel with a free surface at a low Froude number. The configuration is sketched in figure 1. The diameter of the cylinder is denoted as $D$, the water depth is $h = 1.5D$ and the width of the channel is $w = 11.7D$. The approaching stream is a fully developed open-channel flow at a small Froude number (in fact, the Froude number is infinitesimal in the numerical simulation while it is $Fr = 0.32$ in the experiment; see §§ 4 and 3 respectively). We devoted special care to the generation of a fully developed inflow, including the secondary flow structures in the channel (Nezu & Nakagawa 1993). Based on the bulk velocity averaged over the whole cross-section of the channel, $u_{CS}$, the Reynolds number is $Re_D = u_{CS}D/\nu = 39\,000$ in the LES and $Re_D = u_{CS}D/\nu = 37\,165 \pm 7\,\%$ in the experiment. The uncertainty in the experiment is due to uncertainties in the flow rate, flow depth and temperature of the working fluid. Due to the secondary flow developing in the channel, the global bulk velocity $u_{CS}$ differs from the bulk velocity in the symmetry plane $u_b$, such that $u_b = 1.075u_{CS}$ in the LES and $u_b = 1.031u_{CS}$ in the experiment; the corresponding Reynolds numbers are accordingly $Re_b = u_bD/\nu = 41\,900$ in the LES and $Re_b = u_bD/\nu = 38\,300$ in the experiment. We use the bulk velocity of the symmetry plane for normalization in the remainder of this paper, as this allows a better comparison with results from the literature for the quantities in the symmetry plane.

The parameters of the configuration have been chosen to be comparable to the experiments of Dargahi (1989) and preliminary studies of our research group (Pfleger 2011). The results of Dargahi (1989) have frequently been used for validating numerical results (Roulund *et al.* 2005; Escauriaza & Sotiropoulos 2011). The configuration of the experiment of Apsilidis *et al.* (2015) differs from ours in the ratio of the cylinder diameter to the boundary layer thickness and in the ratio of the water depth to the channel width. However, it was performed at a similar Reynolds number. Furthermore, Devenport & Simpson (1990) investigated a wing–body junction flow at a larger Reynolds number and a smaller boundary layer thickness-to-diameter ratio than ours. Nevertheless, many flow features are shared among the cited comparable studies.

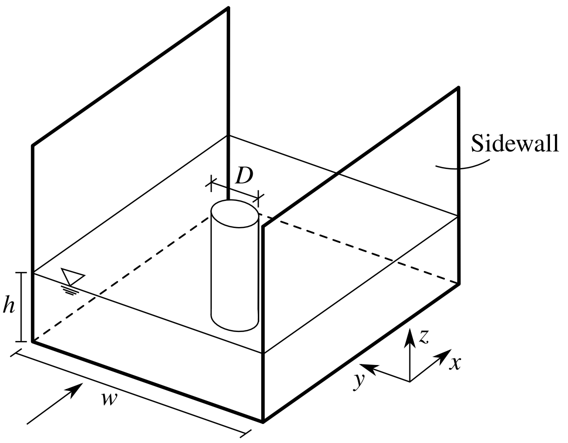

FIGURE 1. The configuration of the flow around a wall-mounted cylinder at $Re_D = 39\,000$.

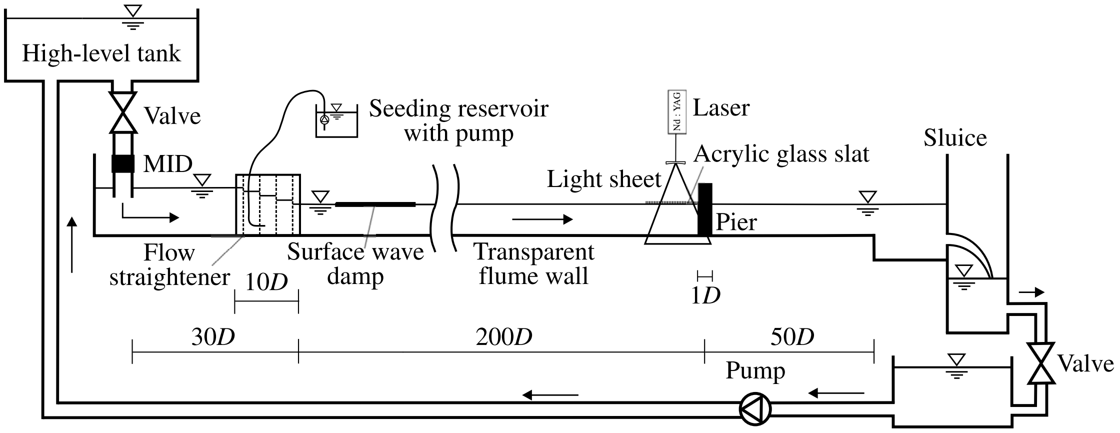

FIGURE 2. Experimental set-up, taken from Pfleger (2011).

## 3. Experimental configuration

We conducted particle image velocimetry (PIV) experiments in the hydromechanics laboratory of the Technische Universität München. First, the experimental set-up is described. Subsequently, the measuring technique and the post-processing parameters are briefly introduced.

### 3.1. *Experimental domain*

The water channel is sketched in figure 2. A cylinder with a diameter of $D = 0.1$ m is placed in the symmetry plane of a 11.7$D$ wide flume. The latter is fed by a high-level water tank. The flow rate is measured by a magneto-inductive flow meter. A flow straightener damps the flow disturbances introduced by the inlet and a floating body reduces surface waves at the beginning of the channel. The undisturbed section of the flume in which the approaching turbulent open-channel flow develops naturally is approximately 200$D$ long. A sluice placed at the outlet of the flume controls the flow depth to 1.5$D$ before the water recirculates to the inlet periodically. The temperature of the working fluid water was found to be essentially constant at 18.4 °C, which gives a kinematic viscosity of $1.05 \times 10^{-6}\ \mathrm{m^2\ s^{-1}}$.

Since the cylinder disturbs the flow, small-scale surface waves appear and change the angle of refraction locally. Therefore, we used a slat of acrylic glass to damp those impacts to enable the laser light to enter the water body perpendicularly at its surface.

The slat was designed to be just as large as necessary to keep the influence on the flow structure as small as possible. It had a length of $L=1.5D$ in the streamwise direction, a width of $W=0.5D$ in the spanwise direction and was submerged by $0.01D$–$0.05D$. Approximately 4 % of the flume width was covered by the slat. In order to study its influence, the approaching flow with and without the slat was measured. In addition, numerical simulations of the flow around the cylinder with and without such a slat at lower Reynolds numbers were executed. The comparison of both numerical simulation and measurement of the approaching flow indicated that the deviations in the regions of interest near the bottom wall were small.

### 3.2. *Measuring technique*

We used two-dimensional two-component PIV to measure instantaneous velocity vectors in an observation window located in the symmetry plane upstream of the cylinder. A 2 mm $=0.02D$ thick light sheet was generated by a 532 nm Nd : YAG laser and entered the flow from the top through the slat. The images were recorded with a CCD camera at a resolution of 2048 × 2048 px. We applied two different magnifications for the inflow and the flow in front of the cylinder respectively. For the inflow, we covered the whole flow depth, which resulted in a resolution of 87 $\mu$m px$^{-1}$. For the measurements in front of the cylinder, we zoomed in using an $f$-number and a focal length of 2.8 and 105 mm respectively. Thereby, we achieved a magnification factor of 0.155, i.e. 47.6 $\mu$m px$^{-1}$ or 2101 px/$D$.

The seeding particles were hollow glass spheres with a diameter of $d_P=10$ $\mu$m and a density of $\rho_P=1100$ kg m$^{-3}$. The corresponding relaxation time was thus $\tau_P=d_P^2\rho_P/(18\nu\rho)=6.11\times10^{-6}$ s (Raffel *et al.* 2007). With this relaxation time, we could evaluate different Stokes numbers. The Stokes number based on the outer scaling was $St_b=\tau_P u_b/D=2.38\times10^{-5}$. Applying the Kolmogorov time scale $\tau_K=\sqrt{\nu/\epsilon_{macro}}$ (Pope 2011), the corresponding Stokes number was $St_K=\tau_P/\tau_K=4.7145\times10^{-3}$. The macroscale estimation of the dissipation, $\epsilon_{macro}=u_b^3/D$ (Pope 2011), is a conservative estimation, as the discussion of the dissipation in § 6.4 will show. Since the estimated Stokes numbers are considerably smaller than one, the particles can be considered to attain velocity equilibrium with the fluid (Raffel *et al.* 2007). The seeding was given continuously to the flow at the flow straightener at the beginning of the flume (figure 2).

We recorded a total of 27 000 image pairs with a sampling rate of 7.25 Hz and a time delay of 700 $\mu$s. This sampling rate would be too low to trace the evolution of individual flow structures in time or to compute spectra. For our purpose, it was sufficient as we considered time-averaged quantities only. Due to computer capacity, we subdivided the experiment into 18 batches of 1500 image pairs. This allowed us to clean the glass bottom of the flume repeatedly between each run to keep surface reflections at a constant low level. Thus, we recorded the flow statistics within a dimensionless time $Tu_b/D\approx800$ in each batch and $Tu_b/D\approx15\,000$ in total.

To analyse the flow field, we applied a two-dimensional standard PIV vector evaluation with 16 × 16 px interrogation windows at a 50 % overlap. The vectors marked as invalid were replaced by their corresponding 32 × 32 interrogation window counterparts. Thus, the spatial resolution was $0.0038D$, which corresponds to 263 data points per cylinder diameter.

In order to validate our PIV results, we checked various evaluation algorithms. An interrogation window size of 32 × 32 px was too coarse to resolve fine structures in the flow statistics. A standard evaluation with an interrogation window size of

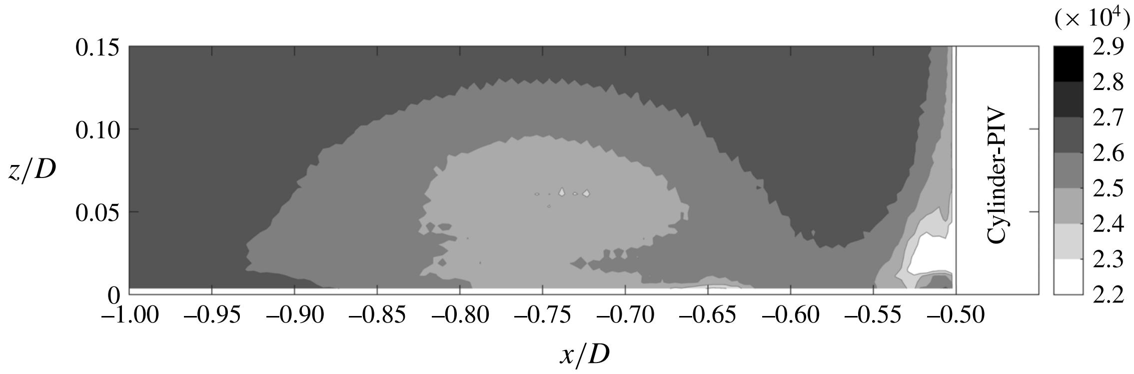

FIGURE 3. The number of valid samples obtained in the PIV experiment.

$16 \times 16$ px yielded a large number of invalid vectors. We explain these invalid vectors by out-of-plane losses due to large spanwise velocity fluctuations perpendicular to the light sheet. Unfortunately, the out-of-plane losses produced some artefacts in the flow fields. The artefacts disappeared when a deformable window algorithm was used. However, this algorithm marked an even larger number of samples as invalid. Therefore, we decided to use a standard $16 \times 16$ interrogation window evaluation and to replace the vectors marked as invalid by their counterparts from a $32 \times 32$ interrogation window evaluation at the same spatial positions. The results obtained with this technique were very similar to the ones obtained by the $16 \times 16$ evaluation with window deformation, although some details were lost. We feel this to be a good compromise between resolution and reliability. In figure 3, the number of valid samples in the region of interest in front of the cylinder is plotted. In wide regions, more than 24 000 samples were achieved. The reduced number of samples near the corner between the cylinder and the wall (figure 3) corresponds to the region of the corner vortex in which there are both large spanwise fluctuations and large spatial velocity gradients.

In addition to the standard interrogation window algorithm, we applied a single-pixel evaluation (Westerweel, Geelhoed & Lindken 2004; Kähler, Scholz & Ortmanns 2006; Strobl, Jenssen & Manhart 2016) to evaluate the time-averaged flow field. This gave a resolution of 2083 data points per diameter. Although these fields were quite noisy, they were useful for assessing the time-averaged wall shear stress and for revealing further details of the flow field.

To document the undisturbed approach flow, the cylinder was removed. The corresponding measurements were conducted at the same streamwise position in the symmetry plane of the channel as the ones with the cylinder. To capture the whole flow depth, they were conducted with a larger field of view. The evaluation was made with interrogation windows of $32 \times 32$ px, which corresponds to 72 data points per cylinder diameter. As this resolution was insufficient for an estimation of the wall gradient, the method of Clauser (1954) was applied to estimate the undisturbed wall shear stress of the approach flow. This is justifiable since the approach flow is considered to be a fully developed open-channel flow. It should be noted that the wall shear stress in front of the cylinder was evaluated by computing the velocity gradient.

## 4. Computational configuration

We complemented our PIV measurements by a highly resolved LES of the same flow configuration, identical to the one described in the study of Schanderl & Manhart

(2016), in which the reliability of the presented simulation has been discussed in detail. In this section, we describe the numerical method and set-up before we discuss the influence of the modelled subgrid-scale stresses on the results.

### 4.1. *Numerical method*

For the highly resolved LES, we applied our in-house code MGLET, which is a finite volume code and parametrizes the subgrid-scale stresses by the wall-adapting local eddy-viscosity (WALE) model (Nicoud & Ducros 1999). Since the subgrid-scale viscosity in this model decreases naturally towards the wall with $\nu_t \propto y^3$, no damping function had to be used. Central differences and a third-order Runge–Kutta procedure provide spatial approximation and time integration respectively. Since the grid is Cartesian, a conservative second-order immersed boundary method (Peller *et al.* 2006; Peller 2010) is applied to constitute the curved surface of the cylinder. The variables are arranged in a staggered way. Zonally embedded grids (Manhart 2004), each reducing the grid spacing by a factor of two, refine the grid in the region of interest around the cylinder.

To model the flow configuration in figure 1, the cylinder and the bottom and sidewalls of the channel are represented as no-slip conditions. The free surface is modelled by a slip condition. Since this slip condition at the top boundary prevents all kinds of surface deformation, the Froude number can be assumed to be infinitesimally small.

We assume that we have a wall-resolved LES, which means that we assess the local instantaneous wall shear stress by the linear gradient between the first off-wall grid cell centre and the wall. This assumption is justified if the wall-nearest cell centres are within the viscous sublayer, which is fulfilled in most of the flow domain, except in the precursor simulation; see below.

After the flow has reached a statistically steady state, a dimensionless time of $Tu_b/D \approx 700$ was simulated to gather statistics. This took approximately 2 million cpu hours on the high-performance computer SUPERMUC of the Bavarian Academy of Sciences.

### 4.2. *Grid resolution*

The computational domain consists of two major parts (figure 4): a precursor grid with periodic boundary conditions in the streamwise direction ($x$-direction) simulating the fully developed open-channel flow and the base grid in which the cylinder is placed. The base grid is one-way coupled to the precursor grid, such that instantaneous velocity cross-sections are taken from the precursor and set as the inflow condition at the base grid. The cylinder is placed at $(x, y) = (0, 0)$, which corresponds to the centre of the base grid.

The region of interest around the cylinder is refined by locally embedded grids. In total, three levels of grid refinement had to be applied. The precursor and base grid correspond to the refinement level zero and the finest grid to refinement level three. The position of each local grid is indicated by grey colour in figure 4. Since each refinement level reduces the grid spacing by a factor of two, the grid spacing of the finest level is eight times smaller than that in the precursor and the base grid. The finest grid uses 250 grid cells per cylinder diameter in the horizontal directions and 1000 grid cells per diameter in the vertical direction ($z$-direction), normal to the bottom wall. This corresponds to $\Delta x^+ = \Delta y^+ = 7.4$ and $\Delta z^+ = 1.9$ in wall units based on the undisturbed wall shear stress $\tau_0$ of the flow in the precursor simulation.

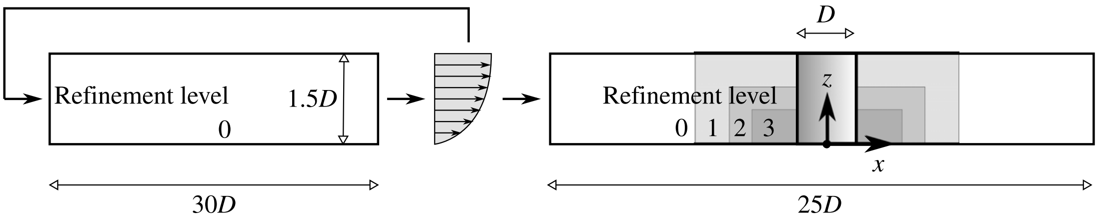

FIGURE 4. Side view of the computational domain. The zonally embedded grids are marked in grey (Schanderl & Manhart 2016).

The wall-nearest grid point, which is in the cell centre of the wall-nearest grid cell, is at $z^+ = 7.5$ in the precursor simulation. In the finest grid around the cylinder, this is at $z^+ = 0.95$ if it is based on the wall shear stress of the oncoming flow. If the local wall shear stress is taken, the maximum inner wall distance of the first grid point in the symmetry plane lies at $z^+ \approx 1.6$.

As the discussion of the dissipation rate in § 6.4 indicates, the finest grid spacing corresponds to approximately 1.5 Kolmogorov length scales in the vertical and approximately 6 Kolmogorov length scales in the horizontal direction. A grid study (Schanderl & Manhart 2016) shows that the three refinement levels applied are sufficient to reach a converged solution of the flow. The convergence of the first-order moments of the flow field is exemplarily discussed in § 5.3, where the wall shear stress distributions of three single simulations with one, two and three levels of grid refinement are presented. All numerical data relating to the region around the cylinder presented in this paper are taken from the simulation with three levels of grid refinement. However, as no locally embedded grids are applied in the inflow section, data characterizing this incoming flow are taken from the grid corresponding to refinement level zero.

The grid is equidistant in the horizontal directions and stretched by a factor of less than 1.01 in the vertical direction. It should be noted that as this stretching factor is applied to the base grid, only every eighth cell of the finest local grid is stretched. In total, the simulation uses $400 \times 10^6$ grid cells.

Application of time steps of $\Delta T u_b/D = 5.34 \times 10^{-4}$ results in a Courant–Friedrichs–Lewy number of $0.55 < CFL_{max} < 0.82$ on the finest locally embedded grid in the region around the cylinder.

### 4.3. *Influence of the subgrid-scale model*

The grid spacing is fine enough to ensure that the influence of the subgrid-scale model is small (Schanderl & Manhart 2016). Compared with the molecular viscosity $\nu$, the time-averaged modelled viscosity does not exceed a value of $\langle \nu_t \rangle = 0.39\nu$ in the symmetry plane in front of the cylinder. Schanderl & Manhart (2016) furthermore demonstrated that the time-averaged molecular shear stress $\nu\partial\langle u\rangle/\partial z$ and the resolved turbulent shear stress $-\rho\langle u'w'\rangle$ exceed the modelled shear stress $\langle \nu_t \partial u/\partial z\rangle$ by two orders of magnitude in the region of the horseshoe vortex system. Here, $u'$, $v'$ and $w'$ are the fluctuations of the corresponding velocities in the streamwise, spanwise and vertical directions $u$, $v$ and $w$ respectively.

Since the presented study focuses on the turbulent kinetic energy balance, we took care that the resolved turbulent kinetic energy $k$,

$$k = \tfrac{1}{2}(\langle u'^2\rangle + \langle v'^2\rangle + \langle w'^2\rangle), \tag{4.1}$$

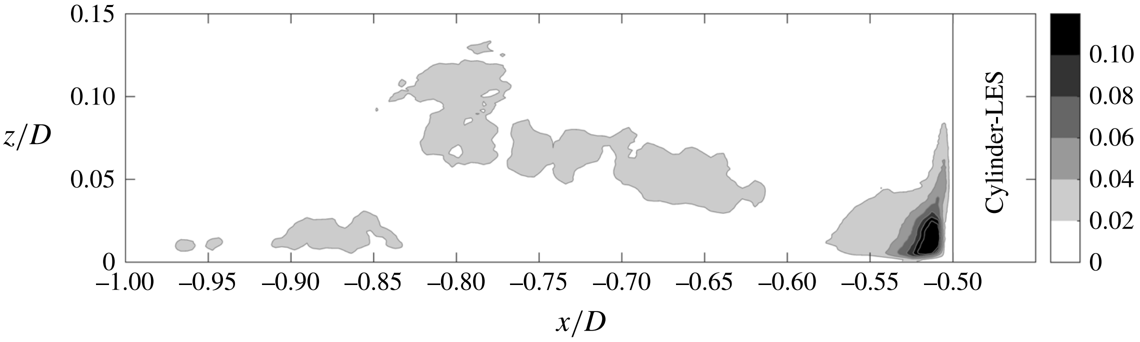

FIGURE 5. Ratio of modelled to resolved turbulent kinetic energy $k_{SGS}/k$ in the symmetry plane in front of the cylinder.

was large compared with the modelled turbulent kinetic energy $k_{SGS}$, which is estimated by (Lilly 1967; Werner 1991)

$$k_{SGS} = \left(\frac{\nu_t}{0.094\Delta}\right)^2 . \tag{4.2}$$

Here, $\Delta$ is the filter width, which is equivalent to the grid spacing.

In figure 5, the ratio of the modelled to the resolved turbulent kinetic energy $k_{SGS}/k$ is evaluated in the symmetry plane in front of the cylinder in an area covered by the horseshoe vortex system. In the region around the horseshoe vortex centre, the modelled turbulent kinetic energy peaks at $k_{SGS} \approx 0.035k$.

At the junction of the bottom wall and the cylinder, values of $k_{SGS}/k \approx 0.15$ can be observed. Here, the subgrid stress model visibly contributes to the energy balance. The peak at this position implies that the grid is too coarse to fully resolve the turbulent kinetic energy of the small corner vortex (see § 5). This is visible in the residual of the turbulent kinetic energy budget discussed in § 6.6. However, for an LES, this magnitude of $k_{SGS}/k$ can be considered as small. Furthermore, the peak is locally restricted, while in large regions, $k_{SGS}/k$ is significantly smaller.

Considering the small contribution of the subgrid stresses, we assume that the observations concerning the turbulent kinetic energy budget discussed in § 6 are representative for this flow, despite the fact that the presented data apart from the dissipation do not include subgrid contributions. As pointed out in § 6.4, the modelled dissipation is approximately 1/10 to 1/3 in the region covered by the horseshoe vortex. For the evaluation of the dissipation, therefore, the sum of both the modelled and the resolved contribution will be considered, as defined in (6.7).

## 5. Flow topology

Since the inflow condition was shown to have a strong influence on the flow around the cylinder (Schanderl & Manhart 2016), we took care to have similar incoming flow profiles in the experiment and the simulation. The following section documents the incoming flow profiles as well as the flow pattern and the wall shear stress distribution for both the experiment and the simulation. Since we could measure only two-dimensional velocity distributions, we concentrate on comparing in-plane quantities and processes in the symmetry plane in front of the cylinder. Any results out of that plane were achieved by LES alone. The discussion of the flow topology is the basis for a deeper investigation of the turbulence structure presented in § 6.

| | PIV | LES |
|---|---|---|
| $u_{CS}/u_b$ | 0.97 | 0.93 |
| $c_{f0}$ | $4.3 \times 10^{-3}$ | $3.9 \times 10^{-3}$ |

TABLE 1. The ratio of the velocity averaged over the whole cross-section $u_{CS}$ to the bulk velocity in the symmetry plane $u_b$, and friction coefficients in the undisturbed symmetry plane flow profile for the experiment and simulation.

### 5.1. *Inflow condition*

We first document the mean streamwise velocity and the Reynolds stresses of the undisturbed flow in the symmetry plane (figure 6). Figure 6(*a*) indicates that the time-averaged velocity profiles of the undisturbed incoming flow follow the logarithmic law of the wall in the experiment as well as in the simulation. The data are made dimensionless by the friction velocity $u_\tau = \sqrt{\tau_0/\rho}$ (Pope 2011). Here, $\tau_0$ is the wall shear stress in the symmetry plane of the undisturbed flow. It was computed by the velocity gradient at the wall in the LES and iteratively by the method of Clauser (1954) in the experiment.

The wake region of the LES is more pronounced than the one in the experiment. There are two possible reasons for this. The first possible explanation for the difference between LES and experiment could be the limited length of the inflow section in the water channel (≈140 water depths), which might be too short for a fully developed secondary flow structure. According to Demuren & Rodi (1984), more than approximately 60 hydraulic diameters are needed for fully developed secondary flow, while in our experiment the inflow length corresponds to only 42 hydraulic diameters. In the spanwise distribution of the streamwise velocity $\langle u \rangle$, these secondary flow structures cause a pronounced maximum in the symmetry plane (Schanderl & Manhart 2016). This leads to different ratios between the bulk velocity in the symmetry plane $u_b$ and the bulk velocity averaged over the whole cross-section $u_{CS}$, which has consequences for the normalization of statistical quantities. Table 1 documents the ratios $u_{CS}/u_b$ and $c_{f0} = \tau_0/(0.5\rho u_b^2)$ from the experiment and simulation. This difference will have an impact on the interpretation of dimensionless variables, as it makes a difference whether centreline or global quantities are used for normalization.

A second explanation for the different mean velocity profiles in experiment and simulation could be the wave damper we use in the experiment to damp surface waves. This is placed directly downstream of the flow straightener at the inflow into the water channel. This dampener slows down the flow at the surface and could lead to smaller surface velocities downstream, thus suppressing a pronounced wake profile. The first flow quantity on which the incoming flow profile will act is the downflow in front of the cylinder as it is induced by the velocity gradient in the incoming profile. We see that there are differences in the downflow in front of the cylinder (figure 8) which might also have an influence on the vortex system.

A comparison of the Reynolds normal stresses $\langle u'^2 \rangle$ and $\langle w'^2 \rangle$ (figures 6*b* and 6*c* respectively) and the Reynolds shear stresses $\langle u'w' \rangle$ (figure 6*d*) indicates accordance of the experimental and numerical inflow turbulence structures. The presented data also match the experimental data of Bruns, Dengel & Fernholz (1992) taken from Fernholz & Finley (1996) with similar Reynolds numbers based on the momentum thickness. Thus, we assume that the flow field of the approach flow is representative of a fully developed turbulent open-channel flow at the investigated

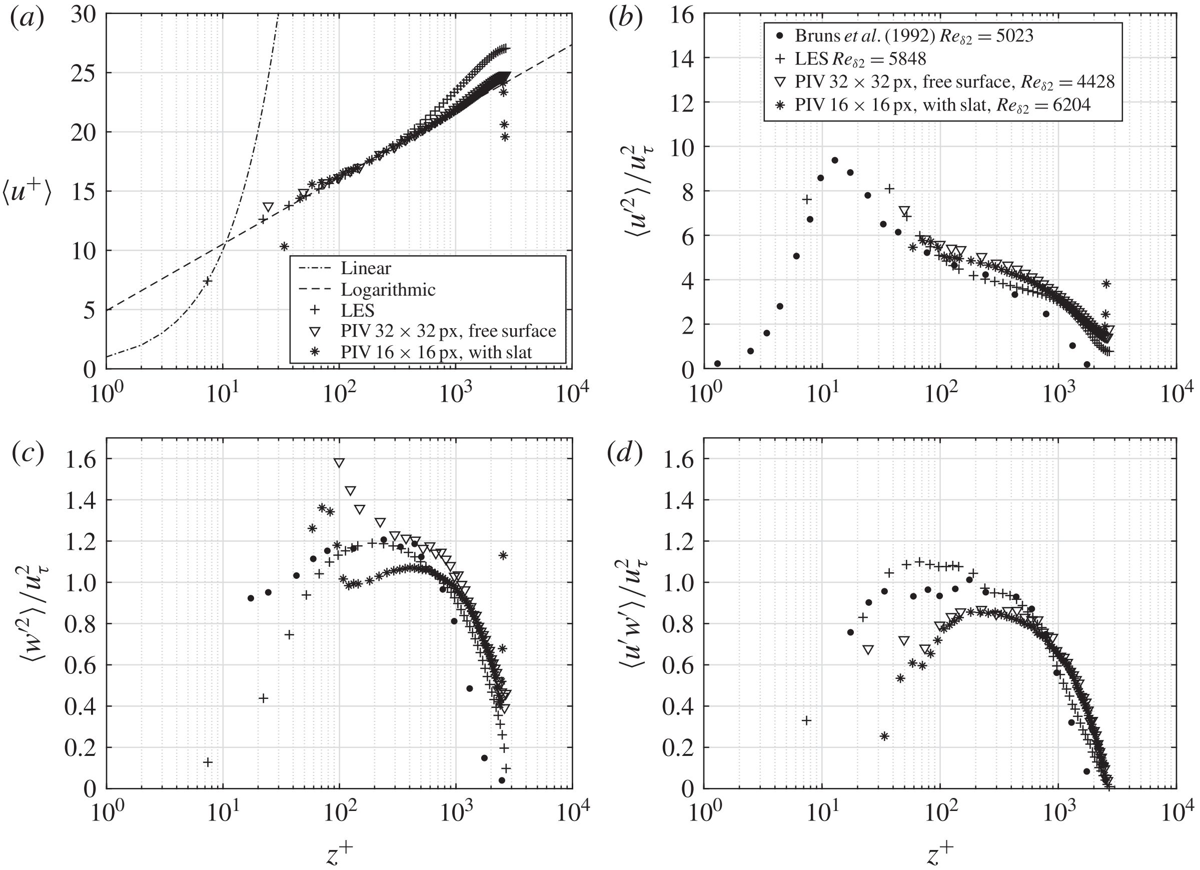

FIGURE 6. Time-averaged velocity profiles $\langle u\rangle/u_\tau$ (*a*), streamwise Reynolds stress $\langle u'^2\rangle/u_\tau^2$ (*b*), wall-normal Reynolds stress $\langle w'^2\rangle/u_\tau^2$ (*c*) and Reynolds shear stress $\langle u'w'\rangle/u_\tau^2$ (*d*) in the precursor grid for PIV and LES. For reasons of visibility, only every third data point is plotted for $z^+ > 150$. The experimental data of Bruns *et al.* (1992) have been digitized from Fernholz & Finley (1996).

Reynolds number. The overprediction of the vertical fluctuations $\langle w'^2\rangle$ by the PIV in the near-wall region is a result of the coarse measurement resolution that was used when investigating the undisturbed flow.

In figure 6, we also include profiles measured under the slat that was placed at the water surface in front of the cylinder to provide optical access through the water surface. These measurements were made without the cylinder. The profiles have been averaged in time and space over a length of $1.25D$ in the middle of the slat. We observe that the influence of the slat is generally strong near the water surface but remains negligible below $z^+ < 1000$, which is approximately $z < D/3$. Near the surface, the profiles measured with the slat seem to be smoother and less affected by artefacts than the ones measured without the slat. This can be explained by the smaller disturbance of the light sheet in the case with the slat.

Throughout this paper, all values denoted as undisturbed or being from the incoming flow (for example $u_b$, $\tau_0$ or those presented in figure 6) are taken from the symmetry plane of the flume.

### 5.2. *Horseshoe vortex system*

Figure 7 presents the measured and simulated time-averaged streamlines in the symmetry plane in front of the cylinder. For both data sets, the seeding points defining

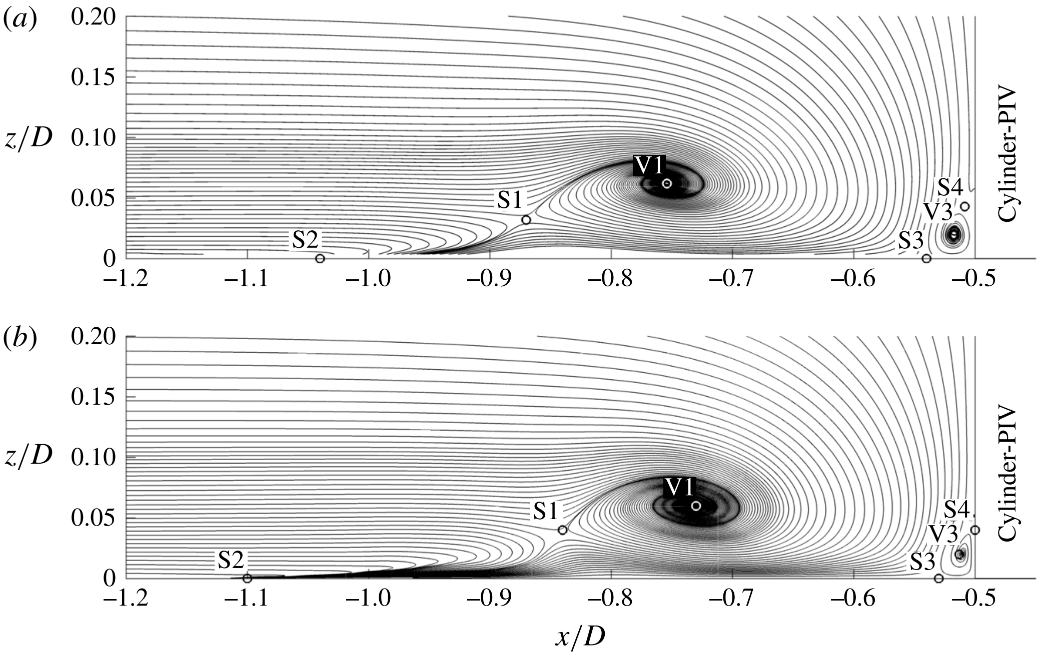

FIGURE 7. Streamlines of the time-averaged flow field in the symmetry plane in front of the cylinder for (*a*) PIV and (*b*) LES.

the streamlines are uniformly distributed on a line between $(x, z) = (-1.2D, 0)$ and $(x, z) = (-0.5D, 0.2D)$. From these seeding points, streamlines are integrated forwards as well as backwards in time. The approach flow profile leads to a vertical pressure gradient in front of the cylinder, which drives the downflow along the cylinder front. The main part of the downflow is turned upstream on reaching the bottom plate and flows upstream under the core of the main vortex V1. One part of this fluid is entrained into the main vortex; the other part forms a jet along the bottom wall directed against the main flow direction. The division between entrained fluid and fluid forming the jet is the stagnation point S1. The upstream-directed wall jet under S1 enters the upstream recirculation zone which ends at the critical point S2. We do not observe a second vortex V2 upstream of V1, in contrast to Apsilidis *et al.* (2015). The critical point S2 is not a separation as the fluid is not moving away from the wall at this point. The vertical velocity component in the vicinity of this point is negative. Instead, it renders itself as a sink in the 2D symmetry plane, which would be a stagnation point in 3D. This finding is different from the commonly used term 'separation' for this critical point and from the topology sketches of Baker (1979) for laminar flows. A discussion on the flow topology can be found in Simpson (2001). We cannot explain the different topology compared with that documented by Apsilidis *et al.* (2015), but suggest that the state of the turbulent boundary layer approaching the obstacle might be a key factor determining whether the point of first flow reversal in front of an obstacle will be a point of separation or a stagnation point.

The downwash at the cylinder front establishes a thin boundary layer at the flow-facing wall of the cylinder, which results in a pressure gradient between stagnation point S3 and the cylinder–wall junction. Thus, a small part of the fluid pushed downwards in front of the cylinder is deflected towards the cylinder on reaching the bottom plate, forming the corner vortex V3. The stagnation point S3 separates the fluid pointing in the upstream direction from that flowing towards the cylinder. The corner vortex V3 is trapped between stagnation point S3 and the

| | PIV | | LES | |
|---|---|---|---|---|
| | $x/D$ | $z/D$ | $x/D$ | $z/D$ |
| S1 | $-0.87D$ | $0.04D$ | $-0.84D$ | $0.04D$ |
| S2 | $-1.04D$ | — | $-1.10D$ | — |
| S3 | $-0.54D$ | — | $-0.51D$ | — |
| S4 | $-0.51D$ | $0.045D$ | $-0.50D$ | $0.04D$ |
| V1 | $-0.76D$ | $0.065D$ | $-0.73D$ | $0.060D$ |
| V3 | $-0.517D$ | $0.025D$ | $-0.515D$ | $0.02D$ |

TABLE 2. The positions of the critical points. If no $z_{Si}$ is given, the corresponding stagnation point is located at the bottom plate.

cylinder–wall junction. The PIV flow field (figure 7*a*) illustrates the similarity between V1, S1 and V3, S4 respectively. One could speculate that at higher Reynolds numbers, or with a better spatial resolution, a cascade of more and more smaller vortices appear in the corner between the cylinder and the wall, which would be cut due to viscous effects. In fact, such an additional corner vortex is visible in the streamline plots of Ryu *et al.* (2016), who simulated the wing–plate junction flow case of Devenport & Simpson (1990), which has a higher Reynolds number than the one of our case. Our single-pixel results for the time-averaged wall shear stress (§ 5.3, figure 11) show another small zone of negative wall shear stress just in front of the cylinder, which suggests a small clockwise-rotating vortex in front of the cylinder. This would be in line with the streamline plot of Ryu *et al.* (2016).

Between the stagnation points S3 and S2, the flow is pointing upstream along the wall, forming a wall jet, as discussed above. The upstream-directed flow is subject to a distinct pattern of acceleration along the streamlines. The rate of change of the distance between two adjacent streamlines is a measure for the velocity acceleration. As streamlines move together in figure 7, the flow accelerates, and *vice versa*. In particular, upstream of the stagnation point S3 in the range $-0.73D < x < -0.53D$, we can observe strong acceleration of the near-wall flow. After passing under the vortex V1, the spacing of the streamlines widens slightly, indicating deceleration. Finally, the fluid reaccelerates towards S2 or to being transported out of the plane in the spanwise direction. The consequences of this acceleration pattern on the budget of turbulent kinetic energy will be discussed in § 6.

The exact locations of the critical points mentioned above are listed in table 2. Comparison of the locations evaluated by PIV and LES shows satisfying accordance. However, the comparison of the streamlines in figure 7 points out a slight difference. In the LES, more fluid is entrained by the main vortex V1, resulting in the vortex being optically larger (figure 7*b*). The streamline approaching S1 from upstream originates from $z/D = 0.05$ in both cases. The streamline approaching S1 from downstream emanates from $z/D \approx 0.11$ in the experiment and from $z/D \approx 0.16$ in the LES. This is the streamline separating the fluid under the main vortex V1 into fluid going upstream along the wall and fluid being entrained into the vortex.

Figure 8 compares the streamwise profiles of the time-averaged vertical velocity component $\langle w \rangle$ from LES and PIV on a horizontal line at $z_{V1} = 0.06D$, which is through the centre of the main vortex V1. Negative values imply downflow, and *vice versa*. The experimental data in single-pixel resolution (dots) were smoothed by applying a moving spatial filter over 16 px (solid line).

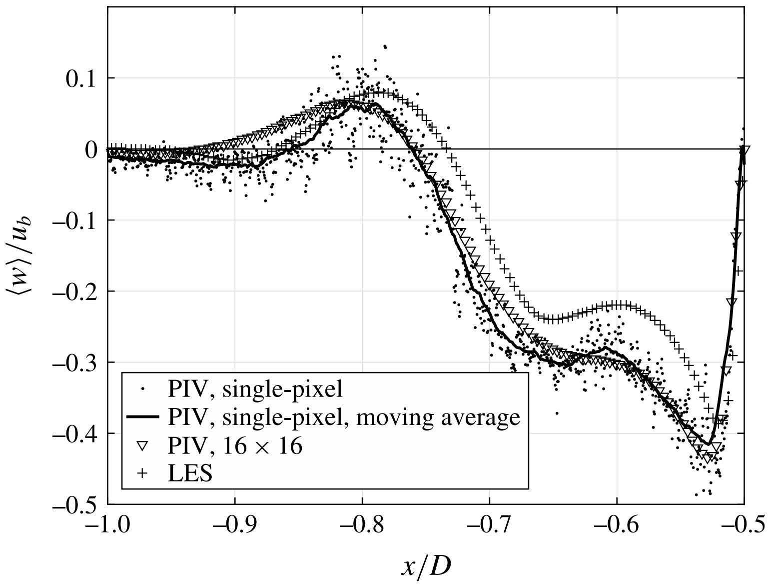

FIGURE 8. Profiles of the wall-normal velocity component $\langle w\rangle$ in the symmetry plane in front of the cylinder at a wall distance of $z_{V1}=0.06D$.

Vortex V1 can be identified in figure 8, as the upward-directed flow upstream and the downflow downstream from $x_{V1}$ indicate a clockwise rotation. The zero crossings between $x/D=-0.8$ and $x/D=-0.7$ indicate the location of the vortex centre. The downflow between the vortex centre and the cylinder shows two local minima separated by a local maximum which is at approximately $x\approx -0.6D$.

There is a qualitative match between the measured and simulated profiles. However, the vortex centre is more upstream in the experiment, which leads to a larger extent of the downflow region. In addition, the magnitude of the downflow is larger in the experiment. We observe that the single-pixel evaluation gives results qualitatively closer to the LES than the standard PIV. The standard PIV does not show the second local minimum at approximately $x/D=-0.65$ and gives visibly larger vertical velocities in the zone upstream of the vortex core than single-pixel PIV. There might be some small-scale events contributing to the time-averaged flow field which cannot be resolved by the relatively large interrogation windows of the standard PIV.

Figure 9(*a*) shows a top view of the simulated streamlines along the bottom plate, i.e. taking the stream- and spanwise velocities at $z=0.001D$. The streamlines are integrated back in time from points distributed equidistantly on a spanwise line at $x=0.8D$. This results in a relatively loose package of streamlines in the cylinder front. The regions dominated by the different vortices are visible here. The thin blank ring around the cylinder marks the corner vortex V3 in which fluid moves from the stagnation line towards the cylinder. The stagnation line collects streamlines which are integrated back in time from the points defined by the probe and go through the stagnation point S3 in the symmetry plane. Upstream of S3, the fluid moves in the upstream direction in a nearly straight manner, i.e. the streamlines close to the symmetry plane between S3 and $x/D\approx -0.75$ are nearly parallel. This indicates that almost all of the fluid close to the symmetry plane remains there and the transport in the spanwise direction is small underneath V1. The transport in the spanwise direction starts in the deceleration region of the wall jet at $x\approx -0.8D$, where the streamlines bear strong curvature, implying that major parts of the fluid leave the symmetry plane.

The streamlines along the bottom plate are linked to the pressure distribution on the bottom plate, shown as pressure coefficient $c_p=\langle p\rangle/(0.5\rho u_b^2)$ in figure 9(*b*). Large

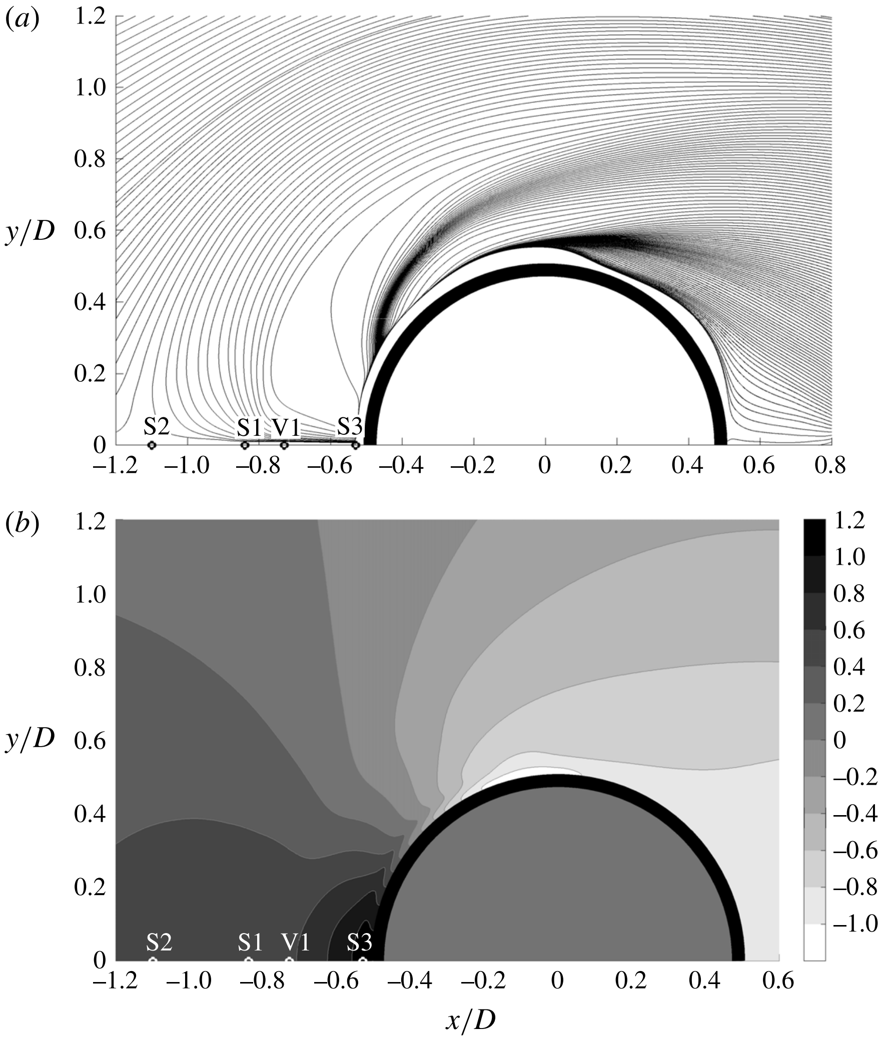

FIGURE 9. Streamlines of the time-averaged flow field (*a*) and the pressure distribution $c_p = \langle p\rangle/(0.5\rho u_b^2)$ (*b*) along the bottom plate around the cylinder taken from the LES.

pressure is indicated by dark colour and small pressure is indicated by light colour. The largest pressure is observed in front of the cylinder where the downflow hits the bottom plate between the main vortex and the cylinder. The near-wall streamlines in this area are pointing upstream in the direction of the steepest pressure gradient. At $x \approx -0.8D$, the pressure gradient is of similar magnitude in both the upstream and spanwise directions, causing the fluid to be transported outwards from the symmetry plane. At the same location, the streamlines in figure 9(*a*) bear the largest curvature and deviate from the symmetry plane. The stagnation line from point S3 would be visible in radial pressure profiles as local maxima.

Further insight into the three-dimensional behaviour of the vortex system can be gained from the instantaneous distributions of the second invariant of the velocity gradient tensor (figure 10). This so-called $Q$-criterion is widely used to visualize vortex structures. The isosurfaces $Qu_b^2/D^2 = 1000$ are rendered in a volume between $z = 0$ and $z = 0.2D$. The value was chosen to enable the identification of vortical structures. In each panel, we overlay two arbitrary time instants to demonstrate the spatial variability of the horseshoe vortex. The isosurface of $Q$ at one instant is rendered in black and the other one in grey. In figure 10(*a*), the wakes behind the cylinder are approximately symmetric. In figure 10(*b*), the two instants are chosen

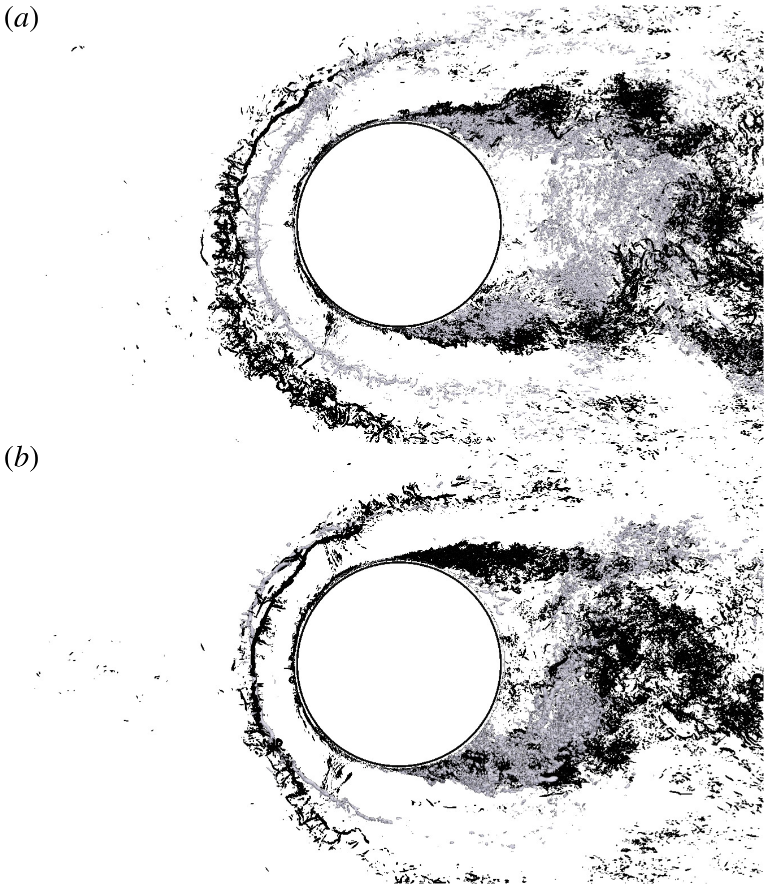

FIGURE 10. Top views of the instantaneous three-dimensional vortex structure visualized by $Qu_b^2/D^2 = 1000$ taken from the LES. In each panel, two realizations at arbitrary times have been plotted on top of each other.

to be during vortex shedding, i.e. the wakes are asymmetric and the vortices are shedding from opposite sides of the cylinder at the two instants.

At all four instants, the main vortex V1 is visible in front (on the left) of the cylinder. It bends around the cylinder like a horseshoe. The four instants demonstrate that the horseshoe vortex can undergo parallel displacements in the streamwise direction, as visible in figure 10(*a*), and a tilting around a vertical axis, as visible in figure 10(*b*). The displacement between the two instants in figure 10(*a*) is relatively large. The streamwise positions of the cores in the symmetry plane are $x/D \approx -0.83$ and $x/D \approx -0.7$ respectively. In figure 10(*b*), both vortices are at the same streamwise position in the symmetry plane at $x/D \approx -0.73$, which is the position of the time-averaged vortex V1. Small secondary vortices are visible at all instants, wrapping around the horseshoe vortex. It seems that they are lifted up upstream of the horseshoe vortex, which is in the region in which the upstream jet under the vortex decelerates. A deceleration of the streamwise velocity component and simultaneous stretching in the vertical direction would give rise to vertical vorticity, which is manifested here in the secondary vortices which mainly occur upstream of the horseshoe vortex. Downstream of the horseshoe vortex, between the vortex and the cylinder, the instantaneous vortical structures render a calm region at all times in the sense that no intense vortices are visible.

The instants rendered in figure 10 do not represent a time sequence. However, one observation can be made on the coherence of the horseshoe vortex. If the vortex is at

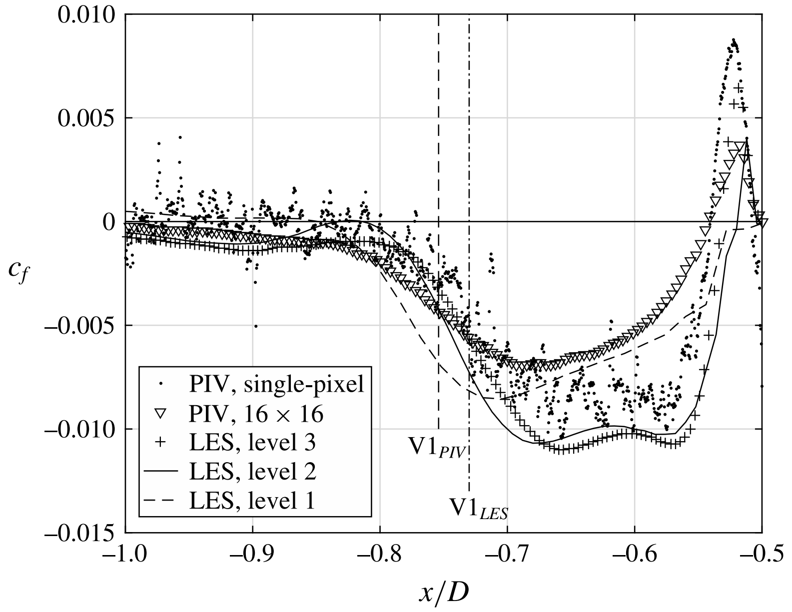

FIGURE 11. The distribution of the friction coefficient $c_f = \langle\tau_w\rangle/(0.5\rho u_b^2)$ over $x/D$ in the symmetry plane in front of the cylinder.

the position closest to the cylinder, the vortex is a coherent tube over a long distance along its core. If the vortex is at the position farthest away from the cylinder, the vortex cannot really be identified as a coherent single vortex. It is more or less a disordered arrangement of small-scaled vortices arranged along a curve in space that resembles a horseshoe vortex. This stage might be what results from a destabilization of the vortex by secondary vortices wrapped around the main vortex.

The vortex structures rendered in figure 10 are quite different from the instantaneous vortical structures documented by Escauriaza & Sotiropoulos (2011) for detached eddy simulations, but consistent with the structures described by Apsilidis *et al.* (2012) for LES.

### 5.3. *Wall shear stress distribution*

The flow described above exerts a specific pattern of wall shear stress on the bottom plate. Figure 11 shows the friction coefficient $c_f = \langle\tau\rangle/(0.5\rho u_b^2)$ in the symmetry plane upstream of the cylinder. The friction factor is negative in the large back-flow zone between the two stagnation points S2 and S3 (figure 7) and positive in the forward flow between the stagnation point S3 ($x/D \approx -0.53$) and the cylinder wall.

The footprints of the two vortices discussed above, V1 and V3, are visible in the distributions of $c_f$. The anticlockwise-rotating vortex V3 causes the strong positive wall shear stress peak at $-0.53D < x < -0.5D$. The stagnation point S3 is located where the wall shear stress is zero at $x \approx -0.53D$. Upstream of S3, the acceleration zone of the described wall jet leads to the broad region of negative wall shear stress at $-0.8D < x < -0.53D$. It should be noted that the maximum magnitudes of the wall shear stress are not found under the vortex core of the horseshoe vortex V1 but in the zone in which the flow is accelerated between stagnation point S3 and the location under the vortex core V1. Under the stagnation point S1, there is a local maximum of the wall shear stress, which means that the magnitude of the wall shear stress has a local minimum as the flow is pointing upstream. We do not observe a local recirculation embedded in this upstream flow as other authors have reported (e.g.

Escauriaza & Sotiropoulos 2011). The upstream jet forming under the main horseshoe vortex V1 reaches up to the stagnation point S2 at $x \approx -1.1D$. This observation can be made for both experiment and simulation, and is consistent with findings by Devenport & Simpson (1990).

As illustrated in figure 9, major parts of the fluid are leaving the symmetry plane and accelerating in the spanwise direction in the zone $-1.1D < x < -0.8D$, which is approximately between the stagnation point S2 and the main vortex core. This could explain why the wall shear stress between V1 and S2 is much smaller than that underneath vortex V1. The local maximum of the amplitude at $x \approx -0.9D$ could be explained by the fluid pointing towards the wall upstream of S1.

The numerical results are documented for three simulations with different grid resolutions. The simulation denoted as level 1 holds one locally embedded grid only, and the wall distance of the wall-parallel velocity is $0.002D$. Since simulation level 2 has two locally embedded grids, the grid spacing around the cylinder is reduced by a factor of two compared with simulation level 1, which leads to a wall distance of the first velocity of $0.001D$. In simulation level 3, the grid spacing is further reduced by a factor of two and the wall distance is $5 \times 10^{-4}D$. Here, the grid is eight times finer than in the precursor and the base grid. The differences between the wall shear stress taken from the simulation with the coarse grid (level 1) and from the one with the medium grid (level 2) are significant. The coarse grid underestimates the amplitude of $c_f$ under the wall jet. Furthermore, it is not able to capture the double peak in the region of large wall shear stress. Obviously, it is also too coarse to resolve vortex V3, as $c_f$ shows no positive peak right in front of the cylinder. In contrast, the differences between the simulations with the medium grid (level 2) and the fine grid (level 3) are rather small. Both exhibit approximately the same amplitude and capture the double peak distribution under the wall jet between $-0.7D < x < -0.55D$. We thus consider the flow to be satisfyingly converged over grid refinement. The grid dependence of the presented LES is discussed in more detail by Schanderl & Manhart (2016). All numerical data relating to the region around the cylinder presented in this paper are taken from the simulation with the fine grid (level 3). It should be noted that the data characterizing the inflow (§ 5.1) stem from level zero, since no local grid refinement is applied in the precursor grid.

The experimental data are documented for both a standard interrogation window and a single-pixel evaluation. The standard method results have a wall distance of at least $0.0019D$, which is half of the interrogation window size. The results obtained are in line with the LES results at a comparable grid spacing, level 1. The dual-peak nature of the strong wall shear stress is not reproduced by these results. The wall distance of the first valid single-pixel vectors is limited by half of the diameter of a particle image (Kähler, Scharnowski & Cierpka 2012), which is 3.4 px. With a pixel size of 48 µm, this gives a wall distance of approximately $8 \times 10^{-4}D$, which is between the wall distances of the finest and second finest LES. Since the single-pixel method is more sensitive to statistics and measurement issues, the corresponding wall shear stress distribution shows significant scatter. However, neglecting these oscillations, the single-pixel data support both the amplitude and the shape of the LES results.

While the overall behaviour of the wall shear stress agrees well between LES (level 3) and standard 16 × 16 px PIV, a detailed look reveals subtle differences. The LES predicts two local wall shear stress minima in the main recirculation zone and a plateau between them. The standard PIV, however, shows only the minimum at $x/D \approx -0.7$ and no plateau. The measured distribution of the wall shear stress between $x/D = -0.7$ and $x/D = -0.53$ resembles the one documented by Roulund *et al.* (2005) for a similar configuration at $Re_D = 170\,000$. However, application of the single-pixel method to the experimental data reveals a similar plateau to that in the LES (level 3).

Under V3 ($x/D > -0.53$), the amplitude of $c_f$ is largest in the single-pixel data, while the wall shear stress from the standard PIV is smallest. The amplitude increases with the data resolution here. This suggests that both LES and standard PIV are too coarse to resolve vortex V3 sufficiently. Furthermore, the single-pixel PIV shows negative values directly at the cylinder. This aspect is in favour of the possibility of an additional vortex rotating in the clockwise direction, as discussed in § 5.2.

## 6. Turbulence structure

The horseshoe vortex system is subject to strong fluctuations, as documented by several authors, e.g. Devenport & Simpson (1990), Escauriaza & Sotiropoulos (2011) and Apsilidis *et al.* (2015). Furthermore, it has been demonstrated that the near-wall momentum balance under the horseshoe vortex and especially in the large-magnitude shear stress region under the downflow is dominated by the convective terms. Reynolds stresses play a minor role here (Schanderl & Manhart 2015). To gain further insight into the dynamics of the vortex system, we investigate the turbulence structure in this section. We restrict ourselves to an analysis in a statistical sense, including the turbulent kinetic energy, Reynolds stresses, and their production, dissipation and diffusion.

### 6.1. *Turbulent kinetic energy*

All previously published works report an enhanced level of turbulent kinetic energy (4.1) near the core of the main horseshoe vortex V1. At moderate Reynolds numbers, such as the one considered here, the main observation is that the distribution of the turbulent kinetic energy follows a characteristic c-shape. There is a main peak around the vortex core V1 and a leg-like structure between the main peak and the bottom wall.

This structure can also be seen in our results (figure 12). The in-plane turbulent kinetic energy $k_{ip} = (\langle u'^2\rangle + \langle w'^2\rangle)/2$ (figure 12*b*) is a fairly good representation of the full turbulent kinetic energy (figure 12*c*). However, the peak value in the horseshoe vortex core of the full turbulent kinetic energy is approximately 20 % larger than the one of the in-plane turbulent kinetic energy. In contrast to the LES results (figure 12*b*,*c*), the position of the corner vortex V3 is visible in the PIV results (figure 12*a*). Overall, the measured peak values of the turbulent kinetic energy are approximately 20 %–30 % larger than the simulated ones and similar to the ones reported for $Re_D = 47\,000$ by Apsilidis *et al.* (2015).

For a detailed view, we investigate the individual Reynolds stresses. We restrict ourselves to presenting the LES results only, as there are minor differences between the measured and simulated distributions. The Reynolds normal stresses in the streamwise direction $\langle u'^2\rangle$ contribute mainly to the leg of the turbulent kinetic energy distribution (figure 13*a*). This leg is located in the near-wall jet underneath the main vortex core. Following the streamlines from the downflow between the vortex V1 and the cylinder (compare figure 7), the streamwise turbulence intensity grows considerably when the local acceleration, as indicated by converging streamlines, diminishes (at $x \approx -0.75D$). The measured level of $\langle u'^2\rangle$ is in general slightly larger than the numerical one.

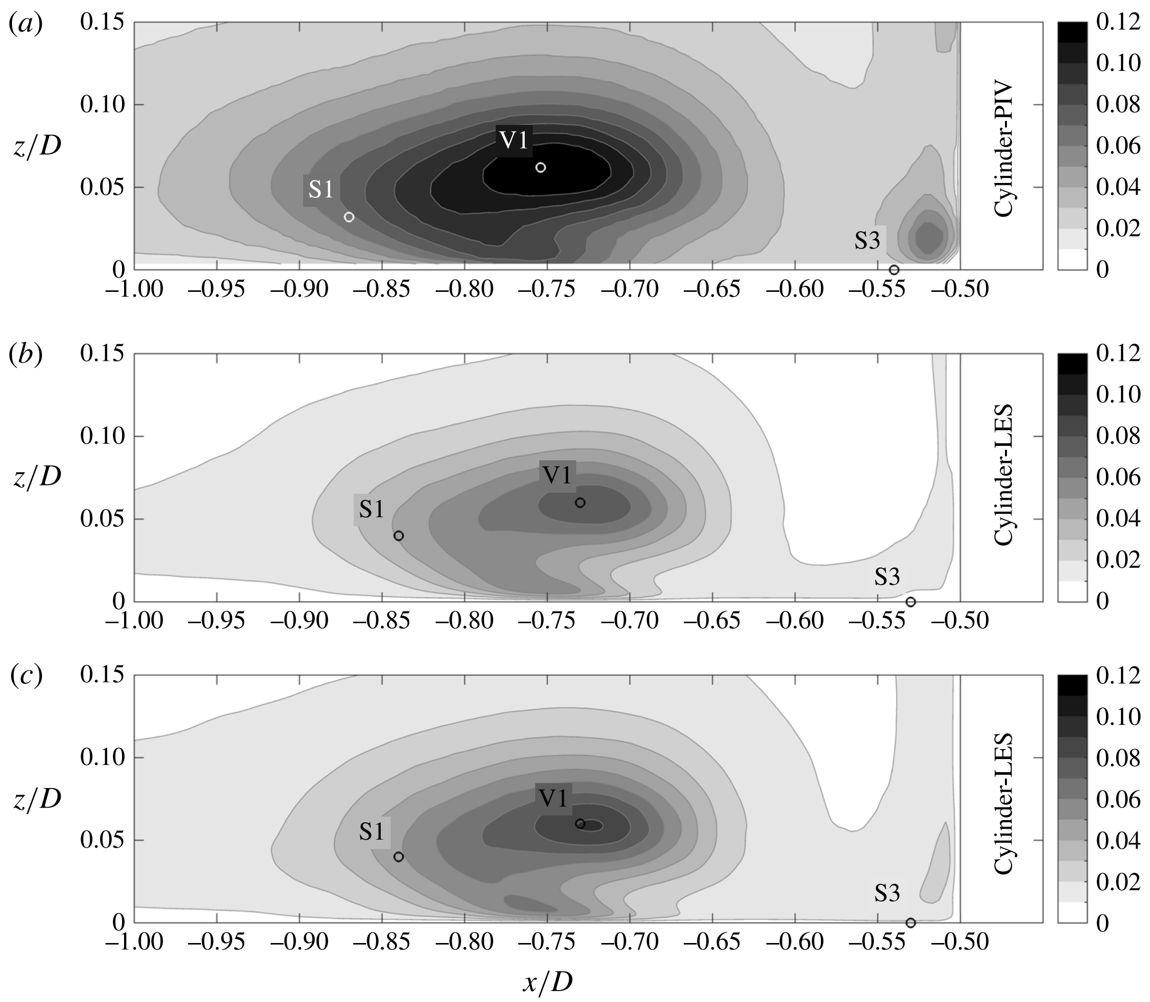

FIGURE 12. The turbulent kinetic energy in the symmetry plane in front of the cylinder: the in-plane turbulent kinetic energy $k_{ip}/u_b^2$ measured by PIV (*a*) and simulated by LES (*b*); the full turbulent kinetic energy $k/u_b^2$ simulated by LES (*c*).

The vertical Reynolds normal stress $\langle w'^2 \rangle$ (figure 13*b*) peaks approximately around the centre of V1, which is consistent with horizontal variations of the main vortex core. Both LES and PIV have similar amplitudes. In addition to the peak around the horseshoe vortex, we can observe enhanced vertical Reynolds stresses in a band along the front of the cylinder in both LES and PIV.

Finally, the Reynolds shear stress $\langle u'w' \rangle$ is presented in figure 13(*c*). There is a large patch with negative shear stress in the left half of vortex V1 slightly downstream of the stagnation point S1, and a patch of positive shear stress downstream of the main vortex.

Figure 14 illustrates three-dimensional isosurfaces of $k/u_b^2 = 0.035$ (red) and $k/u_b^2 = 0.07$ (blue) in the cylinder front. The isosurface of $k/u_b^2 = 0.035$ encloses the region covered by the main vortex V1, while values of $k/u_b^2 > 0.07$ are limited to its core. When V1 is bent around the cylinder and the fluid accelerates, the cross-sectional area enclosed by the isosurfaces shrinks. Furthermore, it is noticeable that in the region between V1 and the cylinder, the turbulent kinetic energy is relatively small. This is the zone where the downflow in front of the cylinder takes place. In the following sections, we further discuss this issue by taking a deeper look at the balance equation of the turbulent kinetic energy.

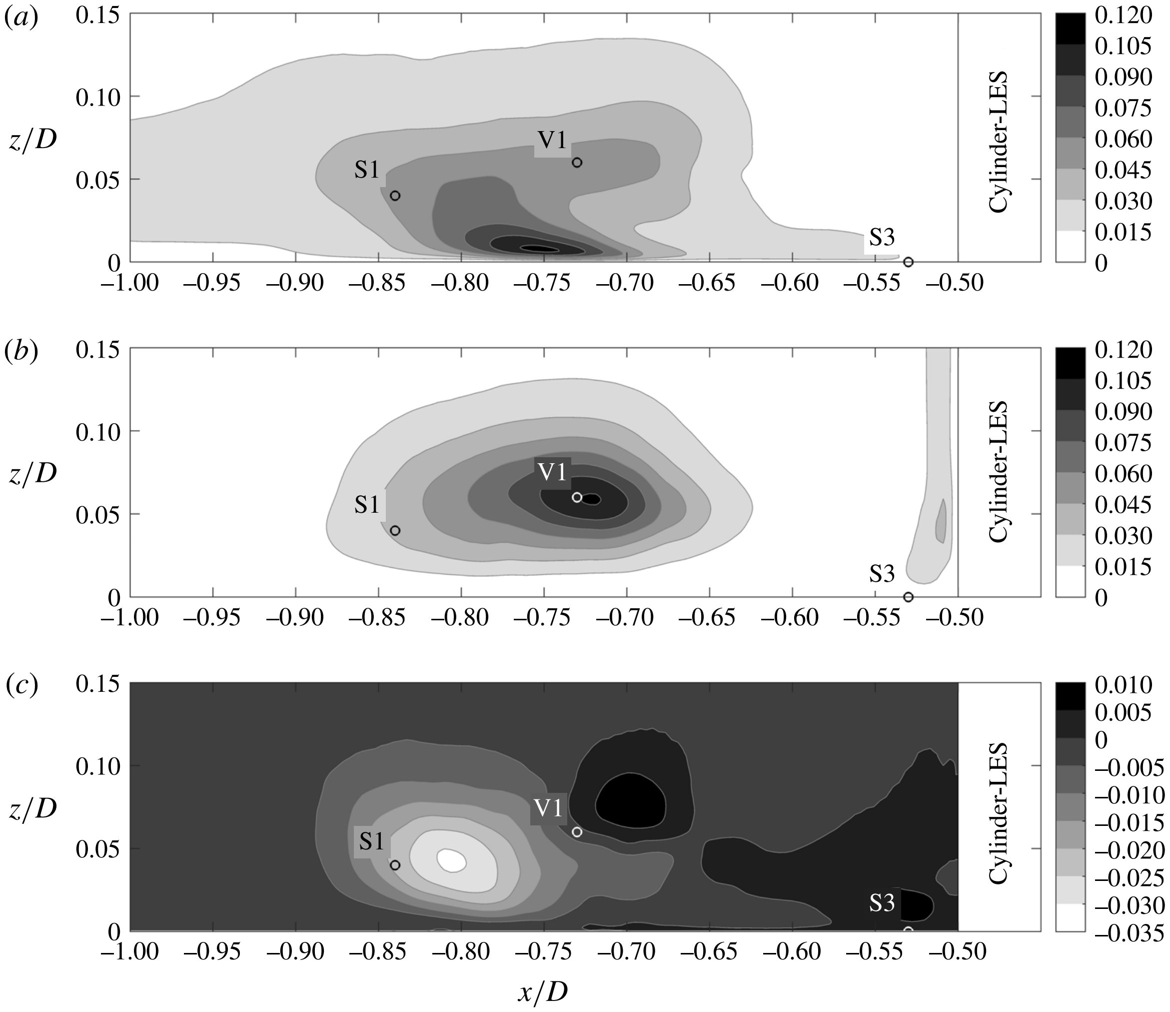

FIGURE 13. Reynolds stresses in the symmetry plane in front of the cylinder obtained from LES: $\langle u'^2\rangle/u_b^2$ (*a*), $\langle w'^2\rangle/u_b^2$ (*b*) and $\langle u'w'\rangle/u_b^2$ (*c*).

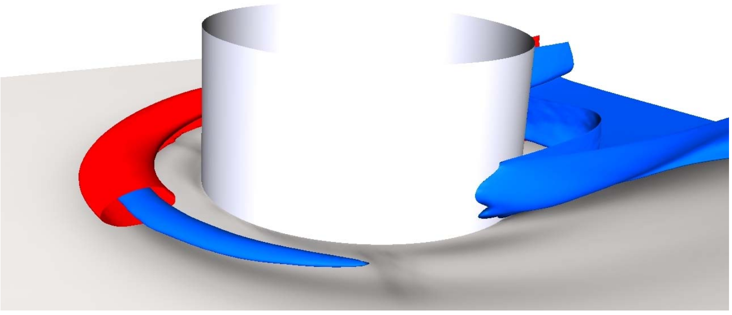

FIGURE 14. Isosurfaces of the turbulent kinetic energy in the cylinder front taken from the LES; $k/u_b^2 = 0.035$ is marked in red and $k/u_b^2 = 0.07$ is marked in blue. The former is only shown up to the symmetry plane.

### 6.2. *Turbulent kinetic energy balance*

In the remainder of this paper, we will investigate the complete budget of the turbulent kinetic energy $k$ (4.1) in front of the wall-mounted cylinder. According to, e.g., Pope (2011), the budget contains convection by the time-averaged flow $C$, turbulent convection $T_{conv}$, pressure transport $T_{pres}$, viscous diffusion $T_{visc}$, production

$P$ and dissipation $\epsilon$,

$$0 = C + T_{conv} + T_{pres} + T_{visc} + P - \epsilon. \tag{6.1}$$

In a statistically steady flow, the convective term $C$ reads as

$$C = -\langle u_i \rangle \frac{\partial k}{\partial x_i}. \tag{6.2}$$

Besides the mean convection $C$, three mechanisms are responsible for redistributing $k$ in space: turbulent convection $T_{conv}$, pressure transport $T_{pres}$ and viscous diffusion $T_{visc}$,

$$T_{conv} = -\frac{1}{2} \frac{\partial}{\partial x_i} \langle u_i' u_j' u_j' \rangle, \tag{6.3}$$

$$T_{pres} = -\frac{1}{\rho} \frac{\partial}{\partial x_i} \langle u_i' p' \rangle, \tag{6.4}$$

$$T_{visc} = 2\nu \frac{\partial}{\partial x_i} \langle u_j' s_{ij}' \rangle. \tag{6.5}$$

The three individual redistribution terms ($T_{conv} + T_{pres} + T_{visc}$) can be taken together as the turbulent transport (Pope 2011). The production term is denoted as $P$,

$$P = -\langle u_i' u_j' \rangle \frac{\partial \langle u_i \rangle}{\partial x_j}. \tag{6.6}$$

It should be recalled that the values defined above do not include subgrid contributions, and we do not attempt to estimate them because the modelled turbulent kinetic energy $k_{SGS}$ is small compared with the resolved one $k$ (figure 5). On the contrary, the dissipation $\epsilon$ as defined in (6.7) is the sum of the modelled and resolved dissipation,

$$\epsilon = \epsilon_{SGS} + \epsilon_{res}. \tag{6.7}$$

Here, $\epsilon_{SGS}$ represents the modelled dissipation,

$$\epsilon_{SGS} = 2\langle \nu_t s_{ij} s_{ij} \rangle, \tag{6.8}$$

while $\epsilon_{res}$ is the resolved one,

$$\epsilon_{res} = 2\nu \langle s_{ij} s_{ij} \rangle. \tag{6.9}$$

In both (6.8) and (6.9), $s_{ij}$ is the fluctuation of the strain rate tensor. Central differences were applied to calculate the spatial derivatives needed to evaluate the terms defined above. The evaluation of the terms from the LES was carried out within the LES code. These routines were carefully validated during the implementation with the help of turbulent channel flow data. The post-processing of the PIV results was implemented in a Matlab code and validated against the LES evaluation and against an independently developed post-processing tool. Thus, we are confident that the computed budget terms are free from bias or programming errors.

In the following, we discuss how the single terms of the budget are linked to the distinct flow topology in the cylinder front and its rich dynamics. This will provide deeper insight into the physics of the horseshoe vortex system.

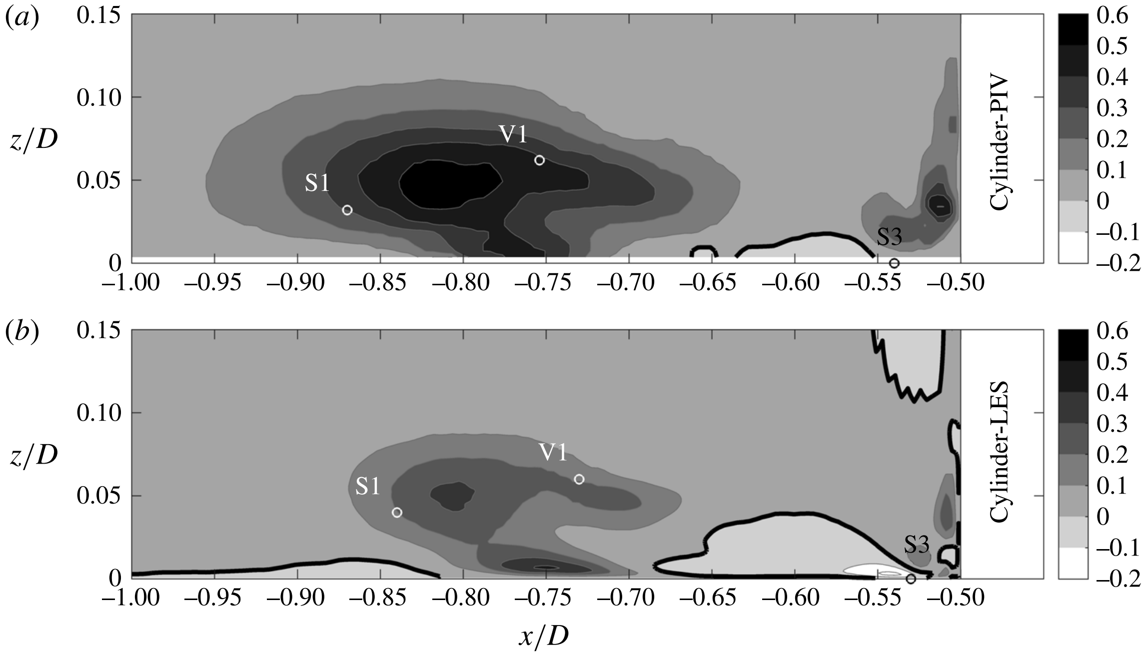

FIGURE 15. The production of turbulent kinetic energy in the symmetry plane in front of the cylinder: in-plane production from PIV (*a*) and total production from LES (*b*). The isoline marks $PD/u_b^3 = 0$.

### 6.3. *Production of turbulent kinetic energy*

The individual production terms of the turbulent kinetic energy (6.6) have been studied by several authors. Devenport & Simpson (1990) identified significant production by normal and shear stress terms around the mean location of the horseshoe vortex and normal stress production due to the deceleration of the jet under the horseshoe vortex. The acceleration of the jet upstream of the stagnation point S3 gives a negative production by the streamwise normal stress term.

The distribution of the production of turbulent kinetic energy is compared between LES and PIV in figure 15. In this figure, the sum of the in-plane production terms is plotted from PIV (figure 15*a*) and the sum of all terms is plotted from LES (figure 15*b*). The difference between full and in-plane turbulent kinetic energy production is small and stems from the only off-plane production term in the symmetry plane, $P_{22} = -\langle v'^2 \rangle \partial \langle v \rangle / \partial y$. It is consistently negative due to the stretching of the flow in the spanwise direction at a magnitude of approximately 20 % of the other terms. Apart from the difference from the off-plane terms, the measured values are larger, peaking at $0.5 u_b^3/D$ between V1 and S1, while the simulated peak values – including the off-plane term – remain at approximately $0.3 u_b^3/D$ in this region.

There is large production of turbulent kinetic energy around the horseshoe vortex V1, especially in the region between the centre of V1 and the stagnation point S1. In both LES and PIV, a local near-wall peak of production can be found under the horseshoe vortex, and a region of negative production close to the wall between V1 and the cylinder.

The distributions of the normal stress production terms from LES are presented in figure 16. The acceleration and deceleration in the upstream-directed jet under the main vortex act on the streamwise stress term $P_{11} = -\langle u'^2 \rangle \partial \langle u \rangle / \partial x$. It is found to be negative at $-0.70D < x < -0.53D$, where the fluid accelerates; figure 16(*a*). As soon as the jet decelerates at $x \approx -0.7D$, $P_{11}$ attains significant positive values. Even though

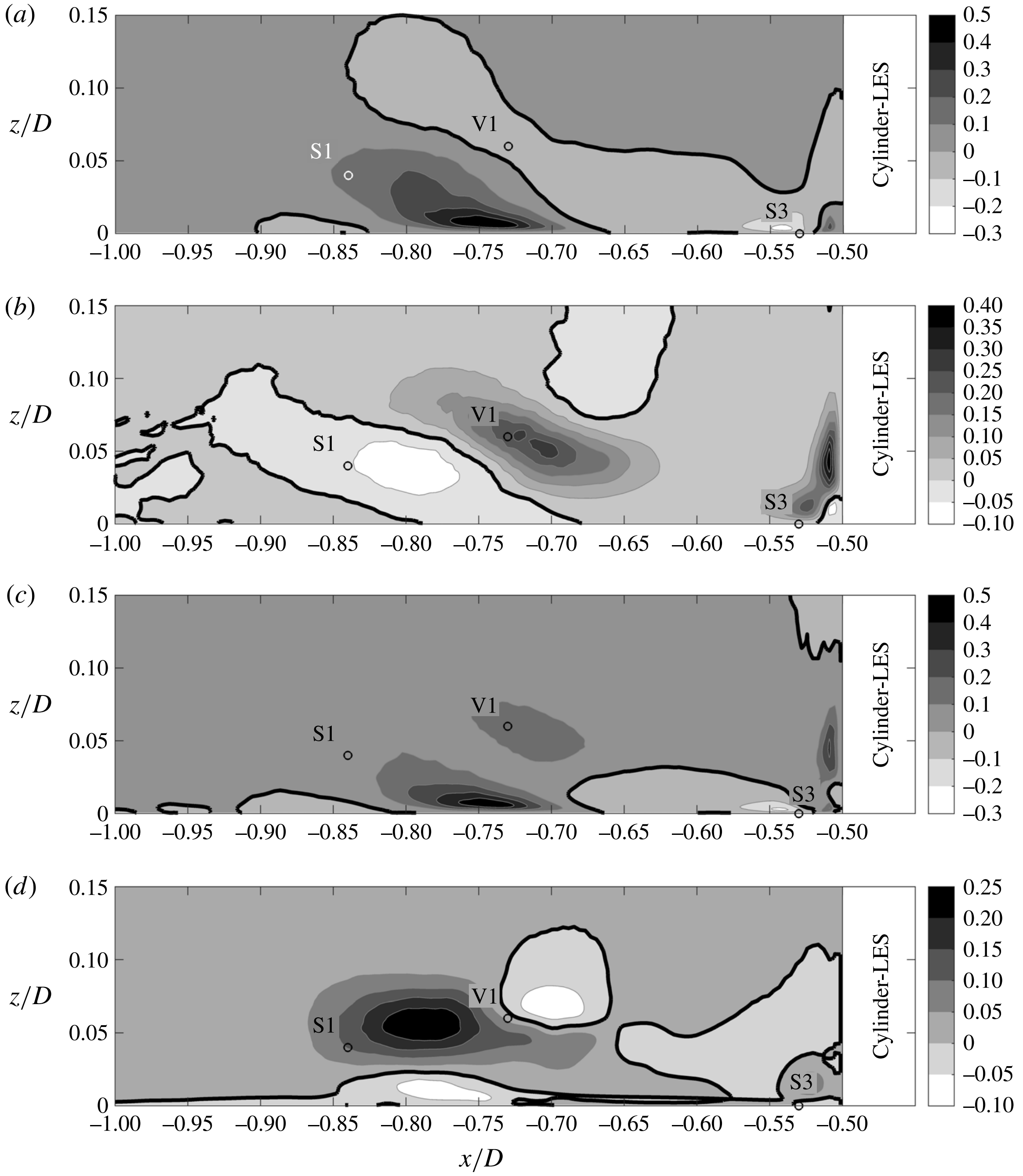

FIGURE 16. Normal and shear stress production of turbulent kinetic energy in the symmetry plane in front of the cylinder from LES: $P_{11}D/u_b^3$ (*a*), $P_{33}D/u_b^3$ (*b*), $(P_{11}+P_{22}+P_{33})D/u_b^3$ (*c*) and $P_{13}D/u_b^3$ (*d*). The isoline marks $PD/u_b^3=0$.

the peak of $P_{11}$ is right above the bottom plate, the patch of positive $P_{11}$ seems to lift from the wall, reaching to stagnation point S1. When the fluid moves further upstream towards stagnation point S2, the jet accelerates again and $P_{11}$ turns negative, as indicated by the isoline around $-0.9D<x<-0.85D$.

In figure 16(*b*), we can observe large positive production rates $P_{33}=-\langle w'^2\rangle\partial\langle w\rangle/\partial z$ slightly downstream of the horseshoe vortex, around $x/D\approx-0.7$, along the front face of the cylinder and above the stagnation point S3. In the region of the stagnation point S1, the production $P_{33}$ becomes negative. Along the bottom plate, $P_{33}$ is small.

In figure 16(*c*), the net production by the normal stress terms $P_{11} + P_{22} + P_{33}$ is shown. This sum indicates the anisotropic contributions of the Reynolds stresses (compare Pope 2011, p. 126). The redistribution of turbulent kinetic energy between individual components due to curved streamlines is removed. We can observe that large parts of the negative and positive production in $\langle u'^2\rangle$ and $\langle w'^2\rangle$ around the main vortex V1 can be associated with a redistribution between those stresses when a fluid particle is rotated when following the curved streamlines. From this distribution, it becomes evident that normal stress terms dominate the production of turbulent kinetic energy at the wall (due to streamwise fluctuations). Furthermore, they have a visible contribution in the downstream part of the main vortex V1 due to wall-normal fluctuations.

The shear stress production $P_{13} = -\langle u'w'\rangle \partial\langle u\rangle/\partial z$ is large in the region between the stagnation point S1 and the core of vortex V1 (figure 16*d*). In this region, the streamlines in figure 7 bear large curvature and there is a large shear rate in the streamwise velocity component. The location of its maximum corresponds approximately to the peak position of $-\langle u'w'\rangle$ (figure 13). This patch of positive shear production is a main contributor to the total production of turbulent kinetic energy, which becomes evident when comparing with figure 15.

Negative shear production can be found in three regions. The first region lies close to the wall between the streamwise positions of S1 and V1. This peak can be explained by the wall-normal gradient of $\langle u\rangle$ in the wall jet. Above the velocity maximum in the jet, the gradient is negative $\partial\langle u\rangle/\partial z < 0$. Below the maximum, it is positive. As $\langle u'w'\rangle$ is negative in the whole region, the production changes sign and becomes negative in the lower part of the jet. The fact that the Reynolds shear stress does not change sign when the velocity gradient changes sign indicates that large-scale fluctuations penetrate this jet and reach the wall.

The second location in which negative shear production can be found is in the upper right part of the main vortex V1 ($x/D \approx -0.7$), in which free-stream fluid is entrained into the vortex. The streamlines are pointing downwards and in the direction of the cylinder. Like in the other regions of the horseshoe vortex, the streamwise velocity has a positive vertical gradient $\partial\langle u\rangle/\partial z > 0$. We find positive $\langle u'w'\rangle$ in this region (figure 13). Together, this gives a negative shear production of turbulent kinetic energy at a significant level. The third location with negative $P_{13}$ is a large area in front of the cylinder for $x/D \gtrsim -0.6$. The magnitude is small but noticeable. Around vortex V3, however, we can see significant positive values of shear production. We do not show $P_{31}$ as its amplitude is approximately one order of magnitude smaller than that of the other terms.

To gain insight into the three-dimensional distribution of production in front of the cylinder, isosurfaces of $P$ are evaluated in figure 17. The isovalues have been chosen to be representative for specific regions of production, as explained in the following. The red isosurface marks values of $PD/u_b^3 = 0.1$ and surrounds the regions in which medium production takes place. Its cross-section has the distinct c-shape typical for the distribution of $k$. The isosurface $PD/u_b^3 = 0.25$ visualizes the two regions of largest production, which are not connected – one is approximately in the position of the vortex core of V1 and the other one is where the leg of the c-shape meets the bottom plate. It should be noted that the green isosurface in the vortex core ends at an angle of approximately 45° to the symmetry plane, while the green region at the bottom plate wraps around the cylinder to an angle of approximately 90°.

In front of the cylinder at the bottom plate, there is a large region of turbulent kinetic energy destruction, i.e. negative production; see the blue isosurface $PD/u_b^3 =$

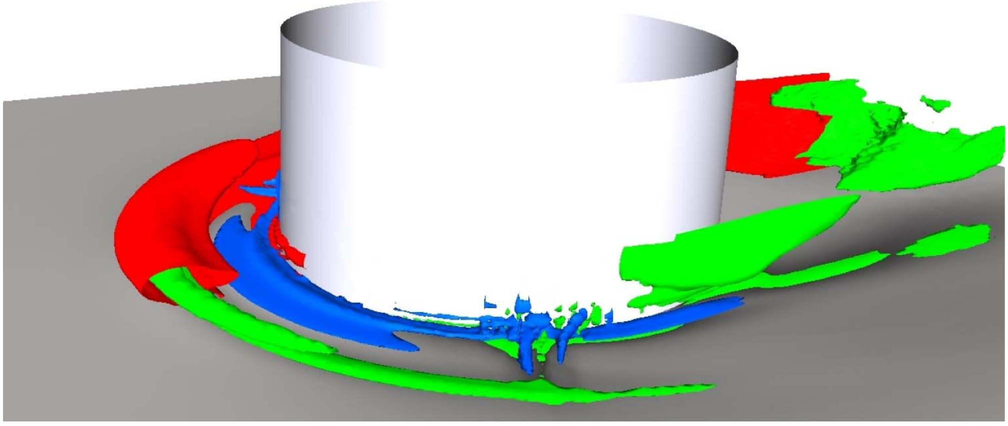

FIGURE 17. Isosurfaces of the total production of turbulent kinetic energy $P$ around the cylinder: $PD/u_b^3 = -0.02$ (blue), $PD/u_b^3 = 0.1$ (red) and $PD/u_b^3 = 0.25$ (green) are evaluated from the LES. The isosurface for $PD/u_b^3 = 0.1$ is only shown up to the symmetry plane.

$-0.02$ in figure 17. This is the region in which the upstream-directed jet along the bottom plate accelerates, leading to negative normal stress production. This negative normal stress production can be found all around the cylinder until approximately 90°. It can explain the low level of turbulent kinetic energy between the cylinder and V1 which extends half way round the cylinder (compare figures 12 and 14).

It should be mentioned that the disturbances of the isosurfaces in the lateral front of the cylinder are artefacts stemming from the numerical scheme. It should be noted that second-order central approximations favour wiggles in strong curvature regions when the cell Reynolds number exceeds a value of 2.0. This is the case here, and we do not intend to damp these wiggles as they indicate an insufficient grid resolution (Gresho & Lee 1981) and have only marginal effects on the flow dynamics in the symmetry plane which is the focus of the present investigation.

### 6.4. *Dissipation*

In this section, we discuss the dissipation $\epsilon$ of turbulent kinetic energy (6.7). The distribution and level of dissipation are of relevance to turbulence modelling in the Reynolds-averaged context. In a flow with local equilibrium, the dissipation would be equal to the production of turbulent kinetic energy. Since local equilibrium cannot be expected in the considered flow, we cannot expect the spatial distribution of the dissipation of turbulent kinetic energy to match the distribution of its production.

The dissipation rates in the symmetry plane in the cylinder front as obtained from PIV and LES are presented in figure 18. Large values of $\epsilon$ can be observed around the core of vortex V1. A second peak is placed right beneath in the leg of the c-shape of the turbulent kinetic energy distribution, where the jet decelerates. A third peak is located in the region of the corner vortex V3. The LES data in figure 18(*b*) show significant levels of dissipation along the bottom plate, where the jet is causing large shear stresses. This stripe of large $\epsilon$ is not visible in the PIV data since the standard PIV algorithm, which has been applied to compute the dissipation terms, does not resolve the wall in a sufficient way.

The spatial distribution of the dissipation does in fact largely resemble the distribution of the turbulent kinetic energy in figure 12. The peaks of both the turbulent kinetic energy and its dissipation are shifted in space with respect to the

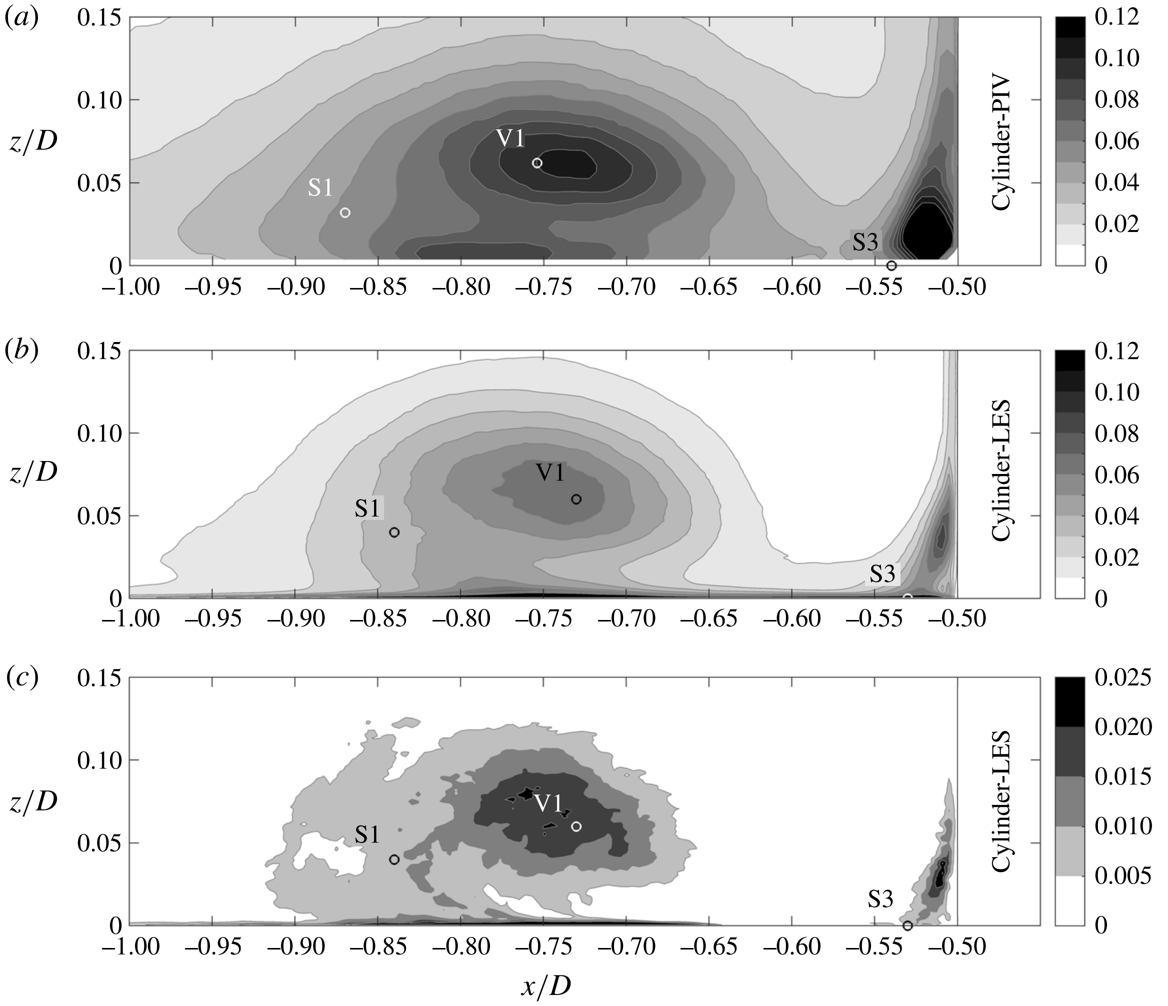

FIGURE 18. The total dissipation of turbulent kinetic energy $\epsilon D/u_b^3$ taken from PIV (*a*) and LES (*b*), and the modelled dissipation $\epsilon_{SGS} D/u_b^3$ taken from LES (*c*) in the symmetry plane in front of the cylinder. The different amplitudes of the colour bars should be noted.

ones of the production (figure 15). In the measured distribution, the peak of $\epsilon$ is downstream of the vortex core V1. The streamlines reaching this location stem from the approach flow, which indicates that the dissipative scales reaching the location of the dissipation peak cannot be transported to this location by the time-averaged flow field. We speculate that the bimodal oscillations of the horseshoe vortex give rise to turbulent transport of small-scale structures from the locations of large turbulent kinetic energy production to the locations where they are dissipated. This process would lead to large magnitudes of the turbulent transport terms $T_{conv}$ and $T_{pres}$. We discuss this hypothesis in the following sections.

The dissipation rate from PIV shown in figure 18(*a*) is computed from in-plane velocity gradients only, while the one from LES is computed from the full tensor including subgrid contributions (6.7). Nevertheless, the measured dissipation rate is larger by a factor of approximately 1.7. This factor is in compliance with the larger levels of turbulent kinetic energy and its production in the experiment. However, it needs to be taken with caution as in the experimental values only the in-plane gradients of the in-plane velocity components have been taken into account. The full dissipation would have larger values. It is known that an estimation of the dissipation rate from PIV data suffers from two sources of error. If the interrogation windows are considerably larger than the Kolmogorov scale, the dissipation will be underestimated. If the interrogation window is in the range of or smaller than the Kolmogorov scale, it can be overestimated by measurement noise (Tanaka & Eaton 2007). It should be noted that we did not apply any correction to our PIV results to account for the noise or insufficient resolution as we did not know the value and distribution of the Kolmogorov scale in advance.

It is natural to assume that the LES is not able to resolve the small dissipative structures of the flow. However, we have to stress that the dissipation taken from the LES includes the modelled dissipation $\epsilon_{SGS}$. The latter is documented in figure 18(*c*). In the region of V1, $\epsilon_{SGS}$ is approximately one third of the total dissipation. This is a perceptible contribution. However, the amplitude of $\epsilon_{SGS}$ is too small to assign the difference in amplitudes of PIV and LES to possible shortcomings of the subgrid stress model. We keep the discussion on the level of the dissipation rate for later when the whole budget is discussed.

To further study the characteristics of the turbulence structure, the pseudo dissipation $\epsilon_p = \nu\langle(\partial u_i'/\partial x_j)^2\rangle$ (Schlichting & Gersten 2006) was investigated. A comparison of the pseudo dissipation $\epsilon_p$ with the dissipation $\epsilon$, both taken from the LES, shows only marginal differences. Therefore, a detailed discussion of the complete $\epsilon_p$ is omitted here. Nevertheless, the structure of $\epsilon_p$ allows us to decompose the pseudo dissipation into dissipation by the streamwise fluctuations $\epsilon_{p,u} = \nu\langle(\partial u'/\partial x_j)^2\rangle$, the spanwise fluctuations $\epsilon_{p,v} = \nu\langle(\partial v'/\partial x_j)^2\rangle$ and the vertical fluctuations $\epsilon_{p,w} = \nu\langle(\partial w'/\partial x_j)^2\rangle$. The resulting distributions are shown in figure 19.

In the region of the main vortex V1, the single components of $\epsilon_p$ look almost the same. This is true for the distributions as well as the amplitudes and suggests that the small-scale turbulence is isotropic here. Along the bottom wall, $\epsilon_{p,u}$ is the dominant contributor to the pseudo dissipation. This is especially true for the deceleration zone of the wall jet, where $\epsilon_{p,u}$ reaches its maximum of up to $\epsilon_{p,u}D/u_b^3 = 0.035$. Further splitting of $\epsilon_{p,u}$ reveals $\langle(\partial u'/\partial z)^2\rangle$ to be the main contributor here, while the other two contributions $\langle(\partial u'/\partial x)^2\rangle$ and $\langle(\partial u'/\partial y)^2\rangle$ are almost zero. This indicates that a vertical flapping of the wall jet is the main source of turbulent dissipation (and fluctuations) in this region.

Along the flow-facing edge of the cylinder, $\epsilon_{p,w}$ dominates the pseudo dissipation. There is a thin layer of large $\epsilon_{p,w}$ along the cylinder front, stretching into the region covered by V3. Nevertheless, for $z < 0.07D$, $\epsilon_{p,u}$ and $\epsilon_{p,v}$ also give significant contributions.

The maximum levels of dissipation reached in the horseshoe vortex are considerably lower than what a macroscale estimation $\epsilon_{macro} = u_b^3/D$ (Pope 2011) gives. Estimation of the Kolmogorov length scale $\eta_K = (\nu^3/\epsilon)^{1/4}$ (Pope 2011) in the core of the horseshoe vortex based on $\epsilon_{macro}$ gives $\eta_{K,macro} \approx D/2800$. Insertion of the PIV measurement $\epsilon_{PIV}$ gives $\eta_{K,PIV} \approx D/1600$, and the dissipation taken from the LES results in a Kolmogorov length scale of $\eta_{K,LES} \approx D/1500$. Using the estimation of Pope (2011) for the required grid resolution in a direct numerical simulation (DNS), $\Delta x_i \lesssim 2\eta_K$, we can conclude that our wall-normal grid resolution would be sufficient for a DNS. On the other hand, our horizontal resolutions are marginally too coarse, which is consistent with a noticeable fraction of modelled dissipation.

### 6.5. *Turbulent transport of turbulent kinetic energy*

In non-equilibrium flow situations such as the considered one, the turbulent kinetic energy needs to be redistributed in space by the convection by the mean velocity

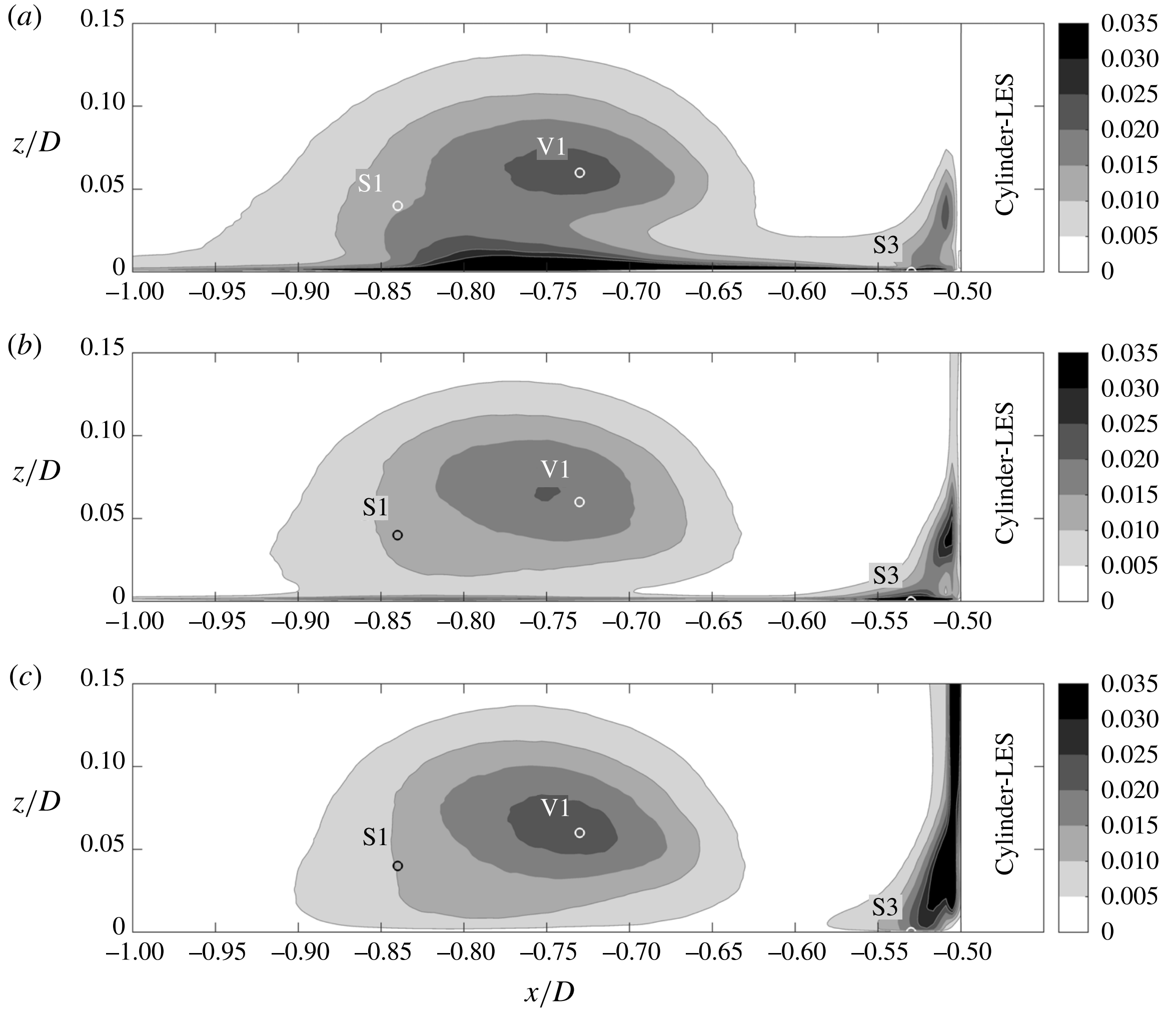

FIGURE 19. Components of the pseudo dissipation in the symmetry plane in front of the cylinder: $\epsilon_{p,u}D/u_b^3$ in the streamwise ($a$), $\epsilon_{p,v}D/u_b^3$ in the spanwise ($b$) and $\epsilon_{p,w}D/u_b^3$ in the vertical direction ($c$), taken from the LES.

field $C$ (6.2) and the turbulent transport terms, namely the turbulent convection $T_{conv}$, the pressure transport $T_{pres}$ and the viscous diffusion $T_{visc}$ (6.3)–(6.5). This subsection concentrates on the turbulent transport mechanisms. The convection by the mean mainly documents whether the turbulent kinetic energy was increasing (negative convection) or decreasing (positive convection) along a streamline. We omit a discussion of its spatial distribution, just pointing out that the main increase of turbulent kinetic energy along a streamline occurs in the deceleration region of the jet under the horseshoe vortex where the streamwise fluctuations are produced. The viscous diffusion term has a significantly smaller amplitude than the other redistribution terms. We therefore omit its discussion as well.

Figure 20 illustrates the turbulent transport terms from LES. There is no noticeable difference between the full and in-plane turbulent convection in the LES results, which indicates out-of-plane turbulent convection to be insignificant in the symmetry plane in front of the cylinder. The distribution of the turbulent convection $T_{conv}$ (figure 20$a$) is similar to the production term illustrated in figure 15. In regions in which large production of turbulent kinetic energy takes place, we see large negative turbulent convection. There are regions, e.g. close to the wall at $x/D = -0.75$, in which the production rate is nearly balanced by turbulent convection. In these areas,

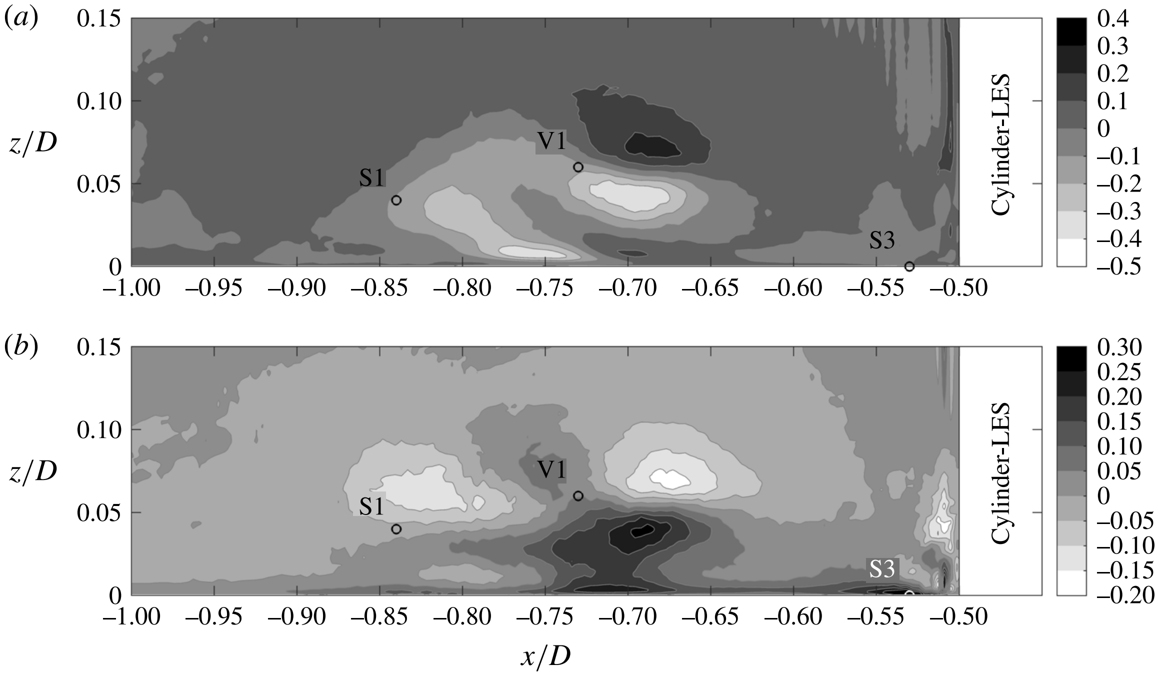

FIGURE 20. Turbulent convection $T_{conv}D/u_b^3$ (*a*) and pressure transport $T_{pres}D/u_b^3$ (*b*) taken from the LES.

the turbulence is characterized by violent eruptions, which might quickly sweep the turbulent fluctuations to another place. This interpretation is in line with what Apsilidis *et al.* (2015) describe when discussing instantaneous flow fields.

The distribution of $\langle p'^2\rangle$ (not shown) implies that the core of the main vortex V1 bounces between $x=-0.78D$ and $x=-0.66D$ due to its bimodality, leading to large pressure fluctuations at these positions. These fluctuations result in the two peaks of large negative $T_{pres}$ in figure 20(*b*), which are located approximately at the upstream and downstream ends of the mentioned range. In addition, there is a peak of positive pressure transport right underneath V1 at $(x, z) \approx (-0.7D, 0.04D)$. This spot has a branch reaching to the bottom plate.

In some regions, the pressure transport has the opposite sign to the turbulent convection and a similar magnitude, $T_{pres} \approx -T_{conv}$. This implies that for a large part of the time, $p' \approx -0.5\rho u_i'u_i'$ (compare (6.3) and (6.4)). This can be observed at approximately $-0.7 < x/D < -0.65$, slightly below and above V1. In these regions, the two terms $T_{conv}$ and $T_{pres}$ seem to cancel each other. We can explain such behaviour by horizontal oscillations of the horseshoe vortex V1. If this vortex is shifted downstream, e.g. from its mean position at $x/D=-0.73$ to approximately $x/D=-0.68$, the vortex core is in a position in which the time-averaged flow has a large negative wall-normal component. The instantaneous vertical velocity in the vortex core is zero, which gives rise to a positive wall-normal fluctuation $w' > 0$. As $u_j'u_j'$ is positive as well, the triple correlation $\langle u_i'u_j'u_j'\rangle$ will obtain a strong positive contribution. As the convective term is the negative gradient of the triple correlation, this situation will give rise to a large negative contribution to $T_{conv}$ under the vortex core and a large positive contribution above the vortex core. It can be assumed that $p' < 0$ in the vortex core, giving rise to a $T_{pres}$ that has the opposite sign to $T_{conv}$.

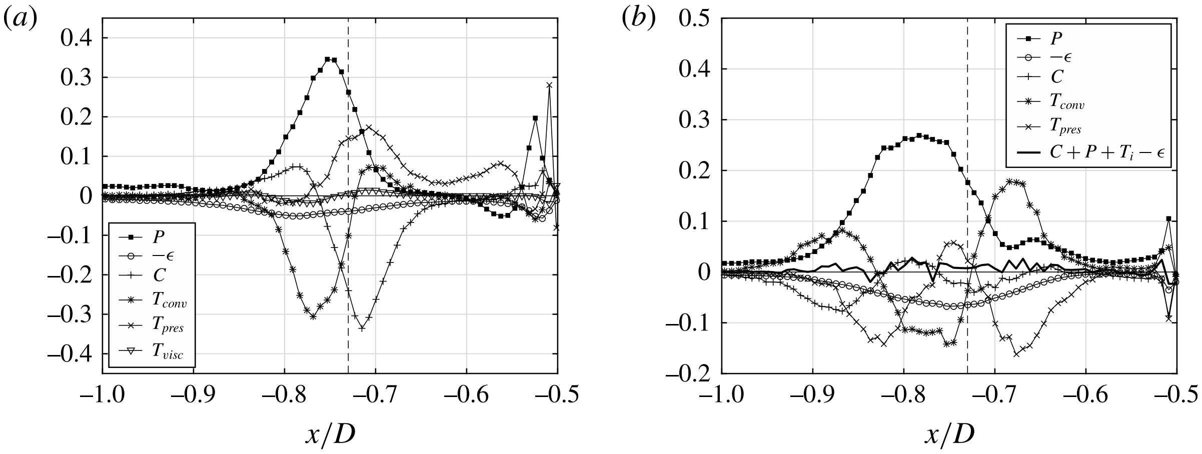

FIGURE 21. The budget of the turbulent kinetic energy in the cylinder front from LES at a wall distance of $z/D = 0.012$ (*a*) and $z/D = 0.065$ (*b*). For reasons of visibility, only every second data point is plotted. The vertical lines indicate the position of V1. All values are normalized by $D/u_b^3$.

### 6.6. *Balance of turbulent kinetic energy*

To further assess the interplay of the previously discussed mechanisms, we discuss the complete balance of turbulent kinetic energy (6.1) along two horizontal lines through the vortex system.

Figure 21(*a*) shows profiles of each term of (6.1) along a horizontal line with a wall distance of $z/D = 0.012$, which is inside the near-wall jet. The distribution along the horizontal line can be divided into four parts. Starting from the cylinder, we first identify the vortex V3, giving rise to large production magnitudes balanced locally in parts by dissipation. Turbulent convection and convection by the mean velocity field also play a role in this region as well as pressure transport.

The zone between V3 and the deceleration of the jet ($-0.55 < x/D < -0.68$) is characterized by nearly zero or even negative production rates. However, we see that the convection by the mean is negative, which means that the turbulent kinetic energy increases along the streamlines. The budget is closed here only if the pressure transport term is included in the balance. This is the only positive term that transports turbulent kinetic energy into the calm zone in front of the cylinder where the downflow turns upstream and accelerates. This pressure transport is balanced by negative production around $x/D = 0.58$ and by mean convection and dissipation further upstream.

When the jet decelerates under the horseshoe vortex, a large amount of production takes place, which has been shown to occur predominantly in the streamwise component. The large negative amplitude of the mean convection term at $x/D \approx 0.72$ indicates that the turbulent kinetic energy rises strongly along the streamlines. This is because the dissipation remains much smaller than the production and the other transport terms remain small or are even positive, such as the pressure transport. Around the peak value of the production term, the mean convection crosses zero, which indicates that this is also the peak of the turbulent kinetic energy. Upstream of this point, the turbulent convection is negative and has larger magnitudes than the production, which leads to a decrease of turbulent kinetic energy along a streamline, as indicated by positive mean convection.

Horizontal profiles of all budget terms at a larger wall distance, $z/D = 0.065$, are shown in figure 21(*b*). This is the wall distance of the vortex core V1. As in the

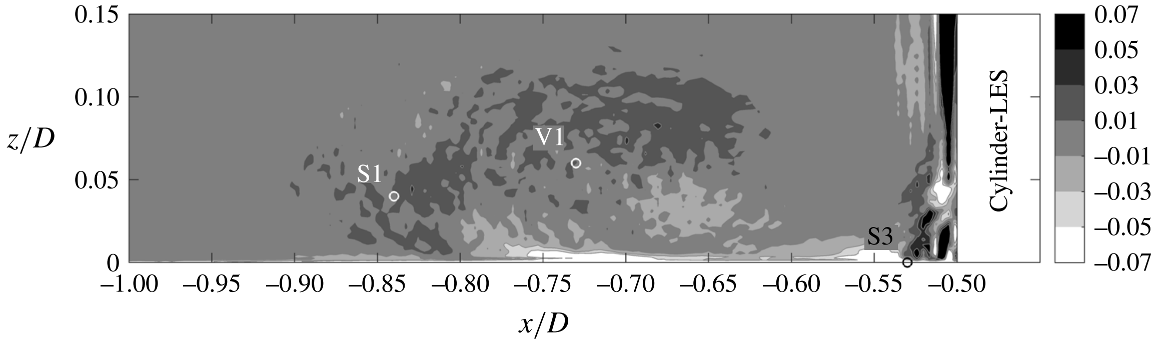

FIGURE 22. The budget residual $RD/u_b^3$ in the cylinder front taken from the LES.

near-wall profiles, there are four regions in which the behaviour of the budget terms differs. On moving upstream from the cylinder, there is the near-cylinder downflow in which locally turbulent kinetic energy is produced. Unfortunately, this layer is not well resolved by the LES and the values do not seem realistic, which is underlined by a large residual of the budget in the wall-nearest point.

Moving upstream from the cylinder in the region $x/D > -0.65$, we see small values of all budget terms. This is the downflow region. However, at $x/D < -0.65$, there is a sudden rise in the levels of turbulent convection and pressure transport. This is the zone in which the turbulent convection approximately balances the pressure transport. We conjecture that this behaviour could be explained by a periodical horizontal displacement of the horseshoe vortex V1 to locations around $x/D = -0.68$.

The production of turbulent kinetic energy has a broad peak slightly upstream of V1. The production is mainly balanced by dissipation and turbulent convection in this zone ($x/D \approx -0.8$). Turbulent convection seems to bring turbulent kinetic energy upstream and downstream from the production peak. Upstream of the production peak, the turbulent convection is positive and adds to the production, while both together seem to be balanced by the mean convection and small but noticeable dissipation.

The budget evaluated by the LES including all terms of (6.1) sums up to zero in a satisfying way (figure 22). In the large grey regions in figure 22, the amplitude of the budget residual $R$ is $|R| = |C + T_{conv} + T_{pres} + T_{visc} + P - \epsilon| < 0.01u_b^3/D$. Regions coloured by slightly lighter or slightly darker grey indicate $|R|D/u_b^3 < 0.03$, which remains below 10 % of the production term. Small spots close to the cylinder front and along the bottom plate show values of $|R|D/u_b^3 < 0.3$. We suspect that the reason for these large errors along the cylinder front is the grid resolution in the horizontal direction, which is four times larger than the vertical one. Thus, the boundary layer along the cylinder cannot be considered to be wall-resolved, resulting in inaccuracies in this limited region. Furthermore, subgrid contributors are not included in the evaluation of the discussed terms except for the dissipation. As figure 5 implies, the contribution of the subgrid stresses is considerable in narrow regions around vortex V3. This further explains the large residual here.

Large errors along the bottom plate in the first line appear where the amplitude of the turbulent convection $T_{conv}$ is large. The triple correlations necessary to evaluate $T_{conv}$ are sensitive to statistical errors and need a large number of samples to converge. Thus, statistics that are not fully converged might be a reason for this large error amplitude here as well. The fact that the residual has positive and negative values is an indication that the level of dissipation predicted by the LES is realistic. As the out-of-plane terms and the pressure transport are missing in the PIV data, we did not make any attempt to compute the total balance for the PIV data.

## 7. Conclusions

The flow field and turbulence structure in front of a wall-mounted circular cylinder were investigated by a combined numerical and experimental study. Special care was devoted to the accordance of the inflow, which consisted of a fully developed turbulent open-channel flow. In the experiment, we applied PIV to measure two-dimensional flow fields in the symmetry plane in front of the cylinder. In the LES, the grid resolution around the cylinder was such that the subgrid stresses played a minor role. We observed a good accordance between the experimental and numerical flow statistics, which gives a high level of fidelity in the generated database. This allowed us to compute all terms of the budget of the turbulent kinetic energy and to link our observations to topological features of the time-averaged and instantaneous flow fields around the horseshoe vortex system. The overall error amplitude of the budget of the turbulent kinetic energy was small for the LES results, which demonstrates the reliability of the conclusions based on the presented data.

We observed two vortices in the time-averaged flow field in the symmetry plane in front of the cylinder, namely the main horseshoe vortex and a corner vortex. Our single-pixel evaluation even suggested a very small vortex between the corner vortex and the cylinder/wall junction. The flow pattern at the bottom plate was compatible with the one reported by Devenport & Simpson (1990). The vortex topology in the symmetry plane as reported by Apsilidis *et al.* (2015) is slightly different from ours. The first point of flow reversal upstream of the cylinder is a separation point in their measurements while it is a stagnation point in our results, which appears as a sink in the symmetry plane. This observation was made in both experiment and simulation, and represents a discrepancy with the commonly used term ‘separation point’ for this point of flow reversal. At the current state of investigation, the reason of this discrepancy is unknown. From our point of view, the most probable explanation is the different state of the incoming boundary layer, which might have an influence on the way in which the flow reverses in front of the cylinder.

The main horseshoe vortex can undergo large variations in position, which can be linked to bimodal velocity distributions in certain areas around the horseshoe vortex, as observed by Devenport & Simpson (1990). The spatial oscillations of the horseshoe vortex are mainly in the horizontal direction, as already observed by Apsilidis *et al.* (2015). This can also be inferred from the fact that the oscillations of the horseshoe vortex mainly induce fluctuations in the vertical velocity component around the vortex core.

The vortex system in the time-averaged flow bears a distinct pattern of flow acceleration and deceleration. Under the main horseshoe vortex, an upstream-directed jet forms due to the deflection of fluid at the bottom plate. The acceleration/deceleration pattern of fluid inside this jet acts on the production of turbulent kinetic energy. The negative production term in the accelerated zone explains the occurrence of a calm region between the horseshoe vortex and the cylinder. This is the region in which the largest wall shear stresses can be observed.

In the deceleration zone of the upstream-directed jet below the horseshoe vortex, the normal stress production of the streamwise component is the main contribution to turbulent kinetic energy production. This production causes the leg of the c-shaped distribution of the turbulent kinetic energy. Besides the bimodal oscillations of the vortex core, the production in the deceleration zone under the horseshoe vortex constitutes the second main production mechanism for turbulent kinetic energy in the horseshoe vortex region.

The spatial distribution of the dissipation of turbulent kinetic energy is similar to that of the turbulent kinetic energy, with two regions of large values, one around the core of the horseshoe vortex and one at the wall below the horseshoe vortex. In the region around the vortex core, the dissipation is nearly isotropic, which indicates an isotropic state of the small scales in this region. The intense dissipation near the wall is anisotropic and is dominated by fluctuations of the vertical gradient of the streamwise velocity component. This indicates a flapping of the wall shear layer at locations between the horseshoe vortex V1 and the stagnation point S1. The dissipation reaches values below 10 % of its macroscale estimation and approximately 15 %–20 % of the production of turbulent kinetic energy. This disequilibrium is settled by turbulent transport, pressure transport and convection by the mean flow field.

Turbulent transport and pressure transport play a prominent role in the balance of turbulent kinetic energy, which can hardly been modelled without taking these processes into account. The pressure transport is the main source of turbulent kinetic energy in the calm near-wall region between the horseshoe vortex and the cylinder. It initiates the increase of turbulent kinetic energy in the decelerated region of the upstream-directed wall jet under the horseshoe vortex and can be regarded as an important agent determining the level of turbulent kinetic energy and its production there. Downstream of the horseshoe vortex, the pressure transport balances the turbulent transport of turbulent kinetic energy. This implies that the instantaneous pressure fluctuations could be expressed as the negative of the instantaneous kinetic energy of the fluctuations. We explain this by downstream excursions of the horseshoe vortex.

The wall shear stress in front of the cylinder is one of the most important flow quantities for applications. Prediction of the development of scour holes around bridge piers requires knowledge of the wall shear stress (e.g. Roulund *et al.* 2005). We found in both experiment and simulation that the wall shear stress reaches three times the value of the undisturbed flow in the symmetry plane in front of the cylinder, which is larger than previously published results (Melville & Raudkivi 1977; Dargahi 1989). Estimation of these large stresses from either measurements or simulations requires a very fine resolution in the wall-normal direction. There have been attempts to model the wall shear stress from velocity or turbulent shear stress measurements at larger wall distances (e.g. Graf & Istiarto 2002; Dey & Raikar 2007; Unger & Hager 2007; Kumar & Kothyari 2011; Pfleger 2011), relying on classical boundary layer relations such as the law of the wall. However, it has been shown that different approaches lead to large scatter in estimated wall shear stresses (Graf & Istiarto 2002). Our results demonstrate that there is little hope of modelling the wall shear stress in front of the cylinder by classical wall functions or turbulent shear stresses, as the dynamics of the wall layer at the maximum wall shear stress is not governed by classical boundary layer dynamics, and Reynolds shear stresses do not have a relation to the wall stress. From the low level of turbulent kinetic energy in the region of the maximum wall shear stress, we conjecture that it is more related to the downflow in front of the cylinder.

## Acknowledgements

The authors gratefully acknowledge the financial support of the DFG under grant no. MA2062/11. Computing time was granted by the Leibniz Computing Centre (LRZ) of the Bavarian Academy of Sciences. We would also like to mention helpful discussions with Professor C. Kähler in the framework of PIV.

## REFERENCES

Apsilidis, N., Diplas, P., Dancey, C. L. & Bouratsis, P. 2015 Time-resolved flow dynamics and Reynolds number effects at a wall–cylinder junction. *J. Fluid Mech.* **776**, 475–511.

Apsilidis, N., Khosronejad, A., Sotiropoulos, F., Dancey, C. L. & Diplas, P. 2012 Physical and numerical modeling of the turbulent flow field upstream of a bridge pier. In *International Conference on Scour and Erosion 6, Paris*, Ecole des Arts et Metiers - Paris Tech.

Baker, C. J. 1979 The laminar horseshoe vortex. *J. Fluid Mech.* **95**, 347–367.

Bruns, J., Dengel, P. & Fernholz, H. H. 1992 Mean flow and turbulence measurements in an incompressible two-dimensional turbulent boundary layer. Part I: data. *Tech. Rep.*, Herman-Föttinger-Institut für Thermo- und Fluiddynamik, TU Berlin.

Clauser, F. H. 1954 Turbulent boundary layer in adverse pressure gradients. *J. Aero. Sci.* **21**, 91–108.

Dargahi, B. 1989 The turbulent flow field around a circular cylinder. *Exp. Fluids* **8** (1–2), 1–12.

Demuren, A. O. & Rodi, W. 1984 Calculation of turbulence-driven secondary motion in non-circular ducts. *J. Fluid Mech.* **140**, 189–222.

Devenport, W. J. & Simpson, R. L. 1990 Time-dependent and time-averaged turbulence structure near the nose of a wing–body junction. *J. Fluid Mech.* **210**, 23–55.

Dey, S. & Raikar, R. V. 2007 Characteristics of horseshoe vortex in developing scour holes at piers. *J. Hydraul Engng* **133** (4), 399–413.

Escauriaza, C. & Sotiropoulos, F. 2011 Reynolds number effects on the coherent dynamics of the turbulent horseshoe vortex system. *Flow Turbul. Combust.* **86** (2), 231–262.

Fernholz, H. H. & Finley, P. J. 1996 The incompressible zero-pressure-gradient turbulent boundary layer: an assessment of the data. *Prog. Aerosp. Sci.* **32** (4), 245–311.

Graf, W. H. & Istiarto, I. 2002 Flow pattern in the scour hole around a cylinder. *J. Hydraul Res.* **40** (1), 13–20.

Gresho, P. M. & Lee, R. 1981 Don't suppress the wiggles – they're telling you something. *Comput. Fluids* **9**, 223–253.

Kähler, C. J., Scharnowski, S. & Cierpka, C. 2012 On the uncertainty of digital PIV and PTV near walls. *Exp. Fluids* **52** (6), 1641–1656.

Kähler, C. J., Scholz, U. & Ortmanns, J. 2006 Wall-shear-stress and near-wall turbulence measurements up to single pixel resolution by means of long-distance micro-PIV. *Exp. Fluids* **41** (2), 327–341.

Kirkil, G. & Constantinescu, G. 2015 Effects of cylinder Reynolds number on the turbulent horseshoe vortex system and near wake of a surface-mounted circular cylinder. *Phys. Fluids* **27**, 075102.

Kumar, A. & Kothyari, U. C. 2011 Three-dimensional flow characteristics within the scour hole around circular uniform and compound piers. *J. Hydraul Engng* **138** (5), 420–429.

Lilly, D. K. 1967 The representation of small-scale turbulence in numerical simulation experiments. In *Proceedings of the IBM Scientific Computing Symposium on Environmental Sciences, IBM Form No. 320–1951*, pp. 195–210. IBM Data Processing Division.

Manhart, M. 2004 A zonal grid algorithm for DNS of turbulent boundary layers. *Comput. Fluids* **33** (3), 435–461.

Melville, B. W. & Raudkivi, A. J. 1977 Flow characteristics in local scour at bridge piers. *J. Hydraul. Res.* **15** (4), 373–380.

Nezu, I. & Nakagawa, H. 1993 *Turbulence in Open-Channel Flows*. A.A. Balkema.

Nicoud, F. & Ducros, F. 1999 Subgrid-scale stress modelling based on the square of the velocity gradient tensor. *Flow Turbul. Combust.* **62** (3), 183–200.

Paik, J., Escauriaza, C. & Sotiropoulos, F. 2007 On the bimodal dynamics of the turbulent horseshoe vortex system in a wing–body junction. *Phys. Fluids* **19**, 045107.

Peller, N. 2010 Numerische Simulation turbulenter Strömungen mit Immersed Boundaries. PhD thesis, Technische Universität München.

Peller, N., Duc, A. L., Tremblay, F. & Manhart, M. 2006 High-order stable interpolations for immersed boundary methods. *Intl J. Numer. Meth. Fluids* **52**, 1175–1193.

PFLEGER, F. 2011 Experimentelle Untersuchung der Auskolkung um einen zylindrischen Brückenpfeiler. PhD thesis, Technische Universität München.

POPE, S. B. 2011 *Turbulent Flows*. Cambridge University Press.

RAFFEL, M., WILLERT, C., WERELEY, S. & KOMPENHANS, J. 2007 *Particle Image Velocimetry – A Practical Guide*, 2nd edn. Springer.

ROULUND, A., SUMER, B. M., FREDSOE, J. & MICHELSEN, J. 2005 Numerical and experimental investigation of flow and scour around a circular pile. *J. Fluid Mech.* **534**, 351–401.

RYU, S., EMORY, M., IACCARINO, G., CAMPOS, A. & DURAISAMY, K. 2016 Large-eddy simulation of a wing–body junction flow. *AIAA J.* **54** (3), 793–804.

SCHANDERL, W. & MANHART, M. 2015 Non-equilibrium near wall velocity profiles in the flow around a cylinder mounted on a flat plate. In *15th European Turbulence Conference*, TU Delft.

SCHANDERL, W. & MANHART, M. 2016 Reliability of wall shear stress estimations of the flow around a wall-mounted cylinder. *Comput. Fluids* **128**, 16–29.

SCHLICHTING, H. & GERSTEN, K. 2006 *Boundary Layer Theory*. Springer.

SIMPSON, R. L. 2001 Junction flows. *Annu. Rev. Fluid Mech.* **33**, 415–443.

STROBL, C., JENSSEN, U. & MANHART, M. 2016 Reconstructing velocity statistics from single pixel ensemble correlation PIV. *Exp. Fluids* (submitted).

TANAKA, T. & EATON, J. K. 2007 A correction method for measuring turbulence kinetic energy dissipation rate by PIV. *Exp. Fluids* **42** (6), 893–902.

UNGER, J. & HAGER, W. H. 2007 Down-flow and horseshoe vortex characteristics of sediment embedded bridge piers. *Exp. Fluids* **42**, 1–19.

WERNER, H. 1991 Grobstruktursimulation der turbulenten Strömung über eine querliegende Rippe in einem Plattenkanal bei hoher Reynoldszahl. PhD thesis, Technische Universität München.

WESTERWEEL, J., GEELHOED, P. F. & LINDKEN, R. 2004 Single-pixel resolution ensemble correlation for micro-PIV applications. *Exp. Fluids* **37** (3), 375–384.

# C. Appendix: Publication 3, summarised in chapter 8

Flow Turbulence Combust
https://doi.org/10.1007/s10494-017-9865-3

# Near-Wall Stress Balance in Front of a Wall-Mounted Cylinder

**Wolfgang Schanderl**[1] · **Ulrich Jenssen**[1] ·
**Michael Manhart**[1]

Received: 20 March 2017 / Accepted: 7 October 2017

**Abstract** The stress balance in the near-wall flow in front of a cylinder mounted on a flat plate at moderate Reynolds number is investigated by applying highly resolved Large-Eddy Simulation (LES). The flow around wall-mounted bluff bodies is subject of research due to its wide relevance for engineering applications. However, the structure of the vortex system in front of such a bluff body is complex, bears strong velocity and pressure gradients in each spatial direction and has rich dynamics. Furthermore, the vortex system is located close to the investigated flat bottom wall (Dargahi, Exp. Fluids **8**(1-2):1–12, 1989; Devenport and Simpson, J. Fluid Mech. **210**:23–55, 1990). Thus, classical models for the treatment of the near-wall flow based on the logarithmic law of the wall or a power law cannot be expected to suffice in such kind of flow (Pope 2011). This paper assesses which contributors to the stress balance have significant influence on the balances residual and thus have to be considered by an approach to model the investigated near-wall flow. To do so, the momentum equation in streamwise direction is integrated in wall-normal direction and applied to the results gained from the LES. The evaluation of the stress balance along four selected wall-normal profiles indicates that the significance of each single term depends on where the profile is located. Outside the viscous layer, no term except the viscous stresses can be neglected in general. The amplitude of the pressure gradient as well as horizontal gradients of mean and fluctuating velocity are multiples of the estimated wall shear stress. Wall models not including a spatial approach are therefore most likely to fail in such kind of flow.

**Keywords** Large-eddy simulation · Stress balance · Near-wall modelling · Wall-mounted bluff-body

---

✉ Michael Manhart
michael.manhart@tum.de

[1] Professorship for Hydromechanics, Technical University of Munich, Arcisstr. 21,
D-80333 Munich, Germany

## 1 Introduction

Even in simple geometries turbulent flows can result in complex flow structures. The flow around a wall-mounted bluff body is one of these cases. The geometry is easy to describe, however, the flow topology in front of the body is complex and bears rich dynamics. The main feature of this flow is the occurrence of a horseshoe vortex in front of the body. Devenport and Simpson [1] were the first to show that the horseshoe vortex system undergoes strong oscillations in space that lead to bi-modal velocity distributions in the region of the vortex system and close to the wall. A number of subsequent publications were able to document this flow behaviour in various configurations, e.g. [2–5]. When it comes to bluff bodies of finite height, the formation of tip vortices around the free end of the body further enhances the complexity of the flow [6]. Palau-Salvador et al. [7] as well as Krajnović [8] descriptively explain the complex interplay between the horseshoe vortex, the tip vortices at the free end and the flow in the wake of the body. The large interest in this kind of flow is driven by unwanted effects of the vortex formation in various technical applications, such as wing-body junction or turbomachinery blades. Our interest is focused on the interdependence of the flow structure close to the bottom wall and the local wall shear stress enhancement around bridge structures which can cause the development of local scour [9].

The prediction of the scour development by numerical means requires the understanding of some highly complex physical phenomena and processes, such as the flow field and its interaction with the sediment. At the very beginning of the modelling chain, the flow field stands together with induced wall shear stresses. If the forces on the bed (or wall) cannot be predicted reliably, all following modelling steps are affected by more or less severe bias and need calibration. The main problem in determining the wall shear stress numerically around a real configuration is the complexity of the flow field which inhibits the use of Reynolds averaged approaches but inevitably demands eddy resolving simulation methods and a high data resolution in the near-wall region. The highly charged nature of this issue becomes clear when reviewing the literature on the flow around wall-mounted cylinders published in the last decades. Dargahi [10] conducted an experiment of the flow around a circular cylinder mounted in a flume at moderate Reynolds number. He estimated the wall shear stress distribution in the symmetry plane in front of the cylinder, which was reproduced and used for validation by subsequent numerical studies, e.g. [3, 11–13]. However, Schanderl and Manhart [14] demonstrated recently that Dargahi [10] in fact underestimated the amplitude of the wall shear stress by a factor of approximately two. This was confirmed by an experimental study [15]. Due to limited experimental resolution, Dargahi [10] was not able to measure the velocity close enough to the wall. Roulund et al. [16] conducted both experiment and simulation of a similar setup at a larger but still moderate Reynolds number. They measured the wall shear stress with a hot wire probe. It is not surprising that their Reynolds averaged simulation significantly underestimates the amplitude of the wall shear stress below the horseshoe vortex.

There are various approaches to reduce the required near-wall data resolution by modelling the flow in close vicinity of the wall. Classical wall models avoid resolving the viscous layer and bridge the distance between wall and first grid point by assuming the wall normal velocity to be zero and the wall parallel velocity to follow the logarithmic law of the wall [17], a power law [18] or a modification of these laws. However, these models have to fail in complex flow where the assumptions made cannot hold [19, 20]. As descriptively discussed by Knopp et al. [21], there is not even an agreement on what happens to the law of the wall as soon as there is a mild adverse pressure gradient. Does the law of the wall hold? Does it suffice to modify it's constants? Does it break down? Knopp et al. [21] name a limited data base documented in literature as one of the main reasons for this missing agreement.

Balaras et al. [22] suggested a more sophisticated approach for Large-Eddy Simulation. Between the wall and the first grid point, they solve a simplified set of equations which describe the wall-parallel velocity by two dimensional boundary layer equations. The wall-normal velocity component is then estimated from mass conservation. Balaras et al. [22] report satisfying results for relative simple flow cases.[1] However, representing the near-wall flow with the boundary layer equations requires the boundary layer assumptions (small gradients in wall-parallel direction) to be satisfied in this near-wall flow [23]. This is at least questionable in the complex flow situation in front of a wall-mounted bluff body. Thus, approaches as the ones based on the boundary layer equations struggle to predict the near-wall region of complex flow, especially in presence of an adverse pressure gradient [24].

It shall be mentioned that not only numerical but also experimental attempts were made to estimate the wall shear stress around a cylinder in a scour geometry without resolving the viscous layer. To counteract the low data resolution some studies [25, 26] applied measured Reynolds shear stresses to estimate the wall shear stress. Melville and Raudkivi [27] calibrated their wall shear stress estimation around the cylinder with the slope of the logarithmic velocity profile of the approach flow. However, due to a lack of reliably comparative data, an error estimation of such wall shear stress estimations is hardly possible.

The frequent underestimation of the wall shear stress by the numerical studies rises two issues. First, the computational resources demanded to achieve the necessary wall resolution still can hardly be afforded for a sizable number of specific flow cases. Second, the models applied in the near wall region are not able to capture the flow in a satisfying way.

Our aim is to contribute to wall-modelling of complex, three dimensional flow by investigating the near-wall flow in front of a circular cylinder mounted on a flat plate by a wall-resolved Large-Eddy Simulation (LES) at moderate Reynolds number. The stress balance in the streamwise direction is derived by integrating the momentum balance in the wall-normal (vertical) direction. We assess the relative magnitude of each term as obtained by our LES.

The questions we address in this paper are: Which stresses have a significant contribution to the stress balance in the near-wall flow in front of a wall-mounted cylinder? Which stresses thus have to be considered in a general approach for describing this near-wall flow as well as for wall shear stress modelling? And which requirements do arise from this for a numerical simulation?

The paper is structured as follows: The computational configuration and the investigated setup is presented in Section 2, including an estimation of the influence of the subgrid stress model (Section 2.3). Second, the flow topology in front of the cylinder and the convergence of the results over grid refinement is discussed in Section 3. In Section 4 the stress balance is discussed. Each contributor to this balance is evaluated at four selected positions in the cylinder front (Section 4.1). Finally, the relevance of these contributors for the stress balances residual and for a possible reconstruction of the wall shear stress is discussed in detail (Section 4.2).

---

[1] Balaras et al. [22] investigated a plane channel flow, flow through a square duct and a rotating channel.

## 2 Computational Configuration

The computational configuration is presented briefly in the following. The flow solver (Section 2.1) and the applied grid (Section 2.2) are described first. Since this study focuses on the stress balance, the influence and a possible biasing of the applied subgrid stress model on the stress balance are discussed afterward in Section 2.3. The associated grid study is exemplified in Section 3, where the flow topology is described.

The reliability of the presented LES is discussed in detail by Schanderl and Manhart [14]. A further validation of the LES is provided by the comparison to an associated experiment of the same setup by Jenssen et al. [28]. It shall be mentioned that the simulated flow topology as well as its second and third order moments are in satisfying agreement with the measurements from that experiment [15, 28].

### 2.1 Numerical method

The in-house code MGLET [29] was applied to conduct the LES. It is a Finite Volume code based on a Cartesian grid and staggered arrangement of the variables. A central difference scheme is applied for spatial approximation and a third order Runge-Kutta method for the time integration. The curved surface of the body is represented by a conservative Immersed Boundary Method [30, 31]. Zonal grids allow for a local grid refinement in the critical flow regions [32]. Both the code and the Immersed Boundary Method are of second order spatial accuracy [30, 32].

The subgrid stresses (SGS) are modelled by the Wall-Adapting Local Eddy-Viscosity (WALE) model [33] in which the turbulent viscosity $\nu_t$ is defined as

$$\nu_t = C_w \overline{\Delta}^2 \frac{\left(S^d_{ij} S^d_{ij}\right)^{3/2}}{\left(\overline{S}_{ij}\overline{S}_{ij}\right)^{5/2} + \left(S^d_{ij} S^d_{ij}\right)^{5/4}} \tag{1}$$

where, $C_w = 0.1$ and

$$S^d_{ij} = \frac{1}{2}\left(\overline{g}^2_{ij} + \overline{g}^2_{ji}\right) - \frac{1}{3}\delta_{ij}\overline{g}^2_{kk} \quad . \tag{2}$$

with $\overline{g}_{ij} = \partial u_i / \partial x_j$. In the WALE model, the turbulent viscosity decreases naturally towards the wall with the correct limiting behaviour of $\nu_t \propto y^3$. Thus, no damping function has to be applied. In the presented configuration, both the turbulent viscosity as well as the modelled stresses decrease quadratically with grid refinement [14]. The code MGLET has been used and validated in various configurations for both LES and DNS, e.g. [32, 34–36].

After the simulation had reached a statistically steady-state, statistics were gathered over a time of $T \approx 700 D/u_b$ where $D$ is the cylinder diameter and $u_b$ the depth averaged bulk velocity in the symmetry plane of the incoming flow. For the simulation with the finest grid (LES #3, see Section 2.2) this took $\approx 2 * 10^6$ cpu hours. For the LES with the finest grid the size of the time steps was $\Delta T \approx 5.34 * 10^{-4} D/u_b$. This time stepping results in a Courant-Friedrichs-Lewy number of $0.55 < CFL_{max} < 0.82$.

### 2.2 Domain and grid

The computational domain is sketched in Fig. 1. To keep similarity to the associated experiment [15, 28], which is conducted in a flume, bottom and side walls of the $11.7D$ wide domain are defined as no-slip condition. $D$ is the cylinder diameter. The free surface is modelled by a slip condition, which suppresses all surface deformation. This corresponds

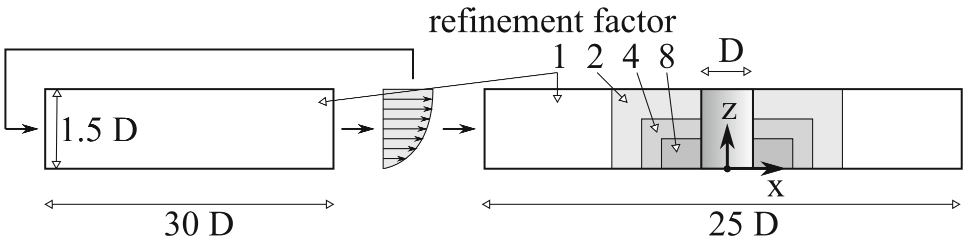

**Fig. 1** Sketch of the computational domain used for the LES

to the limiting case of zero Froude number. The computational grid consists of two major parts: a precursor grid and a base grid containing the cylinder. The first uses periodic boundary conditions in the streamwise direction to simulate a fully developed turbulent open-channel flow with a flow depth of $H = 1.5D$. The Reynolds number is $Re_D = 39000$ and $Re_\theta = 5570$ based on the incoming bulk velocity $u_b$ and the cylinder diameter $D$ and the momentum thickness $\theta$ of the incoming flow, respectively. The precursor is one-way coupled to the base grid in such a way that instantaneous flow profiles are set as inflow condition in the base grid. It was applied in respect of the strong influence of the incoming flow on the vortex system around the cylinder [14]. A comparison to open-channel flows documented in literature [37] and the associated experiment [15, 28] indicates the approach flow to be a good representative of an open-channel flow at the corresponding Reynolds number.

In the region of interest around the cylinder the grid is refined by locally embedded grids [32]. The locations of the embedded grids are indicated in Fig. 1 by grey color. Each local grid refines the grid spacing by a factor of two. To investigate the grid dependency of the flow, three simulations have been conducted. All simulations hold precursor and base grid but differ in the number of locally embedded grids: LES #1 holds one local grid (grid 1), LES #2 two (grid 1+2) and LES #3 three grids (grid 1+2+3). In overlapping regions, the grid spacing of the finer grid is respected. The grid resolution of each grid is listed in Table 1. LES #3 indicates the solution to be converged with respect to the grid resolution. The grid study is exemplified in Section 3.2. In addition to the local refinement, the grid is compressed towards the bottom wall by a compression factor smaller than 1.01. However, since this refinement factor is applied on the precursor and the base grid solely, only every eighth cell is stretched in grid 3.

The resolution of the finest grid is $\Delta x^+ = \Delta y^+ \approx 7.8$ in horizontal and $\Delta z^+ \approx 1.9$ in vertical direction. The wall nearest data point of the wall-parallel velocity is thus evaluated at a wall distance of $z^+ \approx 0.95$. Note that these wall units are based on the wall shear stress in the undisturbed region of the precursor, not on the local one. The grid is fine enough

**Table 1** Grid resolution of precursor, base grid and locally embedded grids applied in the presented LES. Inner units refer to the wall shear stress of the undisturbed flow in the symmetry plane in the precursor

| Grid | Refinement factor | Cells per diameter horizontal/vertical | Grid spacing $\Delta x^+/\Delta y^+/\Delta z^+_{wall}$ | Grid points |
|---|---|---|---|---|
| precursor | 1 | | 60/60/15 | $44 \cdot 10^6$ |
| base | 1 | 31.25/125 | 60/60/15 | $35 \cdot 10^6$ |
| grid 1 | 2 | 62.5/250 | 30/30/7.5 | $80 \cdot 10^6$ |
| grid 2 | 4 | 125/500 | 15/15/3.7 | $64 \cdot 10^6$ |
| grid 3 | 8 | 250/1000 | 7.5/7.5/1.9 | $177 \cdot 10^6$ |

**Fig. 2** Contributors to the stress balance on a wall-normal profile at $x = -0.73D$ through the horseshoe vortex. The core of the latter is located at $z^+ \approx 140$. The data is taken from LES #3. Inner units refer to the local wall shear stress

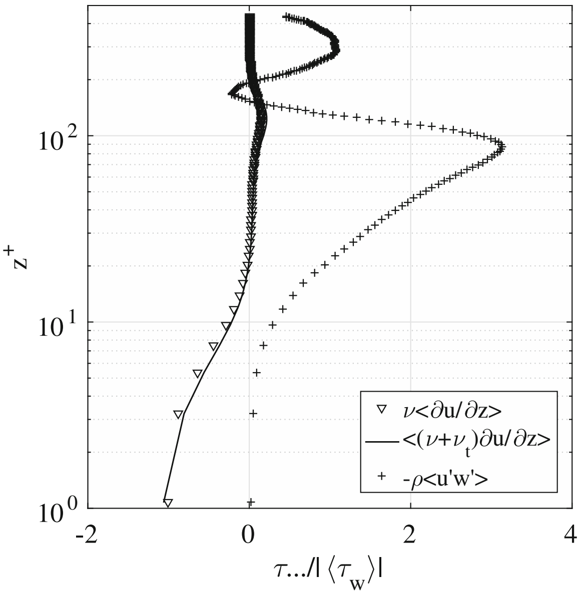

to resolve the viscous sublayer, see Section 3.2. The resulting number of grid points per diameter and the total number of grid points are given in Table 1. As the discussion of the dissipation rate of turbulent kinetic energy by Schanderl et al. [15] indicates, the grid spacing corresponds to $\Delta z \approx 1.6\eta_K$ and $\Delta x = \Delta y \approx 6.4\eta_K$. Here $\eta_K$ is the Kolmogorov length scale [20].

### 2.3 Influence of the subgrid stress model

Since this study focuses on the stress balance, the contribution of the subgrid stresses to the stress balance is discussed briefly. In Fig. 2 three contributors to the balance normalized by the time-averaged local wall shear stress $\langle\tau_w\rangle$ are evaluated on a wall-normal profile in the symmetry plane in front of the cylinder. The streamwise position of the profile is $x = -0.73D$, which corresponds to the location of the main horseshoe vortex (Section 3). Evaluated are the viscous stresses neglecting and including modelled stresses $\nu\langle\partial u/\partial z\rangle$ and $\langle(\nu + \nu_t)\partial u/\partial z\rangle$ respectively, as well as a representative of the resolved turbulent stresses $-\rho\langle u'w'\rangle$. Here $\langle\rangle$ is the operator for time-averaging. $u_i'$ is the fluctuation of the corresponding velocity $u_i = \langle u_i\rangle + u_i'$. $\nu_t$ is the turbulent viscosity modelled by the WALE model. $u$ is the velocity component in the streamwise ($x$-) direction, $z$ is the wall-normal coordinate. In the wall-normal direction, the profile covers a distance of $\approx 0.2D$ in outer scaling. The core of the vortex is located at $z = 0.06D$ and $z^+ \approx 140$ respectively. The wall units are based on the local wall shear stress. The evaluated triple indicates the modelled stresses to be of minor relevance for the momentum balance: Close to the wall at $z^+ < 10$, where the viscous stress is largest, the contribution of the modelled stress is small. Further away from the wall at $z^+ \approx 140$, there is a slight deviation between the viscous stresses including and excluding subgrid stresses, which is hardly visible in Fig. 2. However, except directly at the wall the viscous stresses in general are of minor relevance for the stress balance, as the large amplitude of the resolved stresses indicate. A discussion of the complete stress balance in the streamwise direction follows in Section 4.

In the presented LES, the modelled turbulent kinetic energy $k_{SGS}$ is small compared to the resolved one $k$. In wide regions covered by the vortex system, the modelled fraction is $k_{SGS}/k \approx 0.035$, while there are small spots of $k_{SGS}/k \approx 0.15$ directly at the wall/cylinder junction [15]. The modelled dissipation rate of turbulent kinetic energy is approximately one third of the total one [15]. Since the overall influence of the subgrid stress model can be considered small, the simulation is assumed to be independent of possible shortcomings of the SGS model.

## 3 Flow Topology and Turbulence

To get an overview over the flow topology, the vortex system is discussed in Section 3.1. Special attention is paid to the region close to the wall in Section 3.2.

### 3.1 Horseshoe vortex system

Figure 3 shows the time-averaged streamlines in the symmetry plane in front of the cylinder. The flow facing edge of the cylinder is located at $x = -0.5D$. The incoming flow leads to a vertical pressure gradient in the cylinder front. This pressure gradient causes a down-flow, which feeds the so-called horseshoe vortex system at the cylinder-wall junction. The down-flow itself forms a boundary layer along the cylinder wall, separating from the cylinder at stagnation point S4. When reaching the bottom plate, the down-flow splits up. The streamline which separates the fluid going upstream from the fluid going downstream ends at stagnation point S3. A small fraction of the fluid is deflected towards the cylinder and forms the small corner vortex S3 at the junction of the bottom wall and the cylinder. Most of the down-flow is deflected in upstream direction, feeding the main vortex V1 and a jet along the wall underneath V1. In the time-averaged flow field, the fluid which enters the jet is subject to a distinct pattern of acceleration: first it accelerates from the region of stagnation point S3 in upstream direction between $x = -0.53D$ and $x \approx -0.7D$. It decelerates subsequently between $x = -0.7D$ and $x \approx -0.83D$. The jet fans out here. The acceleration and deceleration sequence is an important factor to explain the production of turbulent kinetic energy around the horseshoe vortex [1, 15]. Above this fanning out region, stagnation point S1 separates the main vortex V1 from an recirculation zone further upstream. This recirculation zone is constrained by stagnation point S2.

Devenport and Simpson [1] described how the upstream directed wall jet under the horseshoe vortex switches between two preferential modes. In the backflow mode, the jet has high momentum and penetrates far into the approaching boundary layer. In the zero-flow mode, the wall jet lifts relatively early from the bottom wall and is ejected vertically. The presented LES reproduces this bimodal behavior, which can be shown by the statistics of both velocity and pressure fields [14, 15]. It is nearby to interpret the fanning out of the streamlines

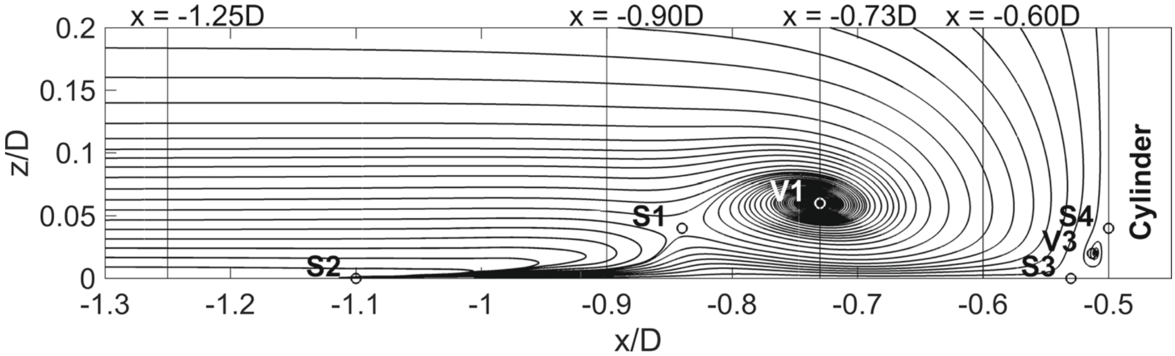

**Fig. 3** Streamlines of the horseshoe vortex system in the symmetry plane in front of the cylinder. The vertical lines indicate the streamwise position of the four selected profiles discussed below

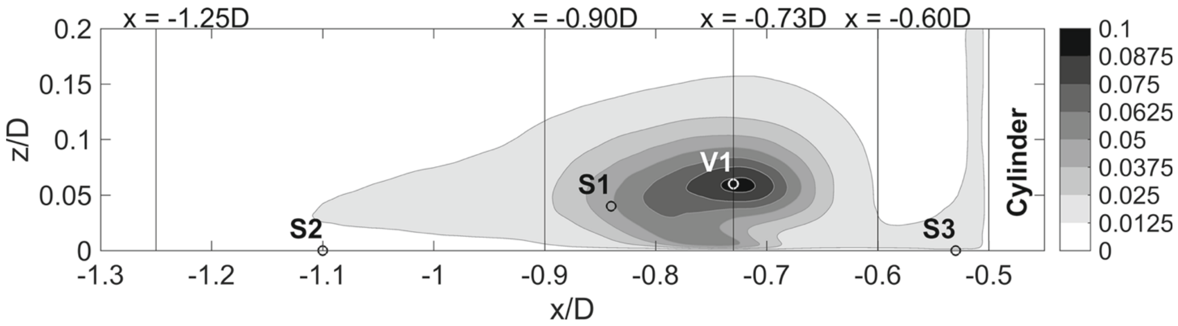

**Fig. 4** Turbulent kinetic energy normalized by the bulk velocity $k/u_b^2$ in the symmetry plane in front of the cylinder

where the wall jet decelerates as the time-averaged representation of the bi-modal dynamics of the horseshoe vortex and the wall jet [1].

Snapshots of instantaneous flow fields reveal hairpin vortices, which originate from the wall under the main vortex and wrap around the latter [15, 38]. Paik et al. [5] argued that these hairpin vortices are a result of centrifugal instabilities of the wall jet under V1. They further state that these hairpin vortices destroy the main vortex V1 and thus cause the bimodal behavior of the vortex system.

The bimodal large scale oscillations of the vortex system cause a characteristic distribution of turbulent kinetic energy $k = 0.5(\langle u'u' \rangle + \langle v'v' \rangle + \langle w'w' \rangle)$, see Fig. 4. Large amplitudes of $k$ resulting from an increased level of vertical Reynolds normal stresses $\langle w'w' \rangle$ can be found in the region of V1. From this peak a region of enhanced turbulent kinetic energy reaches like a leg down towards the bottom wall. This leg is caused by large streamwise Reynolds normal stresses $\langle u'u' \rangle$. As apparent in Fig. 4 the distribution of $k$ forms a typical c-shape, which was described by Paik et al. [5] and confirmed by subsequent studies, e.g. [2, 3].

There is a noticeable region of relatively calm turbulence between the main vortex V1 and the cylinder. Close to the bottom plate around $x \approx -0.6D$ not only the Reynolds normal stresses (Fig. 4) but also the Reynolds shear stress $\langle u'w' \rangle$ have relatively small levels. The latter is plotted in Fig. 5. $\langle u'w' \rangle$ has three positions of enhanced amplitude. Large negative values can be found between the stagnation point S1 and the vortex core of V1, which corresponds to the lower left sector of the main vortex. At the upper right sector enhanced positive values of $\langle u'w' \rangle$ can be observed. Another negative peak is located close to stagnation point S3. The distribution of the Reynolds stress $\langle u'w' \rangle$ is consistent with observations of Devenport and Simpson [1] and Apsilidis et al. [2].

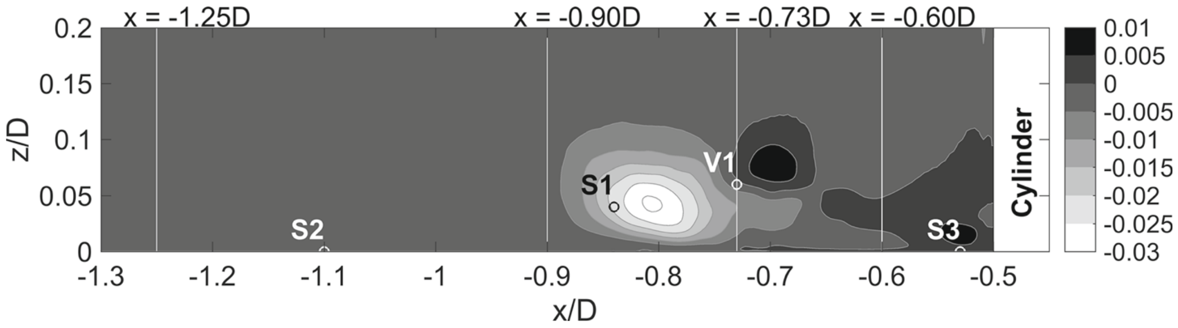

**Fig. 5** Reynolds shear stresses normalized by the bulk velocity $\langle u'w' \rangle/u_b^2$ in the symmetry plane in front of the cylinder

The low levels of turbulence close to the bottom wall between V1 and the cylinder can be explained by the production of turbulent kinetic energy $P = -\langle u_i' u_j' \rangle \partial \langle u_i \rangle / \partial x_j$ [20]. The acceleration of the wall jet in upstream direction gives rise to negative normal stress production $P_{11} = -\langle u' u' \rangle \partial \langle u \rangle / \partial x$, which dominates the total production $P$ at this position [15]. The kinetic energy is transferred from turbulence to the mean flow and thus the turbulence is damped here.

## 3.2 Near-wall flow

The strong pressure gradient at the bottom wall linked to the acceleration of the wall jet becomes apparent in Fig. 6. LES #3 is the simulation with the finest grid, LES #2 the one with the medium grid. The absolute pressure is adjusted in such a way that the pressure coefficient $c_p = \langle p \rangle / (0.5 \rho u_b)$ at the streamwise position $x = -1.5D$ is one in all three simulations. $u_b$ is the bulk velocity in the symmetry plane of the undisturbed incoming flow. The distribution of $c_p$ indicates two flow regimes. Upstream of the position of the main vortex at $x/D = -0.73$ there is a relatively small adverse pressure gradient, and downstream of the main vortex a large adverse pressure gradient can be seen. Both parts are separated by a plateau of constant $c_p$ between $x \approx -0.80D$ and $x \approx -0.75D$. This is in the zone in which the jet fans out (Fig. 3). It is hardly visible in Fig. 6, but $c_p$ in fact exhibits a slight decrease here. $c_p$ in LES #3 reaches its maximum at $x = -0.53D$, which corresponds to the position of stagnation point S3. The small corner vortex V3 and the according positive streamwise velocity at the wall are implied by the decreasing pressure coefficient between S3 and the cylinder at $x = -0.50D$. Considering that the pressure difference between $x \approx -0.73D$ and $x \approx -0.53D$ is approximately sixty percent of the dynamic pressure head of the bulk velocity underlines the change of momentum of the wall jet driven by the pressure gradient.

The differences between the three simulations are small in general. However, it is evident from Fig. 6 that LES #1 and #2 are hardly able to resolve the small corner vortex V3.

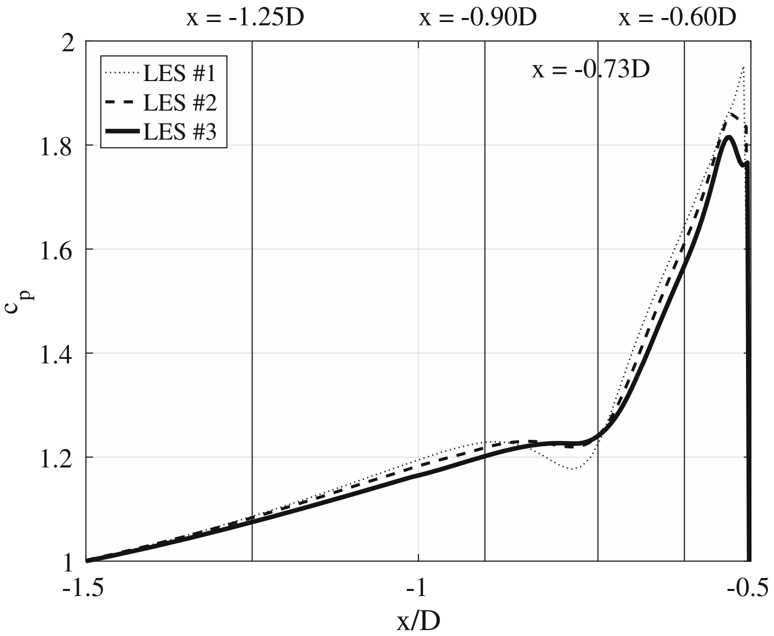

**Fig. 6** Pressure coefficient $c_p$ along the bottom wall in the symmetry plane in the cylinder front taken from LES #1 (coarse grid), LES #2 (medium grid) and LES #3 (fine grid). The pressure coefficient is adjusted such that $c_p = 1$ at $x = -1.5D$ in all simulations

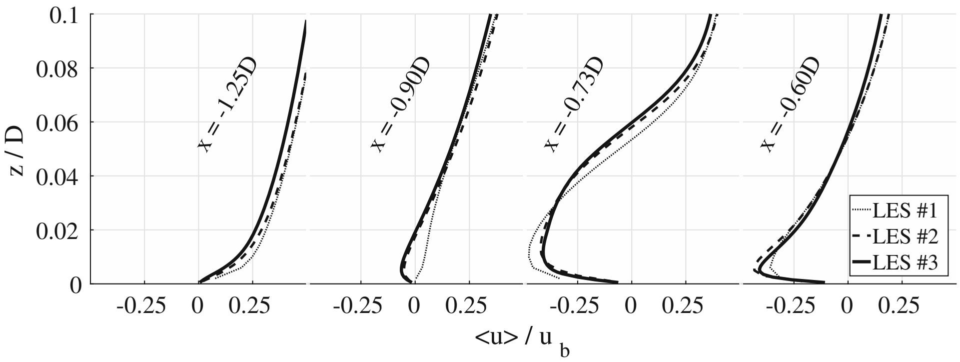

**Fig. 7** Profiles of the streamwise velocity $\langle u \rangle$ at four distinct $x$-positions in the symmetry plane in front of the cylinder. Evaluated are data from LES #1 (coarse grid), LES #2 (medium grid) and LES #3 (fine grid)

The accordance to of the pressure distribution to the one measured by Dargahi [10] is satisfying [14].

In Fig. 7 the time-averaged streamwise velocity $\langle u \rangle$ is evaluated for the three simulations with different grid resolutions. First, the results of the simulation with the finest grid (LES #3) are discussed followed by the influence of the grid resolution.

The profile closest to the cylinder is located at $x = -0.60D$. The upstream directed wall jet described in Section 3.1 is indicated by a narrow peak of negative $\langle u \rangle$ close to the wall. The maximum negative velocity is reached at $\delta_{jet} \approx 0.005D$ above the wall. At this position, the flow in the near-wall region accelerates in upstream direction due to the strong pressure gradient. At $x = -0.73D$, which corresponds to the position of the core of V1, the jet and thus the peak of negative $\langle u \rangle$ significantly expanded in the vertical direction. Furthermore, the peak has slightly lifted off the wall ($\delta_{jet} \approx 0.010D$). Even though the amplitude of $\langle u \rangle$ is approximately the same as at position $x = -0.60D$, the jet decelerates here. The maximum negative velocity of the jet is reached at $x \approx -0.67D$. At both positions $x = -0.60D$ and $x = -0.73D$ the velocity profiles cross zero at a height of $z = 0.06D$, which corresponds to the vertical position of the core of V1.

The profile at $x = -0.90D$ is located upstream of V1 where the jet merges with the recirculation zone located between S1 and S2. The amplitude of $\langle u \rangle$ is significantly smaller. The most upstream position is located at $x = -1.25D$. Here, the approaching flow is not separated yet but already decelerated by the adverse pressure gradient due to the cylinder. This deceleration causes the velocity profile to deviate from the logarithmic law of the wall (which is of course also true for the profiles at the other positions, Fig. 8).

The differences in the velocity profiles of the simulations with different grid resolution are in general small in regions of positive streamwise velocity. However, there are some deviations in the backflow region. LES #1 with the coarsest grid is not able to reproduce the upstream recirculation zone - the flow is not separated yet at $x = -0.90D$. Furthermore, in LES #1 the main vortex V1 is slightly shifted to the upstream and towards the bottom wall. At $x = -0.73D$ LES #1 predicts the position of $\langle u \rangle = 0$ and thus the core of V1 to be closer to the wall than the other simulations. As a result of the shifted topology and/or the coarser grid in general, LES #1 under-predicts the amplitude of $\langle u \rangle$ at $x = -0.60D$ and over-predicts it at $x = -0.73D$. The deviations between LES #2 with the medium grid and LES #3 with the finest grid are significantly smaller than the differences between LES #1 and LES #2. This implies a convergent behavior of the solution with grid refinement.

The velocity profiles discussed above are presented in inner scaling in Fig. 8. Figure 8 allows to draw two conclusions. First, the second grid point from the wall does not lie

**Fig. 8** Velocity profiles in inner scaling at the four selected positions in the symmetry plane in the cylinder front taken from LES #3 (fine grid). The wall units are based on the local wall shear stress

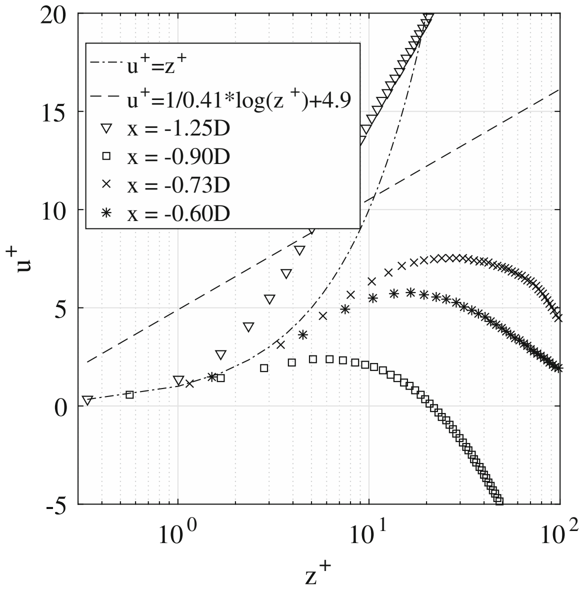

exactly on the theoretical linear velocity profile in any of the investigated profiles. Nevertheless, it is close to the linear profile at all four profiles. This supports our assumption that the first grid point lies in the linear sublayer. Second, none of the profiles is following the logarithmic law of the wall anywhere. At $x = -1.25D$ the momentum of the fluid in the outer region is still large (Fig. 7), however, due to the adverse pressure gradient the wall shear stress has already broken down. The velocity is thus significantly larger than what the logarithmic law would predict for a velocity profile with the corresponding wall shear stress. The flow in the backflow region under the horseshoe vortex at $x = -0.90D$, $x = -0.73D$ and $x = -0.60D$ is subjected to large pressure gradients. Therefore, it is to be expected that the corresponding velocity profiles deviate from the logarithmic law from a certain wall distance on. However, these profiles imply that there is no region in the near-wall layer where the wall jet exhibits a behavior typical for a turbulent boundary layer. An estimation of the wall shear stress based on the logarithmic law of the wall is thus not justified. It should be noted that Fig. 8 does not allow for a general statement regarding the thickness of the viscous layer in inner scaling. Nevertheless, it can be stated that all evaluated velocity profiles deviate from the linear velocity profile approximately between the second and the third grid point above the wall. Since the grid is equidistant, grid points represent the wall distance in outer scaling. This suggests that the thickness of the viscous layer does not scale with the wall shear stress but is determined by the outer flow.

The observations regarding the velocity profiles are in line with those regarding the wall shear stress distribution in the symmetry plane in front of the cylinder (Fig. 9). We plot the friction coefficient $c_f = \langle\tau_w\rangle/(0.5\rho u_b)$, where $\langle\tau_w\rangle$ is the time-averaged local wall shear stress. $\langle\tau_w\rangle$ was estimated by assuming a constant velocity gradient between the wall nearest grid point and the wall. Negative $c_f$ implies backflow. In LES #3 with the finest grid stagnation point S2 (Fig. 3) is indicated by the zero crossing at $x = -1.10D$. The region of relatively weak negative wall shear stress downstream of S2 corresponds to the recirculation zone between S2 and S1. LES #2 exhibits these features, too, while LES #1 fails to represent this weak backflow zone. The wide peak of negative $c_f$ further downstream indicates the large momentum of the wall jet. Both the amplitude and the double peak shape of LES #2 and #3 are matching well. However, LES #1 shows a single peak only and underestimates the amplitude in wide parts of the peak therefore. It should be noted that there is no stagnation point at the bottom plate between the upstream backflow region (due to the upstream

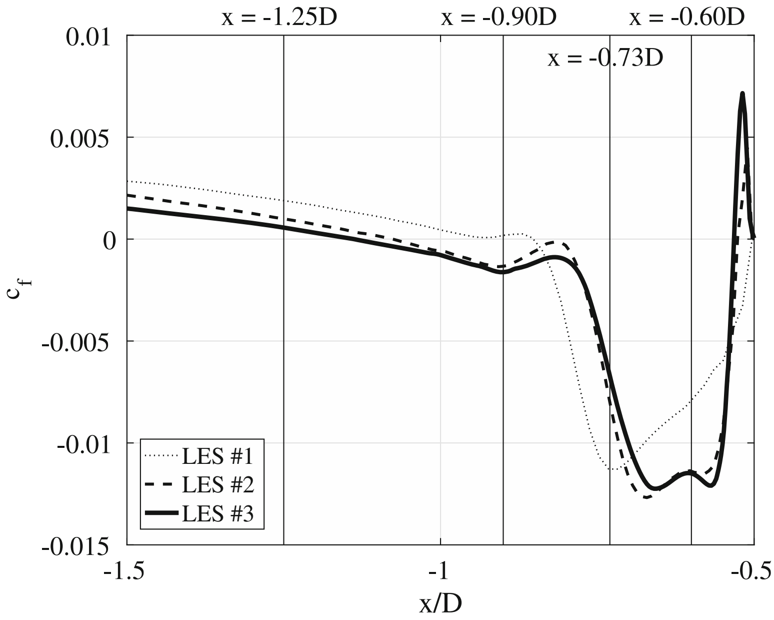

**Fig. 9** Friction coefficient $c_f$ in the symmetry plane in the cylinder front taken from LES #1 (coarse grid), LES #2 (medium grid) and LES #3 (fine grid)

recirculation zone) and the downstream one (due to V1) but these regions are connected by weak backflow. This is in accordance to Fig. 3, which shows the streamlines closest to the wall to connect S2 to S3, and to results documented in literature [1]. The narrow positive peak close to the cylinder is the footprint of the small corner vortex V3. Due to the coarse grid resolution, LES #1 cannot capture this vortex.

Again, the differences between LES #2 and #3 are significantly smaller than those between LES #1 and #2. The deviation of LES #3 to a finer grid can be expected to be even smaller. Furthermore, the wall shear stress is of the same amplitude in LES #2 and #3. We thus consider the wall nearest grid point to lay in the linear sublayer. Due to the enormous computational costs expected for a further refinement of the grid an additional simulation is omitted. All results in the remainder of this paper are taken from LES #3 with the finest grid.

## 4 Near-Wall Stress Balance

In the previous section the flow topology and velocity profiles close to the wall were presented. In the following, the stress balance which underlies these profiles is investigated. To do so, the momentum balance in streamwise direction is integrated in wall-normal direction. The expression for the streamwise wall shear stress $\langle \tau_w \rangle$ gained from this balance is evaluated by integration of the respective terms (Section 4.1) first. Second, it is discussed which of the contributors suffice for an accurate reconstruction of the near-wall stress balance and thus for modelling the wall shear stress (Section 4.2).

### 4.1 Integrated momentum balance

The streamwise ($x$-) component of the momentum balance written as Reynolds equation reads [20]

$$\rho \frac{\partial \langle u \rangle}{\partial t} \quad + \rho \frac{\partial \langle u_i \rangle \langle u \rangle}{\partial x_i} \quad = -\frac{\partial \langle p \rangle}{\partial x} \quad + \rho \frac{\partial}{\partial x_i} (\nu + \nu_t) \frac{\partial \langle u \rangle}{\partial x_i} \quad - \rho \frac{\partial \langle u_i' u' \rangle}{\partial x_i} \tag{3}$$

where $u_i$ is the component of the velocity vector in $x_i$-direction and $u$ the one in x-direction. Integration of Eq. 3 in the wall-normal ($z$-) direction gives an expression for the streamwise wall shear stress $\langle\tau_w\rangle$:

$$\begin{aligned}
\langle\tau_w\rangle \quad = \quad & \underbrace{\rho(\nu+\nu_t)\frac{\partial\langle u\rangle}{\partial z}}_{Muz} \quad \underbrace{-\int_{z_1}^{z}\frac{\partial\langle p\rangle}{\partial x}dz}_{pressure} \\
& \underbrace{-\rho\langle w\rangle\langle u\rangle}_{Mwu} \quad \underbrace{-\rho\langle w'u'\rangle}_{Fwu} \\
& \underbrace{-\rho\int_{z_1}^{z}\frac{\partial\langle u\rangle\langle u\rangle}{\partial x}dz}_{Muu} \quad \underbrace{-\rho\int_{z_1}^{z}\frac{\partial\langle u'u'\rangle}{\partial x}dz}_{Fuu} \\
& \underbrace{-\rho\int_{z_1}^{z}\frac{\partial\langle v\rangle\langle u\rangle}{\partial y}dz}_{Mvu} \quad \underbrace{-\rho\int_{z_1}^{z}\frac{\partial\langle v'u'\rangle}{\partial y}dz}_{Fvu} \\
& \underbrace{+\rho\int_{z_1}^{z}\frac{\partial}{\partial x}(\nu+\nu_t)\frac{\partial\langle u\rangle}{\partial x}dz}_{Mux} \quad \underbrace{+\rho\int_{z_1}^{z}\frac{\partial}{\partial y}(\nu+\nu_t)\frac{\partial\langle u\rangle}{\partial y}dz}_{Muy}
\end{aligned} \tag{4}$$

The labels in the under-braces give the references by which the corresponding terms are referred to in the remainder of this paper. The wall shear stress $\langle\tau_w\rangle$ is the integration constant. We did not apply any wall-modelling, thus our code MGLET evaluates the wall shear stress from the velocity gradient only. To be consistent with this procedure, the integrals in Eq. 4 start at the first grid point of the numerical grid $z_1$, not at the wall $z_0$. $Mwu$ and $Fwu$ are set to zero at $z_1$. The stress balance at the first grid point thus reduces to $\langle\tau_w\rangle = Muz$, which corresponds to the evaluation of $\tau_w$ in the LES.

We computed the terms in Eq. 4 on the four vertical profiles marked in Fig. 3. We plot all terms in Fig. 10 except the viscous stresses in the streamwise ($x$-) and the spanwise ($y$-) direction, $Mux$ and $Muy$ respectively. Due to the high Reynolds number, these contributors remain small at all four positions. Nevertheless, both terms are included in the evaluation of the full balance.

At every position the sum of all terms on the right hand side of Eq. 4 should balance the wall shear stress $\langle\tau_w\rangle$. However, the sum of all these terms (referred to as RHS Eq. 4 in Fig. 10) slightly deviates from the shear stress at the wall. Close to the wall, the deviation is considerably smaller than at $z^+ = 100$ (not shown in Fig. 10), where it is of the same order of magnitude as the wall shear stress. This error is intrinsic to the problem: Some contributors to the stress balance gain amplitude with increasing wall distance and are larger by two orders of magnitudes than the wall shear stress at $z^+ = 100$. Small inaccuracies in these large contributors cause large inaccuracies in the relative small residual of Eq. 4's right hand side. The errors stem from non-convergred statistics and postprocessing which not fully complies with the difference formulae used during the simulation. Furthermore, errors accumulate with increasing wall distance due to the integration. However, the discussed deviation of Eq. 4's right hand side from $\langle\tau_w\rangle$ does not effect the magnitude of the terms relative to each other. The conclusions regarding the relevance of single terms for near-wall modelling drawn from this study thus do not suffer from the observed difference between simulated and reconstructed wall shear stress.

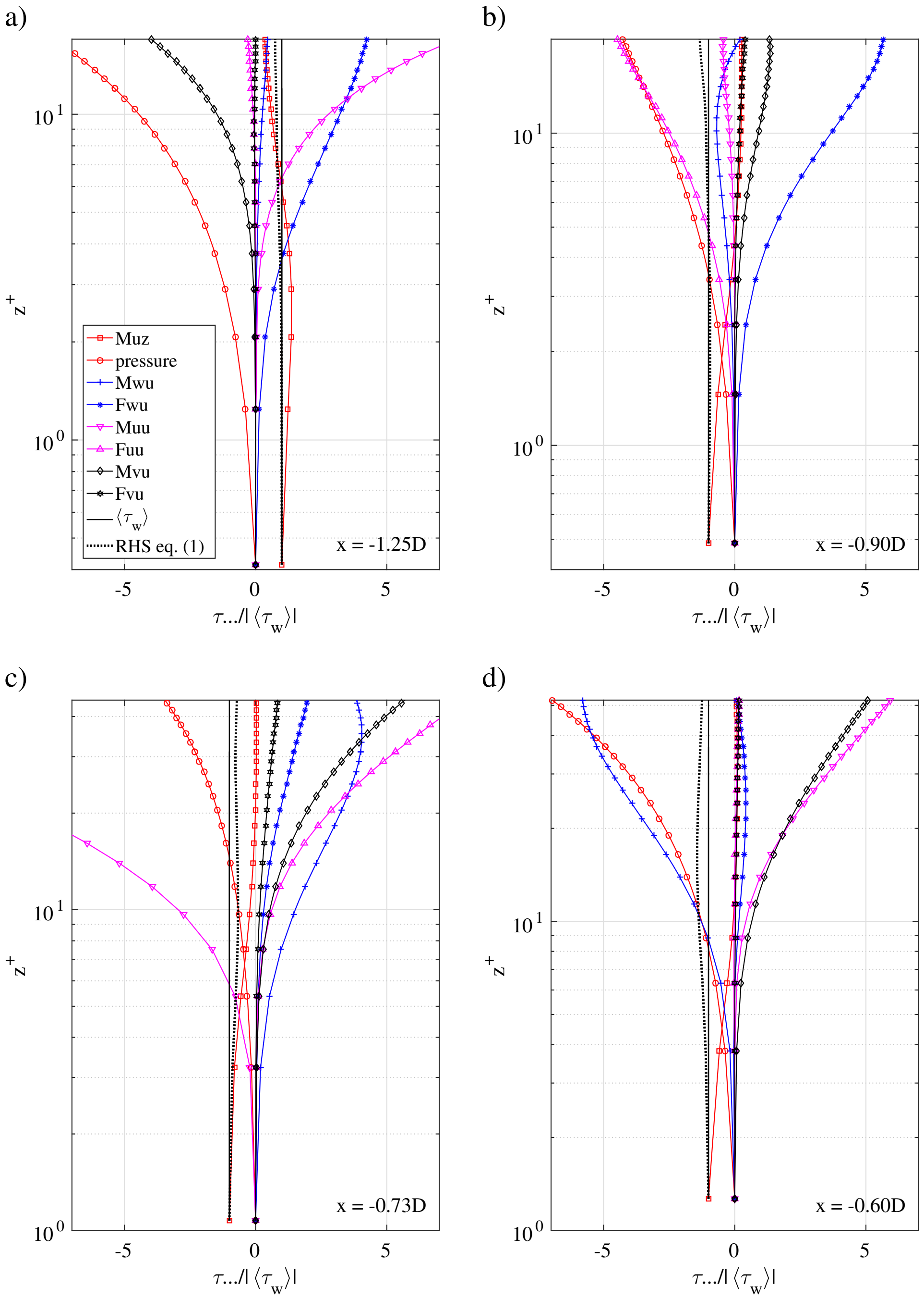

**Fig. 10** Contributors to the stress balance in the streamwise direction as defined in Eq. 4 at four different streamwise positions (Fig. 3) in the symmetry plane in front of the cylinder. The vertical axis is adjusted such that its upper limit corresponds to $z = 0.02D$ in outer scaling. All values are normalized by the magnitude of the local wall shear stress $\langle\tau_w\rangle$

The near-wall flow changes direction at $x \approx -1.1D$, thus the wall shear stress is positive at $x = -1.25D$ (Fig. 10a) and negative at $x = -0.90D$ (Fig. 10b), $x = -0.73D$ (Fig. 10c) and $x = -0.60D$ (Fig. 10d). Due to the treatment of the wall-nearest grid point (Section 4.1), the wall shear stress corresponds to the wall normal gradient of the velocity $Muz$ in this point at all four positions. All other terms are zero. As expected for turbulent flow, $Muz$ decreases rapidly with increasing wall distance and can be considered small at a wall distance $z^+ \geq 10$.

Since the cylinder causes a positive pressure gradient in the approaching flow (Fig. 6), the pressure term in Eq. 4 is negative at all four positions. Starting from zero in the first grid point at $x = -1.25D$ (Fig. 10a) it is already five times as large as the wall shear stress at a wall distance of $z^+ = 10$. The positive pressure gradient causes a deceleration of the flow in the streamwise direction as indicated by a positive $Muu$. It is plausible that the impact of the positive pressure gradient in front of the cylinder is largest in the symmetry plane. Thus the streamwise velocity has a local minimum in the symmetry plane and increases in the spanwise direction (negative $Mvu$ in Fig. 10a). The mentioned terms are balanced by the Reynolds shear stresses $Fwu$ and for $z^+ < 20$ by a streamwise increase of $\langle u'u' \rangle$ (negative $Fuu$). $Fvu$ as well as $Mux$ and $Muy$ remain small in the investigated section of the profile at $x = -1.25D$.

At $x = -0.90D$ (Fig. 10b), the upper limit of the vertical axis $z^+ = 20$ corresponds to the zero crossing of the streamwise velocity. In the region plotted ($z^+ < 20$) the streamwise velocity is thus negative. One can again observe the strong influence of the pressure term on the stress balance. At $z^+ = 10$, however, the term from the streamwise gradient of the streamwise Reynolds stress, $Fuu$, has approximately the same amplitude as the pressure term, which is in line with a increase of $\langle u'u' \rangle$ in $x$-direction at this position (Fig. 4). The term with the largest amplitude at this wall distance is the Reynolds shear stress, $Fwu$, which balances the larger part of the pressure term and $Fuu$. The mean convection of momentum in the spanwise direction, term $Mvu$, is considerably smaller than the previously mentioned terms but of the same order of magnitude as the wall shear stress. $Mvu$ is positive, which means that the spanwise gradient of $\langle v \rangle \langle u \rangle$ is negative. This can be explained by the follwing considerations. $\langle v \rangle$ is close to zero in the symmetry plane and increasing in spanwise direction. As $\langle u \rangle$ is negative, $\langle u \rangle \partial \langle v \rangle / \partial y < 0$. On the other hand $\langle v \rangle \partial \langle u \rangle / \partial y << 1$ as both contributors are small. $Mwu$ is negative at $z^+ = 10$, since the recirculation zone between S2 and S3 results in both negative $\langle u \rangle$ and negative $\langle w \rangle$ (Fig. 3). $Mwu$ turns positive at $z^+ = 20$ where $\langle u \rangle$ turns positive. In the section evaluated in Fig. 10b $Muu$ as well as $Fvu$ remain small. These terms start to gain amplitude at $z^+ > 30$ and $z^+ > 40$ respectively. $Mux$ and $Muy$ again remain small in the entire investigated section of the stress balance at $x = -0.90D$.

The wall shear stress at $x = -0.73D$ (Fig. 10c) is considerably larger than the one at the positions of the previously discussed profiles. The upper limit of the vertical axis is set to $z = 0.02D$. Since the core of the main horseshoe vortex V1 is located at $z = 0.06D$, all data points plotted in Fig. 10c have negative streamwise velocity (Fig. 3). The upstream directed jet along the bottom plate reaches its largest negative velocity at $x \approx -0.67D$ (Section 3), thus the observed profile at $x = -0.73D$ is in the deceleration zone of the jet, which points in negative $x$-direction. This is represented in Fig. 10c by a strong $Muu$ component. The negative $Muu$ is the result of an increasing amplitude of $\langle u \rangle$ in positive $x$-direction, which is against the flow direction of the jet. While $Muu$ is negative, $Fuu$ is positive, which visualises how the production term $P_{11}$ shifts kinetic energy between mean and fluctuating flow field at this position. At a wall distance of $z^+ = 10$ the deceleration is balanced in first line by the mean shear stresses $Mwu$. The streamlines in Fig. 3 indicate that the wall jet fans out and the fluid lifts off the bottom wall at $x = -0.73D$, giving a positive $\langle w \rangle$. Since $\langle u \rangle$ is negative in the whole observed range $Mwu$ has to be positive, too. At $z^+ = 10$ all other terms are relatively small. However, their amplitude starts to increase at approximately fifteen wall units significantly. Even though the pressure term strongly contributes to the stress balance at $z^+ > 20$, it is relatively small close to the wall. However, it should be noted that the wall shear stress, by which the stresses are normalized, is larger by a factor of five at $x = -0.73D$ compared to the positions discussed above, $x = -1.25D$ and $x = -0.90D$ respectively. Furthermore, due to the larger wall shear stress, the wall units are smaller in Fig. 10c. The pressure gradient at position $x = -0.73D$ at a certain wall distance in outer scaling is in fact of larger magnitude than in the previously discussed profiles. $Fvu$ shows a small gradient only but reaches the same amplitude as the wall shear stress at $z^+ \approx 50$. The viscous terms $Mux$ and $Muy$ do not give a significant contribution to the stress balance at $x = -0.73D$.

Last, the stress balance at $x = -0.60D$ is discussed in Fig. 10d. At this position, $\langle \tau_w \rangle$ is larger than at all the other positions discussed. Ten wall units from the wall, there are only four terms contributing significantly to the stress balance. The wall jet accelerates in the upstream direction which gives a positive $Muu$. Since the jet and thus the upstream velocity is strongest in the symmetry plane, $Mvu$ is positive, too. Its large amplitude can be explained by the blockage of the cylinder, which forces the fluid to accelerate in the spanwise direction to bypass the cylinder. However, this spanwise acceleration is still remarkable since visualizations of the horizontal flow field along the bottom plate imply the fluid to move upstream almost parallel to the $x$-axis in the region of the symmetry plane [1, 14]. $Muu$ and $Mvu$ are balanced by a negative pressure term and a negative mean shear stress $Mwu$. The latter results from negative $\langle u \rangle$ and negative $\langle w \rangle$, which in turn are caused by a compression towards the bottom plate of the upstream pointing wall jet at this position (Fig. 3). Further away from the wall, the amplitude of the mentioned stresses increase, while the other terms of Eq. 4 remain small. Especially the small amplitude of terms based on Reynolds stresses $Fwu$, $Fuu$ and $Fvu$ indicate the profile to be located in a region of relative calm turbulence, which is consistent with the distribution of turbulent kinetic energy (Fig. 4).

### 4.2 Reconstruction of the wall shear stress

One goal of this study is to detect the significant contributors to the stress balance (Eq. 4) which enable the reconstruction of the wall shear stress at a wall distance as large as possible by a number of contributors as small as possible - preferred by terms which depend on the local flow situation only and do not contain derivatives in the horizontal directions.

To deepen this issue, the contributors to the stress balance are grouped by the information required for their evaluation to distinct subsets: "local" denotes the sum of all terms which require local information only: $\tau_{local} = Muz + pressure\ term + Mwu + Fwu$. The pressure term is considered to be local even though it contains a derivative in the $x$-direction. To evaluate the influence of the spatial flow situation, "local + streamwise" denotes the sum of all local terms plus the terms containing derivatives in the streamwise direction $\tau_{local+streamwise} = \tau_{local} + Muu + Fuu$ while "local + spanwise" denotes the sum of all local terms plus the terms containing derivatives in the spanwise direction $\tau_{local+spanwise} = \tau_{local} + Mvu + Fvu$. The viscous terms $Mux$ and $Muy$ are small at all considered positions and thus neglected. These groups are plotted in Fig. 11 at the four distinct profiles already discussed above. The deviation between $\langle \tau_w \rangle$ and Eq. 4's right hand side is satisfying small but noticeable (Fig. 10). Since a subset of this right hand side cannot be expected to resemble $\langle \tau_w \rangle$ but the right hand side itself at the most, the data in Fig. 11 is normalized by the residual of Eq. 4's right hand side.

Figure 11 underlines that one needs to consider the full momentum balance (except the viscous terms) in the investigated flow case to predict the wall shear stress. At a wall distance of ten wall units only, the best performing subsets of contributors to the stress balance deviate form Eq. 4's right hand side by approximately 25% ($x = -0.60D$, local plus spanwise), 100% ($x = -0.73D$ and $x = -0.90D$, local plus streamwise) and more than 100% ($x = -1.25D$, local). These large deviations result from the fact that almost every term on the right hand side of Eq. 4 exceeds the wall shear stress by a multiple at $z^+ = 10$. Furthermore, as the discussion in the previous Section 4.1 indicated, the relevance of the single

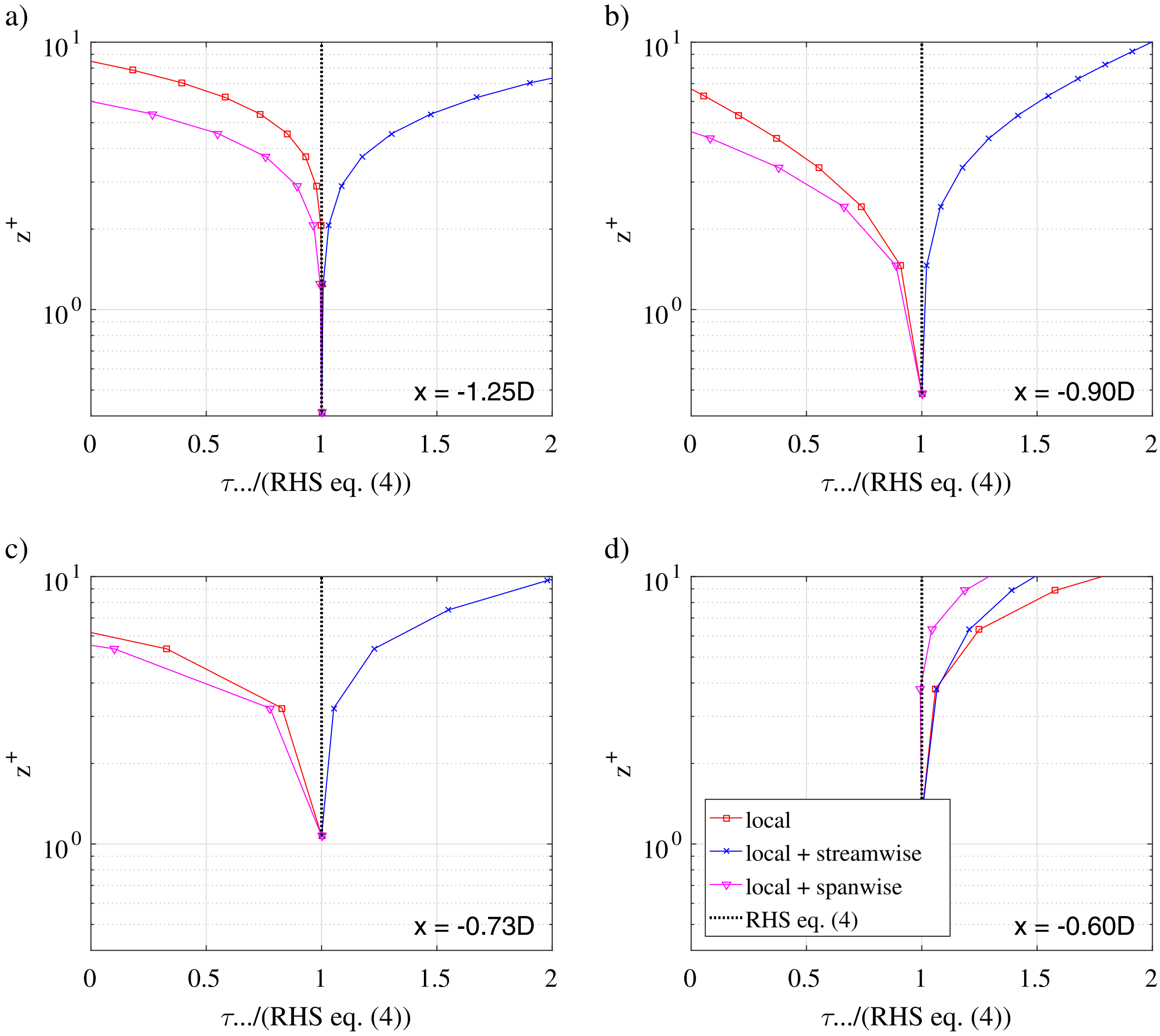

**Fig. 11** Subsets of contributors to the stress balance as defined in Eq. 4 normalized by Eq. 4's right hand side at four different streamwise positions (Fig. 3) in the symmetry plane in front of the cylinder

terms depends on the distinct position of the evaluated profile, as there is a significant local change of the flow situation in the cylinder front. It is thus not surprising that different subsets of stresses perform best at different positions. These observations are not only valid in inner but also in outer scaling, as a analogous comparison of the subsets at a certain grid point above the wall reveals.

When considering the distribution and the amplitude of the single contributors to the stress balance as well as of the defined subsets, it becomes clear that a spatial approach (including the derivatives in horizontal directions) has to be applied when the wall shear stress is estimated based on data at a wall distance larger than two or three wall units in the investigated complex flow situation.

From the necessity of including the horizontal (wall-parallel) derivatives into a wall-shear stress estimation one can draw further conclusions: There are significant velocity gradients in the wall-parallel direction, the boundary layer assumptions do therefore not hold in the considered complex, three dimensional flow. To capture these wall-parallel gradients, the data resolution in the respective directions has to be adequate. When a grid for a numerical simulation is designed, the focus should thus not solely lie on the wall-normal, but also on the wall-parallel grid resolution.

## 5 Discussion

We investigated the near-wall flow under a horseshoe vortex system in front of a vertical cylinder mounted on a flat plate at moderate Reynolds number. The goal of this study was to evaluate the influence of single contributors to the total stress balance and thus to assess their relevance for the evaluation and a possible modelling of the wall shear stress.

The reverse flow under the horseshoe vortex system is fully three-dimensional and characterized by strong acceleration and deceleration. As expected, the velocity profiles strongly deviate from the law of the wall. Large pressure gradients cause acceleration as well as deceleration of the mean flow, which in turn result in significant increase and damping of Reynolds stresses [15]. Accordingly, both Reynolds stresses and stresses due to the mean flow are of major relevance for the total stress balance. However, it might be argued that the mean flow field close to the wall depends on the flow topology in the outer region in first line and thus can be described by outer scaling. Various studies investigating the Reynolds number dependency of the horseshoe vortex system [2, 3, 16] observed no major changes of the flow topology with Reynolds number for moderate Reynolds numbers. Since the wall units become smaller with increasing Reynolds number, the mean stresses $Mwu$, $Muu$, and $Mvu$ are expected to be further away from the wall in inner scaling at higher Reynolds numbers. Consequently, a representation of the mean stresses by a computational grid would not require a grid refinement with increasing Reynolds number.

It can be concluded from the presented data that for modelling the wall shear stresses a balance including the local flow situation (represented by $Muz$, pressure term, $Mwu$ and $Fwu$ in Eq. 4) is not sufficient. Due to the three dimensional nature of the flow, the convective terms in the streamwise ($Muu$ and $Fuu$) and in the spanwise ($Mvu$ and $Fvu$) direction have to be regarded as well to close the stress balance. An approach to model the near-wall flow and the according wall shear stress which does not consider the spatial flow situation but neglects the horizontal gradients will fail at least in most positions of the examined flow. This is also true for models that assume the wall-normal velocity component to be zero at a grid point outside the viscous sublayer. The viscous terms $Mux$ and $Muy$ (and $Muz$ for $z^+ > 10$) can be considered to be small in the investigated flow. Furthermore, the presented data implies the necessity of a wall-parallel data resolution, which is able to capture wall-parallel gradients adequately.

**Funding Information** The authors gratefully acknowledge the financial support of the DFG under grant no. MA2062/11. Computing time was granted by the Leibniz Computing Center (LRZ) of the Bavarian Academy of Sciences through grant no. pr84gi. No further funding was received.

### Compliance with Ethical Standards

**Conflict of interests** The authors declare that they have no conflict of interest.

## References

1. Devenport, W.J., Simpson, R.L.: Time-dependent and time-averaged turbulence structure near the nose of a wing-body junction. J. Fluid Mech. **210**, 23–55 (1990)
2. Apsilidis, N., Diplas, P., Dancey, C.L., Bouratsis, P.: Time-resolved flow dynamics and reynolds number effects at a wall-cylinder junction. J. Fluid Mech. **776**, 475–511 (2015)

3. Escauriaza, C., Sotiropoulos, F.: Reynolds number effects on the coherent dynamics of the turbulent horseshoe vortex system. Flow Turbul. Combust. **86**(2), 231–262 (2011). https://doi.org/10.1007/s10494-010-9315-y
4. Martinuzzi, R., Tropea, C.: The flow around surface-mounted, prismatic obstacles placed in a fully developed channel flow. Trans. ASME J. Fluids Engrg. **115**, 85–92 (1993)
5. Paik, J., Escauriaza, C., Sotiropoulos, F.: On the bimodal dynamics of the turbulent horseshoe vortex system in a wing-body junction. Phys. Fluids **19**(045), 107 (2007)
6. Kawamura, T., Hiwade, M., Hibino, T., Mabuchi, I., Kumada, M.: Flow around a finite circular cylinder on a flat plate: Cylinder height greater than turbulent boundary layer thickness. Bull. JSME **27**(232), 2142–2151 (1984). https://doi.org/10.1299/jsme1958.27.2142
7. Palau-Salvador, G., Stoesser, T., Fröhlich, J., Kappler, M., Rodi, W.: Large eddy simulations and experiments of flow around finite-height cylinders. Flow Turbul. Combust. **84**(2), 239–275 (2010). https://doi.org/10.1007/s10494-009-9232-0
8. Krajnović, S.: Flow around a tall finite cylinder explored by large eddy simulation. J. Fluid Mech. **676**, 294–317 (2011). https://doi.org/10.1017/s0022112011000450
9. Melville, B.W., Coleman, S.E.: Bridge Scour. Water Resources Publications, LLC, Highlands Ranch, USA (2000)
10. Dargahi, B.: The turbulent flow field around a circular cylinder. Exp. Fluids **8**(1-2), 1–12 (1989). https://doi.org/10.1007/bf00203058
11. Chang, W.Y., Constantinescu, G., Lien, H.C., Tsai, W.F., Lai, J.S., Loh, C.H.: Flow structure around bridge piers of varying geometrical complexity . J. Hydraul. Eng. **139**(8), 812–826 (2013)
12. Rivier, A., Bennis, A.C., Pinon, G., Magar, V., Gross, M.: Parameterization of wind turbine impacts on hydrodynamics and sediment transport. Ocean Dyn. **66**, 1285–1299 (2016). https://doi.org/10.1007/s10236-016-0983-6
13. Tseng, M.H., Yen, C.L., Song, C.C.S.: Computation of three-dimensional flow around square and circular piers. Int. J. Numer. Meth. Fluids **34**(3), 207–227 (2000)
14. Schanderl, W., Manhart, M.: Reliability of wall shear stress estimations of the flow around a wall-mounted cylinder. Comput. Fluids **128**, 16–29 (2016)
15. Schanderl, W., Jenssen, U., Strobl, C., Manhart, M.: The structure and the budget of turbulent kinetic energy in front of a wall-mounted cylinder. J. Fluid Mech. **827**, 285–321 (2017). https://doi.org/10.1017/jfm.2017.486
16. Roulund, A., Sumer, B.M., Fredsoe, J., Michelsen, J.: Numerical and experimental investigation of flow and scour around a circular pile. J. Fluid Mech. **534**, 351–401 (2005). https://doi.org/10.1017/s0022112005004507
17. Grötzbach, G.: Numerical simulation of turbulent temperature fluctuations in liquid metals. Int. J. Heat Mass Transf. **24**(3), 475–490 (1981)
18. Werner, H.: Grobstruktursimulation der turbulenten Strömung über eine querliegende Rippe in einem Plattenkanal bei hoher Reynoldszahl. Ph.D. thesis. Technische Universität München, München (1991)
19. Manhart, M., Peller, N., Brun, C.: Near-wall scaling for turbulent boundary layers with adverse pressure gradient. Theor. Comput. Fluid Dyn. **22**(3-4), 243–260 (2008). https://doi.org/10.1007/s00162-007-0055-0
20. Pope, S.B.: Turbulent flows. Cambridge University Press, Cambridge (2011)
21. Knopp, T., Schanz, D., Schröder, A., Dumitra, M., Cierpka, C., Hain, R., Kähler, C.J.: Experimental investigation of the log-law for an adverse pressure gradient turbulent boundary layer flow at $re_\theta =$ 10000. Flow Turbul. Combust. **92**(1), 451–471 (2014). https://doi.org/10.1007/s10494-013-9479-3
22. Balaras, E., Benocci, C., Piomelli, U.: Two-layer approximate boundary conditions for large-eddy simulations. AIAA J. **34**(6), 1111–1119 (1996)
23. Chen, Z.L., Hickel, S., Devesa, A., Berland, J., Adams, N.A.: Wall modeling for implicit large-eddy simulation and immersed-interface methods. Theor. Comput. Fluid Dyn. **28**(1), 1–21 (2014). https://doi.org/10.1007/s00162-012-0286-6
24. Piomelli, U., Balaras, E.: Wall-layer models for large-eddy simulations. Annu. Rev. Fluid Mech. **34**(1), 349–374 (2002). https://doi.org/10.1146/annurev.fluid.34.082901.144919
25. Dey, S., Barbhuiya, A.K.: Turbulent flow field in a scour hole at a semicircular abutment. Can. J. Civ. Eng. **32**(1), 213–232 (2005). https://doi.org/10.1139/l04-082
26. Graf, W., Istiarto, I.: Flow pattern in der scour hole around a cylinder. J. Hydraul. Res. **40**(1), 13–20 (2002)
27. Melville, B.W., Raudkivi, A.J.: Flow characteristics in local scour at bridge piers. J. Hydraul. Res. **15**(4), 373–380 (1977). https://doi.org/10.1080/00221687709499641
28. Jenssen, U., Schanderl, W., Manhart, M.: Cylinder wall junction flow: particle image velocimetry and large eddy simulation. In: ERCOFTAC symposium on engineering turbulence modelling and measurements (2016)

29. Manhart, M., Tremblay, F., Friedrich, R.: MGLET: a parallel code for efficient DNS and LES of complex geometries. In: Jenssen, C.B., Kvamdal, T., Andersson, H.I., Pettersen, B., Ecer, A., Periaux, J., Satofuka, N., Fox, P. (eds.) Parallel Computational Fluid Dynamics 2000. Elsevier Science B.V., Amsterdam (2001)
30. Peller, N.: Numerische Simulation turbulenter Strömungen mit Immersed Boundaries. Ph.D. thesis, Technische Universität München (2010)
31. Peller, N., Duc, A.L., Tremblay, F., Manhart, M.: High-order stable interpolations for immersed boundary methods. Int. J. Numer. Methods Fluids **52**, 1175–1193 (2006)
32. Manhart, M.: A zonal grid algorithm for DNS of turbulent boundary layers. Comput. Fluids **33**(3), 435–461 (2004)
33. Nicoud, F., Ducros, F.: Subgrid-scale stress modelling based on the square of the velocity gradient tensor. Flow Turbul. Combust. **62**(3), 183–200 (1999). https://doi.org/10.1023/a:1009995426001
34. Breuer, M., Peller, N., Rapp, C., Manhart, M.: Flow over periodic hills – Numerical and experimental study in a wide range of Reynolds numbers. Comput. Fluids **38**(2), 433–457 (2009). https://doi.org/10.1016/j.compfluid.2008.05.002
35. Gallardo, J.P., Andersson, H.I., Pettersen, B.: Turbulent wake behind a curved circular cylinder. J. Fluid Mech. **742**, 192–229 (2014). https://doi.org/10.1017/jfm.2013.622
36. Manhart, M.: Vortex Shedding from a Hemisphere in a Turbulent Boundary Layer. Theor. Comput. Fluid Dyn. **12**(1), 1–28 (1998). https://doi.org/10.1007/s001620050096
37. Fernholz, H.H., Finley, P.J.: The incompressible zero-pressure-gradient turbulent boundary layer: An assessment of the data. Prog. Aerosp. Sci. **32**(4), 245–311 (1996). https://doi.org/10.1016/0376-0421(95)00007-0
38. Schanderl, W., Manhart, M., Link, O.: Discussion of the impact of pressure fluctuations on local scouring. In: River Sedimentation - Proceedings of the 13th International Symposium on River Sedimentation, ISRS 2016, pp. 394–401 (2017)

# D. Appendix: Publication 4, summarised in chapter 9

**Noname manuscript No.**
(will be inserted by the editor)

# Dissipation of turbulent kinetic energy in a cylinder wall junction flow

**Wolfgang Schanderl** · **Michael Manhart**

Received: date / Accepted: date

**Abstract** Subject of this study is the discussion of the dissipation of turbulent kinetic energy in front of a wall-mounted cylinder at three moderate Reynolds numbers by conducting highly resolved Large-Eddy Simulation (LES). To achieve reliable results, we ensured that the grid of the LES was fine enough to resolve most of the scales. A perceptible fraction of the total dissipation was modelled. However, this fraction - about one third - was small enough so that the total dissipation suffered only marginally from possible shortcomings of the turbulence model. Individual terms of the pseudo dissipation tensor and their Reynolds number scaling were discussed and compared among each other. It was shown that this tensor and thus the turbulent small scale structures were not isotropic at the Reynolds numbers investigated.

The turbulent length scale showed a strong spatial variability. In the region of the vortex system in the cylinder front, its distribution revealed a similar shape as the one of the turbulent kinetic energy and its amplitude was in the order of magnitude of the cylinder diameter. In contrast to the region dominated by the approach flow, the turbulent length scale was independent of the Reynolds number in the region dominated by the vortex system.

Even though the flow investigated was non-equilibrium common a priori estimations of the Kolmogorov length scale based on macro scales gave satisfying results.

**Keywords** Dissipation · non-equilibrium flow · Large-Eddy simulation

## 1 Introduction

The knowledge of the dissipation rate of turbulent kinetic energy is of crucial importance in turbulence modelling. It is also required to assess the Kolmogorov scales, the smallest scales of motion in turbulent flow. A priori knowledge about these scales is needed for designing both experiments and numerical simulations. However, an explicit evaluation of the

---

Wolfgang Schanderl · Michael Manhart
Professorship for Hydromechanics
Technical University of Munich
Arcisstr. 21, D-80333 Munich
Tel.: +49-89-289-22583
Fax: +49-89-289-28332
E-mail: michael.manhart@tum.de

dissipation is difficult, as Direct Numerical Simulation (DNS) without turbulence model is still rare for practical flow problems. In Reynolds-Averaged Simulation (RANS) and Large-Eddy Simulation (LES), the dissipation can be biased by the turbulence model. Furthermore, it is extremely difficult to measure the dissipation rate, e.g. from laser based measurements, since it is highly sensitive to noise in the recorded data [1].

"One of the cornerstone assumptions of turbulence theory" [24] is that the dissipation of turbulent kinetic energy $\varepsilon$ scales with the turbulent kinetic energy $k = U_t^2$ and a time scale $l_t/U_t$ [23]

$$\varepsilon = \frac{k^{3/2}}{l_t} C_\varepsilon \quad . \tag{1}$$

The energy is cascaded from large scale structures to structures of smaller scales to structures of such small scale that viscous effects become active and the energy is dissipated [17,27]. The characteristic velocity and length scales of the according structures are $U_t$ and $l_t$ respectively. The time scale $l_t/U_t$ is a measure for the time required to pass the energy $U_t$ through turbulent structures of the length scale $l_t$. As in homogeneous, isotropic and statistically stationary turbulence the energy driving the flow has to be equivalent to the energy dissipated by the smallest scales of motion, the energy flux through the cascade of motion is constant in a given situation and thus $C_\varepsilon = const$. As reviewed comprehensibly by Vassilicos [27], a multitude of studies investigated the dissipation coefficient $C_\varepsilon$ in the last decades. The discussion in most of these studies is on the evaluation of the dissipation in a periodic or closed box, in which turbulence was driven by an external source [5,22] (among others), or on the region of decaying turbulence in the wake of an obstacle like a grid or a cylinder [26,25] (among others). In these flow cases $C_\varepsilon$ is expected to be approximately one and spatially constant, as the dissipation has to balance the available turbulent kinetic energy [27].

However, as Nedić and Tavoularis [11] point out, homogeneous or, as they call it, fully-developed flow conditions "may be achieved in carefully designed and meticulously operated laboratory settings and possibly in some environmental systems with a high level of regularity" [11], but not in the majority of practical flow configurations. In the latter, the turbulent kinetic energy is not necessarily dissipated at the same location as it is produced, but transported away to other regions of the flow by the convection and the turbulent transport. The contribution of these terms to the budget of turbulent kinetic energy can be tremendous [19]. Nevertheless, if the energy is not cascaded continuously through all scales at the same position, $C_\varepsilon$ can neither be expected to be approximately one nor to be spatially constant. Thus, one can only expect that the dissipation rate of turbulent kinetic energy scales with macro scale quantities, $U_t$ and $l_t$, but not that it can be directly calculated from them.

Eddy-viscosity models for Reynolds-averaged Simulation (RANS) are based on the "cornerstone assumption" [24] mentioned above. These models express the momentum transport effectuated by turbulent motion by an artificial viscosity $\nu_t$ which can be formulated by the product of a turbulent velocity scale $U_t$ and the length scale $l_t$ and the model coefficient $C_\mu$ [16]. In two-equation models, the dissipation rate has been used as a surrogate of the length, now termed $l_\varepsilon$ [8],

$$l_\varepsilon = k^{3/2}/\varepsilon \quad , \tag{2}$$

and the turbulent viscosity then becomes

$$\nu_t = C_\mu k^2/\varepsilon \quad . \tag{3}$$

In this context it is not only crucial to understand the characteristics of the turbulent kinetic energy $k$ (and thus the turbulent velocity scale $U_t$) and its dissipation, but also of the turbulent length scale $l_\varepsilon$. Therefore we investigated the dissipation rate in the flow around a wall-mounted cylinder at three moderate Reynolds numbers $Re_D = 20000$, $Re_D = 39000$ and $Re_D = 78000$ by highly resolved LES. The Reynolds numbers were based on the cylinder diameter $D$ and the velocity averaged over the whole cross section of the approach flow. To gain further insight in the characteristics of these quantities, we evaluated the turbulent kinetic energy and its dissipation and estimated the turbulent length scale from these quantities. The investigated flow configuration and the resulting flow topology are introduced in section 2. The grid employed was fine enough to resolve approximately seventy percent of the total dissipation. Accordingly, the influence of the modelled contribution to the solution is small [19, 18]. The numerical methods used to simulate the flow as well as the measures taken to validate the presented data are presented in section 3. We present the dissipation $\varepsilon$ in front of the cylinder, where the so-called horseshoe vortex system causes rich dynamics and large time-averaged gradients in all spatial directions, in section 4. In addition, individual terms of the pseudo dissipation are evaluated and compared among each other as well as their Reynolds number scaling. Based of the evaluated dissipation, the turbulent length is estimated in section 5.

## 2 Flow configuration

In this study a cylinder wall junction flow is considered. The flow configuration is documented in section 2.1 and the resulting flow topology in section 2.2. The numerical methods and their validation employed to simulate this flow are presented in section 3.

### 2.1 Physical domain

We simulated the flow around a circular cylinder placed in an open channel with a flow depth of $H = 1.5D$, where $D$ is the diameter of the cylinder. We investigated three different Reynolds numbers $Re_D = 20000$, $Re_D = 39000$ and $Re_D = 78000$ based on $D$ and the velocity averaged over the whole cross section of the approach flow. The free surface was modelled by a slip boundary condition (which corresponds to an infinitesimal small Froude number), while a noslip condition was assigned to the bottom wall, the side walls and the cylinder surface. The setup is sketched in figure 1. A precursor simulation was applied to provide a fully-developed, turbulent open-channel flow as inflow condition [20].

### 2.2 Flow topology

A boundary layer flow, such as our open-channel flow, approaching a bluff body induces a vertical pressure gradient in the body front. The resulting down-flow is deflected by the bottom wall and forms the so-called horseshoe vortex system. Figure 2 illustrates the time-averaged flow pattern in the symmetry plane in the cylinder front close to the bottom at $Re_D = 39000$. The flow facing edge of the cylinder was located at $x = -0.5D$. The down-flow established a thin boundary layer along the surface of the cylinder which separated from the cylinder at stagnation point S4. Fluid inside this boundary layer entered the small corner vortex V3, while fluid in the freestream of this boundary layer was deflected in the upstream

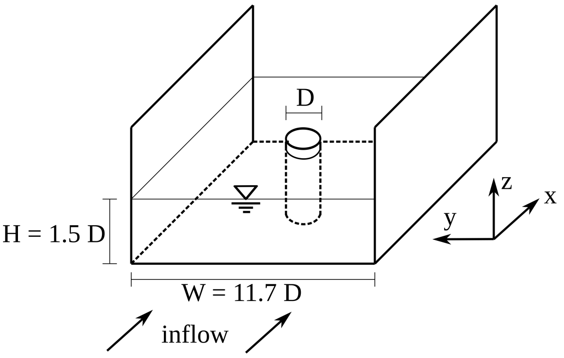

Fig. 1: Flow configuration: A circular cylinder mounted vertically on the flat bottom of an open channel.

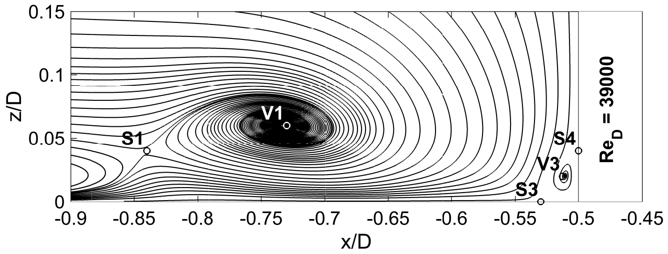

Fig. 2: Time-averaged streamlines in the symmetry plane in front of the cylinder at $Re_D = 39000$.

direction along the bottom wall. The dividing streamline ended at stagnation point S3. Parts of the fluid moving in the upstream direction formed the main vortex V1, while other parts entrained a jet along the wall underneath. The fluid inside this wall jet was subject to a strong acceleration between S3 at $x = -0.53D$ and $x \approx -0.7D$ and deceleration from there on to $x \approx -0.84D$ as indicated by the decreasing and increasing distance between the streamlines in figure 2. The latter position corresponded to the streamwise position of stagnation point S1, which separated the main vortex V1 from an additional weak recirculation further upstream. This recirculation zone was constrained by the most upstream stagnation point S2 at $x = -1.10D$ (not shown in figure 2) at this Reynolds number. Since the fluid had to bypass the obstacle, V1 bent around the cylinder. For this reason the vortex system is called horseshoe vortex.

The data presented in figure 2 was taken from the simulation at $Re_D = 39000$. At the investigated Reynolds numbers, the main vortex V1 was slightly shifted upstream with increasing Reynolds number, whereas the most upstream stagnation point was slightly shifted downstream. However, since the the flow topology did not change in general with Reynolds number, presenting the flow topologies at $Re_D = 20000$ and $Re_D = 78000$ was omitted here.

Devenport & Simpson [6] observed a bi-modal behaviour of the vortex system: In the backflow mode, vortex V1 is located further upstream in the cylinder front and the wall jet penetrates far into the oncoming boundary layer. The zero-flow mode is characterized by V1 located closer to the cylinder and the wall jet lifts and is ejected vertically off the wall directly upstream of the main vortex V1. This bimodality was also observed in the presented simulations. The consequences of this flapping of the jet for the dissipation of turbulent kinetic energy will be discussed in section 4.

## 3 Computational configuration

The following section introduces the numerical method and the grid used for our simulations (section 3.1) and discusses the measures taken to validate the employed approach (section 3.2). It should be noted that the simulation at the medium Reynolds number presented in this study is exactly the same as the one discussed by Schanderl and Manhart [20], Schanderl et. al [19] and Schanderl and Manhart [18].

### 3.1 Numerical methods

We conducted Large-Eddy simulation (LES) which was processed with our in-house Finite Volume-code MGLET. Spatial gradients were approximated by central differences and time-integration was done by a third order Runge-Kutta scheme. Since the grid was Cartesian, the curved surface of the cylinder was represented by a conservative second order Immersed Boundary Method [15, 14]. The subgrid stresses were modelled by the wall-adapting local eddy-viscosity (WALE) model [12]. This model facilitates the use of an Immersed Boundary Method, as it does not require for a damping function. The turbulent viscosity decreases naturally with proximity to the wall in this model.

The computational grid consisted of two major parts. First, a precursor (precursor grid) with a length of approximately $30D$ and periodic boundary conditions in the streamwise ($x$-) direction simulated a fully-developed, turbulent open-channel flow with a boundary layer thickness of $1.5D$. Instantaneous samples of this flow profile were set as inflow condition at the second part of the grid (base grid), which contained the cylinder. MGLET provides the possibility to refine the grid locally by nested grids [10]. This was used to achieve the required grid resolution in the region of interest around the cylinder. In total, three levels of refinement had to be applied until the grid study showed satisfying convergence of the solution. Each refinement level reduced grid spacing by a factor of two, thus the total refinement factor of the finest grid was eight relative to the precursor grid and the base grid. The grid is stretched in the wall-normal ($z$-) direction by a stretching factor smaller than 1.01. However, since this stretching was applied to the base grid and the precursor grid solely, only every eighth cell of the finest embedded grid was incremented. It was shown that the resolution was fine enough to resolve the viscous sublayer [20, 18]. As the evaluation of the dissipation of turbulent kinetic energy later in this study will show, grid spacing was approximately two Kolmogorov length scales in the vertical ($z$-) direction and approximately eight Kolmogorov length scales in the horizontal ($x$- and $y$-) directions. Parameters of the finest locally embedded grids at each Reynolds number are listed in Table 1.

The instantaneous Courant-Friedrichs-Lewy number was $0.50 < CFL_{max} < 0.85$. The statistical data was time averaged over a time between $T \approx 900D/u_b$ at the low Reynolds number and $T \approx 570D/u_b$ at the high Reynolds number after a statistically-steady state was observed.

Table 1: Grid parameters for all three Reynolds numbers investigated. The grid spacing refers to the finest locally embedded grid around the cylinder. $\eta_K$ was evaluated based on the maximum total dissipation in the core of the main vortex in front of the cylinder and the molecular viscosity $\nu$.

| $Re_D$ | grid cells | cells per diameter horizontal; vertical | Kolmogorov lengths $\Delta x/\eta_K = \Delta y/\eta_K$; $\Delta z/\eta_K$ |
|---|---|---|---|
| 20000 | $166 \cdot 10^6$ | 148; 571 | 8.0; 2.0 |
| 39000 | $400 \cdot 10^6$ | 250; 1000 | 6.4; 1.6 |
| 78000 | $1.6 \cdot 10^9$ | 440; 1778 | 6.8; 1.7 |

### 3.2 Validation

A grid study was conducted for each Reynolds number separately. Starting with the precursor grid and the base grid, the grid was successively refined in the region of interest around the cylinder. Three levels of grid refinement turned out to be sufficient to achieve results converged over grid spacing at each Reynolds number investigated. In figure 3 the grid study at $Re_D = 39000$ is exemplified, where the turbulent kinetic energy $k = 0.5\langle u_i'^2 \rangle$ is evaluated for three different simulations. $u_i'$ is the fluctuation of the velocity $u_i$ in direction $x_i$ while $\langle\rangle$ denotes time averaging. The simulation referred to by LES39k #1 held one locally embedded grid, LES39k #2 two local grids and in LES39k #3 the grid around the cylinder was refined by three nested grids. Thus, grid spacing in LES39k #3 was four times smaller than in LES39k #1 and eight times smaller than in the precursor grid and the base grid. A discussion of the convergence of first order moments of the velocity field of the presented LES at $Re_D = 39000$ can be found in [20, 19, 18].

In figure 3, the turbulent kinetic energy normalized by $u_b$ was evaluated on a horizontal profile in the symmetry plane in front of the cylinder. $u_b$ was the bulk velocity in the symmetry plane of the approach flow. The wall distance was $z = 0.06D$, which corresponded to the wall distance of the core of V1 in the simulation with the finest grid. The distribution of $k$ can be divided in three regions. The first one corresponds to the down-flow region in front of the cylinder downstream of $x \approx -0.65D$, where the turbulence level was relatively low. The second region indicates the presence of the main vortex V1 by significantly enhanced $k$. However, as a comparison to the flow topology in figure 2 reveals, the peak of turbulent kinetic energy reaches further upstream and also covers the area around stagnation point S1. For $x < 0.95D$, $k$ was again relatively small.

Figure 3 implies two kinds of changes with grid refinement: the amplitude of the peak increased with grid refinement, and its position slightly moved downstream. The peak of turbulent kinetic energy moved downstream together with the position of the main vortex V1. This shift represents a change of the flow topology, which is the first order moment of the statistics of the velocity field. The increasing amplitude represents changes in the second order moments of the statistics of the velocity field. For both quantities the change from LES39k #1 to LES39k #2 was significantly larger than the change from LES39k #2 to LES39k #3, which indicates that the simulations were in the convergent regime. As the conducted LES used implicit filtering with a filter width defined by the grid spacing, the solution converged towards the solution of a DNS [4]. However, as it is not possible to separate the numerical error from the error of the model in a LES with implicit filtering, a decrease of the error by second order cannot be expected, even though the used numerical methods are

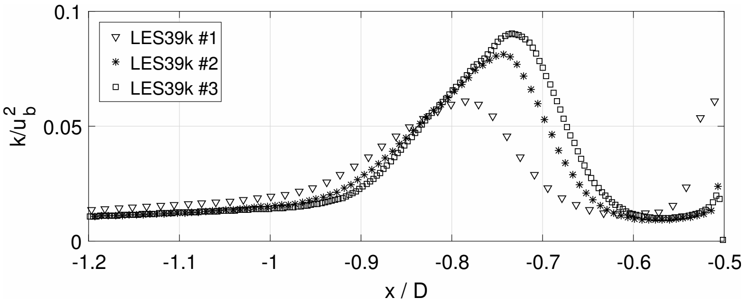

Fig. 3: Turbulent kinetic energy on a horizontal line in the symmetry plane in front of the cylinder at $Re_D = 39000$, taken from three simulations with different grid refinement. The vertical position corresponds to the one of the core of the main vortex V1.

of second order [4]. As the differences between simulation LES39k #2 and LES39k #3 were reasonably small, and changes between LES39k #3 and a simulation with further refined grid were considered to be even smaller, a further grid refinement was omitted. A similar behavior was observed in the simulations at $Re_D = 20000$ and $Re_D = 78000$.

In figure 4, the inplane turbulent kinetic energy $k_{ip}$ normalized by $u_b$ from the simulation LES39k #3 (figure 4a) is opposed to the one taken from the PIV measurements (figure 4b) by Ulrich Jenssen, documented in Schanderl et al. [19]. The inplane turbulent kinetic energy $k_{ip} = 0.5\langle u'^2 + w'^2 \rangle$ was chosen since the PIV data contained the velocity components in the streamwise ($x$-) direction $u$ and in the vertical ($z$-) direction $w$ only, but not the one in spanwise ($y$-) direction $v$. Even though the amplitude of the inplane turbulent kinetic energy $k_{ip}$ was smaller than the one of the total turbulent kinetic energy $k$ by approximately 20%, the distribution of $k_{ip}$ was similar to the one of $k$ [19]. The main peak of $k_{ip}$ was located in the region of vortex V1, from where a foot-like structure of enhanced $k_{ip}$ reached to the bottom plate. Together, the peak around V1 and the foot-like structure formed the typical c-shape, which was described by Paik et al. [13] and confirmed by various studies, e.g. [7,2], among others. Around V1 the Reynolds stresses in vertical direction $\langle w'^2 \rangle$ were the dominant contributor to the turbulent kinetic energy, while $\langle u'^2 \rangle$ was the main contributor to the branch reaching to the bottom plate [19]. The region between the main vortex and the cylinder exhibited relatively calm turbulence.

The accordance of PIV and LES39k #3 was satisfying. This was especially true for the distribution of $k_{ip}$, which showed a similar c-shape in both data sets. As the whole vortex system was located slightly more upstream in the PIV (see the marked positions of V1 in figure 4a and 4b respectively), this was also true for the distribution of turbulent kinetic energy. However, the overall amplitude was larger by 20% to 30% in the PIV. An investigation of the Reynolds normal stresses revealed that this deviation stemmed from a larger $\langle u'^2 \rangle$ in the region of the main vortex V1 in the experiment, while the amplitude of $\langle w'^2 \rangle$ was approximately the same [19].

It should be noted that the deviation of the amplitudes cannot be caused by the fact that the modelled turbulent kinetic energy $k_{SGS}$ was neglected in the evaluation of the numerical data. In the presented study the modelled turbulent kinetic energy was defined as $k_{SGS} = (\nu_t/(0.094\Delta))^2$ [28,9], where $\Delta$ was the filter width equivalent to grid spacing and $\nu_t$ was the modelled viscosity. The ratio of the modelled to the resolved turbulent kinetic energy $k_{SGS}/k$ in figure 5 is approximately 0.02 in the region covered by the vortex system

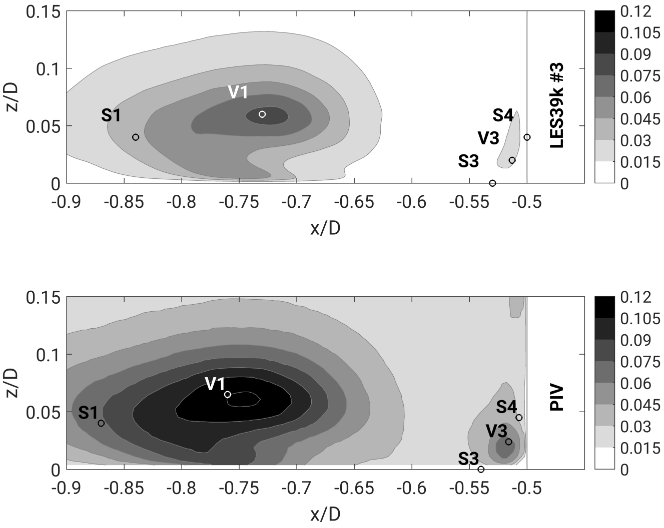

Fig. 4: Inplane turbulent kinetic energy $k_{ip}/u_b^2$ in the symmetry plane in front of the cylinder at $Re_D = 39000$, (a) taken from the simulation LES39k #3 and (b) experimental data from the same setup, taken from [19].

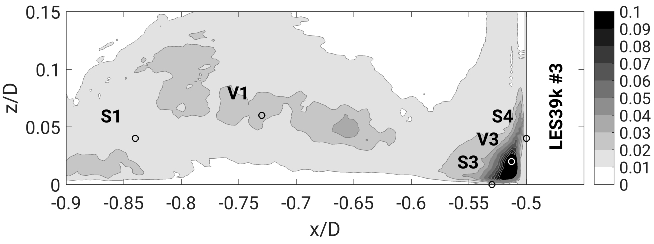

Fig. 5: Ratio of the modelled turbulent kinetic energy to the resolved one $k_{SGS}/k$ in the symmetry plane in front of the cylinder at $Re_D = 39000$, taken from LES39k #3.

and less than 0.01 outside of this region. The influence of the subgrid scale model on the distribution of turbulent kinetic energy was thus considered small. Solely the region covered by the small corner vortex V3 exhibits an enhanced ratio of $k_{SGS}/k \approx 0.15$ in figure 5. Since the grid spacing in the horizontal directions was four times larger than in the wall-normal direction, the grid was not fine enough to capture the thin boundary layer along the cylinder and the small corner vortex V3 without noticeable contribution of the subgrid-stress model. However, this region was spatially constrained. The relatively enhanced contribution of the subgrid stresses was also observed in the evaluation of the total budget of turbulent kinetic energy [16] by Schanderl et al. [19]. They evaluated the budget and although the modelled contributors to each term except the dissipation rate were neglected, the residual of the budget was reasonable small (less than 10% of the production term) in the region covered by the horseshoe vortex. Solely in the region close to the cylinder the residual showed an enhanced amplitude [19]. However, as the residual did not exhibit a constant shift but positive and negative values alternated in wide regions, it can be acted from the assumption that no budget term was over- or underestimated and the numerical dissipation of the employed setup was marginal [19]. In addition, an evaluation of modelled and resolved stresses implied that the modelled ones were small compared to the resolved ones [18].

All data presented in the following was taken from the simulation with the finest grid at the corresponding Reynolds number.

## 4 Dissipation rate

In this section, the distribution and the modelled share of the dissipation rate are discussed and compared to the so-called pseudo dissipation first (section 4.2). Afterward, contributors to the pseudo dissipation and their Reynolds number scaling are evaluated.

### 4.1 Total dissipation

In an eddy-viscosity LES, the dissipation of turbulent kinetic energy $\varepsilon$ is obtained by [16]

$$\varepsilon = \underbrace{2\nu\langle s_{ij}s_{ij}\rangle}_{\varepsilon_{res}} + \underbrace{2\langle \nu_t s_{ij}s_{ij}\rangle}_{\varepsilon_{SGS}} \quad . \tag{4}$$

$\varepsilon$ is calculated based on the fluctuation of the strain rate tensor $s_{ij} = 1/2\left(\partial u'_i/\partial x_j + \partial u'_j/\partial x_i\right)$, while the direct dissipation due to the time-averaged strain rate tensor $S_{ij}$ is not included. The first summand in equation (4) is the resolved dissipation $\varepsilon_{res}$ and the second summand the modelled one $\varepsilon_{SGS}$. In the remainder of this study, the dissipation is normalized by the bulk velocity in the symmetry plane of the approaching flow $u_b$ and the cylinder diameter $D$.

The dissipation for all three Reynolds numbers investigated is evaluated in figure 6. Its distribution bears three features: (i) a broad peak in the area covered by vortex V1; (ii) a tail of large $\varepsilon$ along the cylinder, leading into a peak at the junction of cylinder and bottom wall; (iii) a thin stripe of large dissipation where the wall jet moves along the bottom wall under vortex V1. With increasing Reynolds number, the main vortex V1 was slightly shifted upstream as indicated by the corresponding marks in figure 6. Thus, the dissipation peak in this region was shifted as well. Furthermore, the overall amplitude of $\varepsilon$ slightly enhanced and the peak at the wall under V1 became more pronounced with increasing Reynolds number. The cause of this enhanced amplitude will be discussed in section 4.2. However, the changes of $\varepsilon$ with Reynolds number were rather small.

The dissipation in figure 6 is the sum of the resolved and the modelled dissipation. The modelled share is presented separately with adjusted colorbar in figure 7 for $Re_D = 39000$. $\varepsilon_{SGS}$ exhibited the same three features as observed for the total dissipation. In fact, the distribution of the modelled dissipation was similar to the one of the total dissipation while its amplitude was approximately one third of the total one. This fraction is small for LES.

The pseudo dissipation $\varepsilon_p$, which is defined as [21]

$$\varepsilon_p = \nu\langle\left(\frac{\partial u'_i}{\partial x_j}\right)^2\rangle \quad , \tag{5}$$

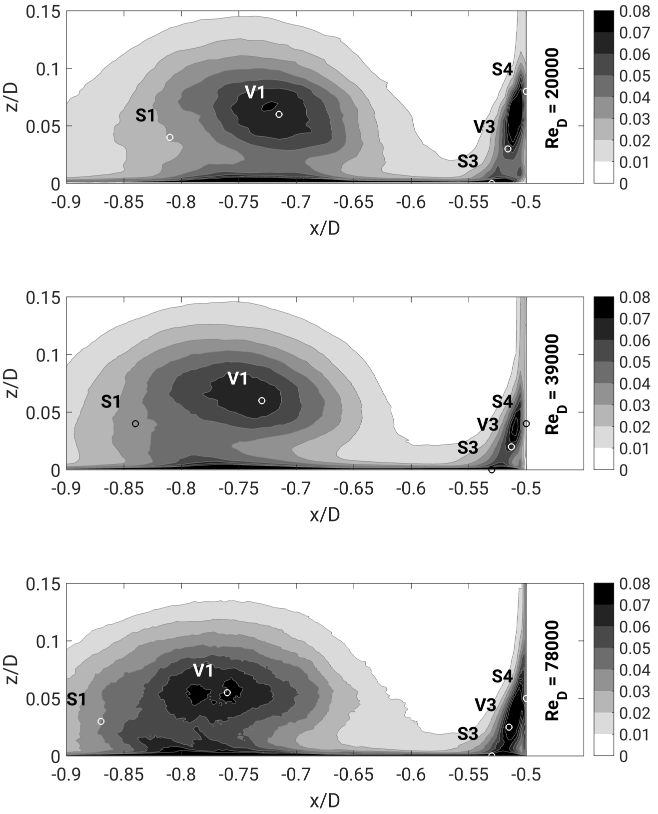

Fig. 6: Dissipation $\varepsilon * D/u_b^3$ in the symmetry plane in front of the cylinder at $Re_D = 20000$ (a), $Re_D = 39000$ (b) $Re_D = 78000$ (c).

facilitates a decomposition into individual contributors according to their spatial orientation. $\varepsilon_p$ as shown in figure 8 for $Re_D = 39000$ does not contain modelled contributions. The pseudo dissipation replicates $\varepsilon$ in figure 6b without observable deviation. This is true for both amplitude and distribution and supports the assumption that the pseudo dissipation is a fairly good approximation of the dissipation in the considered flow setup at the Reynolds numbers investigated.

## 4.2 Term-by-term evaluation of the pseudo dissipation

While the full dissipation rate of turbulent kinetic energy seems to be more or less independent of the Reynolds number in the considered range, we are also interested in whether and - if yes - how the individual contributions to the total dissipation rate change with Reynolds number. This can be estimated from the individual terms of $\varepsilon_{p,ij}$ as given by equation (5) without summation over the indices. We first give an overlook over the full tensor and then concentrate on two individual contributions to the dissipation rate tensor. In figure 9 the

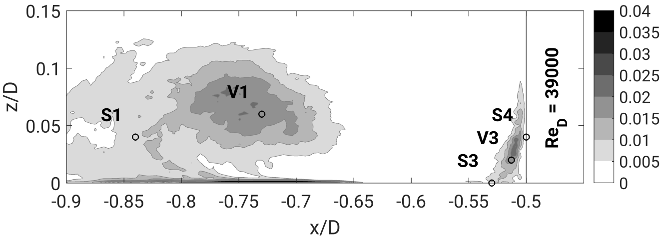

Fig. 7: Modelled dissipation $\varepsilon_{SGS} * D/u_b^3$ in the symmetry plane in front of the cylinder at $Re_D = 39000$.

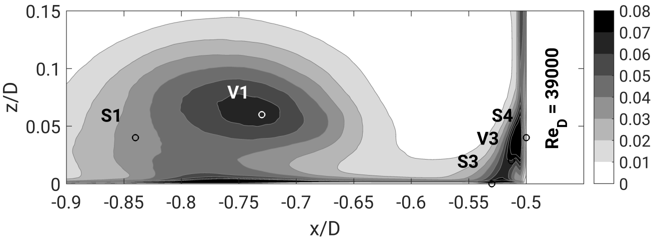

Fig. 8: Pseudo dissipation $\varepsilon_p * D/u_b^3$ in the symmetry plane in front of the cylinder at $Re_D =$ 39000.

full pseudo dissipation tensor is evaluated. In each subfigure one individual term $\varepsilon_{p,ij}$ of the pseudo dissipation $\varepsilon_p$ as given by equation (5) is plotted three times - once for each Reynolds numbers investigated. The distribution on top of each subfigure corresponds to $Re_D = 20000$, the one at the bottom of each subfigure to $Re_D = 78000$. The subfigures are ordered according to their position in the pseudo dissipation tensor and plotted in a color range from $\varepsilon_{p,ij}D/u_b^3 = 0$ to $\varepsilon_{p,ij}D/u_b^3 = 0.02$ with increments of 0.002.

From figure 9 it becomes evident that the dissipation rate was not isotropic as there are terms of relative large amplitude in the region in front of the cylinder while other terms are relatively small. In the center of the main vortex, the streamwise gradients of the wall-normal component, $\varepsilon_{p,31} = \nu\langle(\partial w'/\partial x)^2\rangle$ had the largest contribution, followed by the wall-normal gradients of the streamwise component $\varepsilon_{p,31} = \nu\langle(\partial w'/\partial x)^2\rangle$. Under the main vortex near the wall, the dissipation rate was dominated by the wall-normal gradients of the streamwise component $\varepsilon_{p,31}$. Another interesting feature becomes evident when the individual terms are investigated with increasing Reynolds number. The distributions and amplitudes of the two "large terms" did not change, see for example $\varepsilon_{p,13}$. However, the amplitudes of the "small terms" increased significantly, see for example $\varepsilon_{p,12} = \nu\langle(\partial u'/\partial y)^2\rangle$. With increasing Reynolds number, the small terms caught up to the large terms and the dissipation became more isotropic. This was true for all small terms except the terms in the trace of the tensor $\varepsilon_{p,ii}$, which remained small compared to the other terms. The behavior of the "small terms" was consistent with the conventional picture of the energy cascade and the assumption that the small scales become isotropic only at very large Reynolds numbers. With increasing

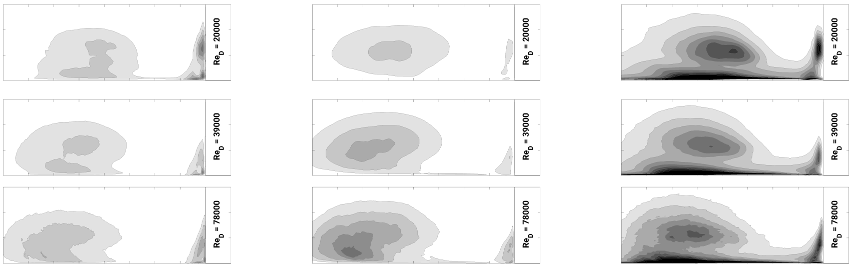

$\nu\langle(\partial u/\partial x)^2\rangle * D/u_b^3$ $\nu\langle(\partial u/\partial y)^2\rangle * D/u_b^3$ $\nu\langle(\partial u/\partial z)^2\rangle * D/u_b^3$

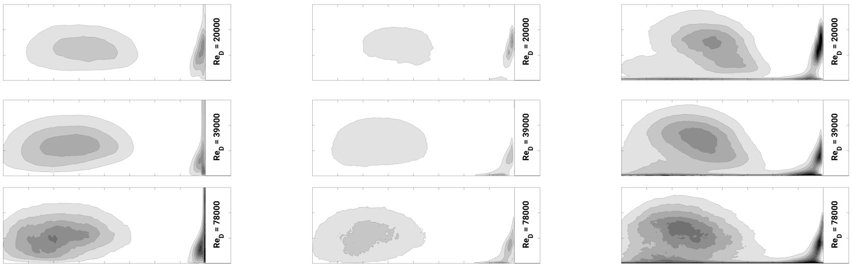

$\nu\langle(\partial v/\partial x)^2\rangle * D/u_b^3$ $\nu\langle(\partial v/\partial y)^2\rangle * D/u_b^3$ $\nu\langle(\partial v/\partial z)^2\rangle * D/u_b^3$

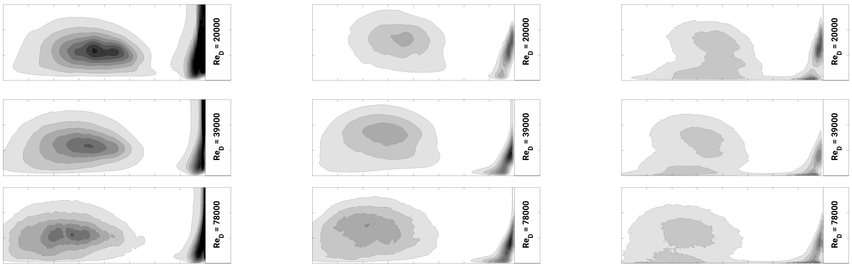

$\nu\langle(\partial w/\partial x)^2\rangle * D/u_b^3$ $\nu\langle(\partial w/\partial y)^2\rangle * D/u_b^3$ $\nu\langle(\partial w/\partial z)^2\rangle * D/u_b^3$

Fig. 9: Pseudo dissipation tensor evaluated for all three Reynolds number investigated. The colorbar ranges from $\varepsilon_{p,ij}D/u_b^3 = 0$ to $\varepsilon_{p,ij}D/u_b^3 = 0.02$ with increments of 0.002.

Reynolds number, the dissipation occurs at successively smaller scales, the cascade is longer and the small structures have more time to develop towards and isotropic state. The increase of the “small terms” was also what caused the mild increase of the total dissipation $\varepsilon$ with Reynolds number (figure 6).

In the following, we concentrate on two individual contributors to the pseudo dissipation in more detail. Individual contributors can be related to specific vortex structures. Small scale vertical vortices, e.g., give rise to large values of $\varepsilon_{p,12} = \nu\langle(\partial u'/\partial y)^2\rangle$ and $\varepsilon_{p,21} = \nu\langle(\partial v'/\partial x)^2\rangle$. From figure 9 it can be inferred that both had similar distributions and amplitudes with a similar Reynolds number dependence. Figure 10 zooms into $\varepsilon_{p,12} =$

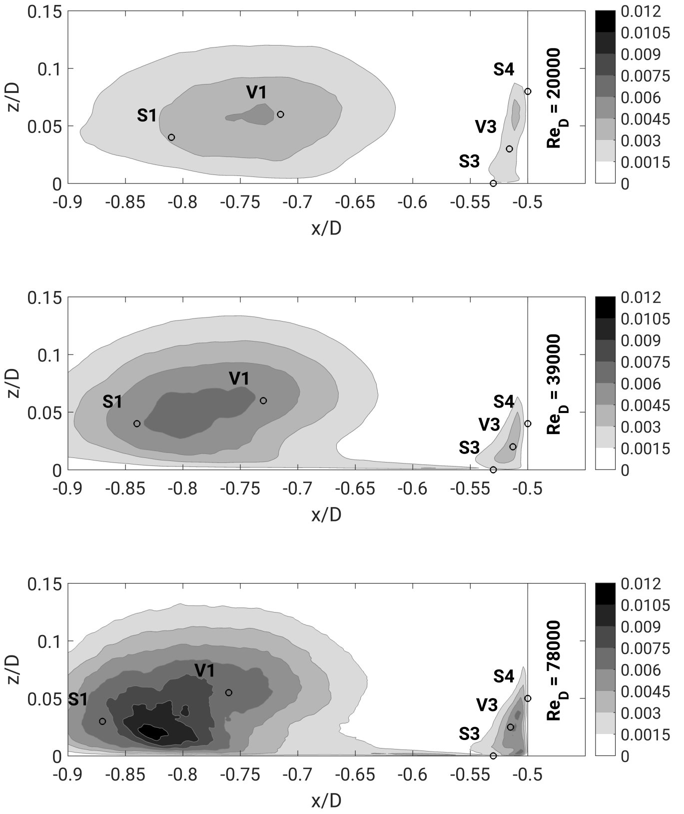

Fig. 10: $\varepsilon_{p,12} * D/u_b^3$ based on the spanwise gradient of fluctuations of the streamwise velocity at $Re_D = 20000$ (a), at $Re_D = 39000$ (b)and at $Re_D = 78000$ (c) in the symmetry plane in front of the cylinder.

$\nu\langle(\partial u'/\partial y)^2\rangle$ which peaked in the upstream half of the main vortex between the core of V1 and stagnation point S1 (and so did $\varepsilon_{p,21}$). The amplitude of $\varepsilon_{p,12}$ was rather small, especially at $Re_D = 20000$. However, with increasing Reynolds number also the overall amplitude of $\varepsilon_{p,12}$ increased and the distribution changed. At $Re_D = 78000$ maximum values appeared closer to the bottom wall in the region, in which the wall jet decelerated and lifted off the wall. The fact that $\varepsilon_{p,12}$ and $\varepsilon_{p,21}$ had similar distributions and amplitudes suggests that in the region in which these two were large, intense small scale vertical vortices occurred. In deed it was observed by [3] and [19] that in front of the main vortex V1 many small scale vertical vortices appear. These vortices are amplified by the vortex stretching mechanism induced by the roll up of the fluid in front of the main vortex. Our results suggest that this mechanism becomes more important with increasing Reynolds number.

Figure 11 shows the pseudo dissipation due to the vertical gradient of the fluctuations of the streamwise velocity $\varepsilon_{p,13} = \nu\langle(\partial u'/\partial z)^2\rangle$. The data was evaluated with adjusted colorbar compared to figure 10. The amplitude of $\varepsilon_{p,13}$ was significantly larger than the one of other contributors at every Reynolds number investigated. Furthermore, $\varepsilon_{p,13}$ held two peaks: one

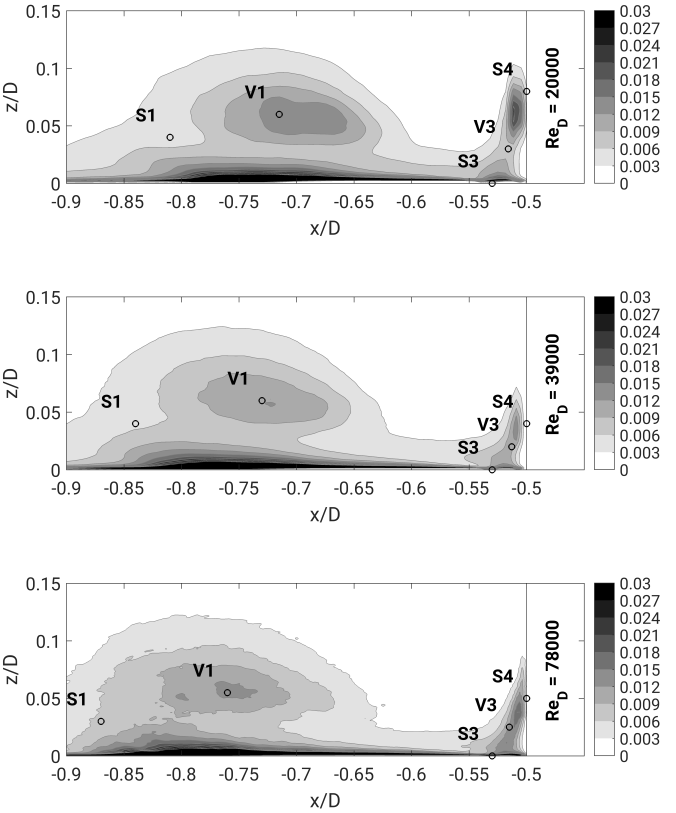

Fig. 11: $\varepsilon_{p,13} * D/u_b^3$ based on the vertical gradient of fluctuations of the streamwise velocity at $Re_D = 20000$ (a), at $Re_D = 39000$ (b) and at $Re_D = 78000$ (c) in the symmetry plane in front of the cylinder.

around the main vortex V1, and the other one underneath V1 at the bottom plate. Around the main vortex, $\varepsilon_{p,31}$ exhibited a similar distribution than $\varepsilon_{p,13}$, which suggests that intense small scale streamwise vortices can be found here. These streamwise vortices eventually can be explained by a further wrapping of wall normal vortices around V1. The second peak in $\varepsilon_{p,13}$ was found at the wall beneath the main vortex. As there was no other contributor to the dissipation rate peaking at this location, we conclude that the large amplitudes of the dissipation rate at the wall can be explained by a vertical flapping of the wall jet underneath V1. With increasing Reynolds number, the overall amplitude increased only marginally, which implies that the effects causing $\varepsilon_{p,13}$ changed only marginally, too.

## 5 Length scales

We now turn our attention to the length scales associated with the dissipation rate. First, we discuss the distributions of the turbulent length scale $l_\varepsilon$ constructed by the turbulent kinetic energy and its dissipation rate (section 5.1). Afterward, we discuss the Reynolds number scaling of the Kolmogorov scale (section 5.2).

### 5.1 Turbulent length scale

In eddy viscosity based Reynolds averaged modelling (RANS), the turbulent viscosity, which furnishes the dissipative effect of turbulence, is formulated as a product of a velocity scale $U_t$ and a length scale $l_t$. The common approach in two equation modelling is to estimate the turbulent length scale by the dissipation rate as a surrogate, hence $l_\varepsilon$, by equation (2). The dissipation rate $\varepsilon$ is evaluated by an additional transport equation. However, in the presented case the dissipation can be estimated from the LES, which allows for an a posteriori evaluation of the turbulent length scale $l_\varepsilon$.

The turbulent length scale in figure 12 reveals a large spatial variability for all three Reynolds numbers. In the oncoming flow and in the down flow in front of the cylinder the length scale was large ($O(D)$). The c-shape found in the kinetic energy distribution (figure 4) was as well found in the length scale distribution. Around the center of the main vortex and in the foot-like peak underneath $l_\varepsilon$ attained a local maximum, which indicates that the fluctuations in this region are mainly due to large-scale spatial oscillations of the main vortex. At the cylinder junction, very small values occurred which can be explained by the spatially small corner vortex system.

The length scale was only mildly dependent on the Reynolds number in the main areas around the horseshoe vortex, which underlines the Reynolds number independence of the horseshoe vortex system. However, in the oncoming flow and the down flow in front of the cylinder, the length scale $l_\varepsilon$ grew from values of $l_\varepsilon \approx 0.3D$ at $Re = 20000$ to $l_\varepsilon \approx 0.8D$ at $Re = 78000$.

### 5.2 Kolmogorov length scale

When performing Direct Numerical Simulation (DNS) or Particel Image Velocimetry (PIV), knowledge about the Kolmogorov length scale is required so that grid spacing in DNS and the particle size in PIV can be adjusted accordingly. As the Kolmogorov length scale [16]

$$\eta_K = (\nu^3/\varepsilon)^{1/4} \tag{6}$$

depends on the dissipation rate $\varepsilon$, $\varepsilon$ has to be estimated a priori by macro scale parameters. In the considered setup, this estimation can be done by the bulk velocity in the symmetry plane of the approach flow and the cylinder diameter $u_b^3/D$ [16], which were also used to normalize the dissipation and the pseudo dissipation presented above. The corresponding approximation of the Kolmogorov length scale is $\eta_{K,macro} = (\nu^3/(u_b^3/D))^{1/4}$. For all three Reynolds numbers investigated, the dissipation computed from the LES was $\varepsilon \approx 0.08u_b^3/D$ in the core of the main vortex V1 and the corresponding Kolmogorov length scale thus $\eta_K = 1.88\eta_{K,macro}$. This indicates, that even if the dissipation rate is locally underestimated by a factor of more than ten, the macro scale estimation of the Kolmogorov length scale $\eta_{K,macro}$ is a fairly good approximation. However, it should be noted the $\eta_K$ is relatively insensitive to a deviation of $\varepsilon$, as the first scales with the latter by a power of $1/4$.

By dimensional arguments, the Kolmogorov length scale is assumed to scale with $1/Re^{3/4}$. Based on this assumption and the Kolmogorov length scale computed from the LES at $Re_D = 20000$ $\eta_{K,20k}$, the Kolmogorov length scales $\eta_{K,39k}$ and $\eta_{K,78k}$ at $Re_D = 39000$ and

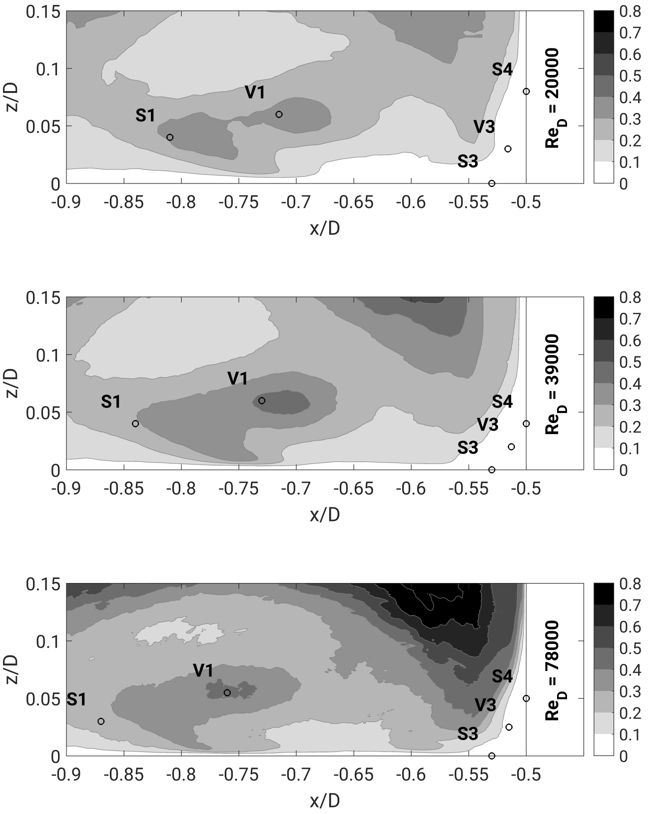

Fig. 12: Turbulent length scale $l_\varepsilon/D$ (equation (2)) at $Re_D = 20000$ (a), at $Re_D = 39000$ (b) and at $Re_D = 78000$ (c) in the symmetry plane in front of the cylinder.

$Re_D = 78000$ respectively were estimated in the main vortex core and compared to a posteriori evaluations of the LES data at the corresponding Reynolds number. Table 2 lists the scaling factors resulting from both approaches. The column "A priori" gives the factor $20000^{3/4}/Re_D^{3/4}$ which needs to be applied to scale the Kolmogorov length scale evaluated at $Re_D = 20000$ to the one at the higher Reynolds numbers according to the a priori estimation. The column "A posteriori" gives the factor $\eta_{K,LES,Re_D}/\eta_{K,LES,20K}$ which has to be applied to scale the Kolmogorov length scale according to the results of the conducted simulations. This comparison demonstrates that the dimensional analysis scaling of the dissipation rate in this flow is fairly good. This was not expected keeping in mind that the considered flow is in strong non-equilibrium.

## 6 Conclusions

We conducted highly resolved Large-Eddy Simulation of the flow around a wall-mounted cylinder at three moderate Reynolds numbers. The results were carefully validated and the

Table 2: A priori and a posteriori estimation of the Kolmogorov length scale.

| $Re_D$ | A priori | A posteriori |
|---|---|---|
| 20000 | 1 | 1 |
| 39000 | 0.61 | 0.70 |
| 78000 | 0.36 | 0.38 |

grid was fine enough to resolve approximately 70% of the total dissipation of turbulent kinetic energy. It was shown that the dissipation can be approximated by the pseudo dissipation. The evaluation of individual terms of the pseudo dissipation tensor implied that the pseudo dissipation and thus the small scale structures are not isotropic in such flow. At $Re_D = 20000$ the terms $\varepsilon_{p,13}$ and $\varepsilon_{p,31}$ were significantly larger than the other ones and maintained both amplitude and distribution when the Reynolds number was increased. The amplitudes of other terms ($\varepsilon_{p,12}$, $\varepsilon_{p,21}$ $\varepsilon_{p,23}$ and $\varepsilon_{p,32}$) - which were relatively small at $Re_D = 20000$ - increased with Reynolds number. This implies that the small scale structures become more isotropic with increasing Reynolds number, as the energy cascade becomes longer and the small scale structures are thus more likely to develop towards an isotropic state. The smallest terms of pseudo dissipation tensor were the ones in its trace ($\varepsilon_{p,ii}$) at all three Reynolds numbers investigated.

The estimation of the turbulent length scale $l_\varepsilon$ exhibited a strong spatial variability. In the region of the main vortex, the distribution of $l_\varepsilon$ had a similar c-shape as observed for the turbulent kinetic energy. Here, the amplitude of $l_\varepsilon$ was in the order of magnitude of the cylinder diameter $D$. In contrast to the region dominated by the approach flow, the Reynolds number dependency of $l_\varepsilon$ was weak in the region of the horseshoe vortex. This suggests that one has to step with caution is the turbulent length scale in the horseshoe vortex system shall be estimated by a model developed for equilibrium flow.

Our results implied that the magnitude of the Kolmogorov length scale can be reasonably predicted by an estimation based on the macro scales in the flow configuration considered. Furthermore, the Reynolds number scaling of the Kolmogorov length scale can be estimated fairly well by $1/Re^{3/4}$.

**Acknowledgements** We would like to thankfully mention fruitful discussions with Ulrich Jenssen, who conducted the companion experiments [19].

Compliance with Ethical Standards:

Funding: We gratefully acknowledge the financial support of the DFG under grant no. MA2062/11 and the computing time, which was granted by the Leibniz Computing Center (LRZ) of the Bavarian Academy of Sciences through grant no. pr84gi. No further funding was received.

Conflict of Interest: We declare that we have no conflict of interest.

## References

1. Adrian, R.J., Westerweel, J.: Particle Image Velocimetry. Cambridge University Press, Cambridge (2011)
2. Apsilidis, N., Diplas, P., Dancey, C.L., Bouratsis, P.: Time-resolved flow dynamics and reynolds number effects at a wall-cylinder junction. Journal of Fluid Mechanics **776**, 475–511 (2015)
3. Apsilidis, N., Khosronejad, A., Sotiropoulos, F., Dancey, C., Diplas, P.: Physical and Numerical Modeling of the Turbulent Flow Field Upstream of a Bridge Pier. In: International Conference on Scour and Erosion 6. Paris (2012)
4. Bose, S.T., Moin, P., You, D.: Grid-independent large-eddy simulation using explicit filtering. Physics of Fluids **22**(10), 105,103 (2010). DOI 10.1063/1.3485774

5. Cadot, O., Couder, Y., Daerr, A., Douady, S., Tsinober, A.: Energy injection in closed turbulent flows: Stirring through boundary layers versus inertial stirring. Physical Review E **56**(1), 427–433 (1997)
6. Devenport, W.J., Simpson, R.L.: Time-dependent and time-averaged turbulence structure near the nose of a wing-body junction. Journal of Fluid Mechanics **210**, 23–55 (1990)
7. Escauriaza, C., Sotiropoulos, F.: Reynolds Number Effects on the Coherent Dynamics of the Turbulent Horseshoe Vortex System. Flow, Turbulence and Combustion **86**(2), 231–262 (2011). DOI 10.1007/s10494-010-9315-y
8. Leschziner, M.: Statistical Turbulence Modelling for Fluid Dynamics – Demystified. Imperial College Press (2016)
9. Lilly, D.K.: The representation of small-scale turbulence in numerical simulation experiments. In: Proceedings of the IBM Scientific Computing Symposium on Environmental Sciences, IBM Form No. 320–1951, pp. 195 – 210 (1967)
10. Manhart, M.: A zonal grid algorithm for DNS of turbulent boundary layers. Comput. Fluids **33**(3), 435–461 (2004)
11. Nedić, J., Tavoularis, S.: Energy dissipation scaling in uniformly sheared turbulence. Phys. Rev. E **93**, 033,115 (2016). DOI 10.1103/PhysRevE.93.033115
12. Nicoud, F., Ducros, F.: Subgrid-Scale Stress Modelling Based on the Square of the Velocity Gradient Tensor. Flow, Turbulence and Combustion **62**(3), 183–200 (1999). DOI 10.1023/a:1009995426001
13. Paik, J., Escauriaza, C., Sotiropoulos, F.: On the bimodal dynamics of the turbulent horseshoe vortex system in a wing-body junction. Physics of Fluids **19**, 045,107 (2007)
14. Peller, N.: Numerische Simulation turbulenter Strömungen mit Immersed Boundaries. Ph.D. thesis, Technische Universität München (2010)
15. Peller, N., Duc, A.L., Tremblay, F., Manhart, M.: High-order stable interpolations for immersed boundary methods. Int. J. Numer. Methods Fluids **52**, 1175–1193 (2006)
16. Pope, S.B.: Turbulent Flows. Cambridge University Press (2011)
17. Richardson, L.F.: Weather Prediction by Numerical Process. Cambridge Univ. Press, Cambridge (1922)
18. Schanderl, W., Jenssen, U., Manhart, M.: Near-wall stress balance in front of a wall-mounted cylinder. accepted for publication by Flow Turbulence and Combustion (2017)
19. Schanderl, W., Jenssen, U., Strobl, C., Manhart, M.: The structure and the budget of turbulent kinetic energy in front of a wall-mounted cylinder. Journal of Fluid Mechanics **827**, 285321 (2017). DOI 10.1017/jfm.2017.486
20. Schanderl, W., Manhart, M.: Reliability of wall shear stress estimations of the flow around a wall-mounted cylinder. Computers and Fluids **128**, 16–29 (2016)
21. Schlichting, H., Gersten, K.: Boundary Layer Theory. Springer (2006)
22. Sreenivasan, K.R.: An update on the energy dissipation rate in isotropic turbulence. Physics of Fluids **10**(2), 528–529 (1998). DOI 10.1063/1.869575
23. Taylor, G.I.: Statistical theory of turbulence. Proceedings of the Royal Society of London A: Mathematical, Physical and Engineering Sciences **151**(873), 421–444 (1935). DOI 10.1098/rspa.1935.0158
24. Tennekes, H., Lumley, J.L.: A First Course in Turbulence. MIT Press, Cambridge, MA (1972)
25. Thormann, A., Meneveau, C.: Decay of homogeneous, nearly isotropic turbulence behind active fractal grids. Physics of Fluids **26**(2), 025,112 (2014). DOI 10.1063/1.4865232
26. Valente, P.C., Vassilicos, J.C.: The decay of turbulence generated by a class of multiscale grids. Journal of Fluid Mechanics **687**, 300340 (2011). DOI 10.1017/jfm.2011.353
27. Vassilicos, J.C.: Dissipation in turbulent flows. Annual Review of Fluid Mechanics **47**(1), 95–114 (2015). DOI 10.1146/annurev-fluid-010814-014637
28. Werner, H.: Grobstruktursimulation der turbulenten Strömung über eine querliegende Rippe in einem Plattenkanal bei hoher Reynoldszahl. Ph.D. thesis, Technische Universität München, München (1991)

# E. Appendix: Publication 5, summarised in chapter 10

# Wall shear stress scaling in front of a wall-mounted cylinder

**Wolfgang Schanderl[1], Ulrich Jenssen[1] Claudia Strobl[1] and Michael Manhart[1]†**

[1]Chair of Hydromechanics, Technische Universität München, Arcisstr. 21, 80333 München

(Received xx; revised xx; accepted xx)

This paper documents and discusses the Reynolds number scaling of the time average velocity field, turbulence structure and the wall shear stress of the flow in front of a cylinder-wall junction. The data were obtained by large-eddy simulations and particle image velocimetry in an open channel at Reynolds numbers of $Re_D = 20000$, 39000 and 78000.

The results indicate that in front of the cylinder, the amplitude of the friction coefficient scales with the square root of the Reynolds number $c_f \sim 1/\sqrt{Re_D}$ similar to the behavior of a Blasius boundary layer. We explain this scaling with the characteristic structure of the turbulent kinetic energy in the cylinder front and the quasi-laminar behavior of the near-wall flow in which no standard boundary layer dynamics can develop due to large flow acceleration.

**This manuscript is in a premature state.**

## 1. Introduction

One of the characteristics of the flow around a wall-mounted bluff body is the vertical pressure gradient in the body front, when a boundary layer approaches the body. Triggered by this pressure gradient, a down-flow transports high momentum fluid towards the bottom wall where the fluid is deflected in the upstream direction. Blocked by the oncoming boundary layer, this fluid recirculates and forms the so-called horseshoe vortex. However, some parts of the high momentum fluid close to the bottom wall constitute a jet (Devenport & Simpson 1990) which starts right in front of the bluff body, passes under the main horseshoe vortex and penetrates far upstream between the wall and the oncoming flow.

The wall jet causes an enhanced wall shear stress at the bottom wall (Dargahi 1989), which is challenging to estimate as the flow in the near-wall region in front of a wall-mounted bluff body is three dimensional and in a non-equilibrium state. Due to the large gradients of mean and turbulent stresses in all spatial directions, the boundary layer assumptions cannot be applied to model the wall shear stress (Schanderl *et al.* 2017*a*), but the data resolution has to be high enough to resolve the wall jet adequately. However, the three-dimensional boundary layer established by the wall jet is very thin and the thickness of the respective linear sublayer - the layer which has to be resolved to estimate the wall shear stress - is less than five wall units (Schanderl & Manhart 2016; Schanderl *et al.* 2017*a*). Thus it is not surprising that numerous previous studies have underestimated the amplitude of the wall shear stress in front of a bluff body (Schanderl & Manhart 2016).

Nevertheless, reviewing the existing literature on the flow around a wall-mounted bluff

---

† Email address for correspondence: michael.manhart@tum.de

body also reveals two issues which can facilitate the wall shear stress estimation. First, the distinct pattern of acceleration of the wall jet strongly affects the turbulence structure in front of the body and especially in the near-wall region (Devenport & Simpson 1990; Schanderl *et al.* 2017*b*). Due to the adverse pressure gradient in the streamwise direction in front of the cylinder, the fluid accelerates first before it decelerates when it faces the oncoming boundary layer (Devenport & Simpson 1990; Schanderl *et al.* 2017*a*). The acceleration gives rise to a negative normal production of turbulent kinetic energy (Devenport & Simpson 1990) which dominates the total production in this region of the jet (Schanderl *et al.* 2017*b*). In contrast, the deceleration of the jet triggers significant positive normal stress production (Devenport & Simpson 1990), which causes a strong increase of turbulent kinetic energy in that region (Devenport & Simpson 1990; Schanderl *et al.* 2017*b*). Though, this turbulent kinetic energy does not disperse towards the bluff body (Schanderl *et al.* 2017*b*), therefore the turbulence level contained by the down-flow is not enhanced and the level of turbulent kinetic energy between the main vortex and the bluff body in turn is relatively mild (Schanderl *et al.* 2017*b*).

The second issue which can be exploited to facilitate the wall shear stress estimation is the Reynolds number scaling of the vortex system. Even though there are some changes in the region of the main vortex with Reynolds number (the size and the position of the main vortex, increase of turbulent kinetic energy in the deceleration region of the jet), various studies document that the topology of the horseshoe vortex system is in general invariant to a moderate Reynolds number (Roulund *et al.* 2005; Apsilidis *et al.* 2015; Schanderl & Manhart 2016, 2017). As the vortex system changes only slightly with the moderate Reynolds number, this also must be the case for the influence of the vortex system on the wall jet and its acceleration. The negative production due to this acceleration as well as the calm turbulent kinetic energy in this region is maintained.

In the present study, we draw conclusions from the turbulence structure and its Reynolds number scaling in the near-wall region in front of a bluff body and propose a specific scaling law for the corresponding wall shear stress. To do so, we have conducted both large-eddy simulation and particle image velocimetry of the flow around a cylinder mounted vertically on the bottom wall of an open channel at three moderate Reynolds numbers. We document the Reynolds number scaling of the flow topology and the corresponding turbulence structure. Based on that, we investigated the Reynolds number scaling of the wall shear stress and explained the scaling behavior by the two issues mentioned above: the weak scaling of the outer flow and the calm turbulence in the near-wall region.

The paper is structured as follows. Section 2 presents the flow configuration considered. Sections 3 and 4 document the experimental and the numerical configuration respectively. The flow topology in front of the wall-mounted cylinder as well as the corresponding distribution of turbulent kinetic energy are presented in section 5 and 6 respectively. Finally, section 7 documents the wall shear stress distribution and a specific scaling law is proposed. The latter section also contains an explicit validation of the wall shear stress, including a grid study of the numerical results and measurements evaluated by two different post-processing algorithms.

## 2. Flow configuration

We investigated the flow around a circular cylinder mounted vertically on the bottom wall of the bottom wall of a water channel with free surface (figure 1). The considered Reynolds numbers were $Re_D = 20000$, $Re_D = 39000$ and $Re_D = 78000$ based on the diameter of the cylinder $D$ and the velocity averaged over the whole cross section of

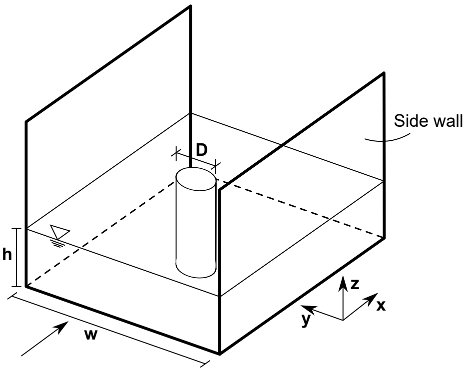

FIGURE 1. Flow configuration investigated. The sketch is taken from Schanderl *et al.* (2017*b*).

the approaching flow. The flow depth was $h = 1.5D$ for all three Reynolds numbers. However, the ratio of the width of the channel $w$ to the diameter $D$ had to be adjusted when the Reynolds number was increased. The width was $w = 11.7D$ at $Re_D = 20000$ and $Re_D = 39000$ and $w = 7.3D$ at $Re_D = 78000$. This difference resulted from experimental constrains: In the experiment, the absolute width of the flume was fixed but the large Reynolds number required a larger flow depth to keep the Froude number low. Since the flow depth to diameter ratio was considered to have a larger influence on the flow field around the cylinder than the width to diameter ratio, the first one was kept constant while the latter one was changed for the high Reynolds number case. To assess the influence of the width-to-diameter ratio, the $Re_D = 20000$ flow case was simulated for both widths $11.7D$ and $7.3D$ and only minor deviations between the two widths were observed. Furthermore, these deviations were significantly smaller than the changes with Reynolds numbers. The smaller aspect ratio of the water channel at $Re_D = 78000$ was therefore considered to have no major influence on the observations made in this study. The inflow condition was a fully-developed, turbulent open-channel flow with small Froude number. In fact, the Froude number was $Fr < 0.32$ in the experiments and infinitesimal in the simulation, since the free surface was approximated by a slip boundary condition, which prevented all deformations of the free surface.

The configuration considered in the scope of this study was the same as described in detail by Schanderl & Manhart (2016); Schanderl *et al.* (2017*b*,*a*); Schanderl & Manhart (2017). It was similar to the configuration investigated by Dargahi (1989), Escauriaza & Sotiropoulos (2011) and Apsilidis *et al.* (2015), which differ from ours in the ratio of boundary layer thickness to cylinder diameter. However, they were performed at the same range of Reynolds numbers.

## 3. Experimental configuration

Particle image velocimetry (PIV) was conducted in the laboratory of the Chair of Hydromechanics at the Technical University of Munich. The experimental setup was the same as the one employed by Jenssen *et al.* (2016); Schanderl *et al.* (2017*b*), who compared the PIV results at $Re_D = 39000$ to the corresponding large-eddy simulation (LES). In the following, the experimental setup is presented first (section 3.1) before the applied measurement techniques are discussed briefly (section 3.2).

### 3.1. *Experimental setup*

The flow configuration described in the previous section was reproduced in a $1.17m$ wide and $30m$ long flume, which was fed by a high-level tank (figure 2). The discharge was controlled by a magneto-inductive flow meter and the flow depth by a sluice gate

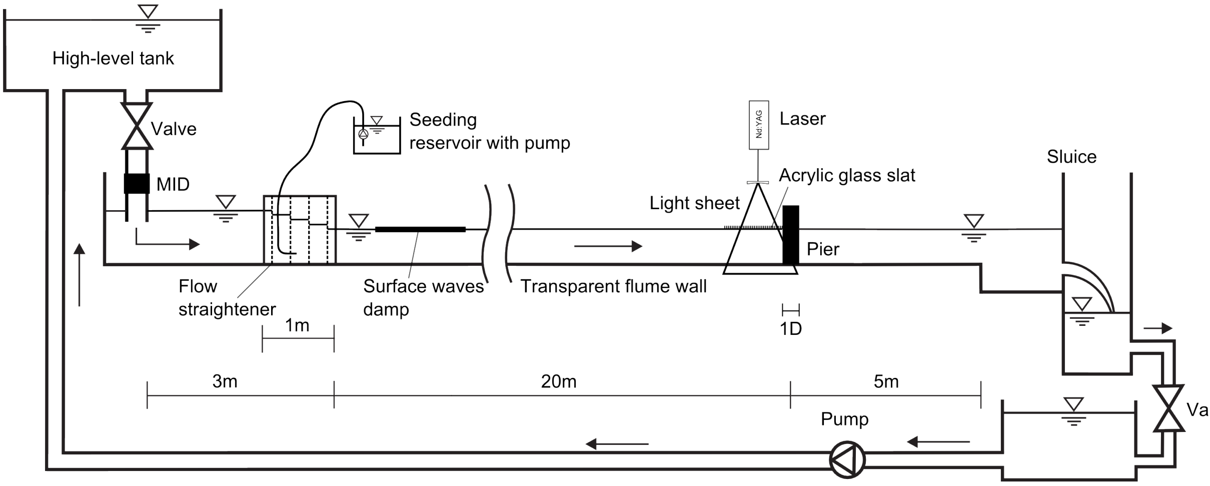

FIGURE 2. Sketch of the experimental configuration, taken from Pfleger (2011)

at the outlet of the flume. A flow straightener damped the disturbances at the inflow and a floating body the surface waves afterwards. Between this floating body and the cylinder, the flow developed naturally over approximately $20m$. The circular cylinder was placed vertically in the symmetry plane of the flume. At $Re_D = 20000$ and $Re_D = 39000$, the diameter of the cylinder was $D = 0.10m$ while it was $D = 0.16m$ at $Re_D = 78000$ owing to the necessity of an increased flow depth as discussed in section 2. Thus, the undisturbed inflow length was $200D$ at $Re_D = 20000$ and $Re_D = 39000$ and $125D$ at $Re_D = 78000$.

To enable the laser light to enter the water in a well-defined way from the top, a slightly submerged slat of acrylic glass was installed at the free surface in front of the cylinder. The slat was constructed such that its influence on the flow at the bottom wall was as small as possible. It had a length of $0.15m$ in the streamwise direction, a width of $0.05m$ in the spanwise direction and was submerged between $1mm$ and $5mm$ into the flow. As indicated by Schanderl *et al.* (2017*b*), the influence of the slat on the flow phenomena investigated in the scope of this study was small. However, there were some influences, which will be discussed in the remainder of this study.

### 3.2. *Measurement techniques*

We employed two-dimensional, two-component PIV in the symmetry plane in front of the cylinder. For the seeding hollow glass spheres with a diameter of $d_p = 10\mu m$ and a density of $\rho_p = 1100kg/m^3$ were given continuously into the inflow. The corresponding relaxation time was $\tau_p = d_p^2\rho_p/(18\nu\rho) = 6.1 * 10^{-6}s$ (Raffel *et al.* 2007), which was small compared to the macro-scale estimation of Kolmogorov time scale $\tau_K = \sqrt{\nu/\epsilon_{macro}} = 4.7 * 10^{-3}$ (Pope 2011) and thus allowed the particles to follow the flow without time delay. As discussed by Schanderl *et al.* (2017*b*); Schanderl & Manhart (2017) the macro-scale estimation of the dissipation of turbulent kinetic energy $\epsilon_{macro} = u_b^3/D$ was a conservative one. $u_b$ was the bulk velocity in the symmetry plane of the undisturbed flow, $\rho$ the water density and $\nu = 1.05 * 10^{-6}m^2/s$ the dynamic viscosity of the water at a water temperature of approximately $18°C$.

A $532nm$ Nd:YAG laser illuminated the particles by a light sheet with a thickness of $2mm$ in the spanwise direction. The light sheet entered the flow from the top through the slat of acrylic glass discussed above. The image pairs with a resolution of $2048 \times 2048px$ and a time delay of $700\mu s$ were recorded by a CCD camera which observed the flow through the glass sidewalls of the open channel. The used sampling rate of $7.25Hz$ was

| $Re_D$ | data points per diameter | pixel per diameter | f-number | focal length | recorded image pairs | valid vectors |
|---|---|---|---|---|---|---|
| 20000 | 339 | 2713 | 2.8 | $105mm$ | 20000 | 18500 |
| 39000 | 339 | 2713 | 2.8 | $105mm$ | 27000 | 24000 |
| 78000 | 551 | 4409 | 5.6 | $105mm$ | 46400 | 39000 |

Table 1. Data resolution and recorded image pairs of the conducted PIV. The numbers of valid velocity vectors refer to the numbers which were achieved in wide regions of the flow.

too low to resolve the the temporal evolution of turbulent structures, however, as in this study only time-averaged quantities were considered, this sampling rate was sufficient. The images were evaluated by a standard PIV algorithm with interrogation windows of $16 \times 16px$ which overlap by 50% and were deformed according to the local velocity gradient. In case of the detection of an invalid velocity vector, this individual $16 \times 16px$ interrogation window was replaced by the corresponding $32 \times 32px$ interrogation window with the same position of the center. The number of image pairs recorded and the achieved data resolution at each Reynolds number investigated are listed in table 1.

The standard PIV evaluation was complemented by the one of a single-pixel algorithm (Westerweel *et al.* 2004; Kähler *et al.* 2006; Strobl *et al.* 2016). This algorithm is not based on interrogation windows but provides a velocity vector for every individual pixel. As the probability to detect a particle at a individual pixel was significant smaller as the probability to detect a particle in an interrogation window, the number of valid samples at each pixel was in the single-pixel PIV was smaller than in an interrogation window in the standard PIV. Therefore the single-pixel results were more noisy. However, as the present results show the achieved statistical convergence was sufficient to complement the employed standard PIV and the LES. Furthermore, the larger data resolution allowed for resolving the wall and thus for an evaluation of the wall shear stress via the wall gradient.

## 4. Computational configuration

The computational configuration and the applied methods of the presented study were corresponding to the ones described by Schanderl & Manhart (2016); Schanderl *et al.* (2017*b*,*a*); Schanderl & Manhart (2017). In fact, the simulation at $Re_D = 39000$ was exactly the same as the one in the mentioned studies. The reliability of the simulation was discussed in detail by Schanderl & Manhart (2016) and the numerical results were compared to the experimental ones by Jenssen *et al.* (2016); Schanderl *et al.* (2017*b*).

In the following, the numerical methods are recapitulated (section 4.1) and the adjustments of the grids to match the individual Reynolds numbers are discussed (section 4.2). The influence of the subgrid-stress model on the solution is evaluated in section 4.3. A further validation of the numerical results is done in the remainder of this study by comparing them to the experimental ones (section 5 and 7) and by demonstrating the convergence of the wall shear stress over grid refinement (section 7).

### 4.1. *Numerical methods*

The LES was done employing our in-house code MGLET, which is a Finite Volume code with Cartesian grids on which the variables are arranged in a staggered way. Central differences were used for spatial approximation and a third order Runge-Kutta procedure for time integration. MGLET provides an algorithm to embed grids zonally for local

| $Re_D$ | cells per diameter<br>**horizontal**/vertical | grid spacing<br>$\Delta x^+/\Delta y^+/\Delta z^+_{wall}$ | grid<br>cells |
|---|---|---|---|
| 20000 | **148**/571 | **7.0/7.0**/1.8 | $166 \cdot 10^6$ |
| 39000 | **250**/1000 | **7.4/7.4**/1.9 | $400 \cdot 10^6$ |
| 78000 | **440**/1778 | **7.8/7.8**/1.9 | $1.6 \cdot 10^9$ |

TABLE 2. Grid resolution in inner and outer scaling in the region of interest around the cylinder for all three Reynolds numbers investigated. The wall shear stress applied for the evaluation of the wall units was taken from the approach flow.

grid refinement (Manhart 2004). Since the grid was Cartesian, the curved surface of the cylinder was represented by a conservative second order Immersed Boundary method (Peller *et al.* 2006; Peller 2010). The WALE model (Nicoud & Ducros 1999) furnished the modelling of the subgrid stresses. As in this model the turbulent viscosity decreases naturally towards the wall, no damping function had to be applied, which facilitates the use of an Immersed Boundary method.

### 4.2. *Computational grids*

A precursor grid with periodic boundary conditions in the streamwise direction simulated the fully-developed, turbulent open-channel flow which was applied by one-way coupling as inflow condition at the grid holding the cylinder. The free surface of the open channel was modelled by a slip boundary condition, which prevented all surface deformations and thus constituted an infinitesimal Froude number. The side walls and the bottom wall of the channel were represented by a no-slip boundary condition. First, the grid at $Re_D = 39000$ was designed. In order to achieve the required grid resolution in the region of interest around the cylinder we used locally embedded grids, each with a refinement factor of two. We successively refined the region around the cylinder until no substantial changes in the results, especially in the wall shear stress, was observed. This status was reached with three locally embedded grids, which corresponded to a total refinement factor of eight compared to the global grid. In addition, the grid was stretched in the vertical direction from the bottom wall by a factor smaller than 1%. Since this stretching was applied on the global grid solely, only every eighth cell of the finest locally embedded grid was augmented. The grid study at $Re_D = 39000$ was discussed by Schanderl & Manhart (2016); Schanderl *et al.* (2017*b*,*a*). To adapt the grid for $Re_D = 20000$ and $Re_D = 78000$, the grid was stretched and compressed respectively in such a way that the grid resolution in inner units (based on the wall shear stress of the approach flow) stayed the same. The grid study at $Re_D = 78000$ was discussed by Schanderl *et al.* (2017*c*); Schanderl & Manhart (2017) and is recapitulated in section 7. The same converging behavior was observed for $Re_D = 20000$, however, the respective grid study is not presented here. The resulting grid spacing of the finest local grids at each individual Reynolds number is listed in table 2. All data in the remainder of this paper was taken from the simulation with the finest grid at the corresponding Reynolds number except it is specified in a different way.

### 4.3. *Influence of the subgrid-stress model*

Figure 3a illustrates the ratio of the time-averaged modelled (turbulent) viscosity to the molecular viscosity $\langle \nu_t \rangle / \nu$ on a profile in the wall-normal ($z$-) direction in front of the cylinder. The streamwise position $x = -0.76D$ corresponded to the core of the main vortex at this Reynolds number $Re_D = 78000$. $\nu_t$ was evaluated for three different

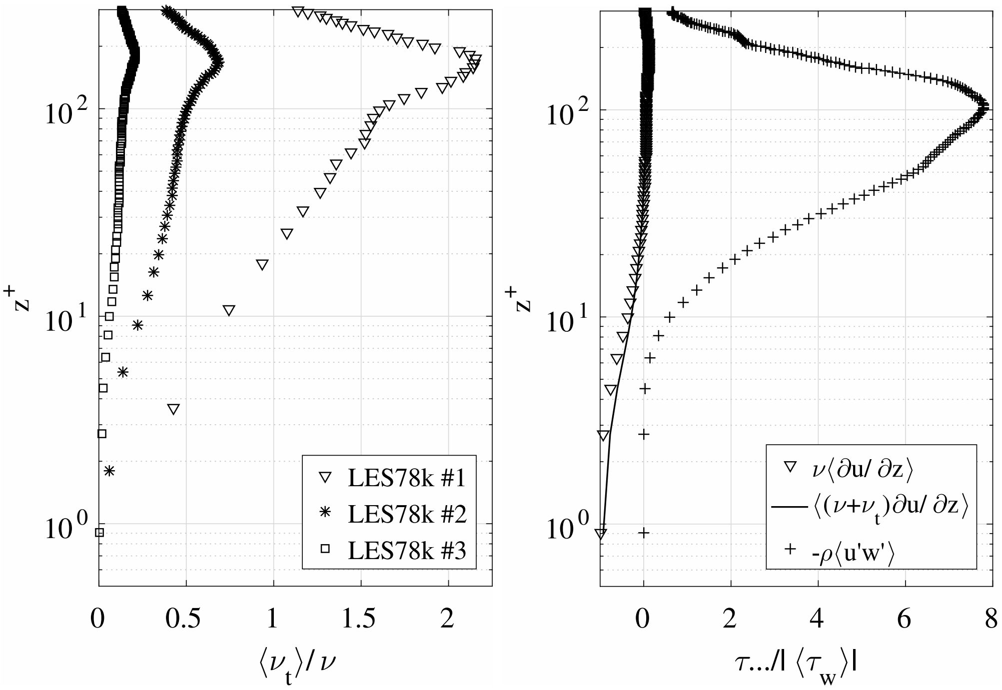

FIGURE 3. Time-averaged turbulent viscosity $\langle\nu_t\rangle$ taken from three different LES with different grid resolution (a) and contributors to the stress balance taken from the simulation with the finest grid LES78k #3 (b) on profiles in the wall-normal ($z$-) direction. The streamwise position $x = -0.76D$ corresponded to the center of the main vortex at the evaluated Reynolds number $Re_D = 78000$. The wall shear stress applied to evaluate $z^+$ was taken from the simulation with the finest grid LES78k #3.

simulations, each holding a different number of local grids for grid refinement. LES78k #1 refers to the simulation with only one locally embedded grid, while LES78k #2 held two of them. As LES78k #3 was refined by three local grids and the grid spacing was accordingly four times smaller than the one of LES78k #1 therefore. However, even though the data was taken from three different simulations, the wall units employed for normalizing the wall distance was based on the wall shear stress from the simulation with the finest grid LES78k #3 for all three profiles. This shall facilitate the comparison of the individual profiles.

In all three simulations the modelled viscosity decreased in the desired way with proximity to the wall. The maximum of $\langle\nu_t\rangle$ at $z^+ \approx 180$ indicated the position of the center of the main horseshoe vortex (figure 3a). In all three simulations, the modelled viscosity had a similar distribution but the amplitude decreased with approximately second order as the grid spacing was reduced.

Figure 3b exhibits the influence of this modelled viscosity on the stress balance. Evaluated were three contributors to the stress balance in the streamwise direction normalized by the local time-averaged wall shear stress $\langle\tau_w\rangle$ on a wall-normal profile at the same position as the profiles in figure 3a. However, the data evaluated in figure 3b was taken from the simulation with the finest grid LES78k #3 only. Evaluated were the viscous stresses excluding and including the modelled contribution $\nu\langle\partial u/\partial z\rangle$ and $\langle(\nu + \nu_t)\partial u/\partial z\rangle$ respectively as well as the resolved Reynolds shear stresses $-\rho\langle u'w'\rangle$. $u$ denotes the velocity in the streamwise ($x$-) direction while $w$ is the one in the wall-normal direction. $u'$ and $w'$ represent the corresponding velocity fluctuations. $\rho$ is the fluid density. Close to the wall, the viscous stresses dominated the flow. As the modelled viscosity was rather small in this region, the deviation between the viscous stresses excluding and including the modelled contribution was small, too. In the region of the main horseshoe vortex, where $\langle \nu_t \rangle$ had its maximum amplitude, there was a noticeable contribution of the subgrid-stress model to the viscous stresses. However, outside of the near-wall region the resolved Reynolds stresses were significantly larger than the viscous stresses at the Reynolds numbers investigated (3b).

A similar evaluation at $Re = 39000$ was done by Schanderl & Manhart (2016); Schanderl *et al.* (2017*a*). At this Reynolds number Schanderl *et al.* (2017*b*) showed that the fraction of modelled turbulent kinetic energy was smaller by two orders of magnitudes than the resolved one. Furthermore, an evaluation of the dissipation demonstrated that the modelled dissipation was less than 30% of the total dissipation in the region of interest around the cylinder (Schanderl *et al.* 2017*b*; Schanderl & Manhart 2017).

## 5. Flow topology

The focus of this study is on the wall shear stress and its Reynolds number scaling in the cylinder front. This section presents the flow topology, before the underlying turbulence structure is discussed in section 6 and the resulting wall shear stress in section 7.

Figure 4 shows the streamlines of the time-averaged flow field in the symmetry plane in front of the cylinder at the three Reynolds numbers investigated. The data in the left column was taken from the LES, the one in the right column from the PIV. From top to bottom the results correspond to $Re_D = 20000$, $Re - D = 39000$ and $Re_D = 78000$ respectively. The vertical pressure gradient induced by the boundary layer approaching the cylinder resulted in a down-flow, which was deflected when it met the bottom wall - most of it in the upstream direction, little towards the cylinder. The dividing streamline ended at stagnation point S3. Parts of the fluid moving in the upstream direction formed the main vortex V1 of the horseshoe vortex system on the one hand. On the other hand, parts of the fluid established a jet in the upstream direction along the bottom wall underneath V1. This jet dominated the behavior of the wall shear stress, as the further discussion will show. The blockage of the oncoming flow due to the vortex V1 forced the flow to separate from the bottom wall at stagnation point S2 (not shown in figure 4). Downstream of this stagnation point a weak recirculation zone established which was separated from V1 by stagnation point S1. The down-flow along the flow facing edge of the cylinder established a thin boundary layer, which separated from the cylinder at stagnation point S4 and formed a small vortex V3 directly at the wall cylinder junction. In general, the flow topology observed was in accordance to the ones documented in literature (Devenport & Simpson 1990; Agui & Andreopoulos 1992; Paik *et al.* 2007; Escauriaza & Sotiropoulos 2011; Apsilidis *et al.* 2015).

The Reynolds number dependency of the flow topology was rather weak. Both vortex V1 and stagnation point S1 moved slightly upstream thus away from the cylinder with increasing $Re_D$, which was in line with the observations by Agui & Andreopoulos (1992). In contrast, stagnation point S2 and the recirculation zone downstream of it were moving downstream towards the cylinder. This can be explained by the larger near-wall momentum of the approaching flow at the higher Reynolds numbers, which acted against the flow separation and delayed the separation. Therefore, V1 and the weak recirculation zone moved together with increasing Reynolds number in the observed range of Reynolds numbers.

The only vertical shift was observed at the small corner vortex V3 in the simulation, which was largest at $Re_D = 20000$. As this shift was not observed in the experiment, we speculated that it was caused by a grid resolution which was too coarse to resolve the thin boundary layer along the cylinder and V3 properly in the LES at $Re_D = 20000$. In both numerical and experimental data sets at $Re_D = 78000$ (figure 4 e and f) the weak

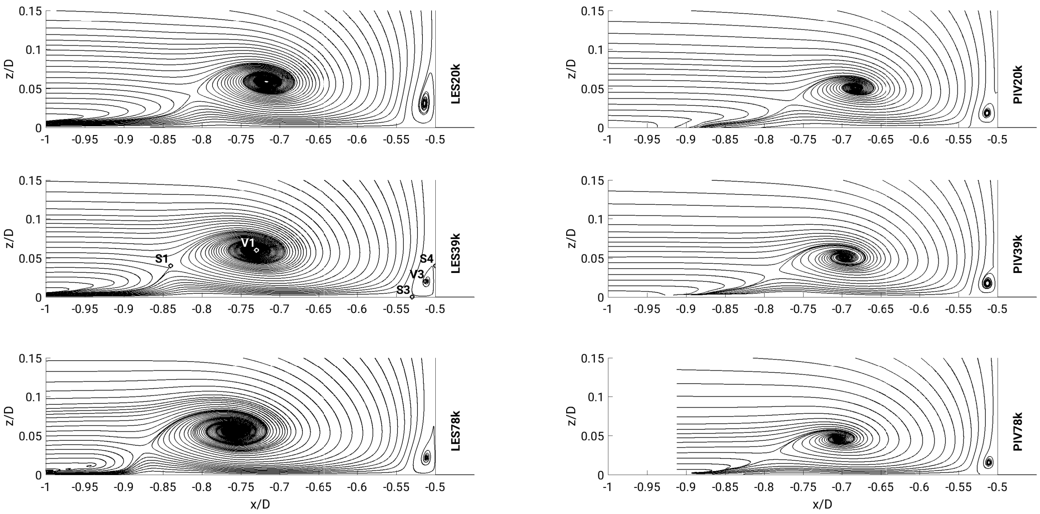

FIGURE 4. Streamlines of the time-averaged flow field in the symmetry plane in front of the cylinder for (a,b) $Re_D = 20000$, (c,d) $Re_D = 39000$ and (e,f) $Re_D = 78000$, computed from LES (left column) and PIV (right column).

recirculation zone between S2 and S1 formed a vortex, as the streamlines performed a full turn. Furthermore, in the LES the recirculation zone was splitting up into a train of several small sub-vortices. However, Agui & Andreopoulos (1992), who did measurements of the horseshoe vortex system at $Re_D = 10^5$ and $Re_D = 2.2 * 10^5$ stated that the corresponding instantaneous flow structures "are very quickly evolving in time and space making it impossible to depict through time-average measurements." Considering this, a possible explanation for the difference between LES and PIV is a more dynamic flow behavior at the highest Reynolds number, which arose the necessity for a longer sampling time to achieve fully-converged statistics.

The accordance of the flow topology between LES and PIV was satisfying. However, in the experiment the main vortex V1 was smaller and located closer to the cylinder at all Reynolds numbers. An investigation of the flow topology over the whole flow depth revealed that in the experiment the stagnation point at the flow facing edge of the cylinder was not located at the very top at $z = 1.5D$ (where it was in the simulation) but at $z \approx 1.25D$. As discussed in section 3, a horizontal slat of acrylic glass had to be employed at the free surface in the experiment to allow the laser light to enter the fluid in a well-defined way. Along this slat a thin boundary layer developed, which caused a reduced boundary layer thickness of the approaching flow. As a consequence, the boundary layer thickness to diameter ration $\delta/D$ was smaller in the experiment than in the simulation, which can explain the smaller vortex system in the experiment.

When discussing the bi-modality of the vortex system, Devenport & Simpson (1990) observed that the upstream-directed jet along the bottom wall under vortex V1 has a distinct acceleration pattern. Figure 4 indicates this pattern by the decreasing and increasing distance between two neighboring streamlines, where a decreasing distance suggests acceleration and vice versa. Starting at stagnation point S3, fluid close to the bottom wall accelerated in the negative $x$-direction. The acceleration was largest right above the wall. The fluid decelerated afterward before it accelerated again and merged with the recirculation zone upstream of the main vortex or was transported out of plane in the spanwise direction. As Schanderl *et al.* (2017*b*) pointed out, this distinct pattern of acceleration directly affected the production of turbulent kinetic energy and thus on the distribution of turbulent kinetic energy itself. How this acceleration pattern changed

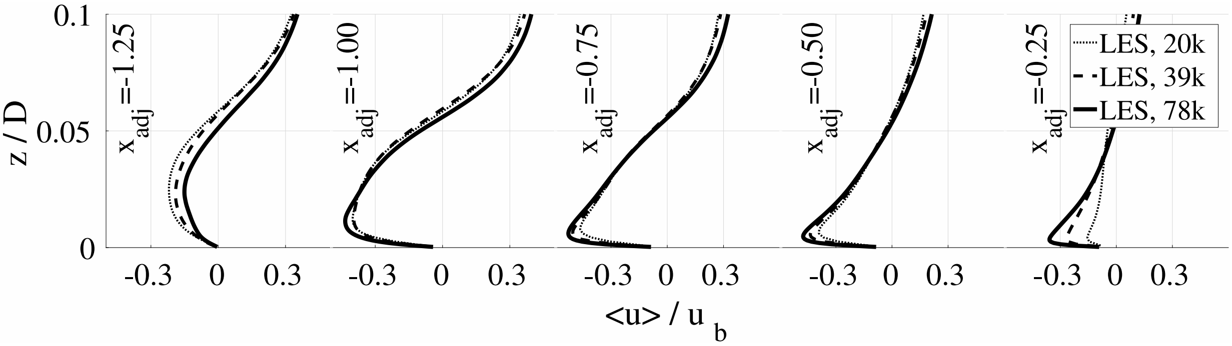

FIGURE 5. Wall-normal profiles of the streamwise velocity component normalized by he bulk velocity $\langle u\rangle/u_b$ in the symmetry plane in front of the cylinder at different positions of the adjusted coordinate $x_{adj}$ taken from the LES.

| $x_{adj} = \frac{x-x_c}{x_c-x_{V1}}$ | 20000 | 39000 | 78000 |
|---|---|---|---|
| 0.0 | -0.50D | -0.50D | -0.50D |
| -0.25 | -0.55D | -0.56D | -0.57D |
| -0.5 | -0.61D | -0.63D | -0.63D |
| -0.75 | -0.66D | -0.67D | -0.70D |
| -1.0 | -0.71D | -0.73D | -0.76D |
| -1.25 | -0.76D | -0.79D | -0.83D |

TABLE 3. Adjusted x-positions of the velocity profiles in figure 5.

with Reynolds number is discussed in the remainder of this section. The consequences of the acceleration pattern on the turbulence structure is pointed out in section 6.

Figure 5 shows profiles of the streamwise velocity component normalized by the bulk velocity $\langle u\rangle/u_b$ at five positions inside the wall jet in the symmetry plane in front of the cylinder. The data was taken from the LES with the finest grid at each Reynolds number. Since the position of vortex V1 changed slightly with Reynolds number, we addressed velocity profiles according to their streamwise position relative to the vortex core of V1 $x_{V1}$ and the flow facing edge of the cylinder $x_c = -0.5D$, which resulted in an adjusted streamwise coordinate $x_{adj}$

$$x_{adj} = \frac{x - x_c}{x_c - x_{V1}} \quad . \tag{5.1}$$

$x_{adj} = 0$ corresponded to the flow facing edge of the cylinder, while $x_{adj} = -1$ was the position of the vortex core of V1. The position of vortex V1 did not change in the wall normal direction, thus a comparable scaling was not applied on the $z$-coordinate. For the profiles evaluated in figure 5, the positions in standard coordinates $x/D$ for each Reynolds number are listed in table 3.

In figure 5 the upstream-directed wall jet which established a boundary layer along the bottom wall is indicated by the negative $\langle u\rangle/u_b$ close to the wall. The peak velocity of the jet at a certain streamwise position is denoted as $u_\delta$ and the corresponding wall distance $\delta$. In the following, the behavior of the jet is described in general first. Afterwards, the differences between the Reynolds numbers are discussed.

Starting from the cylinder at $x_{adj} = 0$, $u_\delta$ increased with increasing distance to the cylinder until it reached a maximum of $u_\delta/u_b \approx 0.5$ at $x_{adj} = -0.75$. Between the cylinder and $x_{adj} = -0.75$, the wall distance of the distinct peak was almost constant at $\delta = 0.004D$. However, with increasing distance from the cylinder the peak became broader and the jet widened up in the vertical direction. When following the jet further in the upstream direction from $x_{adj} = -0.75$ to the position of the vortex core ($x_{adj} = -1$), the fluid slightly decelerated and the peak lifted off the bottom wall. Under V1 at $x_{adj} = -1$, the maximum velocity of the jet was located at $\delta = 0.013D$ above the wall. After passing V1, the jet decelerated tremendously and further lifted off the bottom wall, which is also visible in figure 4 where the streamlines turn away from the wall. At $x_{adj} = -1.25$, $u_\delta$ was smaller by a factor of two approximately compared to the velocity at $x_{adj} = -1$. At all positions, the flow direction changed approximately at the height of the core of the main vortex V1 at $z_{V1} = 0.06D$.

As figure 5 reveals, there were some differences in the velocity profiles between the Reynolds numbers. At $x_{adj} = -0.25$ $u_\delta$ was more than twice as large at $Re_D = 78000$ than at $Re_D = 20000$. Since vortex V1 shifted upstream with increasing Reynolds number the length scale of the adjusted coordinate system $x_c - x_{V1}$ was larger at the high Reynolds number. However, stagnation point S3 stayed in its position at $x_{S3} = 0.53D$ for all Reynolds numbers investigated. The result was that the position $x_{adj} = -0.25$ was significantly closer to stagnation point S3 at the lowest Reynolds number than it was at the highest (table 3). Since the acceleration process started upstream of S3 and the velocity was small at this stagnation point, it is nearby that the velocity profile at a lower Reynolds number held a smaller amplitude than the velocity profile at a higher Reynolds number at $x_{adj} = -0.25$.

Even though between $x_{adj} = -0.25$ and the position of the vortex center at $x_{adj} = -1.0$ $u_\delta$ was consistently largest at $Re = 78000$ and smallest at $Re = 20000$ the velocity difference was small. However, there were notable differences in the deceleration region upstream of V1 as $\langle u\rangle/u_b$ was significantly smaller at the highest Reynolds number at $x_{adj} = -1.25$. The deceleration thus increased with Reynolds number, which is in accordance to the observation that vortex V1 and the upstream recirculation zone moved closer together with increasing Reynolds number (figure 4). However, it should be noted that this change of the deceleration at $x_{adj} = -1.25$ with Reynolds number was emphasized by the adjusted coordinate system. Again, the corresponding length scale $x_c - x_{V1}$ was largest and $x_{adj} = -1.25$ was furthest upstream at the highest Reynolds number. An investigation of the distribution and amplitudes of the velocity gradient $\partial\langle u\rangle/\partial x * D/u_b$ indicated nearly no notable differences when the Reynolds number was changed. In the respective region the gradient of $\langle u\rangle$ in the streamwise direction increased only mildly with Reynolds number.

In figure 5 $u_\delta$ was largest at $x_{adj} = -0.75$. Using this velocity and the respective wall distance $\delta$ to estimate the Reynolds number of the boundary layer caused by the wall jet along the bottom wall $Re_\delta = u_\delta\delta/\nu$ gave $Re_\delta = 80$ in LES20k, $Re_\delta = 140$ in LES39k and $Re_\delta = 240$ in LES78k. These $Re_\delta$ were remarkably low and suggested a laminar near-wall flow. In addition, it should be noted that $Re_\delta$ approximately doubled as $Re_D$ was doubled, which indicated that the Reynolds number $Re_\delta$ scaled with the global Reynolds number $Re_\delta \sim Re_D$.

## 6. Turbulent kinetic energy

In such flow the distribution of the turbulent kinetic energy $k$, which is defined as

$$k = \frac{1}{2}(\langle u'^2\rangle + \langle v'^2\rangle + \langle w'^2\rangle) \quad , \tag{6.1}$$

has a distinct c-shape (Devenport & Simpson 1990; Paik *et al.* 2007; Apsilidis *et al.* 2015; Schanderl *et al.* 2017*b*). The upper branch of the c is formed by a peak of turbulent kinetic energy in the region of the main vortex V1, from where a leg-like peak reaches

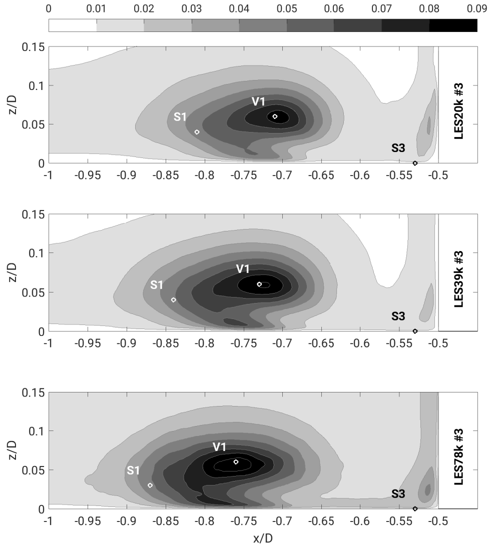

FIGURE 6. Turbulent kinetic energy $k/u_b^2$ in the symmetry plane in front of the cylinder for from top to bottom (a) $Re = 20000$, (b) $Re = 39000$ and (c) $Re = 78000$.

towards the bottom wall and thus forms the lower branch of the c. To the upper branch the fluctuations of the vertical velocity component $w'$ give a strong contribution, while the lower branch is due to large fluctuations in the streamwise direction $u'$ in first line (Devenport & Simpson 1990; Apsilidis *et al.* 2015; Schanderl *et al.* 2017*b*). The lower branch is located where the jet decelerates and as the amplitude of $u'$ increases with Reynolds number here the lower branch of the c-shape becomes more pronounced consequently (Apsilidis *et al.* 2015).

The same features as documented in literature were observed in the presented study (figure 6). In the region covered by the main vortex V1, $k$ peaked at $k/u_b^2 \approx 0.09$. The amplitude of this peak increased slightly with Reynolds number, however, this change was small. In contrast, the increase of $k$ with Reynolds number was noticeable in the lower branch, which was the only region showing such a strong scaling. While the maximum here was $k/u_b^2 \approx 0.05$ at $Re_D = 20000$, it was $k/u_b^2 \approx 0.06$ at $Re_D = 39000$ and $k/u_b^2 \approx 0.07$ at $Re_D = 78000$. As the PIV was two dimensional only and thus did not provide velocity fluctuations in the spanwise ($y$-) direction, the PIV data is not presented here. However, the accordance of the inplane turbulent kinetic energy $k_{ip} = 1/2(\langle u'^2\rangle + \langle w'^2\rangle)$ evaluated by LES and PIV was satisfying, which was true for both amplitude and distribution. A detailed comparison and discussion of the corresponding LES and PIV data at $Re_D = 39000$ was done by Schanderl *et al.* (2017*b*).

The presented distribution of turbulent kinetic energy is not novel. However, we present it in the scope of this study not only to underline the accordance of our results with those documented in literature, but also to point out that there was a region of rather calm turbulence between the main vortex V1 and the cylinder (figure 6). Even though the horseshoe vortex system was violently turbulent, this turbulence did not disperse into the region where the down-flow entered the vortex system. Here the turbulent kinetic energy was of the same amplitude as in the approach flow. Furthermore, the rather calm turbulence was maintained when the down-flow was deflected and formed a jet along the bottom wall in the upstream direction.

This calm turbulence is further documented by figure 7, in which instantaneous samples of the horseshoe vortex system are illustrated by isosurfaces of the Q-criterion. The Q-criterion, which was evaluated for a value of $Q\nu D/u_b^3 = 0.035$ between $z = 0$ and $z = 0.15D$, is the second invariant of the velocity gradient tensor and can be used to

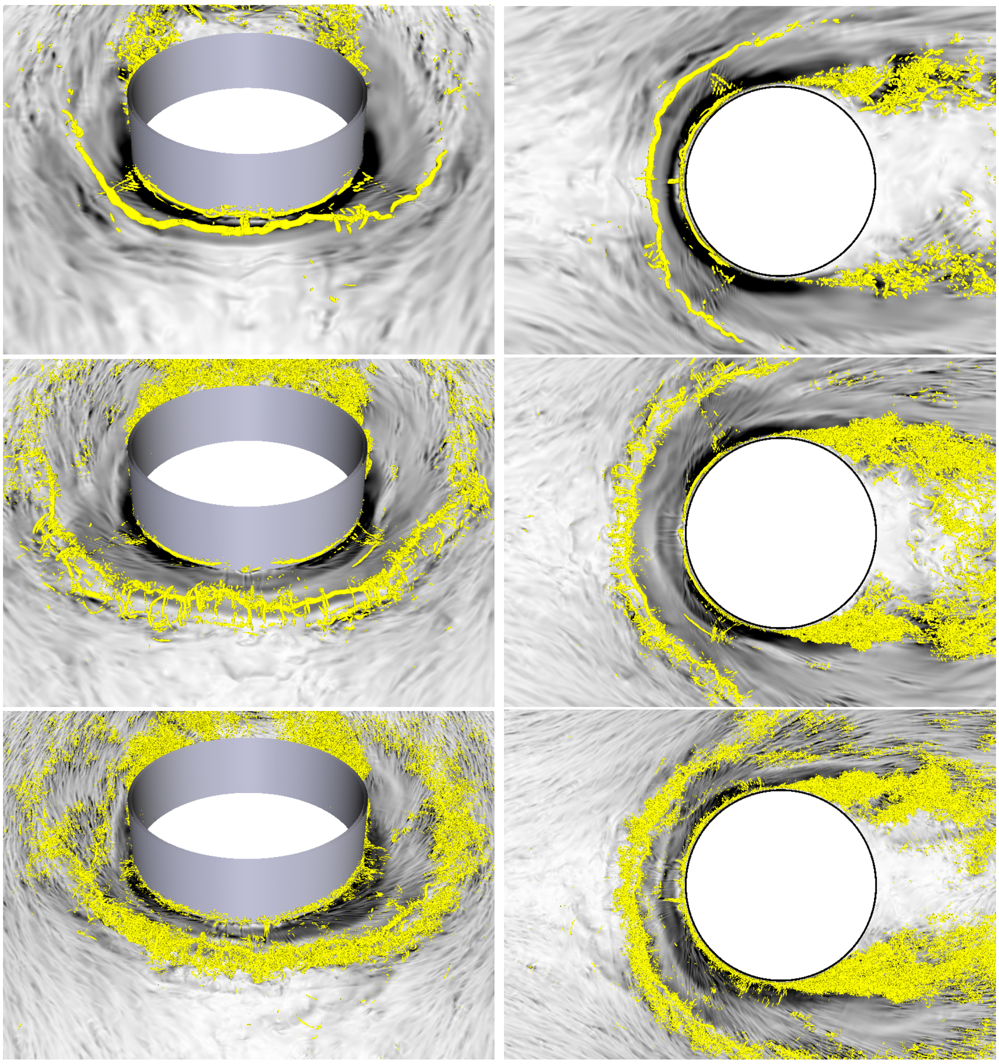

FIGURE 7. Isosurface of the Q-criterion $Q\nu D/u_b^3 = 0.035$ at (a,b) $Re = 20000$, (c,d) $Re = 39000$ and (e,f) $Re = 78000$, computed from LES. The bottom wall is colored by the friction coefficient $c_f$.

identify vortical structures. In addition, the bottom wall was colored by the instantaneous friction coefficient $c_f = \tau_w/(0.5\rho u_b^2)$ of the corresponding time step in all three instances of figure 7. The top row in figure 7 is $Re_D = 20000$ and the bottom row $Re_D = 78000$. At all three Reynolds numbers one can spot the main vortex V1 wrapping around the cylinder. At $Re_D = 39000$ one can also identify secondary vortices wrapping around the main vortex. However, as the vortical structures became smaller in general with increasing Reynolds number, these secondary vortices were not captured by the evaluated thresholds of $Q$ at $Re_D = 20000$ and $Re_D = 78000$. Figure 7 reveals that there were no vortical structures which can be visualized by the chosen threshold of $Q$ in the region where the down-flow enters the vortex system and that this did not change with Reynolds number. Furthermore, in the discussed region the corresponding sample of the friction coefficient $c_f$ was relatively smooth. Upstream of V1 and downstream of the cylinder the pattern of $c_f$ was significantly smaller-sized than in the region between V1 and the cylinder (figure 7). In addition, it is interesting to note that this smooth pattern was not only observed in front of the cylinder but expanded lateral and covered the whole area defined by the semi-circular shape of the vortex and the cylinder.

The smooth pattern of $c_f$ indicated the absence of small-scale turbulence in the near-wall flow between V1 and the cylinder and in fact the turbulent kinetic energy of the

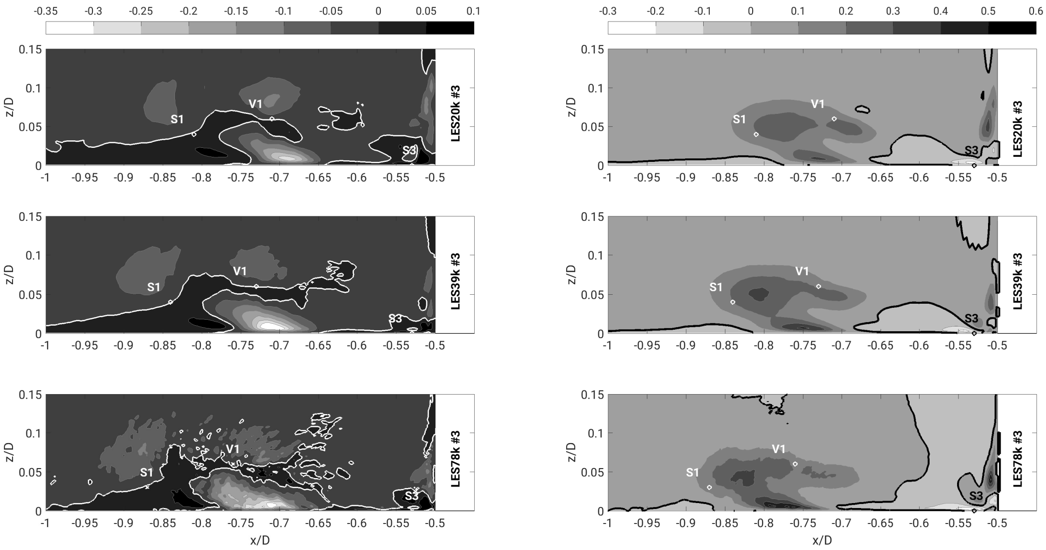

FIGURE 8. Convection $CD/u_b^3$ (left column) and production $PD/u_b^3$ (right column) of turbulent kinetic energy in the symmetry plane in front of the cylinder for $Re = 20000$ (a and b), $Re = 39000$ (c and d) and $Re = 78000$ (e and f). The thick isolines mark $P = 0$ and $C = 0$ respectively.

down-flow did not increase when it was deflected in the upstream direction at the bottom wall and formed the jet along the wall. This can be visualized be the convection of turbulent kinetic energy $C$, which is defined as (Pope 2011)

$$C = -\langle u_i \rangle \frac{\partial k}{\partial x_i} \quad . \tag{6.2}$$

The convection is not only a transport mechanism but also indicates the increase ($C < 0$) and the decrease ($C > 0$) of turbulent kinetic energy along a streamline. $C$ in the symmetry plane in front of the cylinder is shown in figure 8 (left column) for all three Reynolds numbers investigated. The white isoline marks $C = 0$ and thus separates the regions of increasing $k$ from those of decreasing $k$. The convection held its largest amplitude in the region close to the bottom wall where the wall jet decelerated at $x \approx -0.7D$. In the other regions in front of the cylinder, the amplitude of $C$ was rather small, especially in the region of the down-flow. This proofs that the turbulence level did not increase when the outer flow entered the vortex system. In fact, close to the bottom wall where the down-flow was deflected and further upstream where the jet accelerated, the convection was positive and thus indicated a decrease of turbulent kinetic energy. This decrease was observed at all Reynolds numbers investigated, as the corresponding region of positive $C$ did not change with Reynolds number (figure 8, left column). However, this behavior is self-evident considering that neither the flow topology nor the distribution of turbulent kinetic energy changed significantly with Reynolds number.

In the budget of turbulent kinetic energy, the production term $P$ represents the transfer of kinetic energy from the mean flow to the turbulent fluctuations (when $P > 0$) and vice versa (when $P < 0$) (Pope 2011):

$$P = -\langle u_i' u_j' \rangle \frac{\partial \langle u_i \rangle}{\partial x_j} \tag{6.3}$$

The largest amplitude of negative $P$ was located upstream of stagnation point S3, and as the jet decelerated $P$ turned positive at $x \approx -0.7D$ (figure 8, right column). The local maximum in this zone of positive production increased significantly with Reynolds number, it was $PD/u_b^3 \approx 0.3$ at $Re_D = 20000$, $PD/u_b^3 \approx 0.4$ at $Re_D = 39000$ and $PD/u_b^3 \approx 0.5$ at $Re_D = 78000$. This production rate increasing with $Re_D$ was the source of the increase of both $k$ and $C$ in the lower branch of the c-shape (figure 6figure 8, left column respectively).

The production in front of the cylinder in the region of the jet along the bottom wall is dominated by the normal stress production in streamwise direction $P_{11} = -\langle u'u' \rangle \partial \langle u \rangle / \partial x D/u_b^3$ Devenport & Simpson (1990); Schanderl *et al.* (2017*b*). This term is positive if the flow decelerates and vice versa. Recall the distinct pattern of acceleration of the upstream-directed wall jet (figure 4 and 5). The fluid accelerated from stagnation point S3 at $x = -0.53D$ in the negative $x$-direction until it reached the position under V1. Since $P_{11}$ is the dominating contributor to $P$ in the region of the wall jet, also $P$ is negative where the wall jet accelerates (figure 8, right column).

In the acceleration zone of the wall jet upstream of S3, the similarity of the region of positive $C$ (and thus decreasing $k$) and the region of negative $P$ was significant (figure 8). Both distributions had a shape like a spike which reached far upstream along the wall to the region where the jet decelerated again. This similarity suggests that the acceleration of the wall jet, which caused the negative $P_{11}$ thus the negative $P$, induced the decrease or at least prevented an increase of turbulent kinetic energy in the near-wall region. As a consequence, the flow between the main vortex V1 and the cylinder was of rather calm turbulence. How this calm turbulence determined the scaling of the wall shear stress is discussed in the following section.

## 7. Wall shear stress

In the previous section, it was discussed how the flow topology and the turbulence structure in the cylinder front were linked. In this section it is described how this turbulence structure affected the wall shear stress scaling. However, owing to the sensitivity of the wall shear stress to data resolution and the evaluation algorithm, we will start with an explicit validation of the wall shear stress.

### 7.1. *Validation of the wall shear stress*

At each Reynolds number investigated a grid study was conducted to proof the convergence of the results with grid refinement. The grid study at $Re_D = 78000$ is exemplified in figure 9a, which documents the friction coefficient $c_f = \langle \tau_w \rangle / (0.5 \rho u_b^2)$ in the symmetry plane in front of the cylinder. Again, the data referred to as LES78k #1 was taken from the simulation with one locally embedded grid, the data referred to as LES78k #2 from the simulation with two of them and the data named LES78k #3 stems from a simulation with three local grids. Each local grid refined the grid spacing by a factor of two. The experimental data SPPIV78k refers to PIV data evaluated by the single-pixel algorithm. Negative values indicate backflow regions. Because of the small corner vortex V3 there was a thin region of positive wall shear stress close to the cylinder. The broad peak of large negative $c_f$ was caused by the upstream-directed jet along the bottom wall and the region of weak negative $c_f$ further upstream by the weak recirculation zone upstream of the main vortex V1.

There were some differences between the solution of LES78k #1 and LES78k #2 in the shape of the broad, which has a single-peak shape in LES78k #1 and a double-peak shape in LES78k #2. Furthermore, LES78k #1 was too coarse to resolve the small corner vortex V3. However, the solution of LES78k #2 followed the one of LES78k #3 in a satisfying way. In fact, the only substantial difference was in the region of the corner vortex V3. LES78k #2 did not resolve this narrow peak accurately and therefore underestimated its amplitude. Nevertheless, the maximum amplitude did not increase with grid refinement, which indicated that the viscous sublayer was resolved. This was the case for all three Reynolds numbers. The assumption of a wall-resolved LES was further supported by an investigation of the near-wall velocity profiles in front of the cylinder at $Re_D = 39000$ (Schanderl *et al.* 2017*a*). We considered the simulation converged over grid spacing and omitted further refinement. As long as not specified in a different way, all data in the remainder of this paper was taken from the simulation with the finest grid at the respective Reynolds number.

Figure 9a also includes $c_f$ evaluated from the experiment by the single-pixel algorithm (SPPIV78k). This algorithm has the advantage of being based on single pixels instead of interrogation windows, which provides higher data resolution (Westerweel *et al.* 2004; Kähler *et al.* 2006; Strobl *et al.* 2016). By applying this algorithm a similar wall resolution as in the LES was achieved. The large scatter in the single-pixel data was owed to the reduced number of samples compared to an interrogation window method. As the vortex system in the experiment was located closer to the cylinder (figure 4), the peak of negative wall shear stress caused by the wall jet was less broad as in the simulation. Because of the scatter, it was hard to estimate the differences of the amplitude of SPPIV78k and LES78k #3. However, we present the SPPIV78k data to explain the difference in the amplitude compared to the wall shear stress evaluated by the standard PIV algorithm, which is plotted in figure 9b. As the standard algorithm used interrogation windows of $16 \times 16px$, the data resolution at the wall was coarser than the one of LES78k #3 and SPPIV78k. Therefore, the amplitude of the wall shear stress in PIV78k was smaller by a factor of approximately two, even though the shape of the distribution was in accordance to the other data sets. However, when $c_f$ was evaluated based on velocities from SPPIV78k taken not from the data point closest to the wall but from the eighth pixel above the wall (which corresponded to half the window size in the standard PIV), both shape and amplitude were matching in a satisfying way (figure 7.1b). Furthermore, evaluating $c_f$ from LES78k #3 based on velocities with a similar wall distance as the eighth pixel in the PIV data indicated accordance to the experiment as well. We thus concluded that wall shear stresses estimated by experiment and simulation confirm each other. The existing differences were explained by a smaller vortex system in the experiment and an insufficient wall resolution in the standard PIV data.

### 7.2. *Reynolds number dependence of the wall shear stress*

In the previous sections we have shown that the turbulence structure was in general independent of the Reynolds number within the investigated range. Solely in the region where the wall jet decelerated an increase of turbulent kinetic energy with Reynolds number was observed. In the following we propose that the friction coefficient in front of the cylinder scales with the square root of the Reynolds number $c_f \sim 1/\sqrt{Re_D}$ similar to a Blasius boundary layer and explain this behavior by the discussed turbulence structure.

Figure 10a documents the simulated friction coefficients $c_f$ at all three Reynolds numbers investigated taken from the LES. The distribution of the friction coefficient was similar at all three Reynolds numbers. As the wall shear stress was normalized by $0.5\rho u_b^2$ (figure 10a), it decreased with increasing Reynolds number. This was also observed for the wall shear stress amplification factor by Roulund *et al.* (2005) in Reynolds-averaged simulations. However, it should be noted that the amplification factor is defined as the wall shear stress normalized by the undisturbed wall shear stress of the approaching flow. In Figure 10b we present the friction coefficient multiplied with the square root of the Reynolds number. In this normalization, the maximum amplitudes in this region match each other and indicate a scaling of the friction coefficient with the inverse of the square

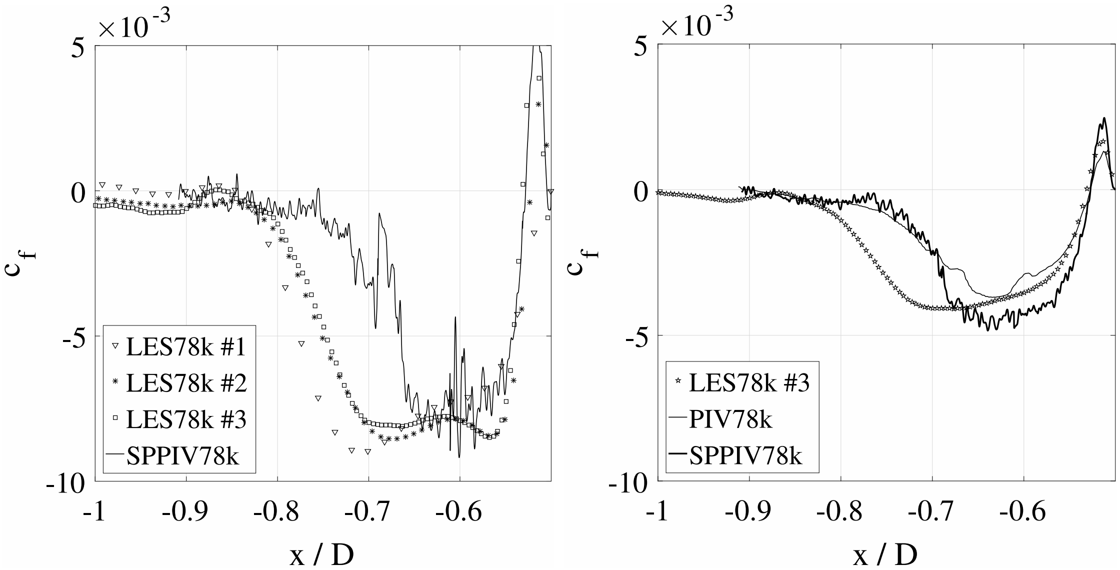

FIGURE 9. Friction coefficient $c_f$ in the symmetry plane in front of the cylinder at $Re_D = 78000$. (a) from three different LES with varying levels of grid refinement and single-pixel PIV and (b) from LES78k #3 and single-pixel PIV evaluated based velocities at different wall distances and PIV. For reasons of visibility, only every second data point is plotted in case of symbols.

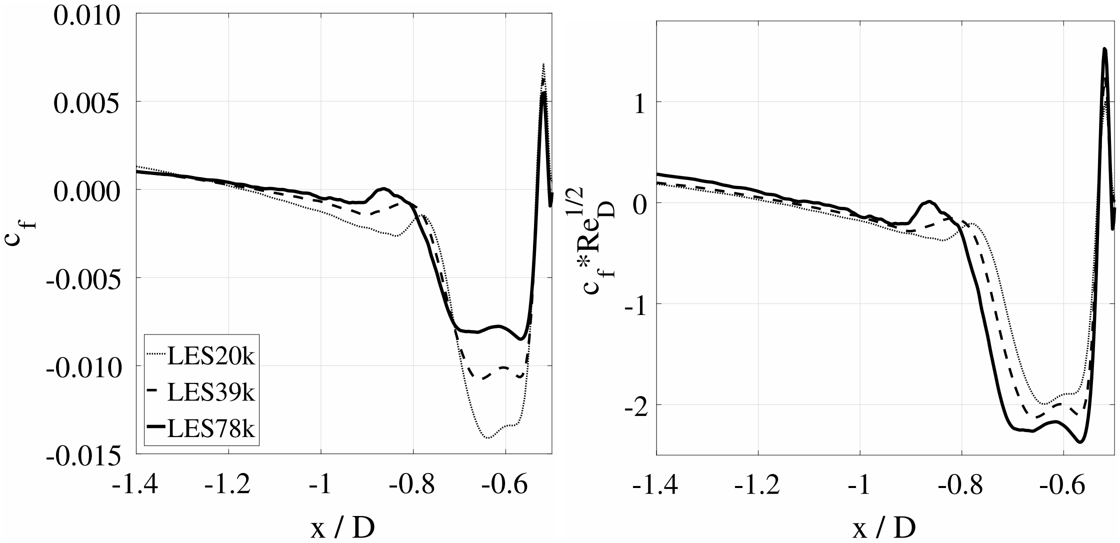

FIGURE 10. Friction coefficient in the symmetry plane in front of the cylinder, taken from the LES.

root of the Reynolds number $c_f \sim 1/\sqrt{Re_D}$. Furthermore, even though the amplitude was different in the standard PIV data and the results were more noisy in the single-pixel PIV data, the same scaling behavior of the wall shear stress was observed in these data sets (figure 11 and 12 respectively).

To evaluate if this scaling behavior is globally valid for the wall shear stress at the bottom wall around a wall-mounted cylinder, we evaluated the profiles of $c_f\sqrt{Re_D}$ at an angle of 54° and 90° with respect to the symmetry plane taken from the LES (figure 13). At 54° the global maximum of $c_f$ was located (Schanderl & Manhart 2016). The edge of the cylinder was at $r = 0.5D$ and $y = 0.5D$ respectively. The strong velocity overshoot next to the cylinder led to a large wall shear stress amplification. Nevertheless, this peak had a width of about $0.15D$ only and its amplitude was decreasing fast with the distance to the cylinder. At an angle of 54°, the friction coefficient scaled with the proposed scaling behavior while this was not the case lateral of the cylinder at 90°, which

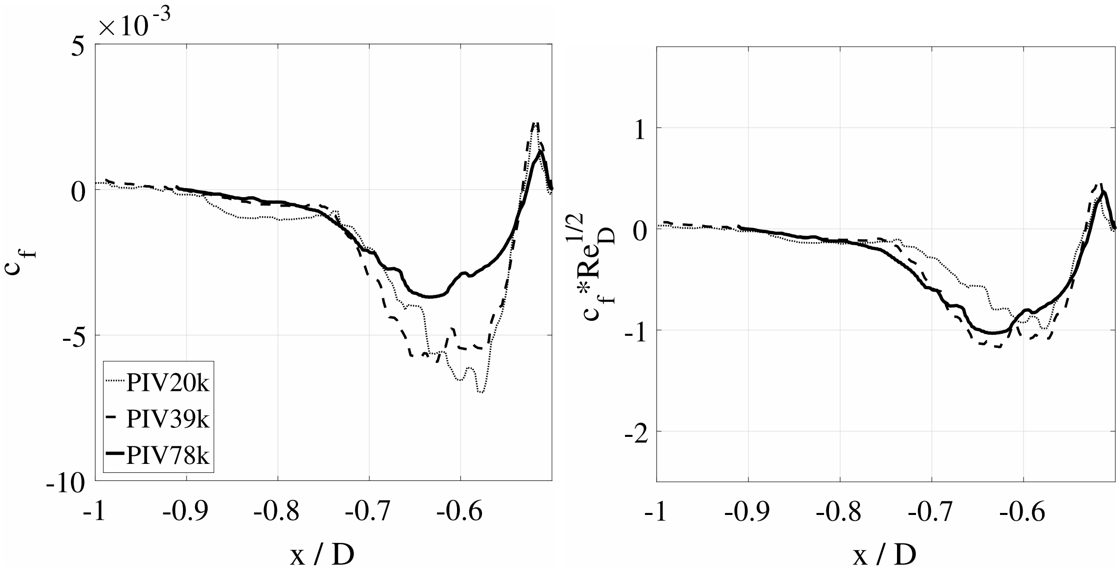

FIGURE 11. Friction coefficient in the symmetry plane in front of the cylinder, taken from the standard PIV.

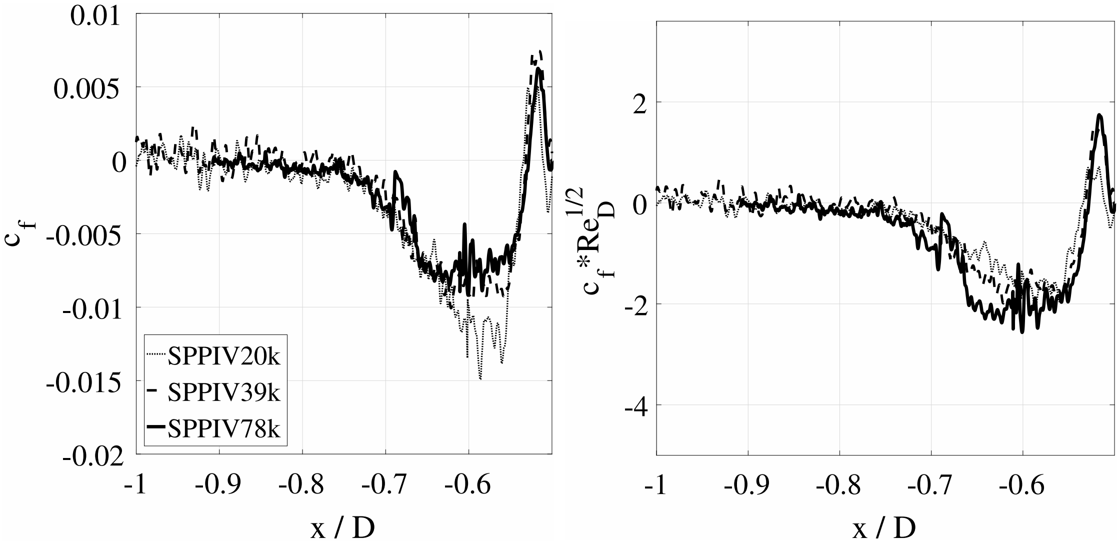

FIGURE 12. Friction coefficient in the symmetry plane in front of the cylinder, taken from the single-pixel PIV. Note the adjusted ordinate compared to figure 10 and 11.

supports the assumption that the scaling was caused by the distinct turbulence structure in the cylinder front. As there was no down-flow and no wall jet at the side of the cylinder, the respective mechanism damping the turbulence did not take effect.

The proposed scaling behavior $c_f \sim 1/\sqrt{Re_D}$ is similar to the one of a laminar boundary layer. In the Blasius solution the wall shear stress scales with $1/\sqrt{Re_x}$, where $Re_x$ is the Reynolds number based on the development length of the boundary layer (Kundu *et al.* 2012). In the setup investigated in this study, the topology was subject to minor changes only, so the development length of the boundary layer caused by the wall jet did not scale with Reynolds number but with the cylinder diameter. Also, the peak velocity of the boundary layer flow along the bottom wall did not scale with Reynolds number but with the bulk velocity of the outer flow $u_b$ (figure 5). Thus, if the friction coefficient scaled with the Reynolds number $Re_x$ based on the development length and the peak velocity of a boundary layer it had to scale in the same way with the Reynolds number $Re_D$ based on the cylinder diameter and bulk velocity. As the wall shear stress in front and lateral of a wall-mounted cylinder behaved like the wall shear stress of a

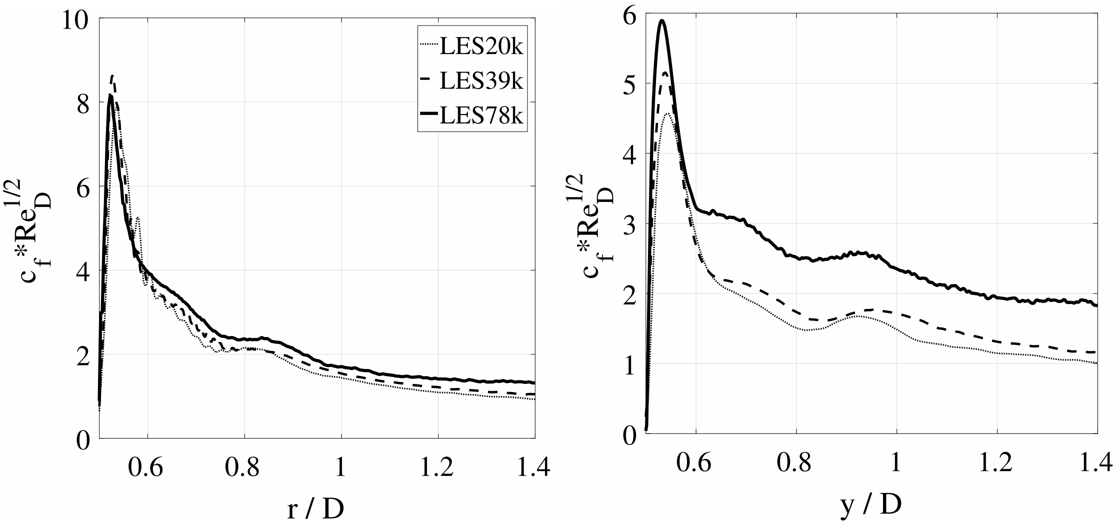

FIGURE 13. Friction coefficient $c_f$ at an angle of 54° (a) and 90° (b) taken from the LES.

laminar boundary layer, it is nearby to assume that the respective near-wall flow in fact was a laminar boundary layer. This assumption is elaborated in the following.

In the conducted simulations, the Reynolds stresses were small in the near-wall flow in the jet region as were the linked contributions to the stress balance (Schanderl *et al.* 2017*a*). This was a consequence of the acceleration of the near-wall flow which led to a negative production of turbulent kinetic energy. The outer flow was independent of the Reynolds number, which suggested that the acceleration of the near-wall flow and the resulting negative production of turbulent kinetic energy will persist at even larger Reynolds numbers. The only mechanism that could end the quasi-laminar scaling of the wall shear stress is the development of instabilities in the boundary layer caused by the wall jet. These instabilities will appear if the local Reynolds number computed by the near-wall velocity peak and its wall distance $Re_\delta$ exceeds a certain threshold. It should be noted that this threshold is hardly to determine a priori as the flow situation is fully three dimensional. In a standard Blasius boundary layer, the critical Reynolds number for Tollmien-Schlichting waves is $Re_{\delta^*} = 520$, $\delta^*$ being the displacement thickness. This corresponds to $Re_\delta = 1481$ which is one order of magnitude larger than $Re_\delta$ in the presented flow (section 5). At $Re_D = 78000$ this local Reynolds number was $Re_\delta \approx 240$. Assuming a linear scaling of the local Reynolds number $Re_\delta$ with $Re_D$, a Reynolds number of approximately $Re_D = 6 * 78000 \approx 470000$ is required to obtain local near-wall profiles in the jet region that are supercritical to the development of Tollmien-Schlichting waves, and thus to trigger turbulence in the boundary layer caused by the wall jet.

## 8. Summary and Conclusions

We investigated the flow in front of a cylinder-wall junction by means of large-eddy simulation and particle image velocimetry. The focus was on the scaling of the wall shear stress for moderate Reynolds numbers. We found that the horseshoe vortex system and the distribution of turbulent kinetic energy was rather independent of the Reynolds number when it was normalized with the bulk velocity of the approaching flow.

However, the wall shear stress did scale with the Reynolds number. We observed a scaling of the friction coefficient by $c_f \sim 1/\sqrt{Re_D}$. This quasi-laminar behavior similar to the one of a Blasius boundary layer was explained by the small Reynolds stresses in this near-wall region between the horseshoe vortex and the cylinder. We expect that this scaling persists to much larger Reynolds numbers as the production term of turbulent kinetic energy was negative in the corresponding region and will stay negative unless the flow topology changes in general. In addition, the local Reynolds number of the boundary layer established by the wall jet is relatively low and a significantly higher Reynolds number is required to trigger instabilities in this boundary layer. In the region where the wall jet decelerated a strong increase of the Reynolds normal stresses in the streamwise direction $u'u'$ with Reynolds number was observed. For this reason, the proposed quasi-laminar scaling of the wall shear stress broke down here.

## Acknowledgements

The authors gratefully acknowledge the financial support of the DFG under grant no. MA2062/11. Computing time was granted by the Leibniz Computing Center (LRZ) of the Bavarian Academy of Sciences.

## REFERENCES

Agui, J. H. & Andreopoulos, J. 1992 Experimental investigation of a 3-dimensional boundary-layer flow in the vicinity of an upright wall mounted cylinder. *Journal of Fluids Engineering - Transactions of the ASME* **114**.

Apsilidis, N., Diplas, P., Dancey, C. L. & Bouratsis, P. 2015 Time-resolved flow dynamics and reynolds number effects at a wall-cylinder junction. *Journal of Fluid Mechanics* **776**, 475–511.

Dargahi, B. 1989 The turbulent flow field around a circular cylinder. *Experiments in Fluids* **8** (1-2), 1–12.

Devenport, W. J. & Simpson, R. L. 1990 Time-dependent and time-averaged turbulence structure near the nose of a wing-body junction. *Journal of Fluid Mechanics* **210**, 23–55.

Escauriaza, Cristian & Sotiropoulos, Fotis 2011 Reynolds Number Effects on the Coherent Dynamics of the Turbulent Horseshoe Vortex System. *Flow, Turbulence and Combustion* **86** (2), 231–262.

Jenssen, U., Schanderl, W. & Manhart, M. 2016 Cylinder wall junction flow: Particle Image Velocimetry and Large Eddy Simulation. In *ERCOFTAC Symposium on Engineering Turbulence Modelling and Measurements*.

Kähler, C.J., Scholz, U. & Ortmanns, J. 2006 Wall-shear-stress and near-wall turbulence measurements up to single pixel resolution by means of long-distance micro-piv. *Experiments in Fluids* **41** (2), 327–341.

Kundu, P. K., Cohen, I. M. & Dowling, D. R. 2012 *Fluid Mechanics*. Academic Press.

Manhart, M. 2004 A zonal grid algorithm for DNS of turbulent boundary layers. *Comput. Fluids* **33** (3), 435–461.

Nicoud, F. & Ducros, F. 1999 Subgrid-Scale Stress Modelling Based on the Square of the Velocity Gradient Tensor. *Flow, Turbulence and Combustion* **62** (3), 183–200.

Paik, J., Escauriaza, C. & Sotiropoulos, F. 2007 On the bimodal dynamics of the turbulent horseshoe vortex system in a wing-body junction. *Physics of Fluids* **19**, 045107.

Peller, N. 2010 Numerische Simulation turbulenter Strömungen mit Immersed Boundaries. PhD thesis, Technische Universität München.

Peller, N., Duc, A. Le, Tremblay, F. & Manhart, M. 2006 High-order stable interpolations for immersed boundary methods. *Int. J. Numer. Methods Fluids* **52**, 1175–1193.

Pfleger, F. 2011 Experimentelle Untersuchung der Auskolkung um einen zylindrischen Brückenpfeiler. PhD thesis, Technische Universität München.

Pope, S. B. 2011 *Turbulent Flows*. Cambridge University Press.

Raffel, M., Willert, C. E., Wereley, S. T. & Kompenhans, J. 2007 *Particle image velocimetry : a practical guide*. Berlin, New York: Springer.

Roulund, Andreas, Sumer, B. Mutlu, Fredsoe, Jorgen & Michelsen, Jess 2005 Numerical and experimental investigation of flow and scour around a circular pile. *Journal of Fluid Mechanics* **534**, 351–401.

Schanderl, W., Jenssen, U. & Manhart, M. 2017*a* Near-wall stress balance in front of a wall-mounted cylinder. *Flow, Turbulence and Combustion* .

Schanderl, W., Jenssen, U., Strobl, C. & Manhart, M. 2017*b* The structure and the budget of turbulent kinetic energy in front of a wall-mounted cylinder. *Journal of Fluid Mechanics* **827**, 285–321.

Schanderl, W. & Manhart, M. 2016 Reliability of wall shear stress estimations of the flow around a wall-mounted cylinder. *Computers and Fluids* **128**, 16–29.

Schanderl, W. & Manhart, M. 2017 Dissipation of turbulent kinetic energy in a cylinder wall junction flow. *submitted to Flow, Turbulence and Combustion* .

Schanderl, W., Manhart, M. & Link, O. 2017*c* Discussion of the impact of pressure fluctuations on local scouring. In *River Sedimentation*. Stuttgart.

Strobl, C., Jenssen, U. & Manhart, M. 2016 Reconstructing velocity statistics from single pixel ensemble correlation PIV. *submitted to Experiments in Fluids* .

Westerweel, J., Geelhoed, P. F. & Lindken, R. 2004 Single-pixel resolution ensemble correlation for micro-piv applications. *Experiments in Fluids* **37** (3), 375–384.